Thèse

Présentée pour obtenir le grade de docteur de l'Université de Strasbourg
Spécialité MATHÉMATIQUES APPLIQUÉES

Guillaume Dollé

Tomographie optique diffuse et de fluorescence pour la détection de tumeurs

Soutenue le 24 septembre 2018
devant la commission d'examen

Christophe Prud'homme	directeur de thèse
Zakaria Belhachmi	co-directeur de thèse
Frédéric Hecht	rapporteur
Stéphanie Salmon	rapporteur
Faker Ben Belgacem	examinateur
Murielle Torregrossa	examinateur (co-encadrant)
Patrice Laquerriere	invité

irma.math.unistra.fr

cnrs
dépasser les frontières

cemosis
Centre de modélisation et de simulation de Strasbourg

IRMA
Institut de Recherche
Mathématique Avancée

Université
de Strasbourg

À la mémoire de mon père, Jean Dollé.

Acknowledgement

Contents

III   Computational framework

Notations

Table 0.0.1: This table highlights the different parameter notations used in the document. These notations may vary slightly for specific sections, but are described in the section introduction anyway. A subscript $\ell \in \{x, m\}$ added to these coefficients for the coupling: x for diffusion and m for fluorescence. Most coefficients are detailed in chapter 2.

Variable	Unity	Description
κ_ℓ		Diffusion coefficient deduced from the Fick law.
n_r		Refraction index of the surrounding environment.
R		Internal reflection coefficient [1].
A		Boundary coefficient depending on R (See section 1.4).
$\mu_{a,\ell}$	mm^{-1}	Absorbtion coefficient.
$\mu'_{s,\ell}$	mm^{-1}	Reduced light scattering coefficient.
c	mm/ps	Light celerity in vaccuum.
c_e	mm/ps	Light celerity in the surrounding environment.
η		Fluorochrome (or fluorophore) yield.
σ	$L.mm^{-1}.mol^{-1}$	Fluorochrome (or fluorophore) molar extinction coefficient.
ξ	$\mu mol.L^{-1}$	Fluorochrome (or fluorophore) concentration.
γ		Fluorochrome (or fluorophore) reaction coefficient.
τ	ps	Fluorochrome (or fluorophore) average lifetime.
R_c	mm	Radius for the cylinder object (phantom).
R_s	mm	Radius for the (virtual) cylinder for sources.
R_f	mm	Radius for the fiber ring.
Δt	ps	Time step.
T	ps	Final time.
h	mm	Mesh characteristic length.
N_f		Number of fibers.
N_s		Number of sources ($N_s = N_f$).
N_d		Number of detectors ($N_d < N_s$).
N_i		Number of inclusions.
α	$\circ$	Fiber cone field of vision angle

Table 0.0.2: This table details notations for the different domains defined in the document and some functionnal spaces used in the document. Most coefficients are detailed in chapter 2 and chapter 4

Notation	Description
Ω	Domain in $\mathbb{R}^d$, for dimension $d = 2, 3$.
$\partial\Omega$	Domain boundary of Ω in $\mathbb{R}^{d-1}$, for dimension $d = 2, 3$.
U	Open bounded domain of Ω.
D	Open bounded domain with $D \subset\subset \Omega$.
Σ_0	Open surface of ∂D.
Σ_e	Smooth surface of ∂D, $\Sigma_0 \cap \Sigma_e = \emptyset$, $\overline{\Sigma}_0 \cup \overline{\Sigma}_e = \partial D$.
Ω_T or Q	Time-space domain $\Omega \times (0, T)$.
$\partial\Omega_T$ or ∂Q	Time-space boundary domain $\partial\Omega \times (0, T)$.
Σ_0^k	Domain in the cone field of vision of the kth fiber on D. This domain represents the source area .
$\Gamma_{d,\varepsilon}^k$	Domain in the cone field of vision of the kth fiber on $\partial\Omega$, $\varepsilon \geq 0$. This domain represents the detection area.
$\mathcal{C}_\alpha^k$	Cone field of vision of the kth fiber.
$\mathcal{M}[0, T]$	Space of measures $C(\Omega) \times [0, T]$.
$M(\overline{\Omega})$	Dual of the space of the continuous functions equipped with its usual norm.
$W^{k,p}$	Sobolev space.
$W_0^{k,p}$	Closure of $C_C^\infty(U)$ in $W^{k,p}$.
H_0^k	Sobolev space $W_0^{k,2}(U)$.

Résumé (version longue)

Guérir les tumeurs est l'un des enjeux majeurs du 21$^{\text{ième}}$ siècle et s'avère être au coeur de nombreuses recherches dans divers domaines. Pour mieux les soigner, il faut en premier lieu être capable de les détecter, les localiser, mais il faut également être en mesure de les qualifier. Nous cherchons à pouvoir identifier le type de tumeur, par exemple maligne ou bénigne et rendre possible leur classification. L'obtention d'informations supplémentaires sur leur nature, par exemple leur taille ou leur densité, permet de les regrouper par type. Parmi les applications possibles, l'adaptation des traitements des patients est rendue possible grâce à une connaissance a priori, un historique. L'assistance à la chirurgie par l'imagerie médicale peut être l'une des pistes futures.

La tomographie optique diffuse et de fluorescence résolue en temps (TR-DOTF), objet de cette thèse, est une méthode qui permet de fournir une information sur les propriétés optiques de diffusion et d'absorption des tissus biologiques. L'objectif ultime du projet est de concevoir un appareil de mesure (tomographe) éventuellement portatif, permettant de reconstruire des images multidimensionnelles 2D/3D des cartes optiques du milieu avec une résolution suffisante pour être utilisée en milieu hospitalier à des fins de diagnostic préclinique. L'avantage notable de cette technique est d'être non-invasive et non-irradiante. Elle est également peu coûteuse en comparaison avec des solutions alternatives telles que l'Imagerie par Résonance Magnétique (IRM).

Le projet est porté par l'équipe IMIS du laboratoire Icube spécialisé dans l'imagerie d'optique. L'équipe dispose d'un tomographe expérimental assemblé sur table de montage donnant accès à des mesures réelles et partielles à partir d'objet translucide ou encore d'êtres vivants (fig. 0.0.1). Le temps de vol des photons diffusés

Figure 0.0.1: Tomographe expérimental construit par l'équipe IMIS de l'hôpital civil de Strasbourg sur une table de montage.

dans cet objet est obtenu par comptage grâce à un jeu de détecteurs disposés de manière régulière tout autour de l'objet. Beaucoup de travaux ont déjà étudié le sujet. Dans cette thèse, réalisée à l'institut de recherche en mathématique avancée IRMA (Strasbourg) en collaboration avec le laboratoire de mathématiques, informatiques et application (LMIA, Mulhouse), nous proposons une formalisation mathématique de certains aspects du problème général. En particulier, nous proposons une analyse détaillée du problème direct qui tient compte du type de mesure physique employée qui nous paraît être un apport novateur pour la communauté. Puis nous proposons des solutions pour résoudre numériquement ce problème de manière efficace grâce à des techniques modernes issues du calcul haute performance qui nous paraissent peu connues de la communauté de la tomographie optique diffuse (TOD).

Ce document de thèse est décomposé en trois parties. Une première partie (part I) explicite le choix du modèle de diffusion utilisé dans le cadre du problème de TOD avec fluorescence. La deuxième partie propose d'étudier le problème d'un point de vue mathématique en détaillant le choix des espaces de solutions pour des sources de type δ-Dirac bien choisies (part II). Enfin, les aspects numériques liés au code de calcul développé pour reconstruire des images des cartes optiques sont détaillés dans la dernière partie (part III). Nous proposons de résumer les principaux résultats ci-dessous.

Modélisation

La première partie de la thèse fait l'état de l'art du problème de tomographie optique diffuse et des différentes techniques existantes. L'équation du transfert radiatif est en général utilisée pour modéliser le phénomène de propagation des photons dans un milieu quelconque. En notant la luminance L, l'équation s'écrit sous la forme

$$\left\{ \frac{1}{c}\frac{\partial}{\partial t} + \mathbf{s} \cdot \nabla + [\mu_a(\mathbf{r}) + \mu_s(\mathbf{r})] \right\} L(\mathbf{r}, \mathbf{s}, t) = \mu_s(\mathbf{r}) \int_{4\pi} p(\mathbf{s}', \mathbf{s}) L(\mathbf{r}, \mathbf{s}', t) d\omega(\mathbf{s}') + q(\mathbf{r}, \mathbf{s}', t).$$

avec respectivement les paramètres d'absorption μ_a et de scattering μ_s, et ω l'angle solide. Cette équation tient compte non seulement des paramètres spatiaux et temporels, mais aussi de l'angle solide sous lequel les photons entrent et ressortent. La résolution de cette équation étant coûteuse en termes de ressources de calculs, on s'intéresse au cas particulier de l'approximation de diffusion

$$-\operatorname{div}(\kappa(\mathbf{r})\nabla\phi(\mathbf{r}, t)) + c_e\mu_{a,x}(\mathbf{r})\phi(\mathbf{r}, t) + \frac{\partial\phi(\mathbf{r}, t)}{\partial t} = q_0(\mathbf{r}, t) .$$

Le paramètre de diffusion s'exprime par la loi de Fick alors

$$\kappa(\boldsymbol{r}) = \frac{c_e}{3(\mu_a(\boldsymbol{r}) + \mu_s'(\boldsymbol{r}))}$$

avec μ_s' un paramètre de scattering réduit. Cette approximation présente l'avantage d'être plus simple, mais introduit une contrainte entre les coefficients d'absorption et de scattering réduit $\mu_a << \mu_s'$ et peut être discutable d'un point de vue de la physique du problème. Pour améliorer le contraste des images, une méthode consiste à ajouter de la fluorescence en utilisant des marqueurs (vert d'indocyanine). Cette méthode permet en outre d'ajouter de l'information dans les mesures lorsque celle-ci est effectuée pour une certaine longueur d'onde. Dans notre modèle, les mesures de fluorescence sont considérées pour une longueur d'onde de réémission des photons d'excitation.

D'un point de vue mathématique, le problème auquel nous nous intéressons s'écrit sous la forme d'un système de deux équations aux dérivées partielles (EDP) faiblement couplées. Notons Ω le domaine d'étude dans $\mathbb{R}^d$ avec d la dimension pour $d = 2, 3$ et $T > 0$ le temps final. Nous utiliserons les indices $\ell \in \{x, m\}$ pour distinguer respectivement les variables de diffusion et de fluorescence. Soient $k \in [1, N_s]$ fibres réparties de manière régulière tout autour de l'objet étudié, nous considérons le système d'équation suivante lorsque la k^{th} fibre est une source de lumière.

$$\begin{cases} -\nabla \cdot (\kappa_x \nabla\phi_x^k) + c_e\mu_{a,x}\phi_x^k + \dfrac{\partial\phi_x^k}{\partial t} = q_x^k & \text{on } \Omega \times (0, T) , \\[2mm] -\nabla \cdot (\kappa_m \nabla\phi_m^k) + c_e\mu_{a,m}\phi_m^k + \dfrac{\partial\phi_m^k}{\partial t} = \gamma q_m^k & \text{on } \Omega \times (0, T) , \\[2mm] \phi_x^k + 2\mathrm{A}\kappa_x \dfrac{\partial\phi_x^k}{\partial\boldsymbol{n}} = 0 & \text{on } \partial\Omega \times (0, T) , \\[2mm] \phi_m^k + 2\mathrm{A}\kappa_m \dfrac{\partial\phi_m^k}{\partial\boldsymbol{n}} = 0 & \text{on } \partial\Omega \times (0, T) , \\[2mm] \phi_x^k(0, \cdot) = \phi_{x,0} , \\[1mm] \phi_m^k(0, \cdot) = \phi_{m,0} , \end{cases} \qquad (0.0.1)$$

La première équation décrit la diffusion des photons dans un milieu pour une mesure prise à une certaine longueur d'onde. La deuxième équation, dite de fluorescence, représente la diffusion de la lumière lorsqu'il y a réémission de photons d'excitation en présence d'un fluorophore dans le domaine. Nous choisissons dans notre mode de prendre en compte les modes de mesures de de contact et de non-contact (chapter 2) pour des pulses de type δ-Dirac.

$$q_x^k = \begin{cases} \delta_{x_0^k}(\mathbf{x})\delta(t_0) & \text{(contact)}, \\ \delta_{\Sigma_0^k}(\mathbf{x})\delta(t_0) & \text{(non contact)}. \end{cases} \qquad (0.0.2)$$

Dans le cas non-contact, la mesure n'est plus ponctuelle, nous devons alors tenir compte du cône de vision de la fibre (fig. 0.0.2). Le modèle de fluorescence considère la diffusion des photons réémis lors de l'excitation du

Figure 0.0.2: Cette figure représente les deux modes de mesure contact et non-contact. Les sources sont situées à l'intérieur du domaine à une distance au bord correspondant au libre parcours moyen.

(a): Mode contact. La fibre est placée en contact avec le bord. La source en x_0 et la mesure en x_d sont ponctuelles.

(b): Mode non-contact. La fibre est placée à une certaine distance du bord. La source en Σ_0 et la mesure en Γ_d sont surfaciques.

fluorophore. Nous considérons alors pour une certaine longueur d'onde de réémission, l'équation de diffusion avec un terme source qui s'exprime

$$q_m^k(\mathbf{x}, t) = \frac{1}{\tau} \int_0^t \phi_x^k(\mathbf{x}, s) e^{(\frac{t-s}{\tau})} ds. \tag{0.0.3}$$

Le couplage des deux équations eq. (0.0.1) s'effectue par le terme source de l'équation de fluorescence qui s'écrit comme un terme de convolution entre la solution de diffusion et un terme en exponentielle. Les inconnues du problème que nous cherchons à déterminer sont les coefficients de diffusion et d'absorption supposés différents pour chacune des deux équations. Pour la fluorescence, nous recherchons également la concentration du fluorophore et son temps de vie.

Reconstruction

Problème direct

Dans une deuxième partie de thèse, nous nous intéressons à la résolution du système d'équations (0.0.1) et du choix des espaces de solutions. On se propose dans un premier temps de faire l'étude du problème direct. Les paramètres d'entrée du modèle complet $\kappa_x, \kappa_m, \mu_{a,x}, \mu_{a,m}, \tau, \gamma$ sont supposés connus, nous cherchons à déterminer le couple de solutions ϕ_x, ϕ_m. Nous distinguons dans notre étude deux types de mesures lorsque les fibres sont placées en contact avec l'objet et en non-contact. Ainsi pour des pulses de Dirac en entrée, d'un point de vue théorique, le terme source q_x n'a pas une régularité définie dans un espace de Sobolev de type $H^{-1}(\Omega)$. Dans ce cas précis, le cadre variationnel classique ne s'applique pas. Le choix des espaces de solutions doit être distingué pour chaque mode de mesure. Nous étudions les cas d'existence et d'unicité du problème pour le cas de la diffusion et de la fluorescence et nous proposons un résultat de convergence. Nous remarquons que dans le cas du modèle de fluorescence, le terme source peut se réécrire sous la forme d'une équation différentielle ordinaire (EDO)

$$q_m'^k - \frac{1}{\tau} q_m^k = \frac{1}{\tau} \phi_x^k. \tag{0.0.4}$$

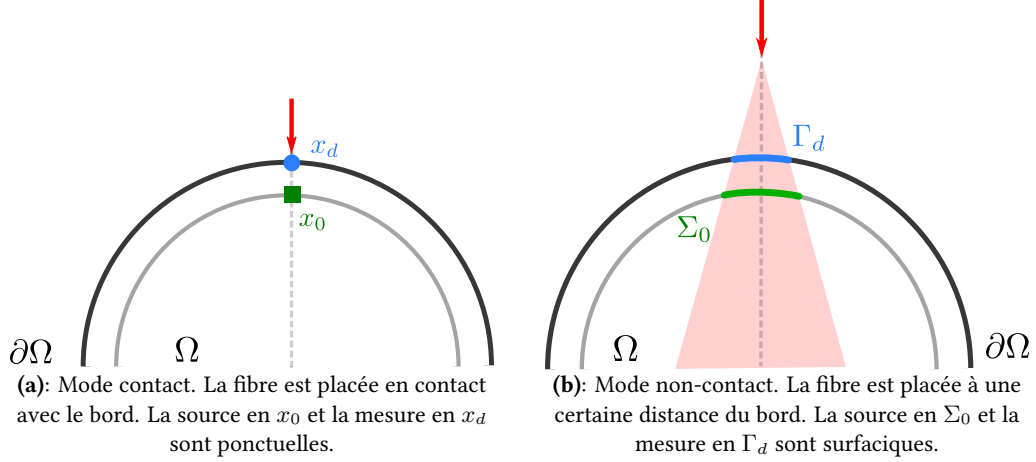Le problème (0.0.1) peut alors être réécrit sous la forme d'un système dégénéré

$$
\begin{cases}
-\nabla \cdot (\kappa_x \nabla \phi_x^k) + c_e \mu_{a,x} \phi_x^k + \dfrac{\partial \phi_x^k}{\partial t} = q_x^k & \text{on } \Omega \times (0,T)\,, \\[2mm]
q_m'^k - \dfrac{1}{\tau} q_m^k = \dfrac{1}{\tau} \phi_x^k & \text{on } \Omega \times (0,T)\,, \\[2mm]
-\nabla \cdot (\kappa_m \nabla \phi_m^k) + c_e \mu_{a,m} \phi_m^k + \dfrac{\partial \phi_m^k}{\partial t} = \gamma q_m^k & \text{on } \Omega \times (0,T)\,, \\[2mm]
\phi_x^k + 2\mathrm{A}\kappa_x \dfrac{\partial \phi_x^k}{\partial \boldsymbol{n}} = 0 & \text{on } \partial\Omega \times (0,T)\,. \\[2mm]
\phi_m^k + 2\mathrm{A}\kappa_m \dfrac{\partial \phi_m^k}{\partial \boldsymbol{n}} = 0 & \text{on } \partial\Omega \times (0,T)\,. \\[2mm]
\phi_x^k(0,\cdot) = \phi_{x,0} \\[1mm]
\phi_m^k(0,\cdot) = \phi_{m,0}.
\end{cases}
\tag{0.0.5}
$$

Le terme source q_m de l'équation de fluorescence peut se calculer soit explicitement en résolvant l'EDO, soit en traitant directement le terme intégral.

Des résultats d'existence et d'unicité peuvent être énoncés sous certaines hypothèses. En considérant des hypothèses de régularité sur les paramètres en entrée suivante,

$$
\begin{cases}
\kappa_\ell, \mu_{a,\ell} \in L^\infty(\Omega)\,, \\[1mm]
\mu_{a,\ell} \geq 0\,, \\[1mm]
0 < \kappa_0 \leq \kappa_x,\ \kappa_m \leq \kappa_1\,,
\end{cases}
\tag{0.0.6}
$$

nous pouvons montrer (cf. section 2.2) l'existence de solution ϕ_x pour l'équation de diffusion et de fluorescence ϕ_m et l'unicité uniquement pour ϕ_m pour le cas contact (cf. section 2.2.1). Nous énonçons le théorème suivant pour le cas de mesure en contact,

Théorème. *Sous l'hypothèse (0.0.6) pour tout $1 \leq q < \frac{d+2}{d+1}$ il existe une solution $\phi_x \in L^q(0,T;W^{1,q}(\Omega))$ du système (2.1.1) et il existe une unique solution ϕ_m telle que: si $d = 2$, $\phi_m \in L^2(0,T;H^1(\Omega)) \cap C([0,T];L^2(\Omega))$, $\phi_m' \in L^2(0,T;(H^1(\Omega))')$. Si $d = 3$, alors $\phi_m, \phi_m' \in L^p(0,T,W^{1,p}(\Omega))$ ($p \leq \frac{3}{2}$).*

Pour le cas non-contact (cf. section 2.2.2), la mesure est surfacique, nous devons introduire un espace de fonction défini pour les surfaces sources Σ_0. Si Σ_0 est une surface ouverte, nous notons Σ_e une surface régulière telle que $\Sigma_0 \cap \Sigma_e = \emptyset$, $\overline{\Sigma_0} \cup \overline{\Sigma_e} = \partial D$, avec D un ensemble ouvert borné $D \subset\subset \Omega$.

$$
H_{\Sigma_0}^1(\Omega) = \mathrm{cl}\big(\{v \in C^\infty(\Omega) \cap H^1(\Omega)\,;\ v = 0 \text{ sur } \Sigma_e\}\big)\,,
\tag{0.0.7}
$$

Notons en particulier que dans le cas de la fluorescence, le terme source est une convolution de la solution de diffusion par une exponentielle. La régularité de ϕ_m dépend donc de la régularité ϕ_x. Ainsi pour le cas de mesure en non-contact, nous pouvons énoncer ce théorème

Théorème. *Sous les hypothèses (2.2.1) il existe une unique solution (ϕ_x, ϕ_m) au système (2.1.1), telle que $\phi_x \in L^2(0,T;H) \cap C(0,T;V')$, et $\phi_m \in L^2(0,T;H^2(\Omega) \cap V) \cap C(0,T;V)$, $\frac{\partial \phi_m}{\partial t} \in L^2(0,T;H)$.*

Notre stratégie pour résoudre numériquement le modèle eq. (0.0.1) se base sur une approche par éléments finis. Nous proposons d'exprimer le problème sous sa forme faible. En notant $\boldsymbol{\phi} = (\phi_x, \phi_m)$, $\boldsymbol{\kappa} = (\kappa_x, \kappa_m)$, $\boldsymbol{\mu_a} = (\mu_{a,x}, \mu_{a,m})$ et $\mathbf{q} = (q_x, q_m)$ pour $k \in [1, N_s]$, nous avons

$$
\int_\Omega \big(\boldsymbol{\kappa}^k \nabla \boldsymbol{\phi}^k : \nabla \boldsymbol{v} + c_e \boldsymbol{\mu_a}^k \boldsymbol{\phi}^k \boldsymbol{v}\big) + \int_{\partial\Omega} \frac{1}{2\mathrm{A}} \boldsymbol{\phi}^k \boldsymbol{v} + \int_\Omega \frac{\partial \boldsymbol{\phi}^k}{\partial t} \boldsymbol{v} = f_v(\mathbf{q}),
\tag{0.0.8}
$$

avec le terme source f_v un opérateur linéaire bien choisi qui dépend du mode de mesure contact ou non-contact (cf. section 2.3). Nous pouvons également utiliser la notation usuelle

$$
a(\boldsymbol{\phi}^k, \boldsymbol{v}) + \int_\Omega \frac{\partial \boldsymbol{\phi}^k}{\partial t} \boldsymbol{v} = l(\boldsymbol{v}),
\tag{0.0.9}
$$

avec a une forme bilinéaire symétrique définie positive et l une forme linéaire.

Notons que le terme source intégrale q_m est un terme mémoire qui peut se décomposer sous la forme $q_m = B_n + R_n$ avec B_n un terme de stockage connu au temps $t \approx t_n$ fixé

$$B_n(\boldsymbol{x}) = \frac{1}{\tau} \int_0^{t_n} \phi_x(\boldsymbol{x}, s) e^{(\frac{t_{n+1}-s}{\tau})} ds \ , \tag{0.0.10}$$

et R_n un terme intégral restant à calculer à chaque itération

$$R_n(\boldsymbol{x}) = \frac{1}{\tau} \int_{t_n}^{t_{n+1}} \phi_x(\boldsymbol{x}, s) e^{(\frac{t_{n+1}-s}{\tau})} ds \ . \tag{0.0.11}$$

Nous écrivons la formulation semi-discrète en temps pour le schéma d'Euler implicite du système (0.0.1)

$$\int_\Omega (\kappa \nabla \boldsymbol{\phi}^{(n+1)} : \nabla \boldsymbol{v} + c_e \mu_a \boldsymbol{\phi}^{(n+1)} \cdot \boldsymbol{v}) + \int_{\partial\Omega} \frac{1}{2A} \boldsymbol{\phi}^{(n+1)} \cdot \boldsymbol{v} + \int_\Omega \frac{\boldsymbol{\phi}^{(n+1)}}{\Delta_t} \cdot \boldsymbol{v}$$
$$= \int_\Omega \begin{pmatrix} q_x^{(n+1)} \\ \gamma(\boldsymbol{x}) B_n(\boldsymbol{x}) \end{pmatrix} \cdot \boldsymbol{v} + \int_\Omega \begin{pmatrix} 0 \\ \gamma(\boldsymbol{x}) R_n(\boldsymbol{x}) \end{pmatrix} \boldsymbol{v} + \int_\Omega \frac{\boldsymbol{\phi}^{(n)}}{\Delta_t} \cdot \boldsymbol{v} \ . \tag{0.0.12}$$

En pratique nous utilisons une méthode de différentiation rétrograde (BDF) pour la discrétisation en temps afin de pouvoir monter à l'ordre élevé. Enfin nous établissons la formulation discrète complète avec traitement du terme intégral de fluorescence. Soit $i \in [1, N_h]$ et N_h le nombre de noeuds du maillage, nous avons

$$\sum_{j=1}^{N_h} \phi_j^{(n+1)} a_{i,j} + \sum_{j=1}^{N_h} \phi_j^{(n+1)} c_e b_{i,j} + \sum_{j=1}^{N_h} \phi_j^{(n+1)} \left(\frac{1}{2A} + \frac{1}{\Delta_t} \right) m_{i,j} - \sum_{j=1}^{N_h} \phi_j^{(n+1)} C_1 f_{i,j}$$
$$= \begin{pmatrix} q_x \\ \gamma(\boldsymbol{x}) B_n(\boldsymbol{x}) \end{pmatrix} \int_\Omega \boldsymbol{\varphi}_i + \sum_{j=1}^{N_h} \phi_j^{(n)} C_2 f_{i,j} + \sum_{j=1}^{N_h} \phi_j^{(n)} \frac{1}{\Delta_t} m_{i,j} \ , \tag{0.0.13}$$

avec C1, C2 des constantes. Nous proposons dans la section 2.3.4 deux résultats de convergence pour les cas de mesure en mode contact et en mode non contact. Dans le cas contact, le théorème est basé sur un résultat de Scott [10],

Théorème. *Si ϕ_x est solution de* (2.1.1) *dans le sens des distributions pour $q_x = \delta_{x_0}$ et $\phi_{x,h}$ est la solution associé au problème variationnel, alors*

$$\|\phi_x - \phi_{x,h}\|_{H^s} \le C(x_0) h^{2m - \frac{d}{2} - s} \quad \text{for } 2m - k \le s < 2m - \frac{d}{2} \tag{0.0.14}$$

si $k \ge 2m$ alors $C(x_0)$ tend vers l'infini lorsque x_0 approche le bord du domaine $\partial\Omega$

En particulier, nous avons dans le cas $d = 2$, $m = 1$ et $\ell = 1$ un taux de convergence de l'ordre de $O(h^{1-s})$ pour $0 \le s \le 1$. Avec $d = 3$, nous obtenons $O(h^{\frac{1}{2}-s})$ pour $0 \le s \le \frac{1}{2}$.

Remark 1. *Nous rappelons que la distance au bord de la source lumineuse de type δ-Dirac $d(x_0, \partial\Omega)$ correspond à la distance de libre parcours moyen qui est la distance parcourue par un photon avant la première collision. Notons que lorsque x_0 s'approche de $\partial\Omega$, alors le théorème précédent indique que $C(x_0)$ tend vers l'infini $+\infty$.*

Dans le cas de mesures en non-contact la proposition est basée sur un résultat de Fabrège-Maury [11]

Proposition. *Nous avons l'estimateur, pour $0 \le r \le 1$, $0 \le s \le \frac{1}{2}$ et en prenant des éléments finis P^1,*

$$\|\phi_x - \phi_{x,h}\|_{H^r} \le C h^{1-r} \left(\inf_{\phi_{x,h} \in V_h} \|\phi_x - \phi_{x,h}\| + h^s |\varphi|_{-1/2+s, \Sigma_0} \right) . \tag{0.0.15}$$

En particulier, en prenant $d = 2$ et dans le cas extrême $r = 1$, si nous supposons que $\phi_x \in H^2$, nous obtenons

$$\|\phi_x - \phi_{x,h}\|_{H^1} \le C \left(\sqrt{h} \|\phi_x\|_{H^2} + h^s |\varphi|_{-1/2+s, \Sigma_0} \right) . \tag{0.0.16}$$

La résolution du problème direct est illustrée par un code de calcul réalisé à l'aide de la librairie Feel++. C'est une librairie proposant un langage embarqué au C++ (DSEL) pour résoudre des équations aux dérivées partielles basé sur les méthodes de Galerkin standard. L'équipe IMIS a développé au cours de ses précédents travaux un code Matlab séquentiel pour reconstruire des images des cartes optiques pour le problème de TOD. Une des difficultés du problème de TOD est de devoir résoudre des problèmes de grandes tailles. En effet, le choix des discrétisations espaces-temps est imposé par la nature même du problème et en fonction de la résolution d'image souhaitée. L'un des apports de cette thèse est de proposer un code générique permettant de passer à l'échelle sur des architectures multicoeurs. Ce code propose une parallélisation spatiale basée principalement sur le standard MPI, gère des dimensions arbitraires et fournit des outils mathématiques embarqués dans le langage pour des méthodes d'ordres élevées en espace et en temps.

Figure 0.0.3: Validation du modèle sur un objet fantôme. Le paramètre de diffusion est estimé approximativement égal à $\mu_a = 0.6$. Cette figure montre une comparaison des solutions numériques $\Phi_x^0(x_i, t)$ obtenu avec deux codes de calculs réalisés en Matlab et avec la librairie Feel++ et des mesures expérimentales pour différent détecteur d'une même source en mode contact. Afin de comparer avec les mesures, les graphes sont recalés par rapport au maximum du pic et normalisé. Les solutions numériques sont également convoluées par la réponse impulsionnelle de l'appareil, qui correspond théoriquement à une mesure à vide. Nous pouvons remarquer que les graphes des simulations se superposent parfaitement. Pour les mesures, le front montant est parfaitement capté, en revanche le résultat est moins bon sur le front descendant. Une explication plausible est que le fantôme plastique n'est pas parfaitement homogène, le paramètre estimé n'est alors pas exactement égal à $\mu_a = 0.6$.
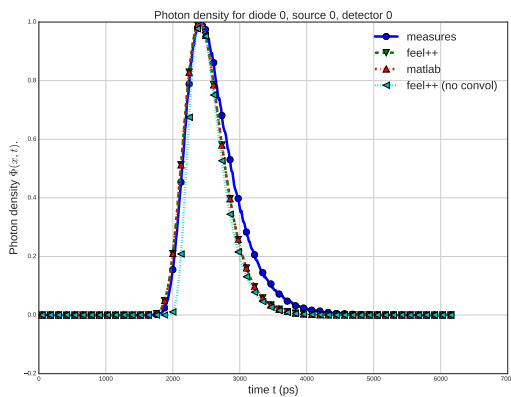
(a): Photon density for the detector 0
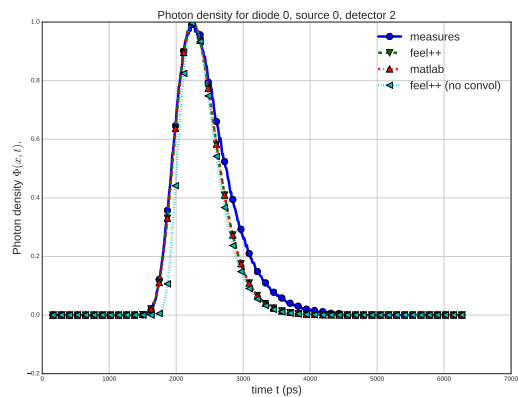
(b): Photon density for the detector 2
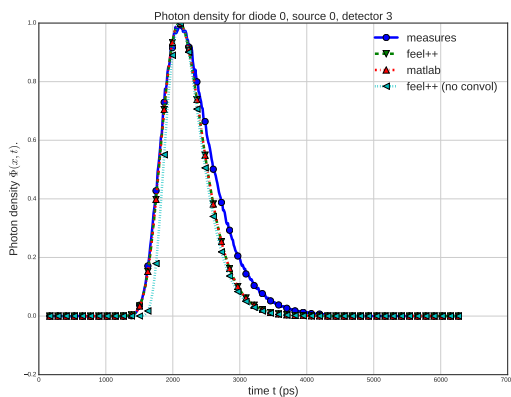
(c): Photon density for the detector 3
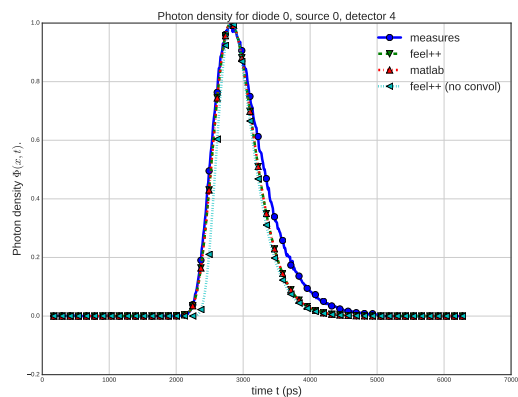
(d): Photon density for the detector 4

Nous proposons une vérification croisée du code avec la version existante du logiciel Matlab. Cette étape nous a permis de confirmer la bonne résolution du problème. Puis le problème direct a été validé sur des mesures expérimentales pour un objet fantôme homogène composé de matière plastique dont les paramètres optiques estimés sont connus (fig. 0.0.3).

Problème inverse

Nous proposons ensuite () une formulation pour le problème inverse, qui est dans la plupart des cas mal posé. Dans ce problème, nous devons reconstruire 2 paramètres spatiaux pour le problème de diffusion, et 4 paramètres spatiaux pour le problème de fluorescence. En considérant le système (0.0.1), les entrées du modèle inverse sont les solutions ϕ_x, ϕ_m et sont supposées connues. Nous cherchons à déterminer le jeu de paramètres $\kappa_x, \kappa_m, \mu_{a,x}, \mu_{a,m}, \tau, \eta$. Un argument basé sur un résultat de Canuto-Kavian précise que nous ne pouvons pas reconstruire plus de 2 paramètres simultanément. En particulier, si nous considérons le problème

$$\begin{cases} \rho \frac{\partial u}{\partial t} - \nabla \cdot (\kappa \, \nabla u) + \mu u & = & 0 & \text{in } \Omega \times (0, T), \\ u(\boldsymbol{x}, 0) & = & u_0 & \text{in } \Omega, \\ u(\boldsymbol{x}, t) & = & f(\boldsymbol{x}, t) & \text{in } \partial\Omega. \end{cases} \tag{0.0.17}$$

alors nous pouvons reconstruire les paramètres ρ, κ, μ selon les cas qui suivent.

(i) Étant donnés $\mu(\boldsymbol{x})$ et $\kappa(\boldsymbol{x})$ de la forme $\kappa(\boldsymbol{x}) = a(\boldsymbol{x})I_N$ ou $\kappa(x)$ est une fonction à valeur scalaire et I_N est la matrice identité $a(\boldsymbol{x})$ est identifiable en supposant que $\Sigma_0 = \Gamma_d = \partial\Omega$

(ii) Étant donnés $\kappa(\boldsymbol{x}) = a(\boldsymbol{x})I_N$, $\rho(\boldsymbol{x}), \mu(\boldsymbol{x})$ est identifiable en supposant que $\Sigma_0 = \Gamma_d = \partial\Omega$

(iii) Étant donnés $\rho(\boldsymbol{x})$ et $\kappa(\boldsymbol{x}) = a(\boldsymbol{x})I_N, \mu(x)$ est identifiable en supposant que $\Sigma_0 \cup \Gamma_d = \partial\Omega$

Le problème inverse que nous devons traiter est plus compliqué dans le sens suivant

1. Pour déterminer les paramètres $\kappa_x, \mu_{a,x}$, les données sont les sources et les mesures au bord. Cependant, nous pouvons reformuler le problème sous la forme de (0.0.17), le résultat de Canuto-Kavian reste valable.

2. Le problème pour déterminer les paramètres de fluorescence $\kappa_m, \mu_{a,m}, \gamma, \tau$ est un problème inverse "mixte" ou les inconnus sont un terme source γ, la conductivité κ_m, l'absorption $\mu_{a,m}$ et le temps de vie τ. Aussi, le précédent résultat peut s'appliquer dans les cas ou l'on reconstruit

   (a) les paramètres κ_m et $\mu_{a,m}$, ou
   (b) les paramètres sources γ et τ.

Nous discutons cette stratégie employée pour le choix de ces deux variables d'intérêts du problème de fluorescence et proposons une stratégie de résolution. L'une de ces stratégies adoptées suppose que ces paramètres de diffusion et d'absorption des tissus varient peu entre le problème de diffusion et celui de fluorescence, ce qui est discutable d'un point de vue de la physique. Dans le choix précédent des paramètres à reconstruire cas, nous devons alors résoudre deux types de problèmes inverses distincts : un problème d'identification de paramètres de la forme bilinéaire du problème et un problème de reconstruction sur les sources.

Nous choisissons de traiter le problème inverse comme un problème d'optimisation basé sur des méthodes adjointes. Différentes fonctionnelles coûts sont détaillées en fonction du type d'échantillon que nous avons à disposition. En pratique, avec le tomographe expérimental, le jeu de détecteur nous permet d'obtenir des mesures au bord partielles. Nous considérons des mesures complètes sur tout le domaine pour tester notre code de calculs à partir d'observations numériques. Dans ce cas précis, le problème d'optimisation s'écrit

$$J(\tilde{\kappa}, \tilde{\mu}) = \min_{\substack{\phi \in V \text{ sol } (0.0.1) \\ \forall \kappa, \mu \in U_{ad}}} J_0(\phi(\kappa, \mu)) + \mathfrak{r}(\kappa, \mu), \tag{0.0.18}$$

ou $\mathfrak{r}(\kappa, \mu)$ est un terme de régularisation bien choisi pour assurer au problème d'optimisation d'être bien posé. Une régularisation classique est la régularisation de Tikhonov

$$\mathfrak{r}(\kappa, \mu) = \frac{\alpha_\kappa}{2} \int_U |\nabla \kappa|^2 dU + \frac{\alpha_\mu}{2} \int_U |\mu|^2 dU \tag{0.0.19}$$

qui ajoute de la diffusion sur la conductivité qui est dans le terme d'ordre 2. La difficulté se situe dans le choix des paramètres de régularisation qu'il faut bien choisir pour assurer la convergence. Dans le cas du problème de diffusion, nous pouvons introduire une équation dite adjointe

$$\begin{cases} -\nabla \cdot (\kappa \nabla p) + c_e \mu p - \dfrac{\partial p}{\partial t} = (\phi - \phi_{obs}) & \text{dans } Q \\[2mm] p + 2A\kappa \dfrac{\partial p}{\partial \mathbf{n}} = 0 & \text{sur } \partial Q \\[2mm] p(\cdot, T) = 0. \end{cases} \tag{0.0.20}$$

Notons que cette nouvelle équation est rétrograde. L'adjoint nous permet de calculer les gradients de la fonctionnelle à minimiser par rapport aux paramètres à déterminer et ainsi de les mettre à jour

$$< \frac{\partial J(\kappa, \mu)}{\partial \kappa}, \delta\kappa > = -\int_Q \nabla\phi \nabla p \delta\kappa + \lim_{\alpha \to 0} \frac{\mathfrak{r}(\kappa^\delta, \mu) - \mathfrak{r}(\kappa, \mu)}{\alpha}$$

$$< \frac{\partial J(\kappa, \mu)}{\partial \mu}, \delta\mu > = -\int_Q c_e \delta\mu \phi p + \lim_{\alpha \to 0} \frac{\mathfrak{r}(\kappa, \mu^\delta) - \mathfrak{r}(\kappa, \mu)}{\alpha}. \tag{0.0.21}$$

Dans le cas du problème de fluorescence ou nous cherchons à reconstruire uniquement les paramètres du fluorophore (problème inverse sur les sources) nous pouvons introduire de la même manière une équation adjointe rétrograde

$$\begin{cases} -\nabla \cdot (\kappa \nabla p) + c_e \mu p - \dfrac{\partial p}{\partial t} = (\psi - \psi_{\text{obs}}) & \text{dans } Q \\[2mm] p + 2A\kappa \dfrac{\partial p}{\partial \mathbf{n}} = 0 & \text{sur } \partial Q \\[2mm] p(\cdot, T) = 0. \end{cases} \tag{0.0.22}$$

Deux méthodes nous permettent d'obtenir les gradients, soit en se basant sur une approche par adjointe sur le système (0.0.1), soit en utilisant le système dégénéré (0.0.5) et en calculant l'adjoint de l'ODE. Les deux méthodes aboutissent au même résultat suivant

$$< \frac{\partial J(\gamma, \tau)}{\partial \gamma}, \delta\gamma > = \int_Q \left(\frac{1}{\tau} \int_0^t \phi_x(s) e^{\frac{t-s}{\tau}} ds \right) p\delta\gamma + \lim_{\alpha \to 0} \frac{\mathfrak{r}(\gamma^\delta, \tau) - \mathfrak{r}(\gamma, \tau)}{\alpha}$$

$$< \frac{\partial J(\gamma, \tau)}{\partial \tau}, \delta\tau > = \int_Q \left(-\frac{\gamma}{\tau^2} \int_0^t \phi_x(s) \left(1 + \frac{t-s}{\tau} \right) e^{\frac{t-s}{\tau}} ds \right) p\delta\tau + \lim_{\alpha \to 0} \frac{\mathfrak{r}(\gamma, \tau^\delta) - \mathfrak{r}(\gamma, \tau)}{\alpha} \tag{0.0.23}$$

Pour mettre à jour les paramètres à reconstruire $\kappa_x, \mu_{a,x}, \tau, \gamma$, nous devons donc résoudre 4 systèmes linéaires pour déterminer les solutions d'états ϕ_x, ϕ_m et les adjoints associés p_x, p_m afin de calculer les gradients des fonctionnelles par rapport aux paramètres. Notons que dans le cas de l'équation rétrograde, la connaissance de la solution d'états est requise pour calculer les termes sources de l'équation adjointe.

Aspects numériques

Dans la dernière partie de la thèse, nous détaillons les apports numériques de ce travail. Pour gérer les différents modes de mesures sur des géométries arbitraires, nous devons être en mesure de sélectionner les éléments du maillage sur lesquels nous désirons imposer les sources de lumière de type Dirac qui dépendent du mode de mesure. Dans cette thèse nous proposons un algorithme basé sur la méthode des levelset pour récupérer une fonction distance au bord. Nous construisons des itérateurs sur des éléments du maillage à partir d'outils mathématiques proposés par la librairie Feel++. Cet algorithme réutilise plusieurs fonctionnalités développées lors de précédents travaux de thèse qui ont été vérifiées, éprouvées, puis mises à profit dans ce projet. (fig. 0.0.4)

Le problème direct consiste à résoudre un système linéaire pour N sources distinctes réparties régulièrement tout autour de l'objet. Nous présentons les outils mis à disposition par la librairie Feel++ pour résoudre le problème sur une source. Nous détaillons différentes approches possibles pour résoudre le modèle direct. Nous introduisons également les différents solveurs utilisés et en particulier celui choisi pour résoudre le cas du problème multi sources.

Figure 0.0.4: Exemple d'extraction d'éléments du maillage sur une géométrie complexe pour construire les marqueurs afin d'itérer sur des zones du maillage. Nous pouvons distinguer sur la partie gauche la fonction distance au bord construite à partir d'une fonction levelset et sur la droite, les différents éléments utilisés pour assembler le terme source de eq. (0.0.1) situés à une distance au bord correspondant au libre parcours moyen.
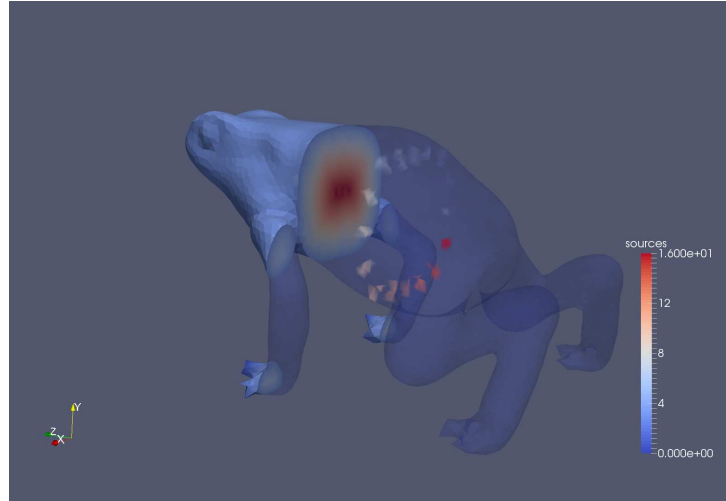
Pour résoudre le problème inverse, nous nous basons sur une méthode de l'adjoint. Le problème de minimisation nécessite une régularisation pour assurer le caractère bien posé du problème. Pour résoudre ce problème de minimisation, nous avons interfacé de manière explicite un certain nombre de librairies dédiées à l'optimisation dont NLOpt ou encore IPopt. Nous proposons des exemples d'utilisation de ces librairies pour résoudre le problème inverse. Nous détaillons les stratégies utilisées pour gérer le terme mémoire de l'équation de fluorescence numériquement grâce à une stratégie d'entrée/sortie sur disque et une approche parallèle.

Figure 0.0.5: Exemple de reconstruction pour le problème de diffusion en 2D. La simulation a été réalisée avec un code de calcul basé sur Feel++ et sur la librairie IPOpt. Une inclusion moins absorbante et moins diffusante a été placée dans le domaine. Les images du bas représentent l'observation complète pour le paramètre de diffusion κ_{obs} (à gauche) et le paramètre d'absorption (à droite). La ligne du haut représente les solutions respectives obtenues pour le paramètre de diffusion κ_x et d'absorption $\mu_{a,x}$ après 22 itérations d'optimisation. Nous pouvons distinguer l'inclusion sur la solution de gauche, en revanche la reconstruction du paramètre d'absorption est moins bonne. Ceci peut s'expliquer par exemple par le jeu de paramètres choisis, ou le choix des paramètres de régularisation.

19

Résumé

Guérir les tumeurs est l'un des enjeux majeurs du 21$^{\text{ième}}$ siècle et s'avère être au coeur de nombreuses recherches dans divers domaines. Pour mieux les soigner, il faut en premier lieu être capable de les détecter, les localiser, mais il faut également être en mesure de les qualifier. Nous cherchons à pouvoir identifier le type de tumeur, par exemple maligne ou bénigne et rendre possible leur classification. L'obtention d'informations supplémentaires sur leur nature, par exemple leur taille ou leur densité, permet de les regrouper par type. Parmi les applications possibles, l'adaptation des traitements des patients est rendue possible grâce à une connaissance a priori, un historique. L'assistance à la chirurgie par l'imagerie médicale peut être l'une des pistes futures.

La tomographie optique diffuse et de fluorescence résolue en temps (TR-DOTF), objet de cette thèse, est une méthode qui permet de fournir une information sur les propriétés optiques de diffusion et d'absorption des tissus biologiques. L'objectif ultime du projet est de concevoir un appareil de mesure (tomographe), éventuellement portatif, permettant de reconstruire des images multidimensionnelles 2D/3D des cartes optiques du milieu avec une résolution suffisante pour être utilisée en milieu hospitalier à des fins de diagnostic préclinique. L'avantage notable de cette technique est d'être non-invasive et non-irradiante. Elle est également peu coûteuse en comparaison avec des solutions alternatives telles que l'Imagerie par Résonance Magnétique (IRM).

Le projet est porté par l'équipe IMIS du laboratoire Icube spécialisé dans l'imagerie d'optique. L'équipe dispose d'un tomographe expérimental assemblé sur table de montage donnant accès à des mesures réelles et partielles à partir d'objet translucide ou encore d'êtres vivants (souris). Le temps de vol des photons diffusés dans cet objet est obtenu par comptage grâce à un jeu de détecteurs disposés de manière régulière tout autour de l'objet. Beaucoup de travaux ont déjà étudié le sujet. Dans cette thèse, réalisée à l'institut de recherche en mathématique avancée IRMA (Strasbourg) en collaboration avec le laboratoire de mathématiques, informatiques et application (LMIA, Mulhouse), nous proposons une formalisation mathématique de certains aspects du problème général. En particulier, nous proposons une analyse détaillée du problème direct qui tient compte du type de mesure physique employée qui nous paraît être un apport novateur pour la communauté. Puis nous proposons des solutions pour résoudre numériquement ce problème de manière efficace grâce à des techniques modernes issues du calcul haute performance qui nous paraissent peu connues de la communauté de la tomographie optique diffuse (TOD).

État de l'art La première partie de la thèse fait l'état de l'art du problème de tomographie optique diffuse et des différentes techniques existantes. L'équation du transfert radiatif est en général utilisée pour modéliser le phénomène de propagation des photons dans un milieu quelconque. La résolution de cette équation étant coûteuse en termes de ressources de calculs, on s'intéresse au cas particulier de l'approximation de diffusion. Cette approximation présente l'avantage d'être plus simple, mais introduit une contrainte entre les coefficients d'absorption et de diffusion et peut être discutable d'un point de vue de la physique du problème.

D'un point de vue mathématique, le problème auquel nous nous intéressons s'écrit sous la forme d'un système de deux équations aux dérivées partielles (EDP) faiblement couplées. La première équation décrit la diffusion des photons dans un milieu pour une mesure prise à une certaine longueur d'onde. La deuxième équation, dite de fluorescence, représente la diffusion de la lumière lorsqu'il y a réémission de photons d'excitation en présence d'un fluorophore dans le domaine. Le couplage s'effectue par le terme source de la seconde équation qui s'écrit comme un terme de convolution entre la solution de diffusion et un terme en exponentielle. Les inconnues du problème que nous cherchons à déterminer sont les coefficients de diffusions et d'absorption supposés différents pour chacune des deux équations. Pour la fluorescence, nous recherchons également la concentration du fluorophore et son temps de vie.

Problème direct et inverse Dans une deuxième partie de thèse, nous nous intéressons à la résolution de ce système d'équations. Dans un premier temps, nous faisons l'étude du problème direct pour des mesures de type contact et en non-contact. Nous étudions les cas d'existence et d'unicité du problème pour le cas de la diffusion et de la fluorescence et nous proposons un résultat de convergence.

La résolution du problème direct est illustrée par un code de calcul réalisé à l'aide de la librairie Feel++. C'est une librairie proposant un langage embarqué au C++ (DSEL) pour résoudre des équations aux dérivées partielles basé sur les méthodes de Galerkin standard. L'équipe IMIS a développé au cours de ses précédents travaux un code Matlab séquentiel pour reconstruire des images des cartes optiques pour le problème de TOD. Une des difficultés du problème de TOD est de devoir résoudre des problèmes de grandes tailles. En effet, le choix des discrétisations espaces-temps est imposé par la nature même du problème et en fonction de la résolution d'image souhaitée. L'un des apports de cette thèse est de proposer un code générique permettant de passer à l'échelle sur des architectures multicoeurs. Ce code propose une parallélisation spatiale basée principalement sur le standard MPI, gère des dimensions arbitraires et fournit des outils mathématiques embarqués dans le langage pour des méthodes d'ordres élevées en espace et en temps. Nous proposons une vérification croisée du code avec la version existante du logiciel Matlab. Cette étape nous a permis de confirmer la bonne résolution du problème. Puis le problème direct a été validé sur des mesures expérimentales pour un objet fantôme homogène composé de matière plastique dont les paramètres optiques estimés sont connus.

Nous proposons ensuite une formulation pour le problème inverse, qui est dans la plupart des cas mal posé. Dans ce problème, nous devons reconstruire 2 paramètres spatiaux pour le problème de diffusion, et 4 paramètres spatiaux pour le problème de fluorescence. Nous soulignons un argument démontré justifiant que nous ne pouvons pas reconstruire plus de 2 paramètres simultanément. Nous discutons la stratégie employée pour le choix de ces deux variables d'intérêts du problème de fluorescence et proposons une stratégie de résolution. L'une de ces stratégies adoptées suppose que ces paramètres de diffusion et d'absorption des tissus varient peu entre le problème de diffusion et celui de fluorescence, ce qui est discutable d'un point de vue de la physique. Dans ce cas, nous devons alors résoudre deux types de problèmes inverses distincts : un problème d'identification de paramètres de la forme bilinéaire du problème et un problème de reconstruction sur les sources.

Aspects numériques Dans la dernière partie de la thèse, nous détaillons les apports numériques de la thèse. Pour gérer les différents modes de mesures sur des géométries arbitraires, nous devons être en mesure de sélectionner les éléments du maillage sur lesquels nous désirons imposer les sources de lumière de type Dirac qui dépendent du mode de mesure. Dans cette thèse nous proposons un algorithme basé sur la méthode des levelset pour récupérer une fonction distance au bord. Nous construisons des itérateurs sur des éléments du maillage à partir d'outils mathématiques proposés par la librairie Feel++. Cet algorithme réutilise plusieurs fonctionnalités développées lors de précédents travaux de thèse qui ont été vérifiés, éprouvés, puis mis à profit dans ce projet.

Le problème direct consiste à résoudre un système linéaire pour N sources distinctes réparties régulièrement tout autour de l'objet. Nous présentons les outils mis à disposition par la librairie Feel++ pour résoudre le problème sur une source. Nous détaillons différentes approches possibles pour résoudre le modèle direct. Nous introduisons également les différents solveurs utilisés et en particulier celui choisi pour résoudre le cas du problème multi source.

Pour résoudre le problème inverse, nous nous basons sur une méthode de l'adjoint. Le problème de minimisation nécessite une régularisation pour assurer le caractère bien posé du problème. Pour résoudre ce problème de minimisation, nous avons interfacé de manière explicite un certain nombre de librairies dédiées à l'optimisation dont NLOpt ou encore IPopt. Nous proposons des exemples d'utilisation de ces librairies pour résoudre le problème inverse. Nous détaillons les stratégies utilisées pour gérer le terme mémoire de l'équation de fluorescence numériquement grâce à une stratégie d'entrée/sortie sur disque et une approche parallèle.

Summary

Heal tumours is one of the major issues of the 21$^{\text{ième}}$ century. Tumours are at the center of many research. In order to better treat them, one must be able to better detect, locate but also qualify them. We desire to identify the type of tumour, for example if it is a malignant or benign tumour to enable their classification. Getting more information about their nature for example their size or density allows to classify them by type. Among possible applications, the patient treatment adaptation is made possible thanks to an a priori knowledge, a history. Medical imaging for surgery assist might be one of the future path.

Time-Resolved Diffuse Optical Tomography (TR-DOT), the main subject of this thesis, is a method for getting specific information on diffusion and absorption optical properties of biological tissues. The project ultimate objective is to build a machine for measurements (tomograph), perhaps portable, for reconstructing optical maps of the medium environment with a good enough resolution to be used in medical environment (hospitals) for preclinical diagnosis. This technic main advantage is to be non-invasive and low cost compared to existing alternatives such as Magnetic Resonance Imaging (MRI).

The project is carried by the Imagerie Multimodale Intégrative en Santé (IMIS) team from the ICube laboratory, specialized in optical imaging. The team own an experimental tomograph assembled on a mount table that give access to real and partial measurements for transparent objects or yet living beings such as mouses. The flight time of photons diffused in this object is obtained via a counting method thanks to a set of detectors regularly dispatched around the object. Many research has studied this topic. In this thesis realized at the Institut de recherche en mathématiques avancée IRMA (Strasbourg) in a collaborative work with the laboratoire de mathématiques, informatiques et application (LMIA, Mulhouse), we proposed a mathematical formalization for some aspects of the general problem. In particular, we propose a detailed analysis of the forward problem that takes into account the employed measurement, that seems to be for us an innovative and interesting contribution to the community. Then we propose solutions to solve this problem numerically in an efficient manner thanks to modern technic coming from the High Performance Computing (HPC) community which seems to be little known among the Diffuse Optical Tomography (DOT) community.

State of art The first part of this thesis focus on state of the art for the DOT problem and the different existing technic in tomography. The Radiative Transfer Equation (RTE) is in general used to modelize the photon propagation phenomenon in a given turbid medium. As solving this equation has a cost in terms of computing resources, we are interested in the particular case of the diffusion approximation. This approximation has the clear advantage to be simpler, but it adds a constraint between the diffusion and absorption coefficients which is questionable from the physical point of view.

From a mathematical side, the problem we are interested can be rewritten as a system of Partial Differencial Equations (PDE) weakly coupled. The first equation describes the photon propagation in a turbid medium for a particular wavelength. The second equation modelizes the fluorescence problem and describes the diffusion of light when photons are remitted by excitation in the presence of a fluorescent marker in the domain. The coupling is performed by the source term of the second equation that is expressed as the convolution of the diffusion problem solution and an exponential term. The problem unknowns we wish to determine are the diffusion and absorption coefficients for the diffusion and the fluorescence that are supposed to be different for each equation. For the fluorescence, we are also looking for the fluorophor concentration and its lifetime.

Forward and inverse problem In the second part, we focus on the system of equation solving. In the first instance, one studies the forward problem for measurements in contact and non-contact mode. The solution existence and uniqueness are detailed for the diffusion and the fluorescence and a convergence result is given.

The forward problem solution is illustrated with a numerical calculation code realized using the Finite Element Embedded Library in C++ (FEEL++) library. This library provides a language embedded in C++ (DSEL) to solve PDE and based on standard Galerkin methods. The IMIS team has developed, during the previous research,

a sequential MathWorks Software (Matlab) code to reconstruct images of the optical maps for the DOT problem. One of the main DOT difficulty is to be able to solve big sized problem. Indeed, the time-space discretization is led by the nature of the problem and depends on the desired image resolution. One of the contribution of this thesis is the development of a generic code which scales. This code offers a spatial parallelization mainly based on MPI standard, manage arbitrary dimensions and gives mathematical tools directly embedded in the language of high order methods in space and time. We suggest a cross-verification with the existing Matlab code. This step permit to check the proper solve the problem for both codes. Then the forward problem has been validated on experimental measurements for a homogeneous phantom object made of plastic materials, which the estimated optical parameters are known.

Then we propose a formulation for the inverse problem which is generally badly posed. In this problem, we must reconstruct two parameters for the diffusion problem and four parameters for the fluorescence. In particular, we highlight one proved argument which establishes that it is not possible to reconstruct more than two parameters simultaneously. We discuss the strategy employed and the possibility to choose these two parameters of interest for the fluorescence and we give a strategy to solve the problem. One of the adopted strategy assume that the diffusion and absorption parameters of biological tissues for the fluorescence slightly vary from those for diffusion which might be dubious from the physical point of view. In that specific case, we have to solve two distinct inverse problems: one parameter identification problems on the bilinear form and one reconstruction problem on the sources.

Numerical aspects   In the last part of this thesis, we detail the numerical contributions. To numerically handle different measurements mode on complex arbitrary geometries, we must be able to select the mesh elements on which we desire to set the light sources. These δ-Dirac type sources depends on the measurement mode. In this thesis, we propose an algorithm based on the levelset methods to retrieve a distance function on the boundary. We construct mesh element iterators based on mathematical tools provided by the FEEL++ library. This algorithm reuse several powerful functionalities developed during the previous thesis that has been verified, tried and tested over time, then leverage in this project.

The forward problem consists in solving the linear system for N distinct sources regularly dispatched around the object. We present the numerical tools provided by the FEEL++ library to solve the problem of one source. We detail different possible approach to solve the forward problem. We also introduce the different solver used and especially the one adopted for the multi-source problem.

To solve the inverse problem, we focus mainly on a adjoint method approach. The minimization problem needs a regularization to ensure the problem well-posedness. To solve this minimization problem, we have explicitly interfaced several libraries dedicated to optimization problem such as Nonlinear Optimizer (NLopt) or Interior Point Optimizer (IPopt). We propose some usage examples within FEEL++ applications to solve inverse problem. We detail the strategies employed to numerically handle the memory term in the fluorescence equation and by pass some difficulties thanks to a disk I/O strategy and a parallel approach.

Introduction

This manuscript presents the works realised for the TR-DOT problem with fluorescence. The document is split in three main parts and two appendices.

The part I focus on the modelisation aspects of the TR-DOT. In particular, the chapter 1 details the choice of the diffusion approximation and presents some limitations of this model.

The part II is dedicated to the reconstruction problem. In the chapter 2, the forward problem is studied from an analytical point of view for two measurement modes, contact and non-contact. The diffusion and fluorescence coupling is considered for both modes. In particular, two methods are proposed to handle the fluorescence source term considering on the one hand, the integral as a memory term. On the other hand, by introducing a new Ordinary Differential Equations (ODE) equation in the original system. The chapter 3 proposes a numerical study in order to verify the implementation of the forward problem we developed using the Finite Element Embedded Language in C++ (FEEL++). A convergence study is given for high order methods in space and time. Our implementation is cross-verified by comparing the results with an existing Matlab code developed in a former thesis on a same test case. The forward model is finally validated for the diffusion problem for both computing codes using real measurements. The inverse problem is considered in chapter 4 as an optimization problem treated by an adjoint method, and preliminary results are given.

The last part III details the numerical ingredients used in order to provide a code for the reconstruction. The section section 5.1 highlights different tools from the FEEL++ library used in the context of TR-DOT reconstruction. We proposed a modification of the existing Backward Differentiation Formula (BDF) framework in section 5.2 in order to handle the adjoint equation used for the inverse problem. The section 5.3 presents the solvers used. To treat numerically the non-contact source term, a method based on the Level-Set Methods (LSM) is proposed in section 5.4. The last section 5.5 presents the optimization external tools adapted to be used in the parallel context of the FEEL++ library.

Finally, the appendix A gives a proof for the theorem 3 on existence of solution for the non contact problem in the chapter 2 and based on the Faedo-Galerkin method. The appendix B presents a proceedings of a side project realised during the Centre d'Eté Mathématique de Recherche Avancée en Calcul Scientifique (CEMRACS) 2015. The ODE and PDE coupling introduced in the model are similar from a mathematical point of view to the ODE coupling presented in chapter 2. Similar tools are used to solve the problem from a numerical point of view.

I   MODELING

Chapter 1 - State of art

DOT is a non invasive technique to explore living being internals using Near Infrared Light Spectrum (NIRS). Hemodynamic changes in biological tissues strongly influence the light scattering inside mediums [1] that makes DOT a preclinical tool well suited for tumours diagnosis as blood flows are more important where tumours are located. DOT emerges in the 1990s as a new alternative to existing imaging system such as MRI. One of the main advantages of DOT is to provide good physiological data where MRI is better suited for retrieving anatomical information in heterogeneous mediums [2, 3]. The DOT measurements can be gathered under three main categories [3, 4]: Continuous waves (CW), Frequency Domain (FD), and Time-Resolved (TR) methods. The first method consists in pulsing a continuous light wave on the skin of a patient. The measure provides a unique information on the intensity of the light which underwents scattering and absorption during the propagation process inside the turbid medium. The second approach employs a modulated intensity of the light source for a range of frequencies. Two information on the intensity and the phase delay can be analyzed for the reconstruction. In this paper, we are interested in using TR measures for different wavelength and provide an information on the light density diffused through the turbid domain over time. The wealth of information and the computational costs increase with the order of the given approach. There are recent good reviews on advances and methods used in DOT [3]. In the literature, most studies consider the FD method as the best compromise [2, 3]. However the strongly scattering nature of DOT in biological tissues [1] makes reconstruction and validation more difficult. The absorption dominance in depth tissues limits the study to small test cases. Absorption strongly depends on the nature of biological tissues, mostly water and hemoglobin, and their distribution in the body. Still absorption may vary depending on hemoglobin oxygenation or deoxygenation [5]. These factors affect the wavelength which constrains measurements to the so-called "biological window" [600, 1200] nm [1, 3].

The existence of solutions for the reconstruction is not certified because of the ill-posed nature of the inverse problem generally non linear. The classical way to handle this problem is to resort to regularization techniques such as the classical Tikhonov regularization. However, resulting images are generally blurred using these methods. Indeed the spatial resolution is not rich enough to expect a democratization of DOT in hospitals. A lot of studies focus on improving these images for example using fluorescence coupling [6] to enhance the contrast in Diffuse Optical Tomography and Fluorescence (DOTF) techniques and more recently considering photoacoustic methods [7].

1.1 Experimental disposal

The Icube/IMIS team developed an experimental tomograph [8, 9] for performing TR photon measures in a black box. The device consists of several optical equipments, a conoscopic holography scanner of which retrieves the distance from the surface of an object (phantom, small animals, brain, breast, muscles ...). Coupled with a set of controllable mirrors, it allows surfacic measurements under different view angles. The surfacic three-dimensionnal shape is reconstructed from these measures with a precision which depends on the mechanical reliability of the device. However, the current setup is limited to measurements of the top surface of the object. The source/detector bloc is made of two rack of 4 picoseconds laser diodes controlled by 8 Micro-Channel Plate

Figure 1.1.1: Picture of the experimental tomograph prepared on a mount table with a mouse placed on the semi-cylindric plastic mount. The left piture depicts all the components of the tomograph. The fibers are not visible installed. The right picture shows the ring of fibers
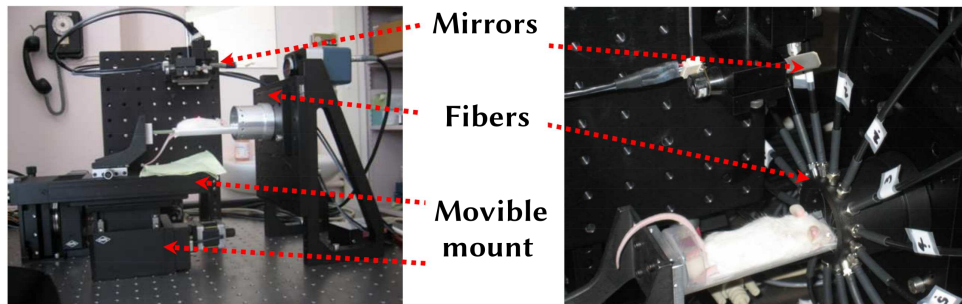

Photo Multiplier Tube (MCP-PMT) and synchronized with 4 Time-Correlated Single Photon Counting (TCSPC). The light can be emitted or acquired using 4 different Near Infrared (NIR) wavelength (690, 785, 830 and $870nm$) sequenced. The object is surrounded by $N_s = 16$ multi-mode optical fibers arranged regularly on a ring with a numerical aperture of 0.22, and a core diameter of $1000\mu m$. A mechanical multiplexor rotates and aligns a fiber for the source diodes regarding $N_d = 7$ others for the MCP-PMT with the 16 fibers. A motorized and transparent mount allows acquisitions over the whole surface of the object by translation.

1.2 Measurements

Observed objects are placed on the mount and centered with respect to the fibers ring. For the experiences detailed in this document, the measurements are performed on engineered build phantom objects made of diffusive plastic materials and owning up to two inclusions with optical properties differing from the background. The
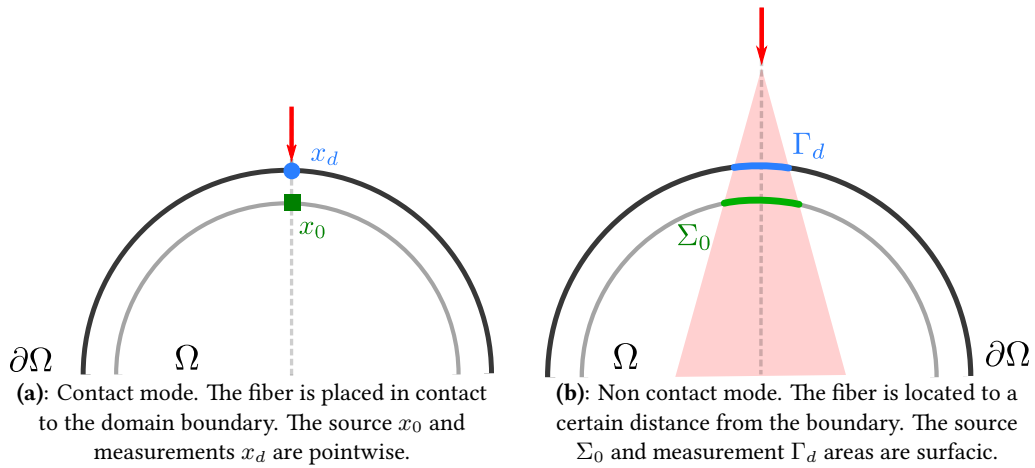
Figure 1.2.1: Scheme representing the path of the light from the infrared source of light (red) to the detectors (green) and crossing several inclusions with different optical properties.
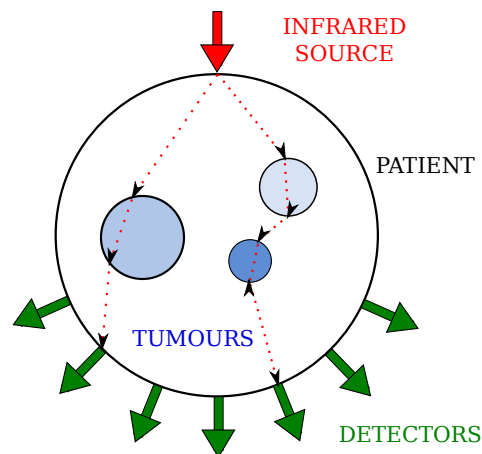
measurements are performed given two typical configurations.

i **Contact**: Each fiber are set in contact with the object to achieve contact measures. As the position of each fiber is fixed in the current experimental assembly, a displacement of each fiber would requier important modification of the current set-up. In order to avoid this situation, one builds cylindrical phantoms sized equal to the dimension of the fibers ring. In that case, the contact area between fibers and object's boundary is supposed to be pointwise (fig. 1.2.2a).

ii **Non-contact** In the contrary, the second configuration set each fiber at a distance d_k from the object's boundary. The detection area depends on the field-of-view cone of each fiber (fig. 1.2.2b) which depends on the Numerical Aperture of the fiber.

Figure 1.2.2: This figure represents the two types of measurement, contact and non contact. The free mean path has to be taken into account. Therefore, the source are located in the domain Ω. The left figure depicts the contact case. The fiber (red arrow) is placed in contact with the boundary. The right figure represents the non-contact mode, the fiber is located to a close distance from the boundary. Thus the fiber cone of vision has to be taken into account.

(a): Contact mode. The fiber is placed in contact to the domain boundary. The source x_0 and measurements x_d are pointwise.

(b): Non contact mode. The fiber is located to a certain distance from the boundary. The source Σ_0 and measurement Γ_d areas are surfacic.

These two configurations have to be taken into account in our model and imply some theoretical changes as we will see in chapter 2.

1.3 Radiative transfer equation (RTE)

The RTE (Boltzmann equation) [3, 9] describes the propagation of the light. The spectral radiance denoted $L(\mathbf{r}, \mathbf{s}, t)$ expressed in $[\mathrm{W\,m}^{-3}]$ follows the equation

$$\left\{ \frac{1}{c} \frac{\partial}{\partial t} + \mathbf{s} \cdot \nabla + [\mu_a(\mathbf{r}) + \mu_s(\mathbf{r})] \right\} L(\mathbf{r}, \mathbf{s}, t) = \mu_s(\mathbf{r}) \int_{4\pi} p(\mathbf{s}', \mathbf{s}) L(\mathbf{r}, \mathbf{s}', t) d\omega(\mathbf{s}') + q(\mathbf{r}, \mathbf{s}', t).$$

It describes the quantity of radiance emitted from a surface and falling within a solid angle ω. $p(\mathbf{s}', \mathbf{s})$ is the scattering phase function which corresponds to a probability of the light coming from direction $\mathbf{s}'$ to leave in the direction $\mathbf{s}$. $q(\mathbf{r}, \mathbf{s}', t)$ the light source from direction $\mathbf{s}'$. μ_a and μ_s are respectively the absorption and scattering coefficients of the turbid medium crossed by the light.

1.4 Diffusion approximation

The diffusion approximation is often considered because of RTE resolution complexity which would require heavy computation resources due to the number of unknowns to reconstruct. This simplification consists in expanding the radiance L by spherical harmonics (P_1 approximation) [2, 3]. The transport equation can then be expressed as a photon density instead of a luminance. One introduces the fluence rate $\phi(\mathbf{r}, t)$ expressed in $[\mathrm{W\,m}^{-2}]$ and

the radiative flux $J(\mathbf{r}, t)$ expressed in $[W]$ such that

$$L(\mathbf{r}, \mathbf{s}, t) = \frac{1}{4\pi}\left(\phi(\mathbf{r}, t) + 3\mathbf{J}(\mathbf{r}, t).\mathbf{s}\right), \quad \phi(\mathbf{r}, t) = \int_{4\pi} L(\mathbf{r}, \mathbf{s}, t)d\mathbf{s}, \quad \mathbf{J}(\mathbf{r}, t) = \int_{4\pi} \mathbf{s}L(\mathbf{r}, \mathbf{s}, t)d\mathbf{s},$$

derives the Fick law

$$\mathbf{J}(\mathbf{r}, t) = -\frac{1}{c_e}\kappa(\mathbf{r})\nabla\phi(\mathbf{r}, t),$$

where the diffusion coefficient $\kappa(\mathbf{r})$ denoted by

$$\kappa(\mathbf{r}) = \frac{c_e}{3(\mu_a(\mathbf{r}) + \mu'_s(\mathbf{r}))}.$$

is defined as the speed of the light in the surrounding medium c_e divided by an attenuation coefficient made of the absorption μ_a and a reduced scattering coefficient μ'_s defined such as $\mu'_s = \mu_s(1 - g)$ with g the anisotropy coefficient of the medium. The inverse of the reduced scattering coefficient corresponds to the free mean path of a photon. Substituting in the RTE equation yields the photon diffusion equation,

$$-\operatorname{div}(\kappa(\mathbf{r})\nabla\phi(\mathbf{r}, t)) + c_e\mu_{a,x}(\mathbf{r})\phi(\mathbf{r}, t) + \frac{\partial\phi(\mathbf{r}, t)}{\partial t} = q_0(\mathbf{r}, t) \,. \tag{1.4.1}$$

The Robin boundary condition can be deduced from the Fick's law assuming that the radiative flux passing though a surface within the normal $\mathbf{n}$ is a fraction of the reflected flux. It depends on a coefficient of reflexion R defined by Egan and Hilgeman [1, 2, 4, 9] as the constant

$$R = -1.44n_r^{-2} + 0.7099n_r^{-1} + 0.668 + 0.0636n_r \,, \tag{1.4.2}$$

where n_r denotes the refraction index of the surrounding environment and (c is the light speed in vacuum $c = 3.10^8 m/s$). The homogeneous Robin boundary condition becomes

$$\phi(\mathbf{r}, t) + 2A\kappa\nabla\phi(\mathbf{r}, t) \cdot \mathbf{n} = 0 \tag{1.4.3}$$

where A denotes a coefficient depending on the internal reflection coefficient such that

$$A = \frac{1 + R}{1 - R} \,. \tag{1.4.4}$$

This approximation is valid only if the hypothesis $\mu_a << \mu'_s$. Indeed the following assumption $\frac{\partial J}{\partial t} = 0$ used in the diffusion approximation would not be acceptable otherwise.

1.5 Conclusion

The chapter 1 gives an overview of the TR-DOT state of art. In the section 1.1, the experimental tomograph realised by the IMIS team was presented with all the machine components used to perform the measurements. In particular, the conoscop instrument let us retrieve a cloud of points only for the top surface of an object. Due to this restriction, only cylindrical objects are considered in the following study. This choice is made to easier the creation of the geometry and to avoid to deal with a geometrical error. Different fibers distributed regularly around the object are used for the light emission and detection. In practice, cylindrical objects with a diameter equal to the diameter of the ring of fibers are used for the measurements in contact. For non-contact, smaller cylindrical objects are considered. The model is adapted for these two configurations. The RTE was presented first in section 1.3. Finally, the section 1.4 details the model of the diffusion approximation which is considered in the following chapters.

References

[1] Egan W.G. and T.W. Hilgeman. *Optical Properties of Inhomogeneous Materials*. Academic Press, 1979.

[2] S.R Arridge. "Optical tomography in medical imaging". In: *IOPScience Inverse problem* 15.2 (1999).

[3] Y. Yamada and S. Okawa. "Diffuse Optical Tomography: Present Status and Its Future". In: *Optical Review* 21.3 (2014), pp. 185–205.

[4] Feng Gao, Huijuan Zhao, and Yukio Yamada. "Improvement of image quality in diffuse optical tomography by use of full time-resolved data". In: *Applied Optics* 41 (2012).

[5] Elizabeth MC Hillman. "Experimental and theoretical investigations of near infrared tomographic imaging methods and clinical applications." PhD thesis. 2002.

[6] Liu Kai, Tian Jie, Lu Yujie, Qin Chenghu, Yang Xin, Zhu Shouping, et al. "A fast bioluminescent source localization method based on generalized graph cuts with mouse model validations". In: *Optics Express* 18.4 (2010).

[7] Jun Xia, Junjie Yao, and Lihong V Wang. "Photoacoustic tomography: principles and advances". In: *Electromagnetic waves (Cambridge, Mass.)* 147 (2014), p. 1.

[8] Bruno Montcel and Patrick Poulet. "An instrument for small-animal imaging using time-resolved diffuse and fluorescence optical methods". In: *Nuclear Instruments and Methods in Physics Research* A 569 (2006).

[9] Farouk Nouizi. "Tomographie optique diffuse et de fluorescence préclinique : instrumentation sans contact, modélisation et reconstruction 3D résolue en temps". PhD thesis. Université de Strasbourg, 2011.

II Reconstruction

Chapter 2 - Forward problem

This chapter states the TR-DOT problem with fluorescence from the mathematical point of view. The model of the diffusion approximation, highlighted in chapter 1, is considered. The section 2.1 formulates the problem as a system of two equations weakly coupled by the source term of the fluorescence equation. The problem is considered for two types of measurements, contact and non-contact. These measurements modes correspond to two different configurations of the tomograph, when the tomograph fibers are set in contact with the object or when they are not in contact (sections 1.1 and 1.2). Thus, the source term for the diffusion has to be handled in two different manners.

The section 2.2 proposes a study for the well-posedness of the coupled system of equations for the contact case, section 2.2.1 and the non-contact case, section 2.2.2. In the section 2.3, the weak formulation is established. Methods are proposed to handle the fluorescence source term which can be seen as a memory source term, but can be treated differently by introducing a new ODE in the initial system. Finally, two convergence results are given depending on the chosen source term for the contact and the non-contact mode.

2.1   Problem definition

We consider $k \in [1, N_s]$ optical fibers ($N_s = 16$) placed on a ring and surrounding a phantom as described in section 1.1. Let Ω be the whole turbid domain of $\mathbb{R}^d$ ($d = 2$ or 3) and $T > 0$ the final time. We denote $\ell \in \{x, m\}$ the subscript respectively for the diffusion and fluorescence excitation wavelength. The system of equations that describes the tomograph setup as a sequence of diffusion problems within each fiber and through Ω is written

$$
\begin{cases}
-\nabla \cdot (\kappa_x \nabla \phi_x^k) + c_e \mu_{a,x} \phi_x^k + \dfrac{\partial \phi_x^k}{\partial t} = q_x^k & \text{on } \Omega \times (0,T) , \\[2mm]
-\nabla \cdot (\kappa_m \nabla \phi_m^k) + c_e \mu_{a,m} \phi_m^k + \dfrac{\partial \phi_m^k}{\partial t} = \gamma q_m^k & \text{on } \Omega \times (0,T) , \\[2mm]
\phi_x^k + 2\mathrm{A}\kappa_x \dfrac{\partial \phi_x^k}{\partial \boldsymbol{n}} = 0 & \text{on } \partial\Omega \times (0,T) , \\[2mm]
\phi_m^k + 2\mathrm{A}\kappa_m \dfrac{\partial \phi_m^k}{\partial \boldsymbol{n}} = 0 & \text{on } \partial\Omega \times (0,T) , \\[2mm]
\phi_x^k(0,\cdot) = \phi_{x,0} , \\[1mm]
\phi_m^k(0,\cdot) = \phi_{m,0} ,
\end{cases}
\tag{2.1.1}
$$

where the diffusion source term q_x^k is considered as a δ-Dirac pointwise or surface function respectively in contact or non contact modes (fig. 1.2.2) that will be more detailed in sections 2.2.1 and 2.2.2,

$$
q_x^k =
\begin{cases}
\delta_{x_0^k}(\mathbf{x})\delta(t_0) & \text{(contact)}, \\[2mm]
\delta_{\Sigma_0^k}(\mathbf{x})\delta(t_0) & \text{(non contact)}.
\end{cases}
\tag{2.1.2}
$$

The fluorescence source term q_m^k is the convolution of the solution of the diffusion by a exponential term as discussed in the chapter 1

$$q_m^k(\mathbf{x}, t) = \frac{1}{\tau} \int_0^t \phi_x^k(\mathbf{x}, s) e^{(\frac{t-s}{\tau})} ds. \tag{2.1.3}$$

$\mu_{a,\ell}$ denotes the absorption coefficients, $\mu'_{s,\ell}$ the scattering coefficients. $\kappa_\ell = c_e/(3(\mu_{a,\ell} + \mu'_{s,\ell}))$ the diffusion coefficients, $\gamma = \eta \sigma \xi$ a fluorophore coefficient which depends on flurorophor concentration ξ, the fluorophore molar extinguishing coefficient σ and the fluorophore yield η. Finally, τ corresponds to the fluorophore average lifetime.

Remark 2. *We assume $t_0 = 0$ the initial time for the diffusion. This hypothesis means we neglect the mean free path otherwise we should have to take into account a direction information for the particles transport (chapter 1). At time t_0, the light already travelled a short distance in the domain. The source has to be chosen in a close distance from the boundary (See chapter 1 fig. 1.2.2). In practice, we choose this distance to be the inverse of the reduced scattering coefficient. We denote $q_{\ell,0} = q_\ell(\boldsymbol{x}_0, t_0)$.*

2.2 Well-posedness

Let Ω be a bounded open set of $\mathbb{R}^d$ and $T > 0$, we denote by $Q = \Omega \times (0, T)$ the time-space domain and by $M(\overline{\Omega}) = C(\overline{\Omega})'$, the dual of the space of the continuous functions equipped with its usual norm. We consider the coupled system of parabolic equations (2.1.1) with measure data. We will drop the index $k \in [1, N_s]$ in this section for brevity. We assume there exists two constants κ_0, κ_1 verifying the following hypothesis for $\ell = \{x, m\}$

$$\begin{cases} \kappa_\ell, \mu_{a,\ell} \in L^\infty(\Omega), \\ \quad \mu_{a,\ell} \geq 0, \\ 0 < \kappa_0 \leq \kappa_x, \ \kappa_m \leq \kappa_1. \end{cases} \tag{2.2.1}$$

The right hand sides are given by (2.1.2) and (2.1.3). For smooth coefficients $\kappa_x, \mu_{a,x}$ (e.g. Hölder continuous) and simple geometries, the first equation may be solved with the fondamental solution and the second one is then completely uncoupled from the previous one and may be solved in the framework of the variational theory [12]. In the general case (2.2.1), we have to consider the framework of parabolic systems with measure data.

We first start by defining the notion of solution to the following scalar parabolic equation: let $\kappa, \mu \in L^\infty(\Omega)$, $0 < \kappa_0 \leq \kappa$ and $\mu \geq 0$. For $f \in M(\overline{Q})$ and $u_0 \in M(\overline{\Omega})$, $\beta > 0$, find u such that

$$\begin{cases} \dfrac{\partial u}{\partial t} - \operatorname{div}(\kappa \nabla u) + \mu u = f, \\ \qquad \dfrac{\partial u}{\partial n} + \beta u = 0, \\ \qquad u(0, .) = u_0. \end{cases} \tag{2.2.2}$$

We look for solutions of (2.2.2) in the following sense [13]: $u \in \cap_{q < \frac{d+2}{d+1}} L^q(0, T; W^{1,q}(\Omega))$

$$\begin{cases} -\displaystyle\int_0^T \int_\Omega u \frac{\partial \eta}{\partial t} - \int_\Omega \eta(0) \, du_0 + \int_0^T \int_\Omega \kappa \nabla u \cdot \nabla \eta + \int_0^T \int_\Omega \mu \, u \, \eta \\ \qquad\qquad + \beta \displaystyle\int_0^T \int_{\partial\Omega} u \, \eta = \int_0^T \int_\Omega \eta \, d f, \\ \eta \in C(\overline{Q}), \ \eta \in \cup_{r>d} L^r(0, T; W^{1,r}(\Omega)), \eta_t \in \cup_{r>d+2} L^r(0, T; W^{1,r}(\Omega)), \eta(T, \boldsymbol{x}) = 0. \end{cases} \tag{2.2.3}$$

The following existence theorem for such parabolic equation with measure data, is proved in [13] for the Dirichlet boundary conditions by an approximation arguments (see also [10, 14], and for other boundary conditions [15])

Theorem 1. *([BG]) There exists a solution for the problem* (2.2.3).

Note that the theorem does not state any uniqueness, which is in fact not true without further assumptions. However, when the data are in L^1, a more precise result ensuring also the uniqueness of solutions is available by restricting also the notion of solution.

2.2.1 The contact case

Let $\ell = \{x, m\}$, $q_\ell \in M(\overline{Q})$, $q_\ell(0) \in M(\overline{\Omega})$. We recall that in our modeling we have $q_x = 0 \in]0, T)$ and $q_{x,0} = \delta_{x_0}$, with $x_0 \in \Omega$.

Theorem 2. *Under the hypothesis* (2.2.1) *for any* $1 \leq q < \frac{d+2}{d+1}$ *there exists a solution* $\phi_x \in L^q(0, T; W^{1,q}(\Omega))$ *to the system* (2.1.1) *and there exists a unique solution* ϕ_m *such that: If* $d = 2$, $\phi_m \in L^2(0, T; H^1(\Omega)) \cap C([0, T]; L^2(\Omega))$, $\phi'_m \in L^2(0, T; (H^1(\Omega))')$. *If* $d = 3$, *then* $\phi_m, \phi'_m \in L^p(0, T, W^{1,p}(\Omega))$ ($p \leq \frac{3}{2}$).

Note that the solutions given by the theorem are such that the initial condition $\phi_\ell(0, .) = q_{\ell,0}$, $\ell = \{x, m\}$ is taken in the classical sense since $\phi_m(t)$ is continuous and ϕ_x, by standard interpolation theory, belongs to $C([0, T]; H^{-s}(\Omega))$ for large $s > 0$ [13].

Proof. The existence of $\phi_x \in L^q(0, T; W^{1,q}(\Omega))$ follows from Theorem 1. Since $\phi_x(t)$ belongs to $C([0, T]; H^{-s}(\Omega))$, a direct computation shows that

$$q'_m - \frac{1}{\tau} q_m = \frac{1}{\tau} \phi_x(t), \ t \in (0, T). \tag{2.2.4}$$

It follows from the ordinary differential equation theory and maximal regularity, that $q_m \in L^q(0, T; W^{1,q})$, $q'_m \in L^q(0, T; W^{1,q})$. In particular, by the Sobolev theorem, $W^{1,q}(Q) \subset L^p(Q)$, $p \in [q, q^*]$, with $q^* \geq 2$ if $d = 2$ and $q^* \geq \frac{3}{2}$ if $d = 3$. Thus, if $d = 2$, then $q_m \in L^2(Q)$ and applying the classical existence theorem of Lions [12], yields a unique solution $\phi_m \in L^2(0, T; H^1(\Omega)) \cap C(0, T; L^2(\Omega))$, $q'_m \in L^2(0, T; (H^1(\Omega)')$. If $d = 3$ then applying the L^p theory of parabolic equation ($p \leq \frac{3}{2}$) we get ϕ_m, ϕ'_m and $\Delta \phi_m \in L^p(\Omega \times (0, T))$ ☐

The theorem is given with a minimal regularity which cannot be much improved in general, under the assumptions (2.2.1). In fact assume that Ω is smooth enough, and if κ_ℓ, $\mu_{a,\ell}$ for $\ell \in \{x, m\}$ are in $W^{1,\infty}(\Omega)$, then we still have $\phi_x \in L^q(0, T; W^{1,q}(\Omega))$. Whereas, since $q_m \subset W^{1,q}(Q) \subset L^r(Q)$, $\frac{1}{r} = \frac{1}{q} - \frac{1}{d}$, with $r < 4$ for $d = 2$ and $r \leq \frac{15}{7}$ for $d = 3$, it follows from the L^p-regularity theory of the parabolic equations [16, 17] that $\phi_m \in W^{2,r}(Q)$, and from the Sobolev-Morrey theorem $\phi_m \in C^{1,\alpha}(\overline{Q})$, $\alpha < \frac{1}{2}$ when $d = 2$ and $\phi_m \in C^{0,\alpha}(\overline{Q})$, $\alpha < \frac{3}{5}$ when $d = 3$.

We emphasize that even if the initial condition in the system (2.1.1) are satisfied in the classical sense, the boundary conditions, assuming that $\partial\Omega$ is regular, are to be understood in a weak sense. In fact, if $\ell = x$, since ϕ_ℓ is only in $W^{1 - \frac{1}{q}, q}(\partial\Omega)$, $q < \frac{d+2}{d+1}$, the Robin condition is satisfied in the weak form of (2.2.3).

It is also interesting to note that, with measure data and $d > 2$, the uniqueness of a solution ϕ_x may not hold in general, without further restrictions. However, it holds for ϕ_m in all cases. The regularization effect of the parabolic equations provides more properties to ϕ_m.

2.2.2 The non-contact case

Let us consider the non contact case $q_x(0) = \delta_{\Sigma_0} \in H^{1\prime}(\Omega)$ when Σ_0 is a closed surface in Ω, as it may be checked that

$$< q_x(0), v >_{H^{1\prime}, H^1} = \int_{\Sigma_0} v \, d\sigma, \quad \forall v \in H^1(\Omega). \tag{2.2.5}$$

If Σ_0 is an open surface, we denote Σ_e a smooth surface such that $\Sigma_0 \cap \Sigma_e = \emptyset$, $\overline{\Sigma_0} \cup \overline{\Sigma_e} = \partial D$, with D a bounded open set and $D \subset\subset \Omega$. We define the space

$$H^1_{\Sigma_0}(\Omega) = \mathrm{cl}\left(\left\{v \in C^\infty(\Omega) \cap H^1(\Omega); \ v = 0 \text{ on } \Sigma_e\right\}\right), \tag{2.2.6}$$

where cl is the closure of the linear space. Thus it is a closed subspace of $H^1(\Omega)$. If $v \in H^1_{\Sigma_0}(\Omega)$ then the trace of v on Σ_0, belongs to $H^{\frac{1}{2}}_{00}(\Sigma_0)$ [12]. We denote by $H^{-1}_{\Sigma_0}(\Omega)$ the dual space of $H^1_{\Sigma_0}(\Omega)$, note that it is not a distribution space. Then we may identify $q_x(0)$ with an element of $H^{-1}_{\Sigma_0}(\Omega)$ and we have

$$< q_x(0), v >_{H^{-1}_{\Sigma_0}, H^1_{\Sigma_0}(\Omega)} = \int_{\Sigma_0} v \, d\sigma, \quad \forall v \in H^1_{\Sigma_0}(\Omega). \tag{2.2.7}$$

For brevity, we denote by V the space $H^1_{\Sigma_0}(\Omega)$ if Σ_0 is open and $H^1(\Omega)$ when it is a closed surface, and V' is the dual of V. Note that if $L^2(\Omega) = H$ then we have $V \subset H \subset V'$ (with continuous injection and in the case where Σ_0 is a closed surface, it's a dense injection).

Theorem 3. *Under the hypothesis* (2.2.1) *there exists a unique solution* (ϕ_x, ϕ_m) *to the system* (2.1.1)*, such that* $\phi_x \in L^2(0,T;H) \cap C(0,T;V')$*, and* $\phi_m \in L^2(0,T;H^2(\Omega) \cap V) \cap C(0,T;V)$*,* $\frac{\partial \phi_m}{\partial t} \in L^2(0,T;H)$*.*

Proof. We consider the first equation of the system (2.1.1). Then, we have to solve the parabolic equation (2.2.2) with $f = 0$ and $u_0 \in V'$. Such an equation cannot be directly studied under a variational form, however the existence and uniqueness of a solution $u \in L^2(Q) \cap C([0,T];V')$, is obtained by the transposition method ([12], Vol 2, Chap 4, theorem 13.1) (We give a direct proof using the Faedo-Galerkin method in appendix A).

The second equation now is given by (2.2.2) with $f \in L^2(Q)$ and $u_0 = 0$. In fact, it is readily checked that $f = q_m \in H^{0,1}(Q)$, ([12]) and thus the standard variational theory of the parabolic equations yields the existence and uniqueness of a solution $\phi_m \in L^2(0,T;V) \cap C([0,T];H)$ and $\frac{\partial \phi_m}{\partial t} \in L^2(0,T;V')$ [12]. $\qquad\square$

We note that when the coefficients $\kappa_\ell, \mu_\ell, \ell = \{x,m\}$ are regular, say $W^{1,\infty}(\Omega)$, the solution $\phi_m \in L^2(0,T;H^2(\Omega) \cap V) \cap C([0,T];V)$ and $\frac{\partial \phi_m}{\partial t} \in L^2(0,T;H)$ (see [12, 17]). In all cases, the solutions satisfy the initial conditions in the classical sense and the Robin boundary condition in the usual sense of traces.

The previous theorem is valid when replacing V by any Sobolev space $H^s(\Omega)$, $\frac{1}{2} < s \leq 1$.

2.3 Weak formulations

2.3.1 Continuous formulation

We consider the system of equation (2.1.1) keeping the same hypothesis. In order to introduce the discretization, we rewrite the problem as follows: We distinguish the contact and non contact case in the following sections.

Contact   Let $V = \cup_{q > \frac{d}{d-1}} W^{1,q}(\Omega)$ be the space for $d \geq 2$. In order to write the weak formulation of (2.1.1) in a unified form, we distinguish the two cases for the diffusion (i) and the fluorescence (ii):

(i) Find $\phi_x(t) \in \cup_{p < \frac{d}{d-1}} W^{1,p}(\Omega)$, and $\frac{\partial \phi_x}{\partial t} \in W^{-1,p}(\Omega)$ for a.e $t > 0$

$$\int_\Omega \kappa_x \nabla \phi_x \nabla v + \int_\Omega c_e \mu_a \phi_x v + \int_{\partial\Omega} \frac{1}{2A} \phi_x v + \int_\Omega \frac{\partial \phi_x}{\partial t} v = (q_x, v) \quad \forall\, v \in V. \tag{2.3.1}$$

Since v is continuous, (q_x, v) is $v(x_0)$. Note that the integral $\int_\Omega \frac{\partial \phi_x}{pt} v$ is to be understood in the duality sense, since $\frac{\partial \phi_x}{\partial t} \in L^p(0,T;W^{-1,p}(\Omega))$ for $p < \frac{d}{d-1}$.

(ii) For the fluorescence, the source term q_m depends on ϕ_x. We look for a solution $\phi_m \in H^1(\Omega)$ more regular than ϕ_x such that

$$\int_\Omega \kappa_m \nabla \phi_m \nabla v + \int_\Omega c_e \phi_m \mu_{a,m} v + \int_{\partial\Omega} \frac{1}{2A} \phi_m v + \int_\Omega \frac{\partial \phi_m}{\partial t} v = \langle \gamma q_m, v \rangle_{H^{1\prime}(\Omega), H^1(\Omega)}. \tag{2.3.2}$$

Note that the integral $\int_\Omega \frac{\partial \phi_m}{\partial t} v$ is to be understood in the duality sense $H^{1\prime}(\Omega), H^1(\Omega)$.

Non contact   We define the space

$$V = \begin{cases} H^1(\Omega) & \text{if } \Sigma_0 = \partial D \subset\subset \Omega, \\ H^1_{\Sigma_0}(\Omega) & \text{if } \Sigma_0 \subsetneq \partial D \subset\subset \Omega. \end{cases} \tag{2.3.3}$$

(i) Find $\phi_x(t) \in L^2(\Omega)$, and $\frac{\partial \phi_x}{\partial t} \in V'(\Omega)$ for a.e $t > 0$

$$\int_\Omega \kappa_x \nabla \phi_x \nabla v + \int_\Omega c_e \mu_a v + \int_{\partial\Omega} \frac{1}{2A} \phi_x v + \int_\Omega \frac{\partial \phi_x}{\partial t} v = (q_x, v)_{V',V} \quad \forall\, v \in V. \tag{2.3.4}$$

We recall that (q_x, v) is $\int_\Sigma v d\sigma$

(ii) For the fluorescence, the source term q_m depending on ϕ_x, we search a solution $\phi_m \in H^1(\Omega)$ more regular than ϕ_x with $\frac{\partial \phi_m}{\partial t} \in L^2(\Omega)$ such that

$$\int_\Omega \kappa_m \nabla \phi_m \nabla v + \int_\Omega c_e \mu_{a,m} v + \int_{\partial\Omega} \frac{1}{2A} \phi_m v + \int_\Omega \frac{\partial \phi_m}{\partial t} v = \langle \gamma q_m, v \rangle_{V',V}. \tag{2.3.5}$$

Note that the integral $\int_\Omega \frac{\partial \phi_m}{\partial t} v$ is to be understood in the duality sense $H^{1\prime}(\Omega), H^1(\Omega)$.

Remark 3. *If $\mu_{a,x} \equiv 0$ on $w \subset \Omega$, then we have to modify V to ensure the Poincaré-Wirtinger inequality. We should look for a wider space to hold the uniqueness.*

Multiple source We consider now the system (2.1.1) for an arbitrary number of source. We set $\phi^k = \left(\phi_x^k, \phi_m^k\right)$ for $r \in [1, N_s]$, the diffusion coefficient $\boldsymbol{\kappa}^k$, a diagonal matrix with entries κ_x^k, κ_m^k. The absorption coefficients $\boldsymbol{\mu}_a^k = \left(\mu_{a,x}^k, \mu_{a,m}^k\right)$. The source term $\mathbf{q}^k = \left(q_x^k, \gamma q_m^k\right)$ The system reads for $k \in [1, N_s]$ as

$$\begin{cases} -\nabla \cdot (\boldsymbol{\kappa}^k \nabla \phi^k) + c_e \boldsymbol{\mu}_a^k \phi^k + \dfrac{\partial \phi^k}{\partial t} = \mathbf{q}^k & \text{on } \Omega \times (0, T) \,, \\[2mm] \phi^k + 2\text{A}\boldsymbol{\kappa}^k \nabla \phi^k \cdot \boldsymbol{n} = 0 & \text{on } \partial\Omega \times (0, T) \,, \end{cases} \tag{2.3.6}$$

with the associated weak form

$$\int_\Omega \left(\boldsymbol{\kappa}^k \nabla \phi^k : \nabla \boldsymbol{v} + c_e \boldsymbol{\mu}_a^k \phi^k \boldsymbol{v}\right) + \int_{\partial\Omega} \frac{1}{2\text{A}} \phi^k \boldsymbol{v} + \int_\Omega \frac{\partial \phi^k}{\partial t} \boldsymbol{v} = \int_\Omega \mathbf{q}^k \boldsymbol{v}, \tag{2.3.7}$$

And with obvious notation,

$$a(\phi^k, \boldsymbol{v}) + \int_\Omega \frac{\partial \phi^k}{\partial t} \boldsymbol{v} = l(\boldsymbol{v}), \tag{2.3.8}$$

2.3.2 Semi-discrete formulation

In the following section, we drop the index k for simplicity. We discretize in time such that $t_n = n\Delta_t$. We denote $\phi^{(n)}(\boldsymbol{x}) = \phi(\boldsymbol{x}, t_n)$. We discretize the time dependent term using a backward Euler scheme in time for $t \approx t_{n+1}$

$$\frac{\partial \phi(\boldsymbol{x}, t)}{\partial t} \simeq \frac{\phi^{(n+1)}(\boldsymbol{x}) - \phi^{(n)}(\boldsymbol{x})}{\Delta_t} \tag{2.3.9}$$

to obtain the following semi-discrete formulation

$$\int_\Omega \left(\boldsymbol{\kappa} \nabla \phi^{(n+1)} : \nabla \boldsymbol{v} + c_e \boldsymbol{\mu}_a \phi^{(n+1)} \boldsymbol{v}\right) + \int_{\partial\Omega} \frac{1}{2\text{A}} \phi^{(n+1)} \boldsymbol{v} + \int_\Omega \frac{\phi^{(n+1)}}{\Delta_t} \boldsymbol{v} = \int_\Omega \mathbf{q}^{(n+1)} \boldsymbol{v} + \int_\Omega \frac{\phi^{(n)}}{\Delta_t} \boldsymbol{v} \tag{2.3.10}$$

We must yet see how to deal with the term $\mathbf{q}^{(n+1)} = \mathbf{q}(\phi_x; \boldsymbol{x}, t_{n+1})$ of the right hand side for the fluorescence part q_m of the forward formulation and defined previously (2.1.3). We can use the Chasle relation to rewrite the integral such that,

$$\begin{aligned} q_m &= \frac{1}{\tau} \int_0^{t_{n+1}} \phi_x(\boldsymbol{x}, s) e^{(\frac{t_{n+1}-s}{\tau})} ds \\ &= \frac{1}{\tau} \int_0^{t_n} \phi_x(\boldsymbol{x}, s) e^{(\frac{t_{n+1}-s}{\tau})} ds + \frac{1}{\tau} \int_{t_n}^{t_{n+1}} \phi_x(\boldsymbol{x}, s) e^{(\frac{t_{n+1}-s}{\tau})} ds \,. \end{aligned} \tag{2.3.11}$$

But the first integral on the right hand side is well known as it is the second one computed at each iteration and its exact value can be hold in buffer memory. So we introduce the sequence $B_n(\boldsymbol{x})$

$$B_n(\boldsymbol{x}) = \frac{1}{\tau} \int_0^{t_n} \phi_x(\boldsymbol{x}, s) e^{(\frac{t_{n+1}-s}{\tau})} ds \,, \tag{2.3.12}$$

which is supposed to be known and $R_n(\boldsymbol{x})$ the remain term such that,

$$R_n(\boldsymbol{x}) = \frac{1}{\tau} \int_{t_n}^{t_{n+1}} \phi_x(\boldsymbol{x}, s) e^{(\frac{t_{n+1}-s}{\tau})} ds \,. \tag{2.3.13}$$

Therefore we just have to compute the integral $R_n(\boldsymbol{x})$ knowing that $\phi_x(\boldsymbol{x}, t)$ is first order polynomial of the time on the restricted interval $[t_n, t_{n+1}]$ and also that its borned values are fixed.

$$\phi_x(\boldsymbol{x}, t) = a(\boldsymbol{x})t + b(\boldsymbol{x}) \,, \tag{2.3.14}$$

where the coefficients a and b are respectively,

$$a(\boldsymbol{x}) = \frac{\phi_x^{(n+1)}(\boldsymbol{x}) - \phi_x^{(n)}(\boldsymbol{x})}{\Delta_t}, \quad b(\boldsymbol{x}) = \phi_x^{(n+1)} - a(\boldsymbol{x})t_{n+1} \,. \tag{2.3.15}$$

Note that we have $t_n = n\Delta_t$. We integrate by parts the integral (2.3.13),

$$
\begin{aligned}
R_n(\boldsymbol{x}) &= \frac{1}{\tau}\left(\left[-\tau\phi_x(\boldsymbol{x},s)e^{\frac{t_{n+1}-s}{\tau}}\right]_{t_n}^{t_{n+1}} + \tau\int_{t_n}^{t_{n+1}}\phi_x'(\boldsymbol{x},s)e^{\frac{t_{n+1}-s}{\tau}}ds\right) \\
&= \left[-(a(\boldsymbol{x})s+b(\boldsymbol{x}))e^{\frac{t_{n+1}-s}{\tau}}\right]_{t_n}^{t_{n+1}} - a(\boldsymbol{x})\tau\left[e^{\frac{t_{n+1}-s}{\tau}}ds\right]_{t_n}^{t_{n+1}} \\
&= -a(\boldsymbol{x})t_{n+1} - b(\boldsymbol{x}) + (a(\boldsymbol{x})t_n+b(\boldsymbol{x}))e^{\Delta_t/\tau} - a(\boldsymbol{x})\tau(1-e^{\Delta_t/\tau}) \\
&= -a(\boldsymbol{x})(t_{n+1}-t_ne^{\Delta_t/\tau}) - b(\boldsymbol{x})(1-e^{\Delta_t/\tau}) - a(\boldsymbol{x})\tau(1-e^{\Delta_t/\tau}) \\
&= -a(\boldsymbol{x})\Delta_t(n(1-e^{\Delta_t/\tau})+1) - b(\boldsymbol{x})(1-e^{\Delta_t/\tau}) - a(\boldsymbol{x})\tau(1-e^{\Delta_t/\tau}) \\
&= -a(\boldsymbol{x})\Delta_t(n\omega_1+1) - (b(\boldsymbol{x})+a(\boldsymbol{x})\tau)\omega_1
\end{aligned}
\tag{2.3.16}
$$

where the coefficients w_1 reads

$$
\omega_1 = 1 - e^{\Delta_t/\tau}
\tag{2.3.17}
$$

Now, if we replace $a(\boldsymbol{x})$ and $b(\boldsymbol{x})$ with their values (2.3.15), the remain term becomes,

$$
\begin{aligned}
R_n(\boldsymbol{x}) &= -a(\boldsymbol{x})\Delta_t(n\omega_1+1) - (b(\boldsymbol{x})+a(\boldsymbol{x})\tau)\omega_1 \\
&= (\phi_x^{(n)}-\phi_x^{(n+1)})(n\omega_1+1) - \left[\phi_x^{(n+1)}-(\phi_x^{(n+1)}-\phi_x^{(n)})(n+1)+\frac{\phi_x^{(n+1)}-\phi_x^{(n)}}{\Delta_t}\tau\right]\omega_1 \\
&= \phi_x^{(n+1)}\left[-1-\frac{\tau\omega_1}{\Delta_t}\right] + \phi_x^{(n)}\left[1+\left(\frac{\tau}{\Delta_t}-1\right)\omega_1\right]
\end{aligned}
\tag{2.3.18}
$$

Finally, the remainder term can be expressed such that

$$
R_n(\boldsymbol{x}) = C_1\phi_x^{(n+1)} + C_2\phi_x^{(n)},
\tag{2.3.19}
$$

where the coefficients C_1 and C_2 are,

$$
\begin{aligned}
C_1 &= \left(-1-\frac{\tau\omega_1}{\Delta_t}\right), \\
C_2 &= \left(1+\left(\frac{\tau}{\Delta_t}-1\right)\omega_1\right).
\end{aligned}
\tag{2.3.20}
$$

We have still to establish the recursive formula for $B_n(\boldsymbol{x})$,

$$
\begin{aligned}
B_n(\boldsymbol{x}) &= \frac{1}{\tau}\int_0^{t_n}\phi_x(\boldsymbol{x},s)e^{(\frac{t_{n+1}-s}{\tau})}ds, \\
&= \frac{1}{\tau}\int_0^{t_{n-1}}\phi_x(\boldsymbol{x},s)e^{(\frac{t_{n+1}-s}{\tau})}ds + \frac{1}{\tau}\int_{t_{n-1}}^{t_n}\phi_x(\boldsymbol{x},s)e^{(\frac{t_{n+1}-s}{\tau})}ds \\
&= e^{\frac{\Delta_t}{\tau}}\left(\frac{1}{\tau}\int_0^{t_{n-1}}\phi_x(\boldsymbol{x},s)e^{(\frac{t_n-s}{\tau})}ds + \frac{1}{\tau}\int_{t_{n-1}}^{t_n}\phi_x(\boldsymbol{x},s)e^{(\frac{t_n-s}{\tau})}ds\right) \\
&= e^{\frac{\Delta_t}{\tau}}\left(B_{n-1}(\boldsymbol{x})+R_{n-1}(\boldsymbol{x})\right).
\end{aligned}
\tag{2.3.21}
$$

In particular we have $B_0 = 0$ and R_0 defined such that

$$
\begin{aligned}
R_0(\boldsymbol{x}) &= -a(\mathbf{r})\Delta_t - (b+a\tau)\omega_1 \\
&= \phi_x^{(0)}(1-\omega_1) - \phi_x^{(1)}
\end{aligned}
\tag{2.3.22}
$$

Finally, we obtain the semi-discrete formulation

$$
\begin{aligned}
&\int_\Omega(\kappa\nabla\boldsymbol{\phi}^{(n+1)}:\nabla\boldsymbol{v}+c_e\mu_a\boldsymbol{\phi}^{(n+1)}\cdot\boldsymbol{v}) + \int_{\partial\Omega}\frac{1}{2A}\boldsymbol{\phi}^{(n+1)}\cdot\boldsymbol{v} + \int_\Omega\frac{\boldsymbol{\phi}^{(n+1)}}{\Delta_t}\cdot\boldsymbol{v} \\
&= \int_\Omega\begin{pmatrix}q_x^{(n+1)}\\\gamma(\boldsymbol{x})B_n(\boldsymbol{x})\end{pmatrix}\cdot\boldsymbol{v} + \int_\Omega\begin{pmatrix}0\\\gamma(\boldsymbol{x})R_n(\boldsymbol{x})\end{pmatrix}\boldsymbol{v} + \int_\Omega\frac{\boldsymbol{\phi}^{(n)}}{\Delta_t}\cdot\boldsymbol{v}.
\end{aligned}
\tag{2.3.23}
$$

Remark 4. *For $n > 0$, the term $B_n(\boldsymbol{x})$ is known and has to be updated for each time step.*

Remark 5. *In practice, a generic BDF scheme has been implemented to enable the extension to higher order methods in time.*

Second method   Instead of handling the memory term in the fluorescence equation, a second method consists in introducing the ODE on the fluorescence source term q_m detailed in section 2.2.1 and solve a degenerated problem (2.3.24) derived from the initial model (2.1.1) and written as follows

$$
\begin{cases}
-\nabla \cdot (\kappa_x \nabla \phi_x^k) + c_e \mu_{a,x} \phi_x^k + \dfrac{\partial \phi_x^k}{\partial t} = q_x^k & \text{on } \Omega \times (0, T) , \\[2mm]
q_m'^k - \dfrac{1}{\tau} q_m^k = \dfrac{1}{\tau} \phi_x^k & \text{on } \Omega \times (0, T) , \\[2mm]
-\nabla \cdot (\kappa_m \nabla \phi_m^k) + c_e \mu_{a,m} \phi_m^k + \dfrac{\partial \phi_m^k}{\partial t} = \gamma q_m^k & \text{on } \Omega \times (0, T) , \\[2mm]
\phi_x^k + 2\mathrm{A}\kappa_x \dfrac{\partial \phi_x^k}{\partial \boldsymbol{n}} = 0 & \text{on } \partial\Omega \times (0, T) . \\[2mm]
\phi_m^k + 2\mathrm{A}\kappa_m \dfrac{\partial \phi_m^k}{\partial \boldsymbol{n}} = 0 & \text{on } \partial\Omega \times (0, T) . \\[2mm]
\phi_x^k(0, \cdot) = \phi_{x,0} \\[2mm]
\phi_m^k(0, \cdot) = \phi_{m,0}
\end{cases}
\tag{2.3.24}
$$

Considering this problem instead of the initial one (2.1.1), we convert a memory cost (or a storage cost) for a computational cost, but more efficient by solving the new ODE equation (2.3.24) explicitly. A possible advantage is for different time grids. As the solution for the fluorescence problem depends on the regularity of ϕ_x, we might choose a coarse grid for the fluorescence and adapt the ODE scheme (e.g high order Runge Kutta (RK) method) to regularize the solution with the aim to reduce the computational cost of the global system.

Remark 6. *Note that if we choose to reconstruct only fluorophore parameters, meaning we assume the diffusion and absorption paramaters to be very close for the diffusion and absorption ($\kappa_x \approx \kappa_m$, $\mu_{a,x} \approx \mu_{a,m}$), the adjoint can be formulated on the diffusion PDE and fluorescence ODE only. The fluorescence equation being used only to calculate the objective function when the error from Tissue Temporal Point Spread Function (TPSF) measurements is computed (see chapter 4)*

2.3.3   Full Discrete formulation

We now turn to the Galerkin approximation of the semi-discrete problem (2.3.23). The space discretization may vary depending on the contact or non-contact case follow section 2.2 analysis. Let $Z_h = V_h \times W_h \subset [H^1(\Omega)]^2$ the discrete spaces of the problem (2.3.23), V_h associated the diffusion and W_h associated to the fluorescence equations respectively. The subscript h denotes the space discretization step.

Remark 7. *In practice, we choose V_h and W_h as the same space, but they could be different, for example to handle with different meshes in the case of mesh adaptation. This is the case when using a Mumford-Shah regularization for the optimization problem we will consider in section 4.2.*

Let $\mathcal{T}_h$ be a space grid for the domain Ω. Let N_i denotes the mesh vertices of $\mathcal{T}_h$ with $i \in [1, N_h]$. We introduce a vectorial basis $\{\boldsymbol{\varphi}_j\}$ for Z_h defined by

$$
\boldsymbol{\varphi}_j(N_i) = \{\varphi_j^k(N_i) \mid k \in \{x, m\}\},
\tag{2.3.25}
$$

the basis function of the space V_h and W_h for $k = x$ and $k = m$ respectively, such that

$$
\varphi_j^k(N_i) = \delta_{i,j} = \begin{cases} 0 & i \neq j, \\ 1 & i = j, \end{cases} \quad i, j = 1, \dots, N_h
\tag{2.3.26}
$$

Remark 8. *The model (2.1.1) is weakly coupled by the source term. Thus we may define a basis function adapted to this particular case to avoid assembling the full system with bloc matrices, but solving each equation separately. Note that the algebraic solver is also adapted for the multi-source case as explained in section 5.3.*

We introduce the Galerkin approximation $\boldsymbol{\phi}_h^{(n)} = \{\boldsymbol{\phi}_x^{(n)}, \boldsymbol{\phi}_m^{(n)}\} \in [V_h]^2$ defined for each $t \approx t_n$ with $n > 0$ of (2.3.23).

$$
\boldsymbol{\phi}_h^{(n)}(\boldsymbol{x}) = \sum_{j=1}^{N_h} \phi_j^n \boldsymbol{\varphi}_j(\boldsymbol{x}).
\tag{2.3.27}
$$

We denote $\phi_h^{(n)} = \phi_h^{(n)}(\boldsymbol{x})$ for brevity. Let $\boldsymbol{v}_h \in Z_h$ the test functions expressed as a basis function in Z_h

$$\boldsymbol{v}_h^{(n)}(\boldsymbol{x}) = \boldsymbol{\varphi}_i(\boldsymbol{x}), \tag{2.3.28}$$

If we inject the approximated solution into the previous established semi-discrete formulation (2.3.23), then we obtain the following relation

$$\int_\Omega (\kappa \nabla \phi_h^{(n+1)} : \nabla \boldsymbol{v}_h + c_e \mu_a \phi_h^{(n+1)} \cdot \boldsymbol{v}_h) + \int_{\partial\Omega} \frac{1}{2A} \phi_h^{(n+1)} \cdot \boldsymbol{v}_h + \int_\Omega \frac{\phi_h^{(n+1)}}{\Delta_t} \cdot \boldsymbol{v}_h$$
$$= \int_\Omega \begin{pmatrix} q_x \\ \gamma(\boldsymbol{x}) B_n(\boldsymbol{x}) \end{pmatrix} \cdot \boldsymbol{v}_h + \int_\Omega \begin{pmatrix} 0 \\ \gamma(\boldsymbol{x}) R_n(\boldsymbol{x}) \end{pmatrix} \boldsymbol{v}_h + \int_\Omega \frac{\phi_h^{(n)}}{\Delta_t} \cdot \boldsymbol{v}_h \ . \tag{2.3.29}$$

We introduce the Galerkin approximation $q_{x,h}^{(n)}$ for the diffusion source term such that for the contact case (i), we have

$$q_{x,h}^{(n)} = \begin{cases} \sum_{j=1}^{N_h} \delta_{h,j} \varphi_j(x) & n = 0 \\ 0 & n > 0 \end{cases} \tag{2.3.30}$$

such that

$$\delta_{h,j} = \begin{cases} 1 & j = j_0 \ (x = x_0) \\ 0 & \text{else} \end{cases} \tag{2.3.31}$$

and for the non contact case, we have

$$q_{x,h}^{(n)} = \begin{cases} \sum_{i=1}^{N_h} \delta_h \varphi_j(x_{\Sigma_0}) & n = 0 \\ 0 & n > 0 \end{cases} \tag{2.3.32}$$

Consequently, from (2.3.29), we develop each term of the formulation

$$\int_\Omega \boldsymbol{\kappa} \nabla \left(\sum_{j=1}^{N_h} \phi_j^{(n+1)} \cdot \boldsymbol{\varphi}_j \right) : \nabla \boldsymbol{\varphi}_i + \int_\Omega c_e \boldsymbol{\mu}_a \left(\sum_{j=1}^{N_h} \phi_j^{(n+1)} \cdot \boldsymbol{\varphi}_j \right) \boldsymbol{\varphi}_i$$
$$+ \int_{\partial\Omega} \frac{1}{2A} \left(\sum_{j=1}^{N_h} \phi_j^{(n+1)} \cdot \boldsymbol{\varphi}_j \right) \cdot \boldsymbol{\varphi}_i + \int_\Omega \frac{1}{\Delta_t} \left(\sum_{j=1}^{N_h} \phi_j^{(n+1)} \cdot \boldsymbol{\varphi}_j \right) \cdot \boldsymbol{\varphi}_i$$
$$= \int_\Omega \begin{pmatrix} q_{x,h} \\ \gamma(\boldsymbol{x}) B_n(\boldsymbol{x}) \end{pmatrix} \cdot \boldsymbol{\varphi}_i + \int_\Omega \begin{pmatrix} 0 \\ \gamma(\boldsymbol{x}) R_n(\boldsymbol{x}) \end{pmatrix} \cdot \boldsymbol{\varphi}_i$$
$$+ \int_\Omega \frac{1}{\Delta_t} \left(\sum_{j=1}^{N_h} \phi_j^{(n)} \cdot \boldsymbol{\varphi}_j \right) \cdot \boldsymbol{\varphi}_i \ . \tag{2.3.33}$$

We recall the remainder term written in the basis

$$R_n = C_1 \sum_{j=1}^{N_h} \phi_j^{(n+1)} \varphi_j + C_2 \sum_{j=1}^{N_h} \phi_j^{(n)} \varphi_j \tag{2.3.34}$$

then we may write

$$\sum_{j=1}^{N_h} \phi_j^{(n+1)} \left(\int_\Omega \boldsymbol{\kappa} \nabla \boldsymbol{\varphi}_j : \nabla \boldsymbol{\varphi}_i \right) + \sum_{j=1}^{N_h} \phi_j^{(n+1)} c_e \left(\int_\Omega \boldsymbol{\mu}_a \boldsymbol{\varphi}_j \boldsymbol{\varphi}_i \right)$$
$$+ \sum_{j=1}^{N_h} \phi_j^{(n+1)} \frac{1}{2A} \left(\int_{\partial\Omega} \boldsymbol{\varphi}_j \boldsymbol{\varphi}_i \right) + \sum_{j=1}^{N_h} \phi_j^{(n+1)} \frac{1}{\Delta_t} \left(\int_\Omega \boldsymbol{\varphi}_j \boldsymbol{\varphi}_i \right)$$
$$= \begin{pmatrix} q_x \\ \gamma(\boldsymbol{x}) B_n(\boldsymbol{x}) \end{pmatrix} \int_\Omega \boldsymbol{\varphi}_i + \sum_{j=1}^{N_h} \phi_j^{(n+1)} C_1 \left(\int_\Omega \gamma(\boldsymbol{x}) \begin{pmatrix} 0 \\ \varphi_j \end{pmatrix} \boldsymbol{\varphi}_i \right)$$
$$+ \sum_{j=1}^{N_h} \phi_j^{(n)} C_2 \left(\int_\Omega \gamma(\boldsymbol{x}) \begin{pmatrix} 0 \\ \varphi_j \end{pmatrix} \boldsymbol{\varphi}_i \right) + \sum_{j=1}^{N_h} \phi_j^{(n)} \frac{1}{\Delta_t} \left(\int_\Omega \boldsymbol{\varphi}_j \boldsymbol{\varphi}_i \right) \ . \tag{2.3.35}$$

We factorize the coefficients such that

$$a_{i,j} = \int_\Omega \boldsymbol{\kappa} \nabla \boldsymbol{\varphi}_j : \nabla \boldsymbol{\varphi}_i \tag{2.3.36}$$

$$b_{i,j} = \int_\Omega \boldsymbol{\mu}_a \boldsymbol{\varphi}_j \boldsymbol{\varphi}_i \tag{2.3.37}$$

$$m_{i,j} = \int_\Omega \boldsymbol{\varphi}_j \boldsymbol{\varphi}_i \tag{2.3.38}$$

$$f_{i,j} = \int_\Omega \gamma(\boldsymbol{x}) \begin{pmatrix} 0 \\ \boldsymbol{\varphi}_j \end{pmatrix} \boldsymbol{\varphi}_i \tag{2.3.39}$$

Then for $0 < i, j < N_h$, let $\boldsymbol{\Phi}^n = \{\phi_j\}$ the solution vector, $M = \{m_{i,j}\}$ the mass matrix, $B = \{b_{i,j}\}$ the attenuation mass matrix $A = \{a_{i,j}\}$ the stiffness matrix, $F = \{f_{i,j}\}$ a fluorescence concentration mass matrix, and $\mathcal{Q}$ the right hand side, this system can be rewritten in an matrix form

$$A\boldsymbol{\Phi}^{(n+1)} + c_e B\boldsymbol{\Phi}^{(n+1)} + M\left(\frac{1}{2A} + \frac{1}{\Delta_t}\right)\boldsymbol{\Phi}^{(n+1)} - C_1 F\boldsymbol{\Phi}^{(n+1)} = \mathcal{Q}^n \tag{2.3.40}$$

Derive from (2.3.35) the following full-discrete form for $i = 1, .., N_h$

$$\sum_{j=1}^{N_h} \phi_j^{(n+1)} a_{i,j} + \sum_{j=1}^{N_h} \phi_j^{(n+1)} c_e b_{i,j} + \sum_{j=1}^{N_h} \phi_j^{(n+1)} \left(\frac{1}{2\mathrm{A}} + \frac{1}{\Delta_t}\right) m_{i,j} - \sum_{j=1}^{N_h} \phi_j^{(n+1)} C_1 f_{i,j}$$
$$= \begin{pmatrix} q_x \\ \gamma(\boldsymbol{x})B_n(\boldsymbol{x}) \end{pmatrix} \int_\Omega \boldsymbol{\varphi}_i + \sum_{j=1}^{N_h} \phi_j^{(n)} C_2 f_{i,j} + \sum_{j=1}^{N_h} \phi_j^{(n)} \frac{1}{\Delta_t} m_{i,j} \ . \tag{2.3.41}$$

2.3.4 Convergence results

A convergence result is given depending on the type of source q_x. The contact case result is based on the proof of [10] whereas the non-contact one is based on [11] results. For the non-contact case, we are taking into account that the surface for the δ-Dirac source can be taken on a different mesh from the domain Ω introducing an interpolation error for the worst scenario.

contact case   The convergence result relies on [10]. We place ourselves under the same hypothesis as [10]. Let us denote Ω the whole domain and $\mathcal{T}_h$ a triangulation on $\Omega \in \mathbb{R}^d$ with $d > 0$ the dimension. We denote V the Sobolev completion of $H^m(\Omega)$. Let V be a Hilbert space associated to the variational formulation of an elliptic problem with right-hand side a Dirac measure δ_{x_0}, $x_0 \in \Omega$, for an operator of order $2m$, $m \geq 1$ (V is the completion of smooth functions in the Sobolev space $H^m(\Omega)$). Let S^h be a finite element subspace of V. We say that S^h approximates to degree k in V if for each smooth u in V:

$$\inf_{v \in S^h} \|u - v\|_{H^s(\Omega)} \leq C(x_0) h^{k-s} \|u\|_k, \quad \text{for } 0 \leq s \leq m. \tag{2.3.42}$$

Typically, for $m = 1$ the degree $k = \ell + 1$, where ℓ is the polynomial degree in S^h. Then we have the theorem (see [10]),

Theorem 4. *If ϕ_x solves (2.1.1) in the sense of distributions for $q_x = \delta_{x_0}$ and $\phi_{x,h}$ is the solution to the associated variational problem, then*

$$\|\phi_x - \phi_{x,h}\|_{H^s} \leq C(x_0) h^{2m - \frac{d}{2} - s} \quad \text{for } 2m - k \leq s < 2m - \frac{d}{2} \tag{2.3.43}$$

if $k \geq 2m$ then $C(x_0)$ goes to infinity as x_0 approaches $\partial\Omega$

In particular, according to (2.3.42), we have for $d = 2$, $m = 1$ and $\ell = 1$ the convergence rate $O(h^{1-s})$ for $0 \leq s \leq 1$. With $d = 3$, we obtain $O(h^{\frac{1}{2}-s})$ for $0 \leq s \leq \frac{1}{2}$.

Remark 9. *The distance $d(x_0, \partial\Omega)$ corresponds to the mean free path which is the medium length of a path covered by a photon (or particle) between subsequent impacts. In practice, this distance is taken equal to the inverse of the reduced scattering coefficient $d(x_0, \partial\Omega) = \frac{1}{\mu'_s}$. Note that as x_0 goes to $\partial\Omega$ the constant $C(x_0)$ goes $+\infty$ [10]*

Non contact case   In the following section, an error estimate is proposed for our special source term of Dirac type. We keep the notation of section 2.2.2 and we adapt it for the non-contact case, the proposition given in [11] taking Ω an open bounded domain of $\mathbb{R}^d$, $d = 2, 3$ and a subdomain $\Sigma_0 \in \partial D \subset\subset \Omega$ in R^{d-1}. We consider our parabolic problem with a right hand side of Dirac type. The method consists in approximating the source term by a sum of Dirac masses for Σ_0. To handle the right hand side $q_x(\boldsymbol{x}, t)$, we denote $q_x(0) = q_x(\boldsymbol{x}, 0) = \delta_{\Sigma_0}$ and Σ_0 a closed or an open surface in Ω as detailed in section 2.3.1, then for any $v \in V \subset H^1(\Omega)$, one has

$$< q_x(0), v >_{H^{-1}, H^1} = < \delta_{\Sigma_0}, v >_{H^{-1}, H^1} = \int_{\Sigma_0} v \tag{2.3.44}$$

Given a triangulation $\mathcal{T}_h$ of Ω we introduce $\mathcal{T}_{\tilde{h}}$ a discretization of Σ_0 of $d - 1$ dimension. One denotes $\mathcal{E}_h$ the interior edges of the mesh $\mathcal{T}_h$. We assume that $\mathcal{T}_{\tilde{h}}$ is not a submesh of $\mathcal{E}_h$ (Note that if $\mathcal{T}_{\tilde{h}}$ is a submesh of $\mathcal{E}_h$, then following calculations are simpler since it is not necessary to interpolate between meshes). We consider V_h as the P_1 finite element space defined by

$$V_h = \{ v_h \in C^0(\overline{\Omega}), v_{h|K} \text{ affine}, \forall K \in \mathcal{T}_h \} \tag{2.3.45}$$

We adapt the first lemma of [11] to the three-dimensional case which will be useful in the next proposition

Lemma 1. *Let $D \in \mathbb{R}^d$ with $d = 1, 2$ be a smooth domain. Let Σ_0 an open curve, Σ_e a smooth curve such that $\Sigma_0 \cap \Sigma_e = \emptyset$ and $\partial D = \overline{\Sigma}_0 \cup \overline{\Sigma}_e$. Let denote $\tilde{h} > 0$ and $\mathcal{T}_{\tilde{h}}$ a family of quasi-uniform d-dimensionnal triangulations of Σ_0 with $\Sigma_i, 1 < i < N$ the subintervals. The quasi-uniformity expresses*

$$c\tilde{h}^d \leq |\Sigma_i| \leq C\tilde{h}^d, \quad \text{with } 0 < c < C. \tag{2.3.46}$$

We consider a set of points in the subsurfaces $x_i \in \Sigma_i$. For $v \in H^1(\Sigma_i)$, the piecewise constant interpolant reads

$$v_{\tilde{h}} = \sum_{i=1}^N v(x_i) \mathbb{1}_{\Sigma_i}. \tag{2.3.47}$$

Then for $0 \leq s < 1/2$, we have

$$\|v - v_{\tilde{h}}\|_{H^s} \leq C\tilde{h}^{1-s} |v|_1, \tag{2.3.48}$$

with $|v|_1$ the H^1 seminorm and the associated usual Sobolev norm

$$\|w\|_{H^s} = \left(\int_{\Sigma_0} |w|^2 \right)^{1/2} + \left(\int_{\Sigma_0} \int_{\Sigma_0} \frac{|w(\boldsymbol{y}) - w(\boldsymbol{x})|^2}{\|\boldsymbol{y} - \boldsymbol{x}\|^{2(s + \frac{d}{2})}} \right)^{1/2}, \quad 0 \leq s < 1/2 \tag{2.3.49}$$

Proof. For d=1 the proof follows [11]. For d=2, let denote $w_{\tilde{h}} = v - v_{\tilde{h}}$, we split the second term in the Sobolev norm (2.3.49) to treat the diagonal term (For the case $\boldsymbol{y} - \boldsymbol{x} = 0$). Thus, we writes

$$\int_{\Sigma_0} \int_{\Sigma_0} \frac{|w_{\tilde{h}}(\boldsymbol{y}) - w_{\tilde{h}}(\boldsymbol{x})|^2}{\|\boldsymbol{y} - \boldsymbol{x}\|^{2(s + \frac{d}{2})}} = \sum_{i=1}^N \sum_{j=1}^N \int_{\Sigma_i} \int_{\Sigma_j} \frac{|v(\boldsymbol{y}) - v(x_j) - v(\boldsymbol{x}) + v(x_i)|^2}{\|\boldsymbol{y} - \boldsymbol{x}\|^{2(s + \frac{d}{2})}}$$

$$= \sum_{i=1}^N \int_{\Sigma_i} \int_{\Sigma_i} \frac{|v(\boldsymbol{y}) - v(\boldsymbol{x})|^2}{\|\boldsymbol{y} - \boldsymbol{x}\|^{2(s + \frac{d}{2})}} + \sum_{i=1}^N \sum_{j=1, j \neq i}^N \int_{\Sigma_i} \int_{\Sigma_j} \frac{|w_{\tilde{h}}(\boldsymbol{y}) - w_{\tilde{h}}(\boldsymbol{x})|^2}{\|\boldsymbol{y} - \boldsymbol{x}\|^{2(s + \frac{d}{2})}} \tag{2.3.50}$$

$$= A + B$$

Let $\boldsymbol{\nu} = \boldsymbol{y} - \boldsymbol{x}$. A majoration for the diagonal term can be determined. Using the Taylor formula with integral remainder

$$v(\boldsymbol{y}) - v(\boldsymbol{x}) = \int_0^1 Dv(\boldsymbol{x} + t\boldsymbol{\nu})(\boldsymbol{\nu}) dt \tag{2.3.51}$$

and applying Cauchy-Schwarz inequality, we have

$$|v(\boldsymbol{y}) - v(\boldsymbol{x})|^2 = \left| \int_0^1 Dv(\boldsymbol{x} + t\boldsymbol{\nu})(\boldsymbol{\nu}) dt \right|^2 \leq \int_0^1 |Dv(\boldsymbol{x} + t\boldsymbol{\nu})|^2 |\boldsymbol{\nu}|^2 dt \tag{2.3.52}$$

then the first term reads

$$A \leq \sum_{i=1}^{N} \int_{\Sigma_i} \int_{\Sigma_i} \left(\int_0^1 |Dv(\boldsymbol{x} + t\boldsymbol{\nu})|^2 dt \right) \frac{|\boldsymbol{\nu}|^2}{|\boldsymbol{\nu}|^{2(s+\frac{d}{2})}}$$

$$\leq \sum_{i=1}^{N} \left(\int_{\Sigma_i} |Dv(\boldsymbol{z})|^2 dz \right) \int_{\Sigma_i} \int_{\Sigma_i} |\boldsymbol{\nu}|^{-2(s+\frac{d}{2})+2} \quad \text{(with } d=2\text{)}$$

(2.3.53)

For the last double integral, we perform a majoration on $\Sigma_i = I_1 \times I_2$, For d=1 the majoration is given in [11]. For d=2, let (x_j, y_j) for $1 \leq j \leq 2$ be a couple of points in Σ_i.

$$\int_{\Sigma_i} \int_{\Sigma_i} |\boldsymbol{\nu}|^{-2s} = \int_{\Sigma_i} \left(\int_{I_1} \int_{I_2} |(y_1 - x_1)^2 + (y_2 - x_2)^2|^{-s} \right)$$

(2.3.54)

we note that $|w|^\alpha$ is convex for $\alpha < 0$. Thus for $\theta \in [0, 1]$ convexity writes as

$$|\theta a + (1 - \theta)b|^\alpha \leq \theta |a|^\alpha + (1 - \theta)|b|^\alpha$$

(2.3.55)

and choosing coefficients

$$a = \frac{(y_1 - x_1)^2}{\theta}, \quad b = \frac{(y_2 - x_2)^2}{(1 - \theta)}$$

(2.3.56)

there exists $C_\theta > 0$

$$|(y_1 - x_1)^2 + (y_2 - x_2)^2|^\alpha \leq C_\theta |y_1 - x_1|^{2\alpha} + C_\theta |y_2 - x_2|^{2\alpha}$$

(2.3.57)

For $\theta = \frac{1}{2}$, the constant is $C_0 = \frac{1}{2^{1-\alpha}}$. For $\alpha = -s$ and going back to (2.3.54) one has the following majoration

$$\int_{\Sigma_i} \int_{\Sigma_i} |\boldsymbol{\nu}|^{-2s} \leq C_0 \int_{\Sigma_i} \left(\int_{I_1} \int_{I_2} |y_1 - x_1|^{-2s} + \int_{I_1} \int_{I_2} |y_2 - x_2|^{-2s} \right)$$

$$\leq C_0 \int_{\Sigma_i} \left(\tilde{h} \int_{I_1} |y_1 - x_1|^{-2s} + \tilde{h} \int_{I_2} |y_2 - x_2|^{-2s} \right)$$

(2.3.58)

$$\leq C_0 \tilde{h}^2 \int_{I_1} \int_{I_1} |y_1 - x_1|^{-2s} + C_0 \tilde{h}^2 \int_{I_2} \int_{I_2} |y_2 - x_2|^{-2s}$$

For the last integral of (2.3.58), let consider the following mapping

$$\varphi_i : \Sigma_i = I_1 \times I_2 \longrightarrow [0, \tilde{h}] \times [0, \tilde{h}]$$
$$(x, y) \longrightarrow \varphi_i(x, y)$$

(2.3.59)

and J_φ the associated jacobian such that $\det(J_\varphi) \leq \tilde{h}^2$. Then the last integral of (2.3.58) can be calculated

$$\int_0^{\tilde{h}} \int_0^{\tilde{h}} |y - x|^{-2s} \det(|J_\varphi|)^{-1} dx dy = \tilde{h}^{-2} \int_0^{\tilde{h}} \left(\int_0^x |y - x|^{-2s} dy + \int_x^{\tilde{h}} |y - x|^{-2s} dy \right) dx$$

$$= \tilde{h}^{-2} \int_0^{\tilde{h}} \left(\int_0^x (x - y)^{-2s} dy + \int_x^{\tilde{h}} (y - x)^{-2s} dy \right) dx$$

$$= \tilde{h}^{-2} \int_0^{\tilde{h}} \left(\left[-\frac{(x - y)^{1-2s}}{1 - 2s} \right]_0^x + \left[\frac{(y - x)^{1-2s}}{1 - 2s} \right]_x^{\tilde{h}} \right) dx$$

$$= \frac{\tilde{h}^{-2}}{1 - 2s} \int_0^{\tilde{h}} \left(x^{1-2s} + (\tilde{h} - x)^{1-2s} \right) dx$$

$$= \frac{\tilde{h}^{-2}}{(1 - 2s)(2 - 2s)} \left[x^{2-2s} - (\tilde{h} - x)^{2-2s} \right]_0^{\tilde{h}}$$

$$= \frac{2\tilde{h}^{-2s}}{(1 - 2s)(2 - 2s)}$$

(2.3.60)

47

From (2.3.58) we have

$$\int_{\Sigma_i} \int_{\Sigma_i} |\boldsymbol{\nu}|^{-2s} \leq \frac{\tilde{h}^{2-2s}}{2^{s-1}(1-2s)(2-2s)} \tag{2.3.61}$$

and from (2.3.53) we obtain

$$A \leq C_1 \tilde{h}^{2-2s} \left(\int_{\Sigma_0} |Dv(\boldsymbol{z})|^2 dz \right) \tag{2.3.62}$$

with a constant $C_1 = \frac{2^{1-s}}{(1-2s)(2-2s)}$. A majoration can be determined for the non diagonal term B using the same techniques.

$$B \leq 4 \sum_{i=0}^{N} \sum_{j=0, j\neq i}^{N} \int_{\Sigma_i} \int_{\Sigma_j} \frac{|w_{\tilde{h}}(\boldsymbol{x})|^2}{|w|^{2s+2}} \tag{2.3.63}$$

Thanks to (2.3.52) and (2.3.61)

$$\begin{aligned}
B &\leq 4 \sum_{i=1}^{N} \sum_{j=1, j\neq i}^{N} \int_{\Sigma_i} \int_{\Sigma_j} \left(\int_0^1 |Dv(\boldsymbol{z})|^2 dz \right) \frac{1}{|\boldsymbol{\nu}|^{2s}} \\
&\leq 4 \left(\int_{\Sigma_0} |Dv(\boldsymbol{z})|^2 dz \right) \sum_{i=1}^{N} \sum_{j=1, j\neq i}^{N} \int_{\Sigma_i} \int_{\Sigma_j} |\boldsymbol{\nu}|^{-2s} \\
&\leq C_2 \tilde{h}^{2-2s} \left(\int_{\Sigma_0} |Dv(\boldsymbol{z})|^2 dz \right)
\end{aligned} \tag{2.3.64}$$

with a constant $C_2 = \frac{2^{3-s}}{(1-2s)(2-2s)}$. Finally, one deduces a majoration for the double integral term in the Sobolev norm

$$\left(\int_{\Sigma_0} \int_{\Sigma_0} \frac{|w(\boldsymbol{y}) - w(\boldsymbol{x})|^2}{\|\boldsymbol{y} - \boldsymbol{x}\|^{2(s+\frac{d}{2})}} \right)^{1/2} \leq C_3 \tilde{h}^{2-2s} |v|_{1,\Sigma_0}^2 \tag{2.3.65}$$

with a constant $C_3 = C_1 + C_2 = \frac{5.2^{1-s}}{(1-s)(2-s)}$. For the L_2 norm, using again (2.3.52) we deduce

$$\begin{aligned}
\int_{\Sigma_0} |w_{\tilde{h}}|^2 &= \sum_{i=1}^{N} \int_{\Sigma_i} |w_h|^2 \\
&\leq \sum_{i=1}^{N} \int_{\Sigma_i} \left(\int_0^1 |Dv(\boldsymbol{z})|^2 dz \right) |\boldsymbol{\nu}|^2 \\
&\leq \sum_{i=1}^{N} \left(\int_{\Sigma_i} |Dv(\boldsymbol{z})|^2 dz \right) \int_{\Sigma_i} |\boldsymbol{\nu}|^2 \\
&\leq C_4 \tilde{h}^2 |v|_{1,\Sigma_0}^2
\end{aligned} \tag{2.3.66}$$

with $C_4 = \frac{1}{6}$. Finally, we deduce the lemma 1 norm with an order 1-s. $\qquad \square$

We adapt the trace theorem lemma in [11]

Lemma 2. *Let $\Omega \in \mathbb{R}^d$ with $d = 2, 3$ and D be a smooth subdomain of Ω. Let Σ_0 an open curve, Σ_e a smooth curve such that $\Sigma_0 \cap \Sigma_e = \emptyset$, $\overline{\Sigma}_0 \cup \overline{\Sigma}_e = \partial D$ the boundary. Let $(\mathcal{T}_h)_h$ be a regular family of triangulations, and V_h the associated P^1 finite element space. Then the trace operator γ_0 maps V_h into $H^1_{\Sigma_0}$ and one has*

$$|\gamma_0(v_h)|_{1,\Sigma_0} \leq \frac{C}{h^{1/2}} |v_h|_{1,\Omega} \tag{2.3.67}$$

Then we adapt the proposition 1 of [11] to find the δ-Dirac approximation error

Proposition 1. *Let Ω be a domain of $\mathbb{R}^d$ with $d = 3$ and $D \subset\subset \Omega$ a smooth subdomain with boundary ∂D. Let define Σ_0 an open curve, Σ_e a smooth curve such that $\Sigma_0 \cap \Sigma_e = \emptyset$ and $\overline{\Sigma}_0 \cup \overline{\Sigma}_e = \partial D$. Let $(\mathcal{T}_h)_h$ be regular family of triangulations with V_h the associated P_1 finite element space. Let $\varphi \in H^{-1/2+s}(\Sigma_0)$. Let $S_{\tilde{h}}$ be a family of quasi-uniform triangulation of $\partial D = \bigcup_i \Sigma_i$ and one denotes $\Sigma_{0,i} = \{\Sigma_i \mid \Sigma_i \in \Sigma_0\}$. Let $x_i \in \Sigma_i$, one defines*

$$\varphi_h^{\tilde{h}} = \sum_{i=1}^{N_{\tilde{h}}} \lambda_i \delta_{x_i} \tag{2.3.68}$$

with the real coefficients λ_i define such that

$$\lambda_i = \langle \varphi, \mathbb{1}_{\Sigma_i} \rangle \tag{2.3.69}$$

the approximation. Then there exists a contant $C > 0$ such that for all $v_h \in V_h$:

$$\left| \langle \varphi, v_h \rangle - \langle \varphi_h^{\tilde{h}}, v_h \rangle \right| \leq C \sqrt{\frac{\tilde{h}}{h}} \tilde{h}^s \, |\varphi|_{-1/2+s,\Sigma_0} \, |v|_{1,\Omega} \tag{2.3.70}$$

where $\langle \cdot, \cdot \rangle$ denotes the dual pairing for $H^{-1/2+s}(\Sigma_0)$ and $H^{1/2-s}(\Sigma_0)$

Proof. From the Dirac source term definition, the interpolant is positive on Σ_0, then

$$\begin{aligned}
\langle \varphi_h^{\tilde{h}}, v_h \rangle &= \langle \sum_{i=1}^{N_{\tilde{h}}} \langle \varphi, \mathbb{1}_{\Sigma_i} \rangle \delta_{x_i}, v_h \rangle \\
&= \langle \sum_{i=1}^{N_{\tilde{h}}} \langle \varphi, \mathbb{1}_{\Sigma_{0,i}} \rangle, v_h(x_i) \rangle \\
&= \sum_{i=1}^{N_{\tilde{h}}} \int_{\Sigma_{0,i}} \varphi v_h(x_i) \\
&= \langle \varphi, \sum_{i=1}^{N_{\tilde{h}}} v_h(x_i) \mathbb{1}_{\Sigma_{0,i}} \rangle
\end{aligned} \tag{2.3.71}$$

If we consider the approximation error, one has

$$\begin{aligned}
\left| \langle \varphi, v_h \rangle - \langle \varphi_h^{\tilde{h}}, v_h \rangle \right| &= \left| \langle \varphi, v_h \rangle - \langle \varphi, \sum_{i=1}^{N_{\tilde{h}}} v_h(x_i) \mathbb{1}_{\Sigma_{0,i}} \rangle \right| \\
&\leq \|\varphi\|_{H^{-1/2+s}(\Sigma_0)} \left\| v_h - \sum_{i=1}^{N_{\tilde{h}}} v_h(x_i) \mathbb{1}_{\Sigma_{0,i}} \right\|_{H^{1/2-s}(\Sigma_0)} \\
&\leq \|\varphi\|_{H^{-1/2+s}(\Sigma_0)} \|v_h - v_{\tilde{h}}\|_{H^{1/2-s}(\Sigma_0)}
\end{aligned} \tag{2.3.72}$$

with the piecewise interpolant of v_h on Σ_0 such that

$$v_{\tilde{h}} = \sum_{i=1}^{N_{\tilde{h}}} v_h(x_i) \mathbb{1}_{\Sigma_{0,i}} \tag{2.3.73}$$

Let denote $w_h^{\tilde{h}} = v_h - v_{\tilde{h}}$, then (2.3.48) gives the following majoration

$$\|w_{\tilde{h}}\|_{H^{1/2-s}(\Sigma_0)} \leq C \tilde{h}^{s+1/2} |v|_{1,\Sigma_0} \tag{2.3.74}$$

for $C > 0$ adapted. Finally, using lemma 2

$$\|w_{\tilde{h}}\|_{H^{1/2-s}(\Sigma_0)} \leq C \sqrt{\frac{\tilde{h}}{h}} \tilde{h}^s |v|_{1,\Omega} \tag{2.3.75}$$

which ends the proof. $\qquad\square$

To get the error for ϕ_x, we start with the Strang lemma

$$\|\phi_x - \phi_{x,h}\|_{H^1} \leq C \left(\inf_{v_h \in V_h} \|\phi_x - v_h\| + \sup_{w_h \in V_h} \left(\frac{|<\varphi, w_h> - <\varphi_h^{\tilde{h}}, w_{\tilde{h}}>|}{\|w_h\|} \right) \right). \tag{2.3.76}$$

We recall the lemma 2 (Scott), the estimate (with $m = 1$),

$$\|\phi_x - \phi_{x,h}\|_{H^r} \leq C h^{1-r} \|\phi_x - \phi_{x,h}\|_{H^1}, \quad 0 \leq r \leq 1. \tag{2.3.77}$$

We obtain from proposition 1

$$\|\phi_x - \phi_{x,h}\|_{H^r} \leq C h^{1-r} \left(\inf_{v_h \in V_h} \|\phi_x - v_h\| + \sqrt{\frac{\tilde{h}}{h}} \tilde{h}^s |\varphi|_{-1/2+s, \Sigma_0} \right). \tag{2.3.78}$$

If h and $\tilde{h}$ are of the same order, then we get

Proposition 2. *We have the estimate, for $0 \leq r \leq 1$ and $0 \leq s \leq \frac{1}{2}$ and with P^1 finite element,*

$$\|\phi_x - \phi_{x,h}\|_{H^r} \leq C h^{1-r} \left(\inf_{\phi_{x,h} \in V_h} \|\phi_x - \phi_{x,h}\| + h^s |\varphi|_{-1/2+s, \Sigma_0} \right). \tag{2.3.79}$$

In particular for $d = 2$ and in the extreme case $r = 1$, if we assume $\phi_x \in H^2$, we obtain

$$\|\phi_x - \phi_{x,h}\|_{H^1} \leq C \left(\sqrt{h} \|\phi_x\|_{H^2} + h^s |\varphi|_{-1/2+s, \Sigma_0} \right). \tag{2.3.80}$$

we retrieve the result of [11]. However such regularity on ϕ_x seems too strong (theorem 4). Moreover, for the case $d = 3$, even with such regularity assumption a similar estimates

$$\inf_{v_h \in V_h} \|\phi_x - v_h\|_{H^1} \leq C \sqrt{h} \|\phi_x\|_2 \tag{2.3.81}$$

to the best of our knowledge, is not known.

In the case $0 \leq r \leq \frac{1}{2}$ and without further assumption on ϕ_x than the theorem 4,

$$\|\phi_x - \phi_{x,h}\|_{H^r} = O(h^{1-r}) \tag{2.3.82}$$

and the approximation of the source term is of higher order.

2.4 Conclusion

Thoughout the chapter 2, we have proposed a mathematical description for the TR-DOT problem for the diffusion and the fluorescence coupled problem and by considering two type of measurement, contact and non-contact. The model which was considered is based on the diffusion approximation highlighted in chapter 1.

In the section 2.2, the well-posedness is detailed for the contact and non-contact case. We show that the fluorescence source term can be treated separately by introducing a new ODE in the initial system of equations (2.1.1). Thus, the problem can be rewritten as a new degenerated system (2.3.24). Moreover, under restrictive assumption on the regularity of the parameters $\kappa_\ell, \mu_{a,\ell}$ with $\ell \in \{x, m\}$, we can prove the existence and the uniqueness of solution for the contact case theorem 2 and the non-contact case theorem 3.

The section 2.3 details the weak formulation of the TR-DOT problem (2.1.1) which is used within our code implementation. We proposed to give a semi-discrete formulation (2.3.23) and precise two methods to handle the fluorescence source term either by treating it as a memory term or by solving the ODE we introduced before. With the ODE method, we have the possibility to convert a storage cost (in memory or on disk) to a computation cost. The full-discrete formulation (2.3.41) is then given.

Finally, we perform in the last section 2.3.4 the convergence analysis for both cases (contact and non-contact). For the contact case, we use the analysis carried on in theorem 4 and for the non-contact case proposition 1, we obtain an error estimates in full generality, in any dimension ($d = 2, 3$ for the physical problem) and in suitable Sobolev norms.

References

[10]   Ridgway Scott. "Finite element convergence for singular data". In: *Numerische Mathematik* 21.4 (1973), pp. 317–327.

[11]   Benoit Fabrèges and Bertrand Maury. "Approximation of single layer distributions by Dirac masses in Finite Element computations". In: *Journal of Scientific Computing* 58.1 (2014), pp. 25–40.

[12]   Jacques Louis Lions and Enrico Magenes. *Non-homogeneous boundary value problems and applications*. Vol. 1. Springer Science & Business Media, 2012.

[13]   Lucio Boccardo and Thierry Gallouët. "Non-linear elliptic and parabolic equations involving measure data". In: *Journal of Functional Analysis* 87.1 (1989), pp. 149–169.

[14]   Thierry Gallouët. "Measure data and numerical schemes for elliptic problems". In: *Elliptic and parabolic problems* (2005), pp. 279–290.

[15]   Alain Prignet. "Conditions aux limites non homogenes pour des problemes elliptiques avec second membre mesure". In: *annales-faculte des sciences toulouse mathematiques*. Vol. 6. Citeseer. 1997.

[16]   Avner Friedman. *Partial differential equations of parabolic type*. Courier Dover Publications, 2008.

[17]   Olga Aleksandrovna Ladyzhenskaia, Vsevolod Alekseevich Solonnikov, and Nina N Ural'ceva. *Linear and quasi-linear equations of parabolic type*. Vol. 23. American Mathematical Soc., 1968.

Chapter 3 - Forward problem numerical experiments

This chapter is dedicated to the results regarding the forward problem for the diffusion only and with a fluorescence coupling. An initial code was developed during the previous thesis [18] followed by [9] from the IMIS research team (Laboratoire des sciences de l'ingénieur, de l'informatique et de l'imagerie (ICube)) to be used in combination with the tomograph presented in chapter 1 section 1.1. This code is written in Matlab and is based on [2].

A generic code has been developed from scratch during this thesis using an open source finite element framework called FEEL++. Ingredients of the implementation are detailed in part III. This framework has been used to reproduce results generated with Matlab in order to first cross-verify both software and to bing new features. This library presents several advantages compared to the previous software. Among these advantages, FEEL++ implements seamless parallelism and give access in an easy way, to high performance solvers. We have at the same time an expressive programming language very close to the mathematical language (variational form based). Several numerical ingredients used in the forward problem are presented in the chapter 5.

In the following chapter, several simulations are presented to explain the research approach from verification to validation. The diffusion problem is detailed and preliminary results are given for the fluorescence. Finally results are compared with physics experiments.

3.1   Simulations

The first simulation showed in fig. 3.1.2 and fig. 3.1.4 depicts the solution for the coupled problem (2.1.1). The initial model parameters choosen for the simulation are details in table 3.1.1

Table 3.1.1: Model parameters for simulations with inclusions. The diffusion κ is deduced from the absorption μ_a and reduced scattering μ_s'. Also the fluorochrome coefficient Γ is computed from the model (See chapter 1)

	parameter	description	background	inclusion 1	inclusion 2
Diffusion	$\mu_{a,x}$	absorption	0.005	0.025	0.005
	$\mu_{s,x}'$	reduced scattering	0.6	0.6	1.2
	κ_x	diffusion	0.1	0.1	0.05
Fluorescence	$\mu_{a,m}$	absorption	0.005	0.025	0.005
	$\mu_{s,m}'$	reduced scattering	0.6	0.6	1.2
	κ_m	diffusion	0.1	0.1	0.05
	τ	fluorochrome average lifetime	0	560	560
	σ	fluorochrome molar extinguishing coefficient	0	13000	13000
	ξ	fluorochrome concentration	0	0.4342	0.4342
	η	fluorochrome yield	0	0.027	0.027
	γ	fluorochrome coefficient	0	152.43736	152.43736

The fig. 3.1.2 and fig. 3.1.3 shows an example of solution for the diffusion and fluorescence problem after 80 ps and 580 ps respectively. The exhibited simulation is made on an numerical phamtom with two inclusions. The right inclusion C_2 is more diffusive than the background and the left inclusion. The left inclusion C_1 is less aborbant than the background and the right inclusions. The system (2.1.1) properties are detailed in table 3.1.1.

The Indocyanine green (ICG) fluorophore is configured ideally to be concentrated exclusively in both inclusions to mimic the fluorophore behaviour in presence of a tumor. (see table 3.1.1 and fig. 3.1.3). With the parameters chosen in table 3.1.1, the fluorescence source term can be seen as a regularized Dirac located at the inclusion with a decrease in time which depends on the diffusion solution and a scaling factor $\frac{\eta}{\tau}$. The virtual designed tomograph showed in both picture has been modeled using the opensource Computer-Aided Design (CAD) software CAD software (FreeCAD) for better comprehensible visuals (See also the fig. 1.1.1) but will be avoided for data analysis in later sections for convenience. The geometry for the virtual phantom is chosen as a cylinder. Each inclusion is modeled by the shape of a cylinder. The inclusions have a smaller size and are distributed symetrically from the cylinder revolution axis. This geometrical shape is motivated by the experimental phantom shape available

Figure 3.1.1: This figure represents the geometry of a cylinder with two inclusions in the domain Ω. These inclusions are represented by the domain C_1 for the first inclusion and C_2 for the second inclusion 2. The table 3.1.1 shows the different parameters used. On this scheme, the light source 0 is on the right side such that both inclusions are symmetric regarding to the source. The different optical parameters, the absorption μ_a and reduced scattering coefficients μ'_s.
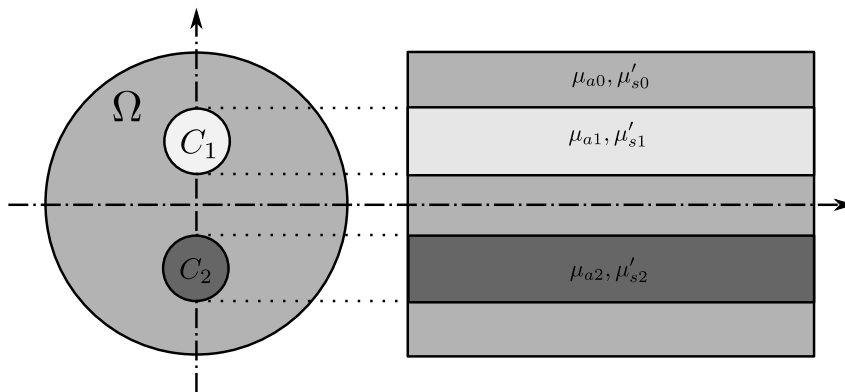
and used for measurements.

Remark 10. *For the forward simulation presented in the chapter 2 diffusion properties κ_x, κ_m and absorption properties $\mu_{a,x}, \mu_{a,m}$ are chosen to be the same. This choice is discussed in section 4.1*

Both figures depict a level of isosurfaces post-processed thanks to Kitware software (Paraview) visualization tool using contouring filter for a certain level luminance. From the previous description, the expected behaviour for the light propagation of the visualized isosurface is a difference of speed.

Remark 11. *With no inclusion and considering several sources distributed all around the object, the isosurface is expected to reach domain boundaries at the same time.*

Photons crossing the diffusion inclusion are deviated in all possible directions whereas less particle are retained by the less absorbant inclusion C_1. A consequence for the isosurface is to be slowered due to the previous two factors when one or several inclusions are crossed. The first figure fig. 3.1.2 shows the solution ϕ_x^0 after few resolution steps. The dirac source term can be viewed.

The fig. 3.1.3 shows by adding contouring filter in the visualization post processing, the difference of light emission depending on sources placement for two inclusions. We notice that, for a fixed time, the light has reached the boundary of the domain faster, for the right inclusion than for the left one. This can be explained by the fact that the fluorophore is exited first.

The figure fig. 3.1.4 shows both solutions for the coupled problem for three different sources (sorted by column). The first row shows the solution of diffusion problem whereas te second row the solution for the fluorescence.

If we compare the fig. 3.1.2 and the fig. 3.1.3, we see that using the fluorescence model, the fluorescence solution seems to provide a better information in time. We can expect to obtain images with better constrast. However, in the fig. 3.1.3, since the source is located on the right side, then photons entering the left inclusion have already crossed and been diffused by the right one. Thus, there will be a slight different if we measure at the boundary. If a third inclusion was added between both inclusions, it would be difficult to determine, by

Figure 3.1.2: Diffusion simulation for an heterogeneous object with 2 inclusions [19]. Parameters are detailed in table 3.1.1. The figure shows a representation of the photon for a specific level of isosurface after 80 ps of diffusion. The source is located on the right side. The light has reached both inclusion, however the effect of the diffusion and absorption can not be observed visually compared to the fluorescence case fig. 3.1.3 (See also the real tomograph in fig. 1.1.1).
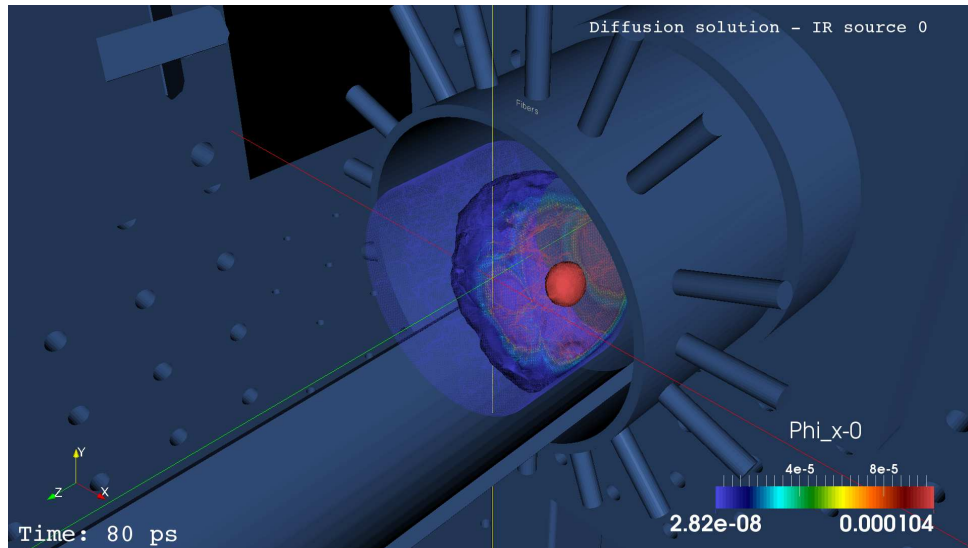
Figure 3.1.3: Fluorescence simulation for an heterogeneous object with 2 inclusions [19]. Parameters are detailed in table 3.1.1. The figure shows a representation of the photons reemitted by fluorescence for a specific level of isosurface after 580 ps of diffusion. The source is placed on the right, diffusion is showed in fig. 3.1.2. Both inclusions have been reached. We see on this figure that less photons have crossed the right inclusions resulting in a difference of speed for one level of the isosurface to reach the boundary of the domain. (See also the real tomograph in fig. 1.1.1)
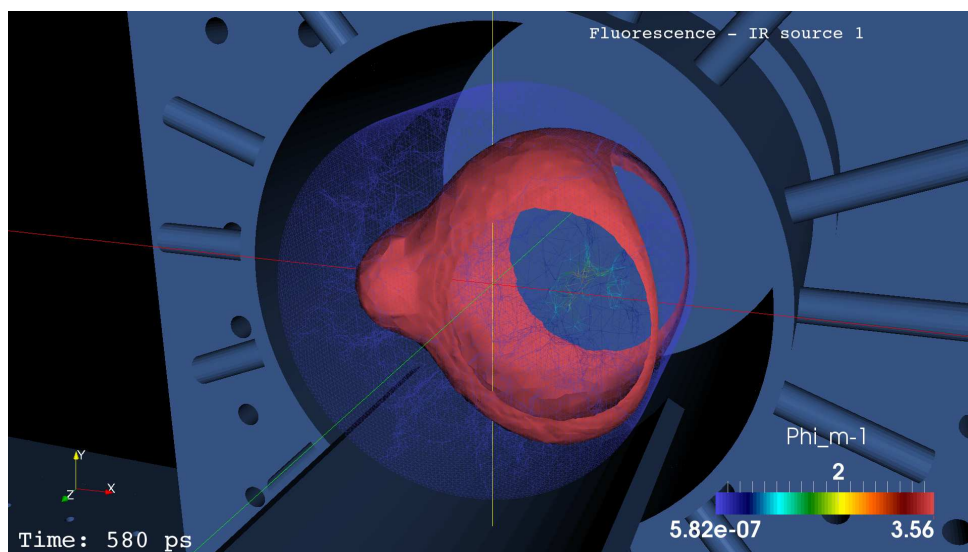
Figure 3.1.4: This figure shows the solution of the forward problem for different source location. The cylindric object has two inclusions, one more diffusive (left) and one more absorbant (right). The first row display the solution for the diffusion ϕ_x, whereas the second row the solution for the fluorescence ϕ_m. From the left column to the right, the source of light is placed respectively on the right side, the top, and the left. After 800 ps, we see that both inclusions are clearly visible when the source is placed at the top, but only one is visible when the source are located on the left or the right. This figure highlight the interest of using multisource measurements and the limits when only a small number of detectors is available.
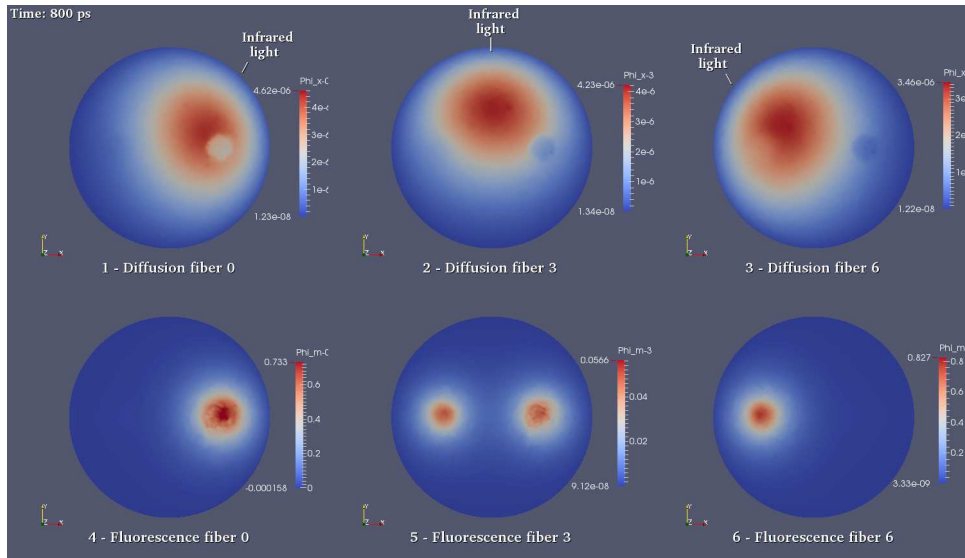
performing only boundary measurement, the number of inclusions. Thus, performing additionnal measurements using source from different locations should improve the quality of the reconstruction. The figure fig. 3.1.4 shows the effect of the source location on the diffusion and fluorescence solution. We see that for the fluorescence solution, at a given time, if the source is located at the top, we can distinguish two inclusions. But if the source is located on the left or on the right, most photons are diffused or absorbed by one of the two inclusions, and only one inclusions can be seen.

3.2 Data verifications

Since the inverse problem depends on how we solve the forward one, before moving to the reconstruction, we need to be sure that the foward problem is solved correctly. The first step consists in performing some verifications to ensure that first the given data are correct. The next steps consist in verifying that we solve properly the equations. For example, we could use analytical solutions, if possible, then proceed with convergence results. Otherwise another possibility is to highlight some convergence results based on observation and using a fine mesh.

We desire first to check that the data are correct. The given data are partial due to the limited number of detectors. The different graphics displayed in this section show the TPSF measurements acquired from several positions corresponding to the placement of the detectors. The setup consist in 16 fibers distributed all around the object. For each source (1 fiber), we have seven detectors (7 opposite fibers), therefore a total of 112 (16*7) measures. The measurements are performed on a plastic object of 40mm diameter. The fig. 3.2.1 shows an example cleaned measurements. We have to take into account also 112 Impulse Response which corresponds to the measure acquired without any objects to calibrate the machine fig. 3.2.3.

Remark 12. *Two measurements on the same detectors for two different sources can differ. There might be several reasons, for example this can be due to a mechanical or eletric noise or again, during the acquisition, due to the rotating effect of the mechanical multiplexor that can be unproperly aligned (See section 1.1).*

We consider a set of measurements on a phantom object named p0116 which is an homogeneous cylindric object made of plastic material. We first proceed with data verifications to ensure that measurements went

properly. The given data are cleaned during a preprocess step which consists in removing erroneous measures and filtering the noise. This preprocessing is made automatically. Sometimes, a diode or a TCSPC card might crash and one measure over the 112 can be wrong and not taken into account during the preprocessing step. One way to check that the given data are correct is to compare measurements realised from different direction using an homogeneous object. Since the object is homogeneous, the diffusion is independent of the chosen source. Indeed, the diffusion will occur in every direction in a same manner up to a rotation.

Remark 13. *Data checking is a process systematically performed before proceeding to numerical computations to improve the reliability of our results.*

Figure 3.2.1: Example of measurements (no Impulse Response deconvolution). In this figure we can see 7 measurements for the 7 detectors for the source 0. The detectors are at the opposite side of the object and dispatched regularly in a symetrical manner. Since the Impulse Response is not taken into account here, the symmetry can not be distinguished visually.
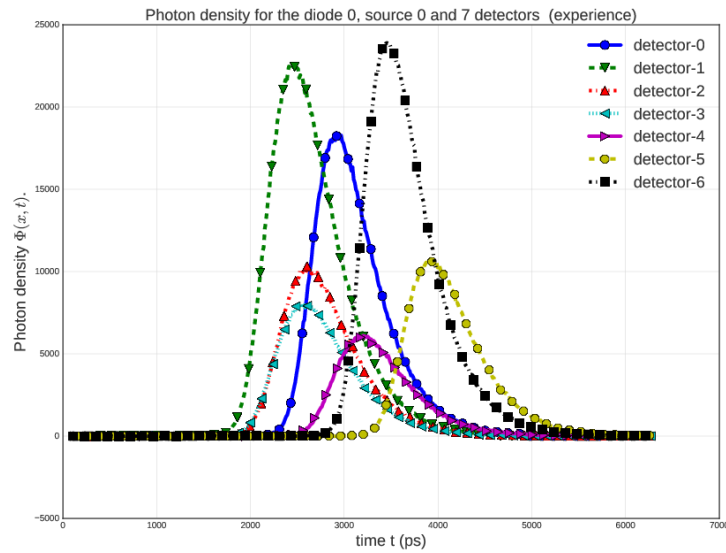
Figure 3.2.2: Example of a normalized Impulse Response for one source and one detector. The blue circle plot shows one measurement made using China ink for retrieving the Impulse Response. This represent an "empty" measurement to determine the system (tomograph) response to a light pulse. The second green squared plot shows a measurement in the p0116 object for the same source, same detector. To obtain the real measurements, we should be able to deconvolve the late measurements by the Impulse Response which is not trivial due to the nature of the data noise
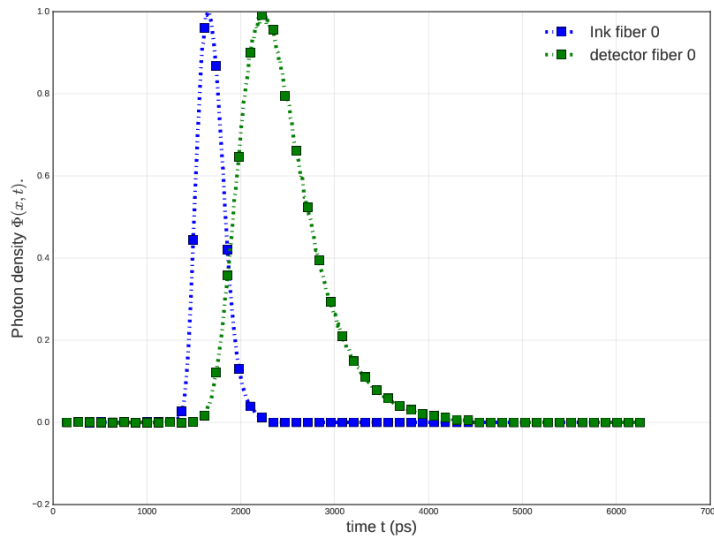
Figure 3.2.3: This figure shows different plots of the further detector TPSF for all the existing sources. Since the object is homogeneous, the diffusion occurs at the same speed in all directions. Since the detector distance are the same, we obtain the same measurement for all sources. This figure shows the expected superpositions of all measures. Note that the Impulse Response has been taken into account in that case to readjust the peaks center and intensity.
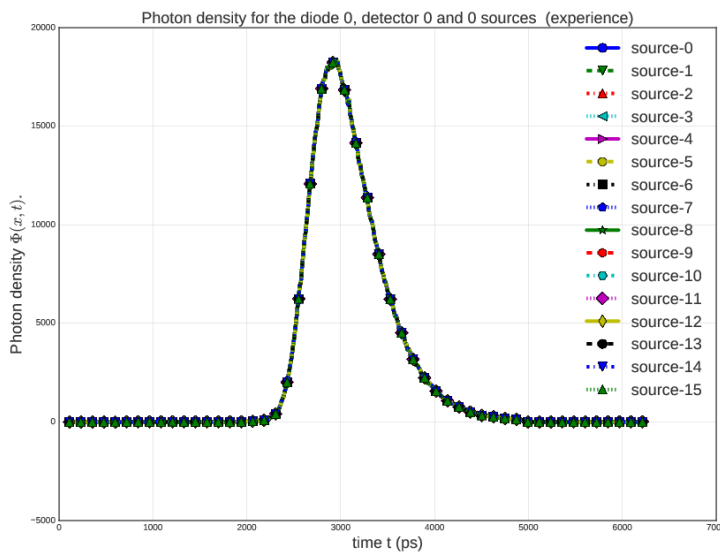
3.3 Model verifications

We checked in section 3.2 that the given data are correct in order to compare them with a solution computed numerically. Now we turn at the verification for the numerical solution obtained with the FEEL++ code. The same type of verification than the one made in section 3.2 can be performed. We verify first that the physics of the problem on an homogeneous object is preserved. We compare on fig. 3.3.1 that the TPSF obtained on several sources produces the same results since the diffusion happens in the same way in all directions. the different TPSF obtained for all detectors for one source are checked to confirm that we preserve the symmetry of the setup, but also the time of propagations depending on the source placement. This symmetry can depend on the quality of the numerical solution with a precision relative to the chosen mesh. This results can be compared with a heterogeneous object and are presented in fig. 3.3.2. Then we present several convergence analysis for high order methods in time (figs. 3.3.3 to 3.3.4, 3.3.6, 3.3.7 and 3.3.10 to 3.3.12) and space (figs. 3.3.8 and 3.3.9). Finally we give a result of cross-verification figs. 3.3.15 and 3.3.16 for two absorption parameters.

Remark 14. *Thanks to the cross-verification, we discovered several issues, in the original FEEL++ code but also in the FEEL++ implementation that have been fixed.*

Figure 3.3.1: This figure shows different plots of the further detector TPSF for all the existing sources. This figure is comparable to the verification performed on the given measurements fig. 3.2.3. Since the object is homogeneous, the diffusion occurs at the same speed in all directions. Since the detector distance are the same, we obtain the same measurement for all sources. This figure shows the expected superpositions of all measures. Note that numerically, we do not need to convolve by the Impulse Response to perform this detector comparison since we do not have the noise due to the experimental acquisition system. Remark also this check has been performed for all detectors.
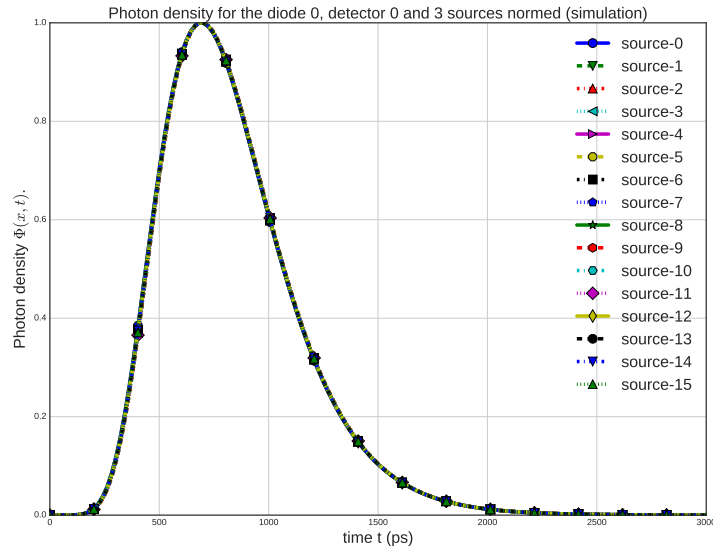
Figure 3.3.2: Comparison of the different detectors for the source 0. We choose a mesh size 2mm, polynomial order 1, the time step 20ps, final time 2000ps, without any inclusion. The object is homogeneous, therefore we can see the expected symmetry of the detectors. Each plot comes by pairs except for the most distant one. Since more photons are diffused and absorbed with long distance, the exact opposite detector has the lowest intensity
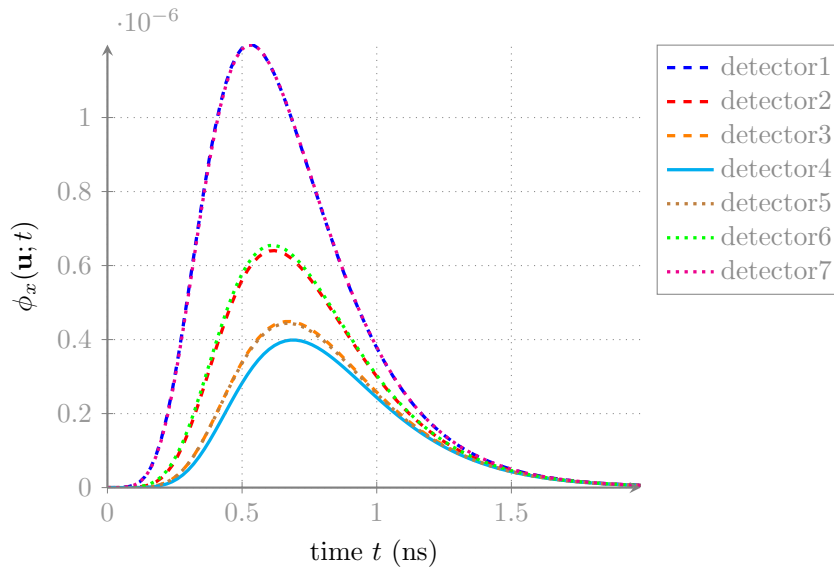
Figure 3.3.3: Comparison between different detectors for the source 0 with 2 inclusions one more diffusive and one more absorbant. In this figure, we see a slighly time shift and a variation in light intensity for several fiber that breaks the symmetry between the detectors. This indicates an inhomogeneity in the diffusive and absorbant domain. We choose a mesh size 4mm, Polynomial order 1, time step 20ps, final time 2000ps.
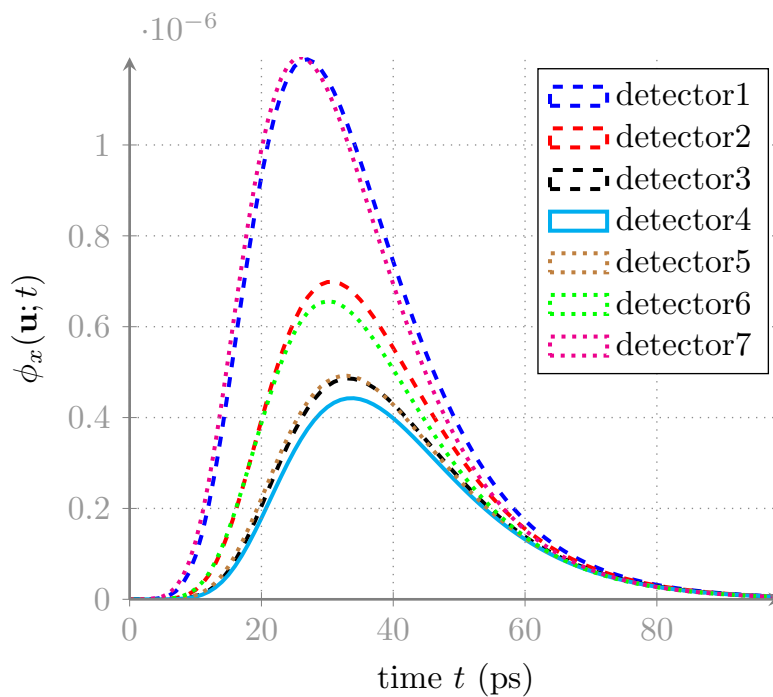
Figure 3.3.4: This figure shows computation results for different time order up to 4 for $\mathbb{P}_2$ solutions on an homogeneous object. The mesh size is 2mm, the time step 20ps and the final time 2000ps. We see that the solution seems to converge from time order 3, but with an acceptable result in time order 2. Note also we have a variation of intensity in that case, we obtain more precise solution at higher order.
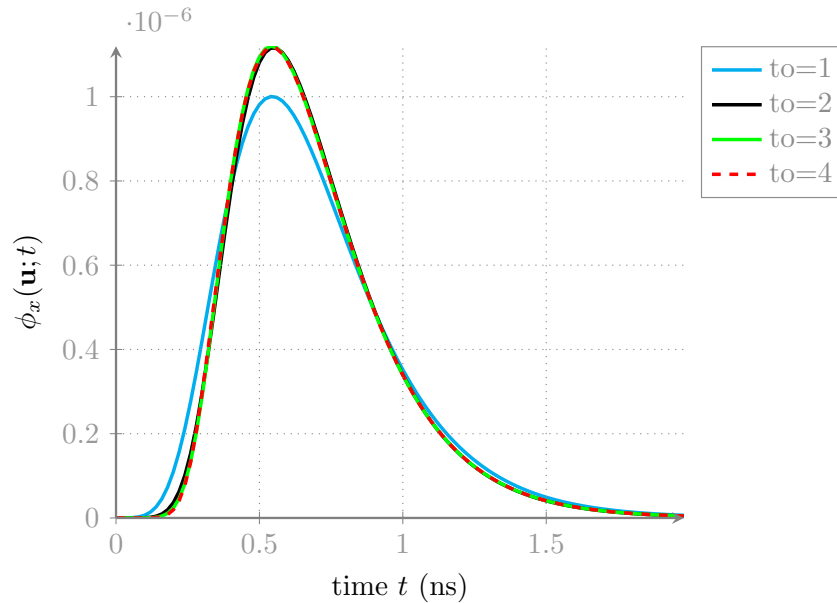
Figure 3.3.5: This figure shows results for different time order up to 4 for $\mathbb{P}_3$ solutions on an homogeneous testcase and using a mesh of size 2mm, time step 20ps, final time 2000ps. The results seem to converge from time order 3, but is acceptable from time order 2 as well as for the $\mathbb{P}_2$ case (fig. 3.3.4).
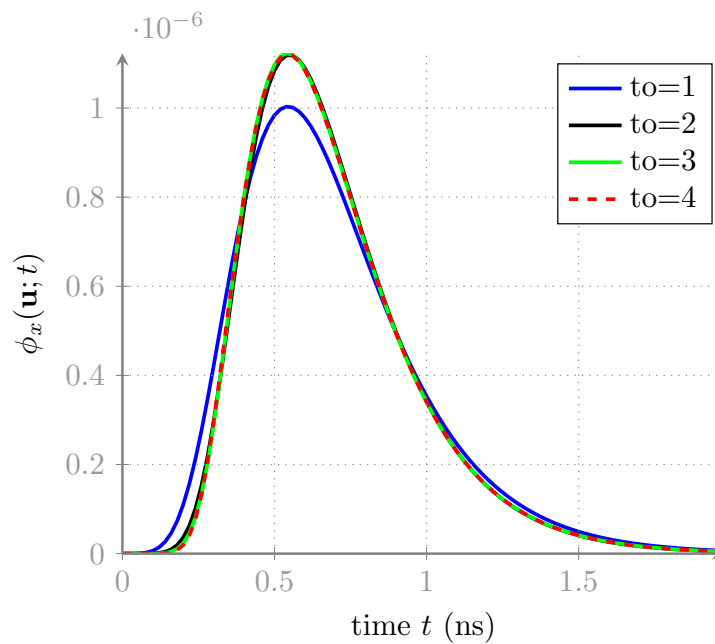
Figure 3.3.6: This figure shows a comparison of $\mathbb{P}_1$ solutions for different time order. The mesh size used is 2mm, the time step 80ps, the final time 2000mm. In this case, we can see the astability of the BDF method at order 4. But results seem to converge to the solution obtained with time order 3.
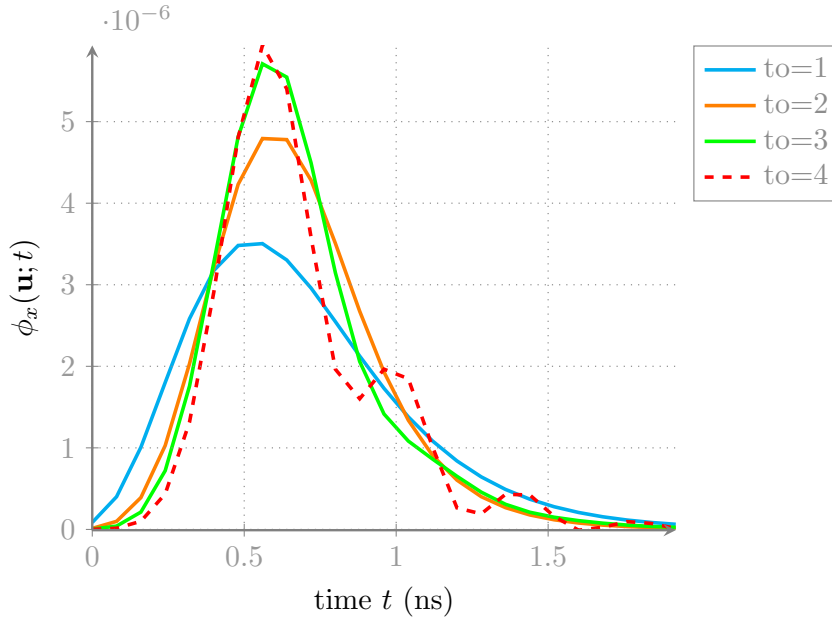
Figure 3.3.7: This figure shows a comparison of $\mathbb{P}_1$ solutions for different time order and smaller time step than fig. 3.3.6. The mesh size used is 2mm, the time step 40ps, the final time 2000ps. In this case, we can slightly see the astability of the BDF method at order 4 on the top of the peak. But results seem to converge to the solution obtained with time order 3. Note also that the peak intensity decreased with the time step for this setting compared to fig. 3.3.6.
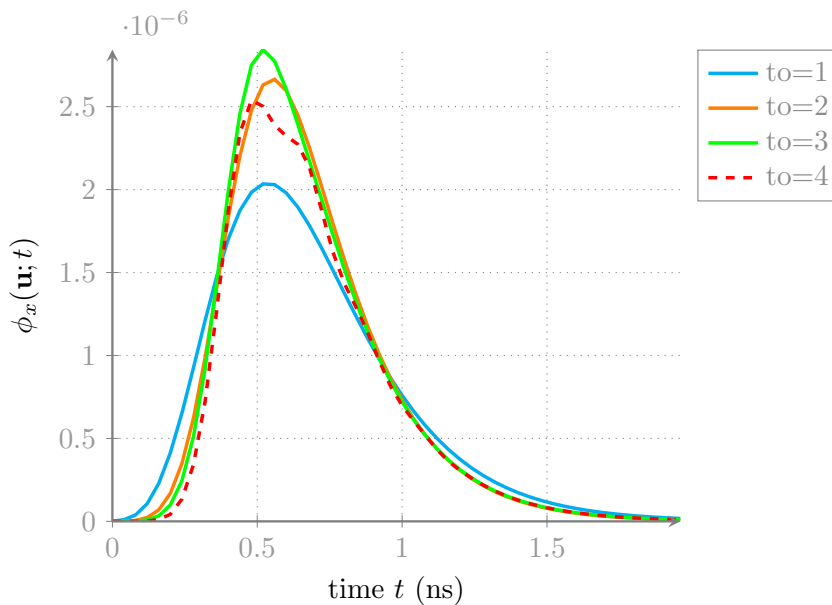
Figure 3.3.8: This figure shows a comparison of $\mathbb{P}_1$ solutions for different time order and smaller time step than fig. 3.3.6 and fig. 3.3.7. The mesh size used is 2mm, the time step 20ps, the final time 2000ps. The results converge to the solution obtained from time order 3. The peak intensity seems to be stable around $1.35e^{-6}$ compared with the previous figures.
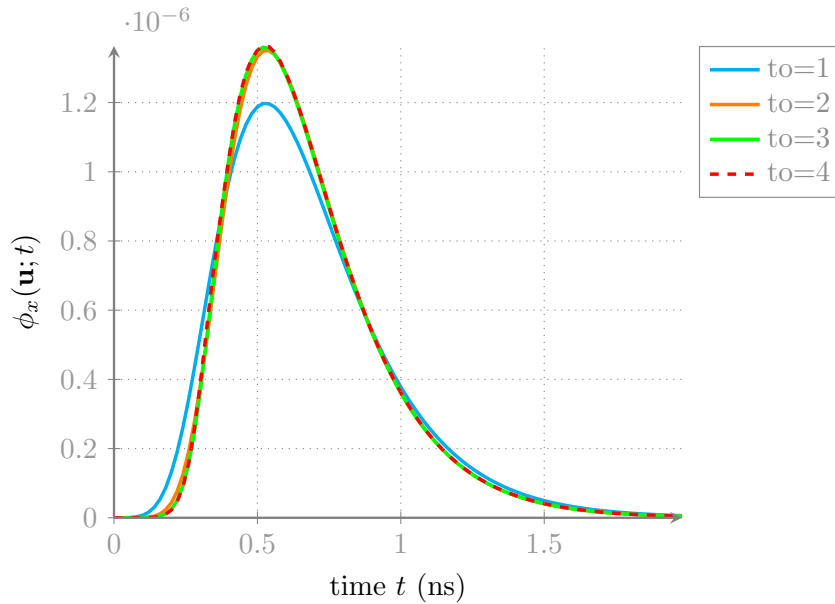
Figure 3.3.9: This figure shows a comparison of different time step for a fixed time order 2 using $\mathbb{P}_1$ solutions. The mesh size is 2mm, the final time 2000ps and a BDF method time order 1 for the finest time step for comparing. The results seem to converge to the solution obtained with a time step of 20ps with time order 2. The peak intensity seems to be stable around $1.3e^{-6}$ compared with the previous figures.
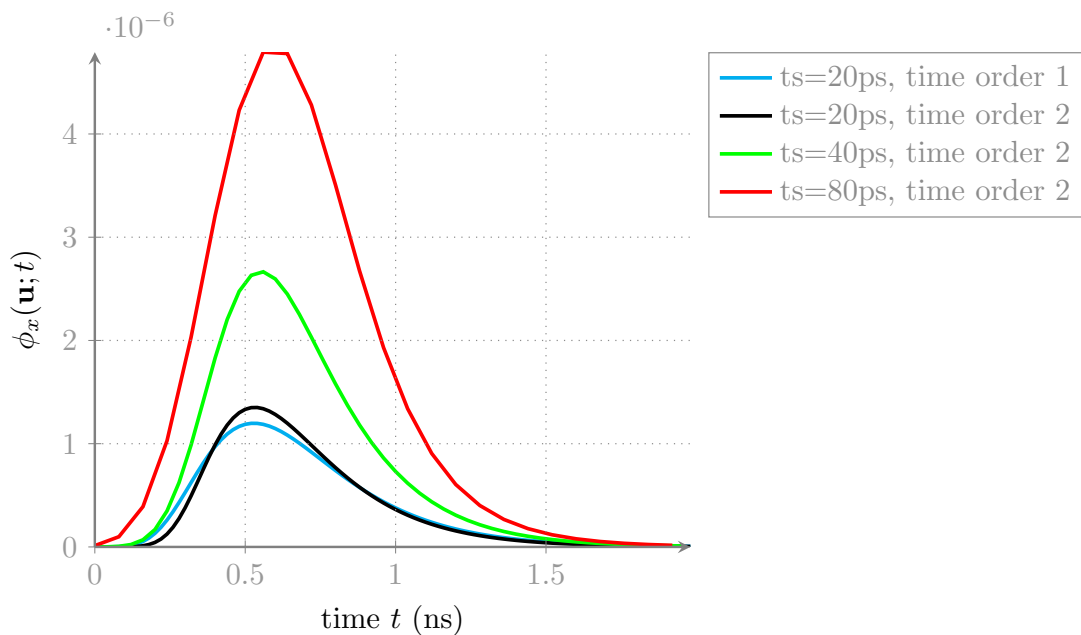
Figure 3.3.10: Comparison of the diffusion solution for several polynomial order from $\mathbb{P}_1$ to $\mathbb{P}_3$ on a homogeneous object. The mesh size chosen is 2mm, the time order 1, the time step 80ps and final time 2000ps. The graphic shows that the solutions match from $P2$ elements. Increasing the polynomial gives a better solution in particular in terms of photons intensity.
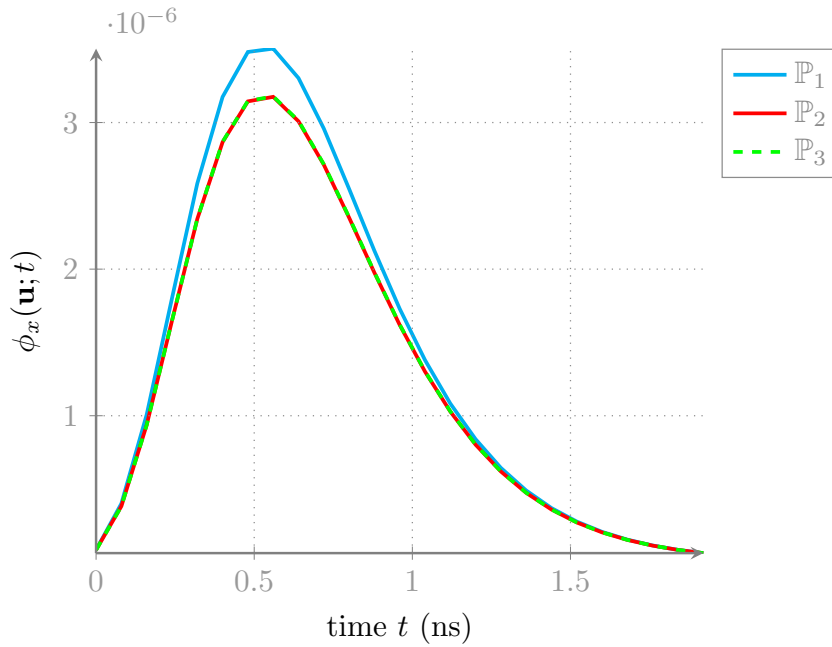
Figure 3.3.11: Comparison of the diffusion solution for several polynomial order from $\mathbb{P}_1$ to $\mathbb{P}_3$ on a homogeneous object. We decrease the time step to 40ps The mesh size chosen is 2mm, the time order 1 and final time 2000ps. As for fig. 3.3.10 the solution seems to converge from the polynomial order 2. Decreasing the time step increases the precision in particular in terms of photons intensity.
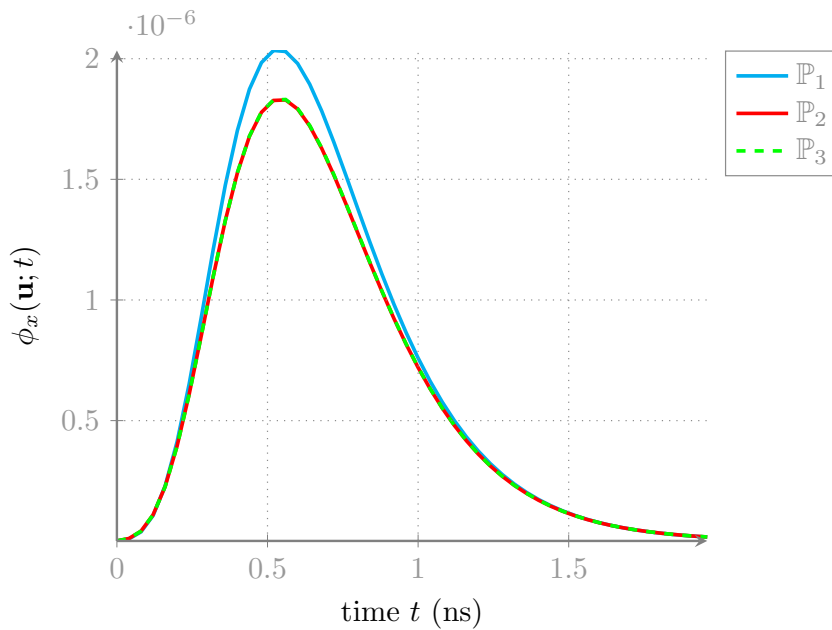
Figure 3.3.12: Comparison of the diffusion solution for several polynomial order from $\mathbb{P}_1$ to $\mathbb{P}_3$ on a homogeneous object. We decrease the time step to 20ps The mesh size chosen is 2, the time order 1 and final time 2000ps. As for fig. 3.3.10 and fig. 3.3.11, the solution seems to converge from the polynomial order 2. Decreasing the time step increases the precision in particular in terms of photons intensity.
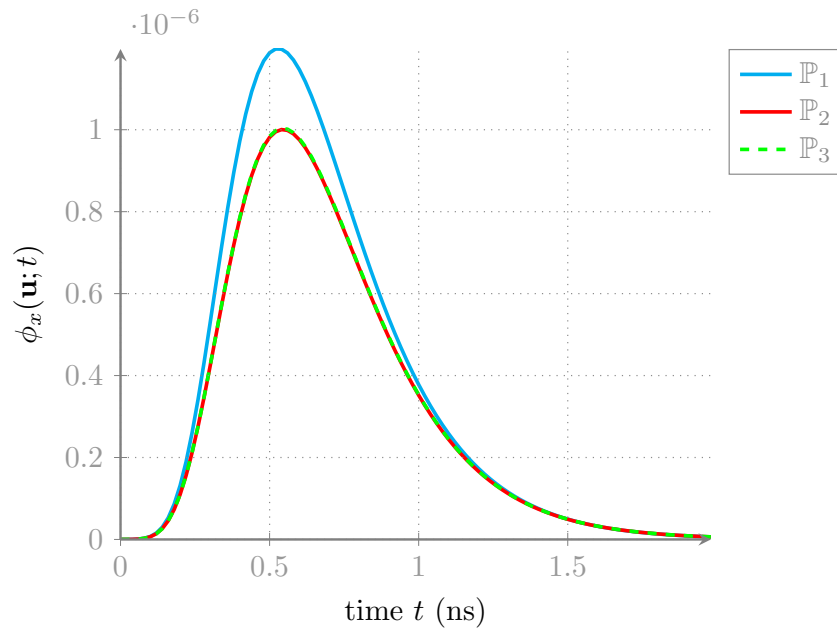
Figure 3.3.13: Comparison of the diffusion solution for several polynomial order from $\mathbb{P}_1$ to $\mathbb{P}_3$ with higher time order 2 on a homogeneous object. The chosen time step is 20ps for a mesh size 2mm, a final time 2000 ps. The solution seems to converge from the polynomial order 2. Compared to fig. 3.3.12, we increase only the BDF time order and we can observe that the intensity seems to be slighly higher. This shows that increasing the time order might be interesting to better catch the heterogeneity when we are limited by the time grid.

65
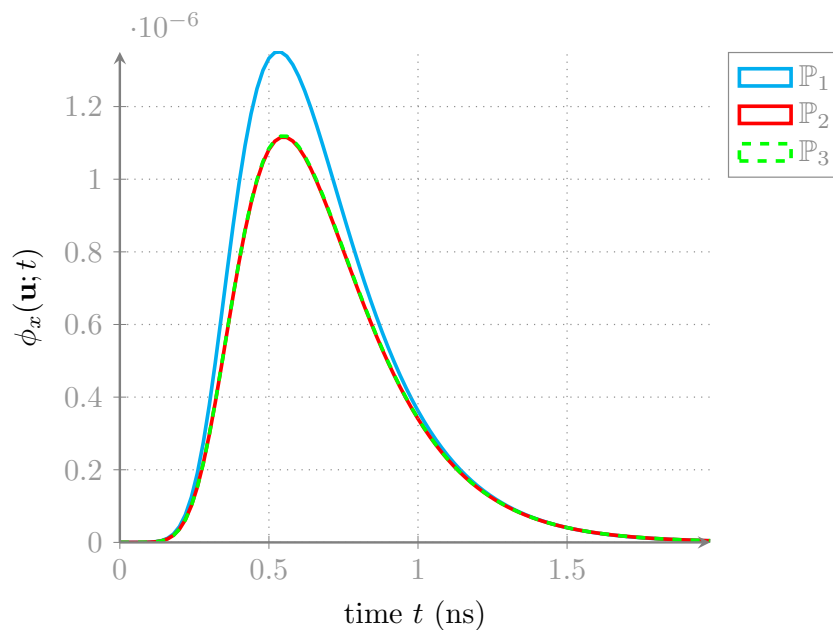
Figure 3.3.14: Comparison of the TPSF solutions between an homogeneous cylindric object, an object with one inclusion and one with 2 inclusions. The graphic shows half of the detectors (=4) from the same side (no symmetry). The chosen time step is 20ps for a mesh size 2mm, a final time 2000ps. The polynomial order of the method is 1 in space and time. The figures show the impact of adding one or two inclusion in the domain depending on the placement of the detector. Since the inclusion are symmetric from the source, we can see that the top right and bottom left images are the detectors that catch the most one of the two inclusions (see also fig. 3.1.1).
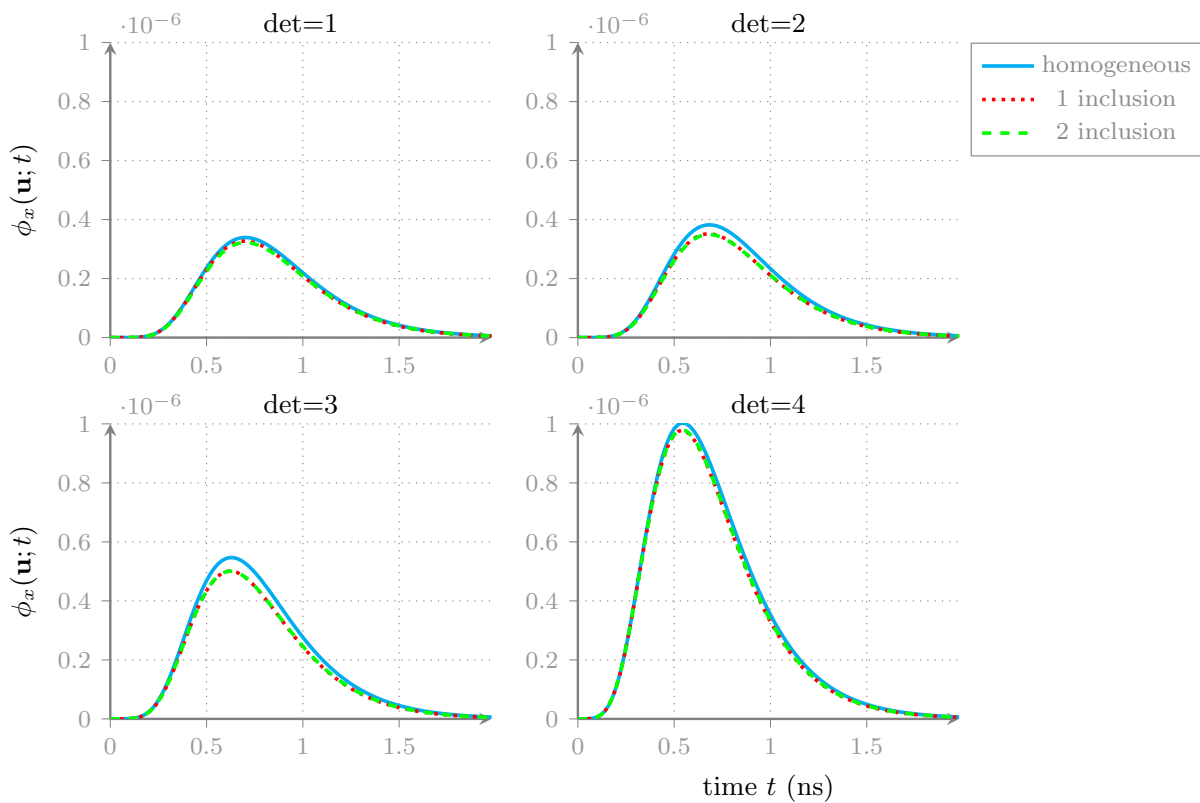
Figure 3.3.15: Cross-verification of the Feel++implementation and the existing Matlab code on the same grid for an absorption parameter $\mu_{a,x} = 0.6$. We see that both codes produces the same TPSF on the opposite detector of the source. Note that this check has been performed for all detectors and for all sources.
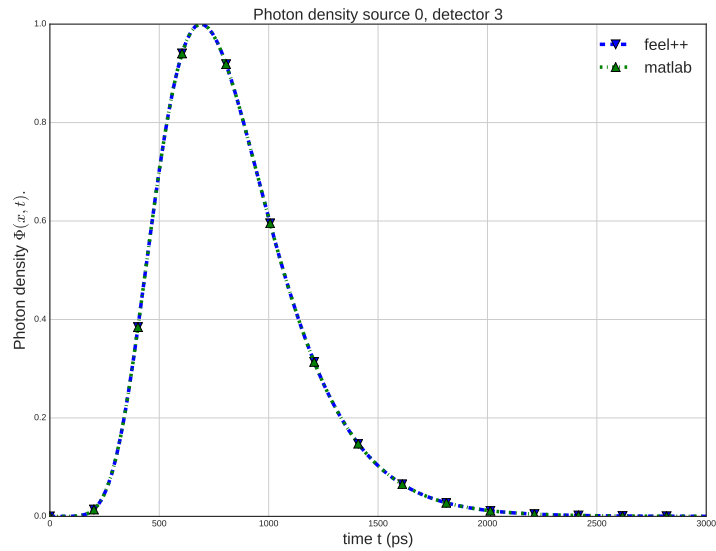
Figure 3.3.16: Cross-verification of the Feel++implementation and the existing Matlab code on the same grid for an absorption parameter $\mu_{a,x} = 0.8$. We see that both codes produces the same TPSF on the opposite detector of the source for a different absorption parameter (see fig. 3.3.15). Note that this check has been performed for all detectors and for all sources.

67
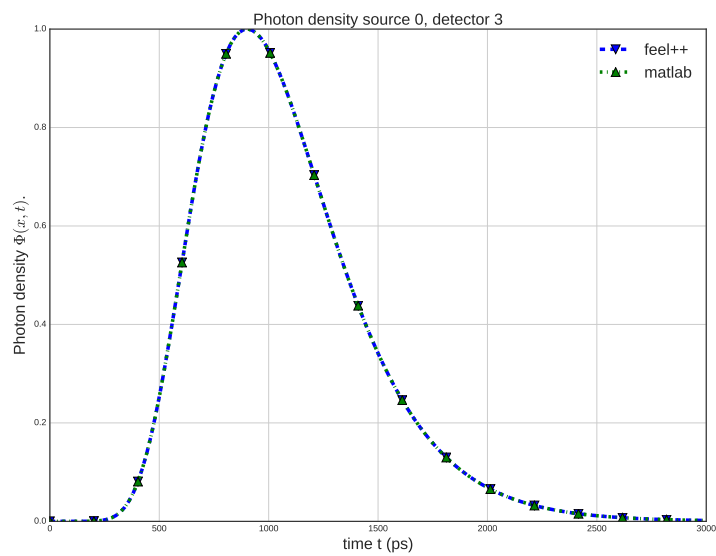
3.4 Model validation

In this section, we present some results regarding the validation of the diffusion model. To validate the model, we used the homogeneous version of phantom object (p0116) of 40mm diameter size which corresponds to the diameter of the fibers ring. We are in contact mode. Some specifications for the object are presented in the table 3.4.1. We validate the forward model comparing for $\mu_a = 0.6$ on the source 0 for the seven detectors (fig. 3.4.1). Note that the current object is an homegeneous object. Theoretically, comparing all detectors for one source is sufficient on an homogeneous object once the verification presented in sections 3.2 and 3.3 to validate the experience in contact mode for all detectors as the light propagates in a same manner in all directions.

Table 3.4.1: Phantom object p0116 parameters. This object does not contain any fluorophore. The table presents some characteristics of the plastic object.

	parameter	description	value
Characteristics		China Ink (%)	0.00065
		Titane Oxyde mg/ml	0.74
		Radius (mm)	20
		Refraction index	1.54
		Material	Roth
Diffusion	$\mu_{a,x}$	absorption	0.005
	$\mu'_{s,x}$	reduced scattering	0.6
	κ_x	diffusion	0.1

Figure 3.4.1: Validation of the model on a phantom (p116). The object diffusion and parameters are estimated ($\mu_a = 0.6$). The figure shows a comparison between the measurements $\Phi^0_{i,obs}(t)$ and the diffusion solutions $\Phi^0_x(x_i, t)$ obtained with FEEL++ and Matlab code for the chosen detectors $i > 0$. These numerical solutions are convolved by the Impulse Response using a same grid, for several detectors of the source 0. These TPSF are readjusted to match the peak maximum. These pictures shows that both codes results match perfectly. For the convoluted solutions, only the rising edge match the measurement data, but slighly differs on the falling edge. This difference can have different explainations. One of the most likely reason is a bad estimation of the phantom optical properties (see fig. 3.4.2). Note that the solution obtained with FEEL++ without convolution is printed to highlight the effect of the Impulse Response on the peak slopes.
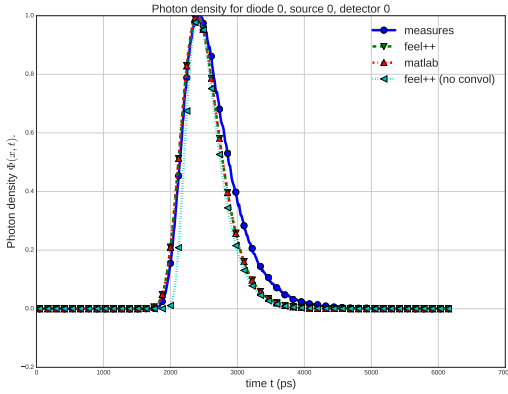
(a): Photon density for the detector 0
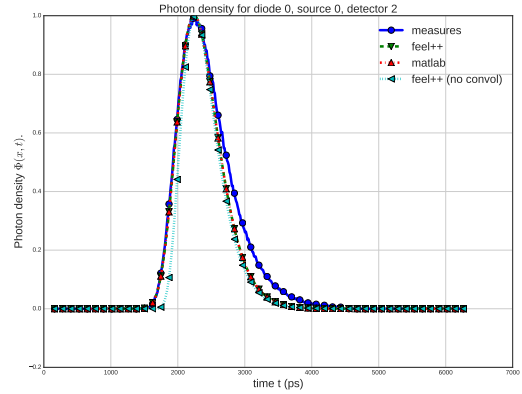
(b): Photon density for the detector 2
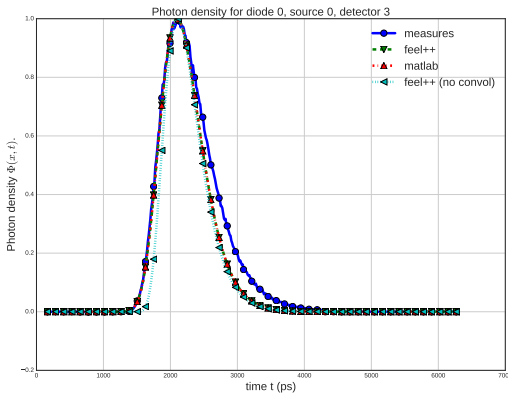
(c): Photon density for the detector 3
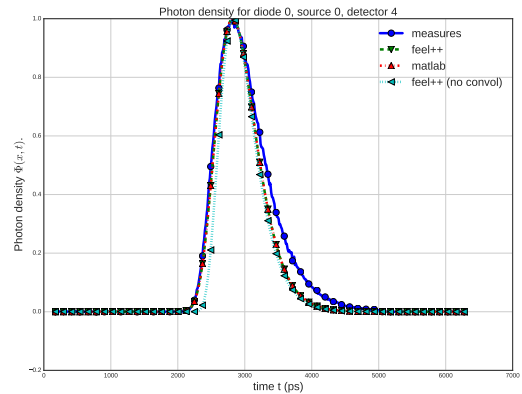
(d): Photon density for the detector 4
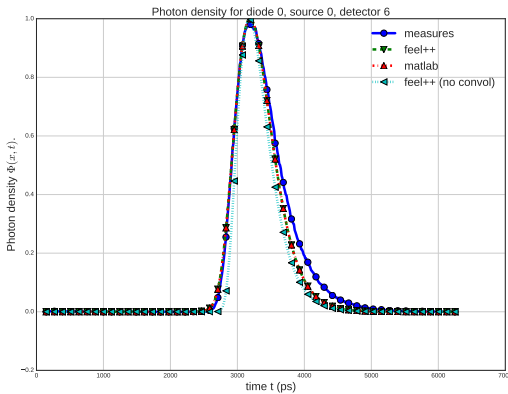
(e): Photon density for the detector 6

Figure 3.4.2: Validation of the model on a phantom (p0116). The object diffusion and parameters are estimated ($\mu_a = 0.6$), but contrary to fig. 3.4.2, we chosed to increase the absorption to $\mu_a = 0.8$. The figure shows a comparison between the measurements $\Phi^0_{i,obs}(t)$ and the diffusion solutions $\Phi^0_x(x_i, t)$ obtained with FEEL++ and Matlab code in contact mode for the chosen $i > 0$ detectors of the source 0. The numerical solutions are convolved by the Impulse Response using a same grid, for several detectors. These TPSF are readjusted to match the peak maximum. These pictures shows that both codes results match perfectly. For the convoluted solutions, only the rising edge match the measurement data, but slighly differs on the falling edge. By increasing the absorption, we can see that the curves match less at the beginning of the rising edge, but more on the falling one. This shows that our model is probably well suited to represent the physical phenomenon. We should now turn on an optimization process to find the best suited input parameters. Note that the raw FEEL++ solution (without convolution) is printed to show the impact the Impulse Response.

(a): Photon density for the detector 0

(b): Photon density for the detector 2

(c): Photon density for the detector 3

(d): Photon density for the detector 4

70
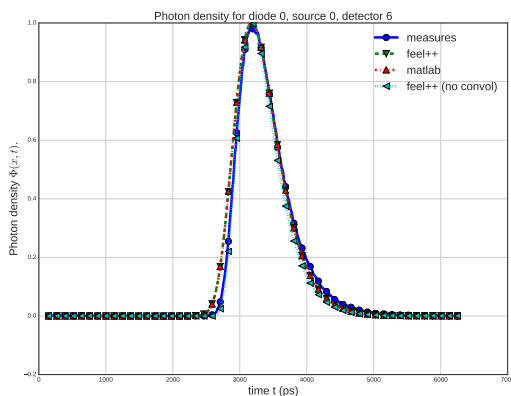
(e): Photon density for the detector 6

3.5   Conclusion

In the chapter 3, we presented several results for the forward problem in order to verify the model then validate the implementation on real measurements. The first section gives an example of solution obtained, with our implementation of the coupled system of equations described in (2.1.1), for an object with two inclusions. Then the process from verification to validation is detailed. First, several verifications are performed with the measurements. These verification are performed to ensure that the data are not erroneous and can be compared. Different numerical verifications have been proposed to check the numerical implementation of the problem (2.1.1). Then several convergence graphics on observations are presented for different mesh and time steps and using high order methods in space and time. From the results, it seems interesting to consider high order from order 2 in space and time since we have a gain in terms of precision. Our numerical implementation has been compared with an existing code developed by the IMIS team. This step let us confirm that both codes provide the same results thanks to cross-verifications. Finally, the model is validated on an homogeneous object. The simulation are compared to the measurements. As a perspective, the same process from verification to validation should be performed in the future for the non-contact mode and then with the fluorescence. Moreover, we highlighted convergence results in chapter 2 we would like to verify in the future.

References

[2]   S.R Arridge. "Optical tomography in medical imaging". In: *IOPScience Inverse problem* 15.2 (1999).

[9]   Farouk Nouizi. "Tomographie optique diffuse et de fluorescence préclinique : instrumentation sans contact, modélisation et reconstruction 3D résolue en temps". PhD thesis. Université de Strasbourg, 2011.

[18] Murielle Torregrossa. "Reconstruction d'images obtenues par tomographie optique dans le proche infrarouge". PhD thesis. Université de Strasbourg, 2003.

[19] Guillaume Dollé, Zakaria Belhachmi, Christophe Prud'homme, and Murielle Torregrossa. *Diffuse Optical Tomography and Fluorescence Simulation*. See also on youtube. June 2014. DOI: 10.5281/zenodo.11830. URL: https://doi.org/10.5281/zenodo.11830.

Chapter 4 - Inverse problem

In chapter 2, we were interested in solving the forward problem (2.1.1) which is: Find a couple of solution ϕ_x, ϕ_m for given input parameters for the diffusion and the fluorescence $\kappa_l, \mu_\ell, \gamma, \tau$, for $\ell \in \{x, m\}$. This chapter 4 studies the inverse problem related to the initial problem (2.1.1). The inverse problem reads as follows. Given ϕ_x, ϕ_m find new parameters $\kappa_l, \mu_\ell, \gamma, \tau$ that minimize the error on the observation.

The first section 4.1 of this chapter details the state of the art for the inverse problem. In particular, we present an argument that proves that we cannot reconstruct more that two parameters simultaneously. In our case, we have six parameters to reconstruct four of which only for the fluorescence problem. One of the Graal in inverse problem is to be able to minimize the detector sampling to lower the cost of building new instruments. Considering the tomograph setup detailed in section 4.1, the current experimental detector sampling can be seen, from a mathematical point of view, as a reconstruction problem with partial data measures on the domain boundary. The difficulty is to guarantee the existence and uniqueness of solutions in that case. To find the set of parameters, we handle the inverse problem as an optimization problem treated by a adjoint method. To handle this type of inverse problem, we details in section 4.2 different objective functions to minimize which depends on the data sampling.

To ensure the well-posedness of the optimization problem, we have to add a regularization term. The section 4.2.2 details the classical approach used based on a Tikhonov regularisation and we give as a perspective an overview of better regularization techniques. The section 4.3 details the adjoint problem for the diffusion and for the fluorescence for the initial problem (2.1.1), but also when we rewrite the problem by introducing the ODE (2.1.1) detailed in chapter 2. Finally, we present some preliminary results for the inverse problem with some test cases.

4.1   State of art

The DOT inverse problem has been largely studied [2, 3] and remains theoretically a challenge for the scientific community. In particular the identifiability of the different coefficients to reconstruct depending on the measure data is a challenging question.

In the DOT problem (2.1.1), six parameters need to be reconstructed. Two parameters for the diffusion problem $\kappa_x, \mu_{a,x}$ and four parameters for the fluorescence $\kappa_m, \mu_{a,m}, \tau, \gamma$.

S.R. Arridge hightlights in the overview [2] the difficulty to prove the uniqueness of the inverse problem and in particular when we set an interior source and the fact that the diffusion approximation is not true close to the source. A counter-example can be constructed to show the non-uniqueness for different measurement types [2].

The main result of [20] prove that it is possible to recover up to two parameters simultaneously from partial boundary measurements. We recall the result. We consider the fiber settings described in chapter 1 with partial measurements at the detector locations the associated modeling is represented by (2.1.1). We consider the following problem

$$\begin{cases} \rho\frac{\partial u}{\partial t} - \nabla \cdot (\kappa \nabla u) + \mu u & = & 0 & \text{in } \Omega \times (0,T), \\ u(\boldsymbol{x},0) & = & u_0 & \text{in } \Omega, \\ u(\boldsymbol{x},t) & = & f(\boldsymbol{x},t) & \text{in } \partial\Omega. \end{cases} \tag{4.1.1}$$

for $\alpha, \beta > 0$, f assigned and under the regularity hypothesis (2.2.1) detailed in section 2.2. We keep the same notations, let $Q = \Omega \times (0,T)$ be the space-time domain and $\partial Q = \partial\Omega \times (0,T)$ the respective space-time boundary domain. Let f be the source for the diffusion either in contact or non contact mode. Let Γ_d be a measurement boundary area for detectors and Σ_0 the source. In contact, it would be reduce to a pointwise area. We fix a time $T_0 \in (0,T]$ for the measure. Let $\kappa(\boldsymbol{x})$ be the diffusion coefficient, $\mu(\boldsymbol{x})$ the absorption coefficient, $\boldsymbol{n}$ the output normal unit vector and u the solution of the forward problem (2.2.2). We introduce the input-output map Λ defined as follows

$$\Lambda : f \to \kappa.\nabla u(T_0) \cdot \boldsymbol{n}_{|\Gamma_d} \tag{4.1.2}$$

and we denote the nonlinear operator

$$\Phi : (\kappa, \mu) \to \Lambda. \tag{4.1.3}$$

If Φ is injective, then we have the uniqueness of the couple of input parameters κ, μ for all pairs $(f, \kappa\nabla u(T_0) \cdot \boldsymbol{n}_{|\Gamma_d})$. Canuto and Kavian showed in [20] that the injectivity of Φ can be proved for the following three cases

(i) given $\mu(\boldsymbol{x})$ and $\kappa(\boldsymbol{x})$ of the form $\kappa(\boldsymbol{x}) = a(\boldsymbol{x})I_N$ where $\kappa(x)$ is a scalar-valued function and I_N is the identity matrix, $a(\boldsymbol{x})$ is identified by supposing that $\Sigma_0 = \Gamma_d = \partial\Omega$

(ii) given $\kappa(\boldsymbol{x}) = a(\boldsymbol{x})I_N$, $\rho(\boldsymbol{x})$, $\mu(\boldsymbol{x})$ is identified by supposing that $\Sigma_0 = \Gamma_d = \partial\Omega$

(iii) given $\rho(\boldsymbol{x})$ and $\kappa(\boldsymbol{x}) = a(\boldsymbol{x})I_N$, we identify $\mu(x)$ is identified by supposing that $\Sigma_0 \cup \Gamma_d = \partial\Omega$

The inverse problem we are dealing with is more complicated in the following sense,

1. for the determination of the parameters $\kappa_x, \mu_{a,x}$, the data are the sources and the boundary measurement. However it may be reformulated in a similar form of (4.1.1). Thus the result of [20] hold.

2. The problem of determining the fluorescence parameters $\kappa_m, \mu_{a,m}, \eta, \tau$ is a "mixed" inverse problem, where the unknown are a source term η, the conductivity κ_m, the absorption $\mu_{a,m}$ and the life time τ. Thus, we may only apply known results for

    (a) the parameters κ_m and $\mu_{a,m}$, or
    (b) the source parameters η and τ.

Hence, we have to make a compromise for the fluorescence problem by selecting the parameters we desire to reconstruct. In the following section; we will focus on the determination of both conductivities and absorption. In a forthcoming work, since our approach is based on optimization methods, we will determine numerically all the parameters using alternate direction algorithms.

4.2 Optimization problem

We presented in chapter 3 several validation results concerning the forward formulation of the TR-DOT problem. In this section we present the TR-DOT optimization formulation for the inverse problem. In order to study this problem, we first have to define the cost function which describes how to evaluate the error on the observation. This functional depends on the type of datasets that are provided (e.g partial or full measurements). The first section details the different cost functions we are interested in, regarding the sampling. For simplicity, we consider the diffusion problem only, we drop the subscripts $\{x, m\}$ and we denote $\phi^k(\boldsymbol{x},t)$ the solution for the kth fiber. For conciseness, we might write ϕ^k or ϕ for k fixed. In the same way, the observations are denoted $\phi_{obs}^k(\boldsymbol{x},t)$ for a measurements when the kth fiber is the source. We write sometimes ϕ_{obs} to ease the notations.

Remark 15. *The optimization problem for the diffusion and the fluorescence are treated separately since we desire to reconstruct 2 parameters simultaneously (See section 4.1).*

In a second part, we introduce the regularization used in the TR-DOT context to guarantee the well-posedness of the optimization problem. Different possible regularization are exposed in a second part which we expect to provide better reconstruction results.

4.2.1 Cost functions

We denote N_f the number of fibers, N_s the number of source and N_d the number of detectors for one source. In practice, we take successive measurements by rotations of the source $N_s = N_d$ and we do not detect on the fiber which act as a source $N_d < N_f$. Let us consider a domain Ω in $\mathbb{R}^d$, $d = 2, 3$, the boundary $\partial\Omega$ and a set of points as a non-connex subset of the boundary domain $\Gamma_{d,\varepsilon}^k \subset \partial\Omega$ for $k \in [1, N_f]$ for measurement locations and Γ_d for k fixed. In practice, the domains $\Gamma_{d,\varepsilon}^k$ with $\varepsilon \geq 0$ are dispatched regularly on the domain boundary. In contact mode $\Gamma_{d,\epsilon}^k$ is reduced to one point. The experiments proved that using regular placement of the detectors, we can obtain good reconstructions [9, 18], but a proper study would be interesting in the future. One of the possible perspective might be to determine the optimal detector placement by solving an inverse problem on the detector location to discover new placement pattern. Or again solve a minimisation problem on the number of detector which interest most physicists in order to reduce the global cost of the machine by reducing the number of instruments. We recall the notations of section 2.1. We denote by $Q = \Omega \times [0, T]$, the space-time domain $T > 0$ the final time, $\partial Q = \partial\Omega \times [0, T]$ the space-time closure. Finally, we will denote $P_{d,\varepsilon}^k = \Gamma_{d,\varepsilon}^k \times [0, T]$ the partial space-time domain and $P_{d,\varepsilon}$ for k fixed. We are interested in several functionals, first for verification purposes and to represent the experimental tomograph which works with partial boundary measurements. We distinguish two types of reconstructions: the one source reconstruction and the multiple sources reconstruction. We introduce the two subscripts s, d for the source and for the detectors. We denote $\Sigma_0^k \subset \Omega$ the source domains not part of the boundary $\partial\Omega$. For a fixed source k, then the detector domains for the source are the $\Gamma_{d,\varepsilon}^j$ domains with $j \in [1, N_d]$ and $j \neq k$ that are either pointwise or surfacic depending on measurement's type: contact or non-contact. The Figure 4.2.1 summarizes the kind of observations in which we are interested. We recall that the source is located inside Ω to a distance corresponding the the mean free path $d = \frac{1}{\mu_s'}$ with μ_s' the reduced scattering coefficient assumed to be known in an area close to the boundary $\partial\Omega$ and not displayed on Figure 4.2.1.

4.2.1.1 Single source reconstruction

In this section, different cost functions are defined. We consider only one source, k in (2.1.1) is fixed. Let N_d be the number of detectors which may vary depending on the sampling type we are considering. These cost functions take into account the sampling viewed in the schematic draw fig. 4.2.1. For conciseness purpose, we denote $\phi = \phi(\boldsymbol{x}, t; \kappa(\boldsymbol{x}), \mu(\boldsymbol{x}))$ the solution of (2.1.1) for a given couple of parameters $\kappa = \kappa(\boldsymbol{x})$ and $\mu = \mu(\boldsymbol{x})$. In addition, we denote $J_i(\phi) = J_i(\phi(\boldsymbol{x}, t; \kappa, \mu))$ the ith cost function ($i > 0$) detailed hereafter.

Domain For the first cost function, we introduce an energy which depends on the residual between the solution of our partial differential equation with the observed data on the whole space-time domain Q and normalized (fig. 4.2.1a)

$$J_0(\phi) = \frac{1}{2} \int_Q |\phi - \phi_{obs}|^2 dQ \tag{4.2.1}$$

This configuration is the ideal case in the sense we own an infinite number of detectors that can give measurements everywhere in the domain Ω. This is never the case in practice.

Remark 16. *A regularization term $\mathfrak{r}(\kappa, \mu)$ should be added to preserve the ellipticity of the minimization problem for the cost function J_0 and ensure the well-posedness of the optimization problem.*

Boundary domain The second energy proposed is an energy which considers the residual but on the whole boundary (fig. 4.2.1b)

$$J_1(\phi) = \frac{1}{2} \int_{\partial Q} |\phi - \phi_{obs}|^2 d\partial Q. \tag{4.2.2}$$

As before, this cost function represents the case of an infinite number of detectors placed on the boundary only. In that case, the problem can be reformulate as a boundary value problem and measurement as boundary condition.

Figure 4.2.1: Different type of measures for a domain Ω. The red colored areas represent the observed data. The figs. 4.2.1a and 4.2.1b are usually not available since from an experimental point of view, we do not dispose of a infinite number of detectors. Thus, these sampling are considered with numerically observation and for testing purpose only. In practice, the TR-DOT measurements are partial on the boundary as showed in figs. 4.2.1c and 4.2.1d. The different related cost functions for these type of measurements are described in section 4.2.1.

(a): Data available on the whole domain Ω.

(b): Partial data available on the whole boundary $\partial\Omega$ only

(c): Partial data available on non-connex parts of the boundary $\Gamma_{d,\varepsilon}^k$ only for $k \in [1, N_f]$.

(d): Partial data available on non-connex pointwise areas of the boundary $\Gamma_{d,0}^k$ only for $k \in [1, N_f]$.
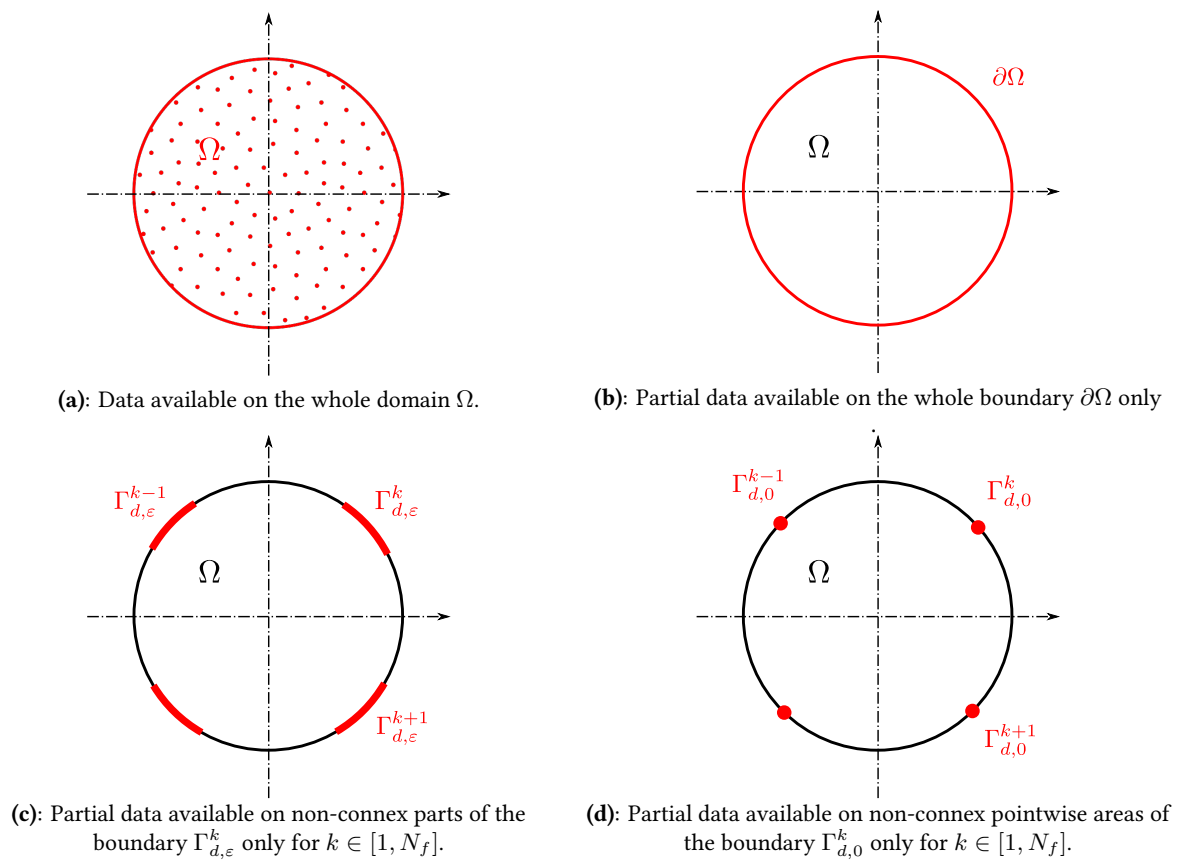
Partial boundary domain Let consider an element $x_i \in \partial\Omega$ for $i \in [1, N_d]$ as the contact point on the boundary for contact measurements or the cross point between the boundary and the axis of the fiber cone of view. We define the partial boundary domains $\Gamma^i_{d,\varepsilon} = \{x \in \partial\Omega \mid \|x - x_i\| < \varepsilon\}$ which is the ball of center x_i with radius $\varepsilon > 0$ for the ith detector fiber on the boundary of the domain. Remark that ε depends on the fiber Numerical Aperture and the partial domains $\Gamma^i_{d,\varepsilon}$ are non connex. ($\Gamma^i_{d,\varepsilon} \cap \Gamma^j_{d,\varepsilon} = \varnothing$ for $i \neq j$). When $\varepsilon > 0$, the setting is in non-contact measurements mode, then the cost function considered takes into account the residual of boundary areas (fig. 4.2.1c)

$$J_2(\phi) = \frac{1}{N_d} \sum_{i=0}^{N_d} \left(\frac{1}{2} \int_{P^i_{d,\epsilon}} |\phi - \phi_{obs}|^2 dP^i_{d,\epsilon} \right). \tag{4.2.3}$$

When $\varepsilon \to 0$, then the $\Gamma^k_{d,\varepsilon}$ are pointwise (fig. 4.2.1d), the previous cost function can be rewritten as follows

$$J_3(\phi) = \frac{1}{N_d} \sum_{i=0}^{N_d} \left(\frac{1}{2} \int_0^T |\phi(x_i, t) - \phi_{obs}(x_i, t)|^2 dt \right). \tag{4.2.4}$$

Tomograph For the real tomograph, we have to introduce another cost function for the non-contact measure mode defined as an hybrid version of both objective functions (4.2.3) and (4.2.4). In that case, the observation for the kth source and the ith detector is a time measurement denoted $\mathcal{M}^k_i(t)$ The measurement corresponds to the number of photons that crossed the domain and "seen" by the cone field of view of the detector i. For the measurement on the boundary domains $\Gamma^k_{d,\varepsilon}$ where ε indicates the measurement area which depends on the Numerical Aperture of the kth fiber. Note that all fibers are of the same type, therefore they own the same Numerical Aperture. With the current fiber settings, remark that when the fiber k acts as a source of light, we do not detect on this fiber (see remark 17).

Remark 17. *Considering the tomograph setup detailed in section 1.1 with the ring of fibers, we introduce a numerotation for the detector different from the fiber indices. For $k \in [1, N_f]$ fibers, if we denote i the index of the ith detector of a given fiber acting as the source, then the fiber index for the ith detector is given by the following relation*

$$f_k(i) = \left(k + \left\lfloor \frac{N_s}{2} \right\rfloor \right) - \left(\left\lfloor \frac{N_d}{2} \right\rfloor + i \right). \tag{4.2.5}$$

Note that for a symmetric configuration, the number of fiber should be an even $N_f = 2k$ whereas the number of detectors should be an odd number $N_d = 2k + 1$ for $k \geq 0$.

From the remark 17, we denote f the mapping f_k and $\mathcal{M}_i$ for a source k fixed. Then the cost function reads

$$J_4(\phi) = \frac{1}{N_d} \sum_{i=0}^{N_d} \left(\frac{1}{2} \int_0^T \left| M_{f(i)}(t) - \mathcal{M}_i(t) \right|^2 dt \right) \tag{4.2.6}$$

where $M_k(t)$ is a measure function for non contact measurements describing the number of photons viewed by a fiber k. This measure is defined such that for $\varepsilon > 0$,

$$M_k(t) = \int_{\Gamma^k_{d,\varepsilon}} \phi(\boldsymbol{x}, t) w(\boldsymbol{x}) d\boldsymbol{x} \tag{4.2.7}$$

where $w : \mathbf{x} \to w(\mathbf{x})$ a weight function which depends on a vision angle of the kth fiber (See section 2.1) [9].

4.2.1.2 Multiple source reconstruction

We keep the notations introduced in section 4.2.1.2. We consider each fiber $k \in [1, N_s]$ acting as sources iteratively and dispatched regularly on the boundary domain and close to the boundary $\partial\Omega$. Then the previous cost functions $J_i, i \geq 0$ can be expressed as the mean of function costs for each source.

Domain We consider the mean of rediduals over the whole domain for each source. Note that the regularization term is independent of the number of sources.

$$J_0(\phi) = \frac{1}{N_s} \sum_{k=1}^{N_s} \left[\frac{1}{2} \int_Q |\phi^k - \phi^k_{obs}|^2 dQ \right] \tag{4.2.8}$$

Boundary domain   The second functional is similar but the residual is taken only on the whole boundary domain.

$$J_1(\phi) = \frac{1}{N_s} \sum_{k=1}^{N_s} \left[\frac{1}{2} \int_{\partial Q} |\phi^k - \phi_{obs}^k|^2 d\partial Q \right] \tag{4.2.9}$$

Partial boundary domain   Similarly to the one source case, we denote k the fibers indices and i the detector indices (see remark 17). we consider the partial boundary measurements. J_2 denotes a surfacic measure in the time-space domain.

$$J_2(\phi) = \frac{1}{N_s} \sum_{k=1}^{N_s} \left[\frac{1}{N_d} \sum_{i=0}^{N_d} \left(\frac{1}{2} \int_{P_{d,\varepsilon}^i} |\phi^k - \phi_{obs}^k|^2 dP_{d,\varepsilon}^i \right) \right] \tag{4.2.10}$$

The J_3 functional takes into account pointwise measures. We consider $x_i \in \Omega$ the observation points on the boundary for $i \in [1, N_d]$

$$J_3(\phi) = \frac{1}{N_s} \sum_{k=1}^{N_s} \left[\frac{1}{N_d} \sum_{i=0}^{N_d} \left(\frac{1}{2} \int_0^T |\phi^k(x_i,t) - \phi_{obs}^k(x_i,t)|^2 dt \right) \right] \tag{4.2.11}$$

And finally for the tomograph in non contact mode, the J_4 (see (4.2.6) and remark 17)

$$J_4(\phi) = \frac{1}{N_s} \sum_{k=1}^{N_s} \left[\frac{1}{N_d} \sum_{i=0}^{N_d} \left(\frac{1}{2} \int_0^T |M_{f_k(i)}(t) - \mathcal{M}_i^k(t)\}|^2 dt \right) \right] \tag{4.2.12}$$

Finally we sum here all cost function for one source and multiple source cases in the table 4.2.1.

Table 4.2.1: This table summarizes the different cost functions depending on the different data sampling for the observations. These sampling are represented in fig. 4.2.1. We distinguish the single and multiple source cases. The notations are detailed in section 4.2.1. We denote $\phi = \phi(\boldsymbol{x}, t; \kappa(\boldsymbol{x}), \mu(\boldsymbol{x}))$ the solution of the diffusion problem (2.1.1).

	Space sampling	Objective	Cost definition
Single source	Domain Ω	$J_0(\phi)$	$\frac{1}{2} \int_Q |\phi - \phi_{obs}|^2 dQ$
	Boundary $\partial\Omega$	$J_1(\phi)$	$\frac{1}{2} \int_{\partial\Omega} |\phi - \phi_{obs}|^2 d\partial Q$
	Partial boundary $\Gamma_{d,\varepsilon}^k$	$J_2(\phi)$	$\frac{1}{N_d} \sum_{i=0}^{N_d} \left(\frac{1}{2} \int_{P_{d,\varepsilon}^i} |\phi - \phi_{obs}|^2 dP_{d,\epsilon}^i \right)$
	Partial boundary $\Gamma_{d,0}^k$	$J_3(\phi)$	$\frac{1}{N_d} \sum_{i=0}^{N_d} \left(\frac{1}{2} \int_0^T |\phi(x_i,t) - \phi_{obs}(x_i,t)|^2 dt \right)$
	Partial boundary (Tomograph)	$J_4(\phi)$	$\frac{1}{N_d} \sum_{i=0}^{N_d} \left(\frac{1}{2} \int_0^T \left| M_{f(i)}(t) - \mathcal{M}_i(t) \right|^2 dt \right)$
Multiple sources	Domain Ω	$J_0(\phi)$	$\frac{1}{N_s} \sum_{k=1}^{N_s} \left[\frac{1}{2} \int_Q |\phi^k - \phi_{obs}^k|^2 dQ \right]$
	Boundary $\partial\Omega$	$J_1(\phi)$	$\frac{1}{N_s} \sum_{k=1}^{N_s} \left[\frac{1}{2} \int_{\partial Q} |\phi^k - \phi_{obs}^k|^2 d\partial Q \right]$
	Partial boundary $\Gamma_{d,\varepsilon}^k$	$J_2(\phi)$	$\frac{1}{N_s} \sum_{k=1}^{N_s} \left[\frac{1}{N_d} \sum_{i=0}^{N_d} \left(\frac{1}{2} \int_{P_{d,\varepsilon}^i} |\phi^k - \phi_{obs}^k|^2 dP_{d,\varepsilon}^i \right) \right]$
	Pointwise partial boundary $\Gamma_{d,0}^k$	$J_3(\phi)$	$\frac{1}{N_s} \sum_{k=1}^{N_s} \left[\frac{1}{N_d} \sum_{i=0}^{N_d} \left(\frac{1}{2} \int_0^T |\phi^k(x_i,t) - \phi_{obs}^k(x_i,t)|^2 dt \right) \right]$
	Partial boundary (Tomograph)	$J_4(\phi)$	$\frac{1}{N_s} \sum_{k=1}^{N_s} \left[\frac{1}{N_d} \sum_{i=0}^{N_d} \left(\frac{1}{2} \int_0^T |M_{f_k(i)}(t) - \mathcal{M}_i^k(t)\}|^2 dt \right) \right]$

4.2.2 Regularization

In the previous section, we detailed different cost functions for different data sampling. As we mentionned in remark 16, the minimization problem is naturally ill-posed. To ensure the well-posedness for the functionals introduced in the table 4.2.1, we have to add a regularization terms on the parameters in order to preserve the ellipticity of the global problem. We sum up different possible regularizations hereafter.

4.2.2.1 Tikhonov

Certainly the most common regularization known in image reconstruction is the Tikhonov regularization. The principle consists of a penalization term on the input parameters. In our case, we have to add a perturbation on the diffusion κ and the absorption μ. For the second order derivative coefficient, we have to apply a penalization of gradient type. Let consider U an open bounded domain of Ω. Then the standard Tikhonov regularization term in our case gives

$$\mathfrak{r}(\kappa, \mu) = \frac{\alpha_\kappa}{2} \int_U |\nabla \kappa|^2 dU + \frac{\alpha_\mu}{2} \int_U |\mu|^2 dU \tag{4.2.13}$$

where α_κ denotes the regularization coefficient for the diffusion and α_μ the regularization coefficient for the absorption. We recall we drop diffusion and fluorescence subscript to keep notation simple. Note that the absorption term is in the term of order 0, no gradient information on it, is required.

4.2.2.2 Other regularizations

The drawback of the classical Tikhonov regularization is to add a diffusion effect on the reconstructed parameters. Therefore, it is difficult to obtain good contouring of inclusions with this type of regularization. It might be interesting to consider other types of regularization for the TR-DOT problem. We have implemented the Tychonov regularization for its simplicity, however its diffusive effect and the difficulty in determining a well suited value of α although a huge theory relating such choice to the noise level we emphasize that other sophisticated regularization methods exist and should be considered for the DOT-RF optical tomography. This is an inexplored field that we plan to do in the future.

4.3 Adjoint method

To solve the inverse problem associated to the model (2.1.1), we chose to proceed with the adjoint method which gives a general approach to compute the derivatives of the objective function by adding a small perturbation on the parameters. To solve optimization problem, most fast numerical iterative methods require the knowledge of the first order derivative. We can cite for example gradient based methods Conjugate gradient (CG), Quasi-Newton (QN), ... Also higher order derivatives might be required, in that case the adjoint method should be applied twice. The part III highlights the numerical tools used for the optimization process.

4.3.1 Diffusion adjoint

We focus for now our study on the initial diffusion problem on a single source with a data given on the whole domain. We drop the subscript for simplicity. The luminance is expressed as $\phi = \phi_x = \phi_x(\mathbf{x}, t)$ and we consider $\kappa = \kappa_x(\mathbf{x})$, $\mu = \mu_x(\mathbf{x})$ such that $\kappa, \mu \in U_{ad}$ the space of admissible diffusion and absorption coefficients. We place ourselves in the condition of section section 2.2 for the source term. We denote by $Q = \Omega \times (0, T)$ and $M(\overline{\Omega}) = C(\overline{\Omega})'$ the dual space of the continuous functions equiped with the usual norm. We recall the initial diffusion problem we want to solve

$$\begin{cases} -\nabla \cdot (\kappa \nabla \phi) + c_e \mu \phi + \dfrac{\partial \phi}{\partial t} = q_x & \text{on } Q \\[2mm] \phi + 2A\kappa \dfrac{\partial \phi}{\partial \mathbf{n}} = 0 & \text{on } \partial Q \end{cases} \tag{4.3.1}$$

We add a regularization term $\mathfrak{r}(\kappa, \mu)$ to guarantee the well-posedness of the minimization problem.

Remark 18. *For the minimization problem to be well posed, a regularization term has to be added in the objective function $J(\kappa, \mu)$. If we look at the Lagrangian form, the problem we are interested in, can be seen as solving a penalized version of the previous equation over desired coefficients κ, μ.*

$$\begin{cases} -\nabla \cdot (\kappa \nabla \phi) + c_e \mu \phi + \dfrac{\partial \phi}{\partial t} = q_x + \mathfrak{p}(\kappa, \mu) & on\, Q \\[2mm] \phi + 2A\kappa \dfrac{\partial \phi}{\partial \mathbf{n}} = 0 & on\, \partial Q \end{cases} \tag{4.3.2}$$

with $\alpha_\kappa, \alpha_\mu \in \mathbb{R}^+$ regularization parameters for the diffusion and absorption coefficients. The penalization $\mathfrak{p}(\kappa, \mu)$ of Tikhonov type would introduce a term

$$\mathfrak{p}(\kappa, \mu) = \alpha_\kappa \Delta \kappa + \alpha_\mu \mu \tag{4.3.3}$$

for the regularization defined in eq. (4.2.13) This kind of regularization introduces some diffusivity in the problem and tends to smooth reconstructed coefficient. κ has to be enough regular. The key point is the choice of the regularization coefficients which will determine the smoothness of our inverse problem solutions on κ and μ. Note that using appropriate methods to determine these regularization coefficient can greatly improve the precision and convergence of the solution (e.g using adaptative methods with an a posteriori estimates).

4.3.1.1 Domain cost function J_0

In this section, we focus on the cost function J_0 (defined in table 4.2.1). Let consider the linear problem (4.3.1). We denote U_{ad} the space of admissible optical parameters, there exists a couple of coefficients $\tilde{\kappa}, \tilde{\mu} \in U_{ad}$ such that for $\tilde{\phi} = \phi(\tilde{\kappa}, \tilde{\mu}) \in V$ solution of the problem (4.3.1) with V a Sobolev space well chosen, $\tilde{\phi}$ minimizes the functional J_0

$$J(\tilde{\kappa}, \tilde{\mu}) = \min_{\substack{\phi \in V \text{ sol (4.3.1)} \\ \forall \kappa, \mu \in U_{ad}}} J_0(\phi(\kappa, \mu)) + \mathfrak{r}(\kappa, \mu), \tag{4.3.4}$$

where $\mathfrak{r}(\kappa, \mu)$ is a regularization term for the minimization problem. We denote $\phi(\kappa, \mu) = \phi(\boldsymbol{x}, t; \kappa(\boldsymbol{x}), \mu(\boldsymbol{x})) \in V$ the solution obtained for a set of parameters κ, μ. To update the coefficients κ and μ using a gradient based method, we need to evaluate the gradient of the functional J over these parameters. We add a small perturbation on input coefficients to determine the gradient of J. Let denotes by

$$\begin{aligned} \kappa^\delta &= \kappa + \alpha \delta \kappa, \\ \mu^\delta &= \mu + \alpha \delta \mu, \end{aligned} \tag{4.3.5}$$

the perturbed coefficients with respective direction $\delta \kappa, \delta \mu$ for $\alpha > 0$. We desire to perturbe the coefficients in such a way that the error decreases at each step

$$0 \leq J(\kappa^\delta, \mu^\delta) \leq J(\kappa, \mu). \tag{4.3.6}$$

Therefore, we determine the descent direction following until we reach the minimum (Note that the best case happen when the exact minimum is found, which is translated by the equality $J(\kappa^\delta, \mu^\delta) = J(\kappa, \mu) = 0$). The derivatives of J_0 reads

$$J_0(\phi^\delta) = J_0(\phi) + \alpha < \frac{\partial J_0(\phi)}{\partial \phi}, \delta \phi > + o(\alpha). \tag{4.3.7}$$

We denote δJ_0 the variation

$$\delta J_0(\phi) = J_0(\phi^\delta) - J_0(\phi). \tag{4.3.8}$$

Remark 19. *The solution for the perturbed parameters κ^δ and μ^δ can be written*

$$\phi(\kappa^\delta, \mu^\delta) = \phi(\kappa, \mu) + \alpha \delta \phi + o(\alpha). \tag{4.3.9}$$

where the descent direction $\delta \phi$ verifies

$$\delta \phi = < \frac{\partial \phi}{\partial \kappa}, \delta \kappa > + < \frac{\partial \phi}{\partial \mu}, \delta \mu > . \tag{4.3.10}$$

The derivative of the objective function can be formulated such that

$$< \frac{\partial J(\kappa, \mu)}{\partial \kappa}, \delta \kappa > + < \frac{\partial J(\kappa, \mu)}{\partial \mu}, \delta \mu > = < \frac{\partial (J_0 \circ \phi)(\kappa, \mu)}{\partial \kappa}, \delta \kappa > + < \frac{\partial (J_0 \circ \phi)(\kappa, \mu)}{\partial \kappa}, \delta \kappa >$$

$$= < \frac{\partial J_0(\phi(\kappa, \mu))}{\partial \phi}, < \frac{\partial \phi}{\partial \kappa}, \delta \kappa >> + < \frac{\partial J_0(\phi(\kappa, \mu))}{\partial \phi}, < \frac{\partial \phi}{\partial \mu}, \delta \mu >>$$

$$= < \frac{\partial J_0}{\partial \phi}, < \frac{\partial \phi}{\partial \kappa}, \delta \kappa > + < \frac{\partial \phi}{\partial \mu}, \delta \mu >>$$

$$= < \frac{\partial J_0(\phi(\kappa, \mu))}{\partial \phi}, \delta \phi >$$

$$(4.3.11)$$

We denote for conciseness $\phi = \phi(\kappa, \mu)$ the solution and $\phi^\delta = \phi(\kappa^\delta, \mu^\delta)$ the perturbed solution. Considering the previous notations and the cost function J_0 (defined in table 4.2.1), we write

$$J_0(\phi) = \frac{1}{2} \int_Q |\phi - \phi_{obs}|^2$$

$$J_0(\phi^\delta) = \frac{1}{2} \int_Q |\phi^\delta - \phi_{obs}|^2 .$$

$$(4.3.12)$$

From a direct calculation using classical remarkable identities and rearranging the terms by $\phi^\delta - \phi$, it derives

$$\delta J_0(\phi) = \frac{1}{2} \int_Q \left(|\phi^\delta - \phi_{obs}|^2 - |\phi - \phi_{obs}|^2 \right)$$

$$= \frac{1}{2} \int_Q \left(\phi^\delta - \phi \right) \left(\phi^\delta + \phi - 2\phi_{obs} \right)$$

$$(4.3.13)$$

Then using (4.3.5), we deduce

$$\delta J_0(\phi) = \frac{1}{2} \int_Q \left(\alpha \delta \phi \right) \left(2(\phi - \phi_{obs}) + \alpha \delta \phi \right)$$

$$(4.3.14)$$

We divide this relation by α. Then we tend $\alpha \to 0$ to deduce the following expression

$$< \frac{\partial J_0(\phi)}{\partial \phi}, \delta \phi > = \int_Q \delta \phi \left(\phi - \phi_{obs} \right)$$

$$(4.3.15)$$

Now we turn back to the equation (4.3.1) and we consider both perturbed and non-perturbed equations

$$\begin{cases} -\nabla \cdot (\kappa \nabla \phi) + c_e \mu \phi + \dfrac{\partial \phi}{\partial t} = q_x & \text{on } Q \,, \\[2mm] -\nabla \cdot (\kappa^\delta \nabla \phi^\delta) + c_e \mu^\delta \phi^\delta + \dfrac{\partial \phi^\delta}{\partial t} = q_x & \text{on } Q \,, \end{cases}$$

$$(4.3.16)$$

with their respective boundary conditions

$$\begin{cases} \phi + 2A\kappa \dfrac{\partial \phi}{\partial \mathbf{n}} = 0 & \text{on } \partial Q \,, \\[2mm] \phi^\delta + 2A\kappa^\delta \dfrac{\partial \phi^\delta}{\partial \mathbf{n}} = 0 & \text{on } \partial Q \,. \end{cases}$$

$$(4.3.17)$$

We substract the first equation from the second one for both (4.3.16) and (4.3.17) to look at the tangent equation

$$\begin{cases} -\nabla \cdot (\kappa^\delta \nabla \phi^\delta) + c_e \mu^\delta \phi^\delta + \dfrac{\partial \phi^\delta}{\partial t} = -\nabla \cdot (\kappa \nabla \phi) + c_e \mu \phi + \dfrac{\partial \phi}{\partial t} & \text{on } Q \,, \\[2mm] \phi^\delta + 2A\kappa^\delta \dfrac{\partial \phi^\delta}{\partial \mathbf{n}} = \phi + 2A\kappa \dfrac{\partial \phi}{\partial \mathbf{n}} & \text{on } \partial Q \,. \end{cases}$$

$$(4.3.18)$$

We multiply the first equation by a test function $p \in V$ and integrate over the domain Q. Then using the Green formula, we obtain the following equation

$$\int_Q \left(\kappa^\delta \nabla \phi^\delta \nabla p + c_e \mu^\delta \phi^\delta p + \frac{\partial \phi^\delta}{\partial t} p \right) - \int_{\partial Q} \kappa^\delta \frac{\partial \phi^\delta}{\partial \boldsymbol{n}} p$$
$$= \int_Q \left(\kappa \nabla \phi \nabla p + c_e \mu \phi p + \frac{\partial \phi}{\partial t} p \right) - \int_{\partial Q} \kappa \frac{\partial \phi}{\partial \boldsymbol{n}} p \,. \tag{4.3.19}$$

We expand the parameters κ^δ, μ^δ as in (4.3.5) and we arrange terms by $\phi^\delta - \phi$ to be on the Left Hand Side (LHS) and shifts $\delta \kappa, \delta \mu$ on the Right Hand Side (RHS). We obtain the following equation

$$\int_Q \left(\kappa \nabla (\phi^\delta - \phi) \nabla p + c_e \mu (\phi^\delta - \phi) p + \frac{\partial (\phi^\delta - \phi)}{\partial t} p \right) - \int_{\partial Q} \kappa \frac{\partial (\phi^\delta - \phi)}{\partial \boldsymbol{n}} p$$
$$= \int_Q \left(-\alpha \delta \kappa \nabla \phi^\delta \nabla p - c_e \alpha \delta \mu \phi^\delta p \right) + \int_{\partial Q} \alpha \delta \kappa \frac{\partial \phi^\delta}{\partial \boldsymbol{n}} p \,. \tag{4.3.20}$$

From (4.3.5), we can rewrite the $\phi^\delta - \phi$, then divide by α as before and finally tend $\alpha \to 0$

$$\int_Q \left(\kappa \nabla \delta \phi \nabla p + c_e \mu \delta \phi p + \frac{\partial \delta \phi}{\partial t} p \right) - \int_{\partial Q} \kappa \frac{\partial \delta \phi}{\partial \boldsymbol{n}} p$$
$$= \int_Q \left(-\delta \kappa \nabla \phi \nabla p - c_e \delta \mu \phi p \right) + \int_{\partial Q} \delta \kappa \frac{\partial \phi}{\partial \boldsymbol{n}} p \,. \tag{4.3.21}$$

We integrate by part a second time the first term of this relation to obtain a formulation with $\delta \phi$ in factor

$$\int_Q \left(-\nabla \cdot (\kappa \nabla p) \delta \phi + c_e \mu \delta \phi p + \frac{\partial \delta \phi}{\partial t} p \right) - \int_{\partial Q} \kappa \left(\frac{\partial \delta \phi}{\partial \boldsymbol{n}} p - \frac{\partial p}{\partial \boldsymbol{n}} \delta \phi \right)$$
$$= \int_Q \left(-\delta \kappa \nabla \phi \nabla p - c_e \delta \mu \phi p \right) + \int_{\partial Q} \delta \kappa \frac{\partial \phi}{\partial \boldsymbol{n}} p \,. \tag{4.3.22}$$

If we reformulate the tangent boundary condition in (4.3.18) by expanding κ^δ, rearranging the terms by $\phi^\delta - \phi$, then use the relation (4.3.5), divide by α and tend $\alpha \to 0$ we deduce the following equation

$$\delta \phi + 2A\kappa \frac{\partial \delta \phi}{\partial \mathbf{n}} = -2A \delta \kappa \frac{\partial \phi}{\partial \mathbf{n}} \,. \tag{4.3.23}$$

If we multiply this equation by p and integrate on the boundary domain ∂Q, we obtain this relation

$$\int_{\partial Q} \frac{1}{2A} \delta \phi p + \int_{\partial Q} \kappa \frac{\partial \delta \phi}{\partial \mathbf{n}} p = - \int_{\partial Q} \delta \kappa \frac{\partial \phi}{\partial \mathbf{n}} p. \tag{4.3.24}$$

This expression can be substituted in (4.3.22) in the LHS boundary term in order to obtain a formulation depending on $\delta \phi$. The RHS boundary terms vanished.

$$\int_Q \left(-\nabla \cdot (\kappa \nabla p) \delta \phi + c_e \mu \delta \phi p + \frac{\partial \delta \phi}{\partial t} p \right) + \int_{\partial Q} \left(\frac{1}{2A} \delta \phi p + \kappa \frac{\partial p}{\partial \boldsymbol{n}} \delta \phi \right)$$
$$= \int_Q \left(-\delta \kappa \nabla \phi \nabla p - c_e \delta \mu \phi p \right) \,. \tag{4.3.25}$$

Finally we have to deal with the time dependent term in the LHS. By integrating by parts, we can write

$$\int_Q \left(-\nabla \cdot (\kappa \nabla p) \delta \phi + c_e \mu \delta \phi p - \frac{\partial p}{\partial t} \delta \phi \right) + \int_\Omega \left(\delta \phi(T) p(T) - \delta \phi(0) p(0) \right) + \int_{\partial Q} \left(\frac{1}{2A} \delta \phi p + \kappa \frac{\partial p}{\partial \boldsymbol{n}} \delta \phi \right)$$
$$= \int_Q \left(-\delta \kappa \nabla \phi \nabla p \right) - c_e \delta \mu \phi p \,. \tag{4.3.26}$$

By arranging terms with $\delta\phi$ in factor, we can rewrite the previous equation as

$$\int_Q \left(-\nabla \cdot (\kappa \nabla p) + c_e \mu p - \frac{\partial p}{\partial t} \right) \delta\phi + \int_\Omega \left(\delta\phi(T)p(T) - \delta\phi(0)p(0) \right) + \int_{\partial Q} \left(\frac{1}{2A}p + \kappa\frac{\partial p}{\partial \boldsymbol{n}} \right) \delta\phi$$
$$= \int_Q \left(-\delta\kappa\nabla\phi\nabla p - c_e\delta\mu\phi p \right) . \tag{4.3.27}$$

If we look at (4.3.27) LHS and (4.3.15), then considering $p \in L^2(0,T;V)$ solution the following system (adjoint equation)

$$\begin{cases} -\nabla \cdot (\kappa \nabla p) + c_e \mu p - \dfrac{\partial p}{\partial t} = (\phi - \phi_{obs}) & \text{on } Q \\[2mm] p + 2A\kappa\dfrac{\partial p}{\partial \mathbf{n}} = 0 & \text{on } \partial Q \\[2mm] p(\cdot, 0) = 0 \\[2mm] p(\cdot, T) = 0 \end{cases} \tag{4.3.28}$$

then for u solution of the forward problem and p solution of the adjoint equation (4.3.28)

$$< \frac{\partial J_0(\phi)}{\partial \phi}, \delta\phi > = - \int_Q (\delta\kappa\nabla\phi\nabla p + c_e\delta\mu\phi p) \tag{4.3.29}$$

Then we can express the gradient of the parameter we wish to optimize. Due to (4.3.11) we have

$$< \frac{\partial J}{\partial \kappa}, \delta\kappa > + < \frac{\partial J}{\partial \mu}, \delta\mu > = < \frac{\partial J_0}{\partial \phi}, \delta\phi > \tag{4.3.30}$$

We deduce the gradients

$$< \frac{\partial J(\kappa,\mu)}{\partial \kappa}, \delta\kappa > = - \int_Q \nabla\phi\nabla p\delta\kappa + \lim_{\alpha \to 0} \frac{\mathfrak{r}(\kappa^\delta, \mu) - \mathfrak{r}(\kappa, \mu)}{\alpha}$$
$$< \frac{\partial J(\kappa,\mu)}{\partial \mu}, \delta\mu > = - \int_Q c_e\delta\mu\phi p + \lim_{\alpha \to 0} \frac{\mathfrak{r}(\kappa, \mu^\delta) - \mathfrak{r}(\kappa, \mu)}{\alpha} . \tag{4.3.31}$$

To solve the optimization problem, we need to solve both linear systems for the forward and the adjoint problem in order to evaluate the objective function and to compute the gradient if the stop criterion is not reached.

Remark 20. *The adjoint state is backward in time, thus the forward solution has to be stored for each adjoint state iteration. Remark that we could choose different times grid to lower the computation cost. A possible strategy is to choose a fine grid for the forward problem and a coarse grid for the adjoint as the quality of the adjoint depends on the regularity of the forward solution.*

Remark 21. *The process is similar for the other cost functions to obtain the adjoint equation. However for boundary data measurements, the residual is taken into account as the RHS of the adjoint boundary condition.*

Remark 22. *Note that we reconstruct only the diffusion and the fluorescence parameters for the fluorescence, then the ajdoint is the same as for the diffusion problem with a cost function on $J(\kappa_m, \mu_{a,m})$ instead of $J(\kappa_x, \mu_{a,x})$*

Remark 23. *The minimization problem (4.3.4) can be rewritten as a lagrangian formulation which can be expressed as the minimization function J with a residual of the problem (4.3.1)*

$$\mathcal{L}(\kappa, \mu, \phi, p) = J_0(\phi) + \mathfrak{r}(\kappa, \mu) + \int_Q \left(-\nabla \cdot (\kappa\nabla\phi)p + c_e\mu\phi p + \frac{\partial\phi}{\partial t}p \right) - \int_Q q_x p \tag{4.3.32}$$

with $p \in V$ and V a function space well chosen.

4.3.2 Fluorescence adjoint

We consider the fluorescence equation now and hereafter. The process is similar to the previous section. For simplicity, we denote ψ the solution for the fluorescence $\phi_m^k(\mathbf{x}, t)$ for one source $k \geq 0$ fixed and for $\kappa = \kappa_m(\boldsymbol{x}), \mu = \mu_m(\boldsymbol{x})$ the corresponding input parameters. We recall the fluorescence equation for a domain $Q = \Omega \times (0, T)$ and $\partial Q = \partial\Omega \times (0, T)$

$$\begin{cases} -\nabla \cdot (\kappa \nabla \psi) + c_e \mu \psi + \dfrac{\partial \psi}{\partial t} = \gamma q_m \quad \text{on } Q \\[2mm] \psi + 2A\kappa \dfrac{\partial \psi}{\partial \mathbf{n}} = 0 \quad \text{on } \partial Q \end{cases} \tag{4.3.33}$$

We recall also the formulation of the fluorescence source term q_m defined such that

$$q_m = \frac{1}{\tau} \int_0^t \phi_x(s) e^{\frac{(t-s)}{\tau}} ds \tag{4.3.34}$$

and the ODE introduced in section 2.2.1 on the source term

$$q_m' - \frac{1}{\tau} q_m = \frac{1}{\tau} \phi_x \tag{4.3.35}$$

In the previous thesis [9, 18] for this project, one was interested at identifying the unknown input parameters $\kappa, \mu, \gamma, \tau$. We highlighted in the section 4.1 that Canuto et al [20] showed that due to limited observation, it is not possible to find a solution to this problem for more than two parameters. Thus we make the choice to smartly select only two parameters to be reconstructed. The first natural choice we can make is to reconstruct only the optical properties κ, μ and drop the fluorophor parameters. In that case, the adjoint is described by the analysis made in the previous section 4.3.1. For the remain of this section, we will assume that the diffusion and absorption parameters for the fluorescence problem (κ_m, μ_m) are almost the same than the ones for the diffusion (κ_x, κ_m). This choice is not proved to be consistent with the physics, but we assume from a mathematical point of view that the fluorescent markers will insignificantly perturbe these coefficients compared to the diffusion problem. Then a statistical method could be used to retrieve them as a next step. We desire to identify only γ, τ which is an inverse problem on the source. We consider the energy defined by the functional J_0 on the whole domain Ω and over time. The problem reads as find a set of two parameters $\tilde{\gamma}, \tilde{\tau}$ that minimize the following objective function

$$J(\tilde{\gamma}, \tilde{\tau}) = \min_{\substack{\psi \in V \text{ sol } (4.3.1) \\ \forall \gamma, \tau \in U_{ad}}} J_0(\psi(\gamma, \tau)) + \mathfrak{r}(\gamma, \tau) \tag{4.3.36}$$

where U_{ad} is the space of admissible parameters. As before, the $\mathfrak{r}$ is a regularization term for the minimization problem depending on the desired parameters. We consider the perturbed system and denote $\gamma^\delta, \tau^\delta$ the perturbed input coefficients, ψ^δ the perturbed solution for the fluorescence such that

$$\begin{aligned} \tau^\delta &= \tau + \alpha\delta\tau \\ \gamma^\delta &= \gamma + \alpha\delta\gamma \end{aligned} \tag{4.3.37}$$

Similarly to section 4.3.1, we write

$$\psi^\delta = \psi + \alpha\delta\psi + o(\alpha) \tag{4.3.38}$$

and we can adapt the eq. (4.3.11) in this case. We denote the perturbation on the functional energy δJ_0 We use the following notation

$$\delta J_0(\psi) = J_0(\psi^\delta) - J_0(\psi). \tag{4.3.39}$$

and from a direct computation, we obtain

$$\delta J_0(\psi) = \int_Q \delta\psi(\psi - \psi_{obs}) \tag{4.3.40}$$

We consider the system (4.3.33) and for the initial input parameters and the perturbed ones. We have

$$\begin{cases} -\nabla \cdot (\kappa \nabla \psi^\delta) + c_e \mu \psi^\delta + \dfrac{\partial \psi^\delta}{\partial t} = \gamma^\delta q_m^\delta \quad \text{on } Q \\[2mm] -\nabla \cdot (\kappa \nabla \psi) + c_e \mu \psi + \dfrac{\partial \psi}{\partial t} = \gamma q_m \quad \text{on } Q \end{cases} \tag{4.3.41}$$

and the boundary conditions

$$
\begin{cases}
\psi^\delta + 2A\kappa \dfrac{\partial \psi^\delta}{\partial \mathbf{n}} = 0 & \text{on } \partial Q \\[2mm]
\psi + 2A\kappa \dfrac{\partial \psi}{\partial \mathbf{n}} = 0 & \text{on } \partial Q
\end{cases}
\tag{4.3.42}
$$

We deduce the tangent equation by subtracting the equations. After arranging terms on the left by $\alpha \delta \psi = \psi^\delta - \psi$ we deduce the following equation

$$
\begin{cases}
-\nabla \cdot (\kappa \nabla (\alpha \delta \psi)) + c_e \mu (\alpha \delta \psi) + \dfrac{\partial (\alpha \delta \psi)}{\partial t} = \gamma^\delta q_m^\delta - \gamma q_m & \text{on } Q \\[2mm]
\alpha \delta \psi + 2A\kappa \dfrac{\partial (\alpha \delta \psi)}{\partial \mathbf{n}} = 0 & \text{on } \partial Q
\end{cases}
\tag{4.3.43}
$$

We can write the perturbation of the source term such that

$$
q_m^\delta = q_m + \alpha \delta q_m + o(\alpha)
\tag{4.3.44}
$$

Considering (4.3.37), the source term of the tangent equation (4.3.43) reads

$$
\gamma^\delta q_m^\delta - \gamma q_m = \alpha \gamma (\delta q_m) + \alpha (\delta \gamma) q_m = \alpha \delta (\gamma q_m)
\tag{4.3.45}
$$

Similarly to section 4.3.1 to obtain the adjoint equation, we multiply the tangent equation by a test function p. Then we perform two integrations by parts on the div-grad term. We substitute the tangent boundary condition. We regroup LHS terms by $\delta \psi$ and leave the RHS as is. We divide the obtain expression by α and tend α to 0. The formulation eq. (4.3.43) becomes

$$
\int_\Omega \left(-\nabla \cdot (\kappa \nabla p)\delta\psi + c_e \mu (\delta \psi p) - \frac{\partial p}{\partial t}\delta\psi \right) + \int_\Omega (\delta\psi(T)p(T) - \delta\psi(0)p(0))
$$
$$
+ \int_{\partial\Omega} \left(\frac{1}{2A}p + \kappa \frac{\partial p}{\partial \boldsymbol{n}} \right) \delta\psi = \int_\Omega \delta(\gamma q_m)p
\tag{4.3.46}
$$

If we look at (4.3.40), as before we deduce the adjoint equation.

$$
\begin{cases}
-\nabla \cdot (\kappa \nabla p) + c_e \mu p - \dfrac{\partial p}{\partial t} = (\psi - \psi_{\text{obs}}) & \text{on } Q \\[2mm]
p + 2A\kappa \dfrac{\partial p}{\partial \mathbf{n}} = 0 & \text{on } \partial Q \\[2mm]
p(\cdot, 0) = 0 \\[2mm]
p(\cdot, T) = 0
\end{cases}
\tag{4.3.47}
$$

and we have the relation

$$
< \frac{\partial J_0}{\partial \psi}, \delta\psi > = \int_Q \delta(\gamma q_m)p
\tag{4.3.48}
$$

The problem now consists in finding an expression for the descent direction $\delta(\gamma q_m)$ which depends possibly on $\delta\gamma$ and $\delta\tau$.

First method   A first method consists in writing the differentiation using this expression

$$
\alpha \delta(\gamma q_m) = \gamma^\delta q_m^\delta - \gamma q_m = \frac{\gamma^\delta}{\tau^\delta} \int_0^t \phi_x e^{\frac{(t-s)}{\tau^\delta}} ds - \frac{\gamma}{\tau} \int_0^t \phi_x e^{\frac{(t-s)}{\tau}} ds
\tag{4.3.49}
$$

We see that this expression is cleary non linear on $\frac{\gamma}{\tau}$ and has to be linearized. We use the classical trick

$$
\frac{\gamma^\delta}{\tau^\delta} = \frac{\gamma^\delta}{\tau^\delta} + \frac{\gamma}{\tau^\delta} - \frac{\gamma}{\tau^\delta} = \frac{\alpha \delta\gamma}{\tau^\delta} + \frac{\gamma}{\tau^\delta}
\tag{4.3.50}
$$

Then we have the following formulation

$$
\delta(\gamma q_m) = \frac{\alpha \delta\gamma}{\tau^\delta} \int_0^t \phi_x e^{\frac{(t-s)}{\tau^\delta}} ds + \left[\frac{\gamma}{\tau^\delta} \int_0^t \phi_x e^{\frac{(t-s)}{\tau^\delta}} ds - \frac{\gamma}{\tau} \int_0^t \phi_x e^{\frac{(t-s)}{\tau}} ds \right]
\tag{4.3.51}
$$

or again

$$\delta(\gamma q_m) = \frac{\alpha\delta\gamma}{\tau^\delta} \int_0^t \phi_x e^{\frac{(t-s)}{\tau^\delta}} ds + \gamma \int_0^t \phi_x \left[\frac{1}{\tau^\delta} e^{\frac{(t-s)}{\tau^\delta}} ds - \frac{1}{\tau} e^{\frac{(t-s)}{\tau}} ds \right] \tag{4.3.52}$$

Let us consider the function g defined such that

$$g(\tau^\delta) = \frac{1}{\tau^\delta} e^{\frac{(t-s)}{\tau^\delta}} - \frac{1}{\tau} e^{\frac{(t-s)}{\tau}} \tag{4.3.53}$$

Then we have $g(\tau) = 0$. We can write the taylor series of order one

$$g(\tau^\delta) = g(\tau) + g'(\tau)(\tau^\delta - \tau) + O((\tau^\delta - \tau)^2) \tag{4.3.54}$$

which is

$$g(\tau^\delta) = \left[-\frac{1}{\tau^{\delta 2}}(1 + \frac{t-s}{\tau^\delta})e^{\frac{t-s}{\tau^\delta}} \right] (\alpha\delta\tau) + O((\alpha\delta\tau)^2) \tag{4.3.55}$$

We get back to the equation (4.3.52), we have

$$\delta(\gamma q_m) = \frac{\alpha\delta\gamma}{\tau^\delta} \int_0^t \phi_x e^{\frac{(t-s)}{\tau^\delta}} ds + \gamma \int_0^t \phi_x \left[\left(-\frac{1}{\tau^{\delta 2}}(1 + \frac{t-s}{\tau^\delta})e^{\frac{t-s}{\tau^\delta}} \right) (\alpha\delta\tau) + O((\alpha\delta\tau)^2) \right] ds \tag{4.3.56}$$

which can be rewritten

$$\delta(\gamma q_m) = \frac{\alpha\delta\gamma}{\tau^\delta} \int_0^t \phi_x e^{\frac{(t-s)}{\tau^\delta}} ds - \frac{\alpha\delta\tau\gamma}{\tau^{\delta 2}} \int_0^t \phi_x \left((1 + \frac{t-s}{\tau^\delta})e^{\frac{t-s}{\tau^\delta}} \right) ds + O((\alpha\delta\tau)^2) \tag{4.3.57}$$

Finally we obtain the desired expression. If we divide by α and tend to zero $\alpha \to 0$ from the source term , we deduce

$$\delta(\gamma q_m) = \frac{\delta\gamma}{\tau} \int_0^t \phi_x e^{\frac{(t-s)}{\tau}} ds - \frac{\delta\tau\gamma}{\tau^2} \int_0^t \phi_x \left((1 + \frac{t-s}{\tau})e^{\frac{t-s}{\tau}} \right) ds. \tag{4.3.58}$$

Finally, reporting this equation into (4.3.48), we deduce the descent directions

$$< \frac{\partial J(\gamma,\tau)}{\partial\gamma}, \delta\gamma > = \int_Q \left(\frac{1}{\tau} \int_0^t \phi_x e^{\frac{(t-s)}{\tau}} ds \right) p\delta\gamma + \lim_{\alpha\to 0} \frac{\mathfrak{r}(\gamma^\delta,\tau) - \mathfrak{r}(\gamma,\tau)}{\alpha}$$
$$< \frac{\partial J(\gamma,\tau)}{\partial\tau}, \delta\tau > = \int_Q \left(-\frac{\gamma}{\tau^2} \int_0^t \phi_x \left(\left(1 + \frac{t-s}{\tau}\right) e^{\frac{t-s}{\tau}} \right) ds \right) p\delta\tau + \lim_{\alpha\to 0} \frac{\mathfrak{r}(\gamma,\tau^\delta) - \mathfrak{r}(\gamma,\tau)}{\alpha} \tag{4.3.59}$$

Second method Now we propose to consider the adjoint problem based on the ODE equation (4.3.35). We rewrite this ODE as follows

$$\tau \left[\frac{\gamma}{\tau} \int_0^t \phi_x e^{\frac{(t-s)}{\tau}} ds \right]' - \frac{\gamma}{\tau} \int_0^t \phi_x e^{\frac{(t-s)}{\tau}} ds = \phi_x \tag{4.3.60}$$

Then the perturbed system of ODEs is

$$\begin{cases} \tau^\delta \gamma^\delta q_m^{\delta \prime} - \gamma^\delta q_m^\delta = \gamma^\delta \phi_x \\ \tau\gamma q_m' - \gamma q_m = \gamma\phi_x \end{cases} \tag{4.3.61}$$

derive then the tangential equation

$$\tau^\delta \gamma^\delta q_m^{\delta \prime} - \tau\gamma q_m' - \alpha\gamma\delta q_m - \alpha\delta\gamma q_m = \alpha\delta\gamma\phi_x \tag{4.3.62}$$

we develop the $q_m^{\delta \prime}$ term

$$\tau^\delta(\gamma q_m' + \alpha\gamma\delta q_m' + \alpha\delta\gamma q_m') - \tau\gamma q_m' - \alpha\gamma\delta q_m = \alpha\delta\gamma\phi_x \tag{4.3.63}$$

then by expanding the terms, we have

$$\tau\alpha\delta\gamma q_m' + \tau\alpha\gamma\delta q_m' - \alpha\gamma\delta q_m - \alpha\delta\gamma q_m = -\alpha\gamma\delta\tau q_m' + \alpha\delta\gamma\phi_x \tag{4.3.64}$$

we divide by α and look for $\alpha \to 0$, then we have

$$\tau\delta\gamma q_m' + \tau\gamma\delta q_m' - \gamma\delta q_m - \delta\gamma q_m = -\gamma\delta\tau q_m' + \delta\gamma\phi_x \tag{4.3.65}$$

We remark we have almost the same ODE than (4.3.35) but on $\delta(\gamma q_m)$ with a new RHS term. We can express the solution of this ODE

$$\delta(\gamma q_m) = \frac{\delta\gamma}{\tau}\int_0^t \phi_x e^{\frac{t-s}{\tau}}ds - \frac{\gamma\delta\tau}{\tau}\int_0^t q_m'(s)e^{\frac{t-s}{\tau}}ds \tag{4.3.66}$$

We have an expression of q_m depending on $\delta\gamma, \delta\tau$. Now we have still to transform the expression of the second integral in the previous formulation to treat the derivative of q_m. Thanks to the ODE (4.3.35), we write

$$
\begin{aligned}
-\frac{\gamma\delta\tau}{\tau}\int_0^t q_m'e^{\frac{t-s}{\tau}}ds &= -\frac{\gamma\delta\tau}{\tau}\int_0^t q_m e^{\frac{t-s}{\tau}}ds - \frac{\gamma\delta\tau}{\tau}\int_0^t \phi_x e^{\frac{t-s}{\tau}}ds \\
&= -\frac{\gamma\delta\tau}{\tau}\int_0^t \frac{1}{\tau^2}\int_0^s \phi_x(w)e^{\frac{s-w}{\tau}}dw e^{\frac{t-s}{\tau}}ds - \frac{\gamma\delta\tau}{\tau}\int_0^t \frac{1}{\tau}\phi_x(s)e^{\frac{t-s}{\tau}}ds
\end{aligned} \tag{4.3.67}
$$

We interchange the double integrals to obtain

$$
\begin{aligned}
-\frac{\gamma\delta\tau}{\tau}\int_0^t q_m'e^{\frac{t-s}{\tau}}ds &= -\frac{\gamma\delta\tau}{\tau}\int_0^t \phi_x(w)\frac{1}{\tau^2}\left(\int_w^t e^{\frac{s-w}{\tau}}e^{\frac{t-s}{\tau}}ds\right)dw - \frac{\gamma\delta\tau}{\tau}\int_0^t \frac{1}{\tau}\phi_x(s)e^{\frac{t-s}{\tau}}ds \\
&= -\frac{\gamma\delta\tau}{\tau}\int_0^t \phi_x(w)\frac{1}{\tau^2}\left(\int_w^t e^{\frac{t-w}{\tau}}\right)dw - \frac{\gamma\delta\tau}{\tau}\int_0^t \frac{1}{\tau}\phi_x(s)e^{\frac{t-s}{\tau}}ds \\
&= -\frac{\gamma\delta\tau}{\tau}\int_0^t \phi_x\frac{1}{\tau^2}\left(e^{\frac{t-w}{\tau}}\right)(t-w)dw - \frac{\gamma\delta\tau}{\tau}\int_0^t \frac{1}{\tau}\phi_x(s)e^{\frac{t-s}{\tau}}ds \\
&= -\frac{\gamma\delta\tau}{\tau}\int_0^t \frac{\phi_x(s)}{\tau}\left(1+\frac{t-s}{\tau}\right)e^{\frac{t-s}{\tau}}ds
\end{aligned} \tag{4.3.68}
$$

Finally, from equations (4.3.48) and (4.3.66) , we deduce the following descent directions

$$
\begin{aligned}
< \frac{\partial J(\gamma,\tau)}{\partial\gamma}, \delta\gamma > &= \int_Q \left(\frac{1}{\tau}\int_0^t \phi_x(s)e^{\frac{t-s}{\tau}}ds\right)p\delta\gamma + \lim_{\alpha\to 0}\frac{\mathfrak{r}(\gamma^\delta,\tau)-\mathfrak{r}(\gamma,\tau)}{\alpha} \\
< \frac{\partial J(\gamma,\tau)}{\partial\tau}, \delta\tau > &= \int_Q \left(-\frac{\gamma}{\tau^2}\int_0^t \phi_x(s)\left(1+\frac{t-s}{\tau}\right)e^{\frac{t-s}{\tau}}ds\right)p\delta\tau + \lim_{\alpha\to 0}\frac{\mathfrak{r}(\gamma,\tau^\delta)-\mathfrak{r}(\gamma,\tau)}{\alpha}
\end{aligned} \tag{4.3.69}
$$

which are the same than the one found with the first method (4.3.59).

4.4   Test cases

We present in this section some preliminary results regarding the inverse problem. Details about the implementation are explained in the final chapter 5.

The fig. 4.4.2 shows a test case based on a simplified model given in [21]. This problem is slightly different from the DOT as we drop the time dependent term to consider only the stationnary diffuse problem and use different boundary conditions. This test case is interesting since numerically, the implementation is similar. Note that we consider only one source.

Remark 24. *Contrary to the instationnary problem, we don't have to go backward in time for the problem* (4.4.1) *contrary to the DOT* (2.1.1)

The original context of this study is nuclear waste buried in high depth ground. In this study they desire to understand the radioactive diffusion in the soils. We are interested in two parameters, the diffusion $\kappa(\boldsymbol{x})$ and the porosity $\mu(\boldsymbol{x})$ of the soil that is a reaction coefficient divided by a radioactive decay coefficient λ. For the simplified model, we consider the rectangular domain Ω, and different part of the boundary domain denoted Γ_{inj} for the radioactive source, Γ_D the ground surface and Γ_N the remaining boundary. The simplified diffuse model reads

$$
\begin{cases}
-\nabla.\kappa\nabla u + \lambda\mu u = 0 & \text{on } \Omega \\
\kappa\nabla u \cdot \boldsymbol{n} = g & \text{on } \Gamma_{inj} \\
\kappa\nabla u \cdot \boldsymbol{n} = 0 & \text{on } \Gamma_N \\
u = 0 & \text{on } \Gamma_D
\end{cases} \tag{4.4.1}
$$

We set homogeneous Neumann boundary condition on the boundary Γ_N, non-homogeneous Neumann on source boundary Γ_{inj} and a homogeneous Dirichlet boundary condition on the top surface Γ_D. For our test case, we consider the setting described in the fig. 4.4.1, but we choose to add instead an opaque diffuse inclusion. The

Figure 4.4.1: Test case geometry
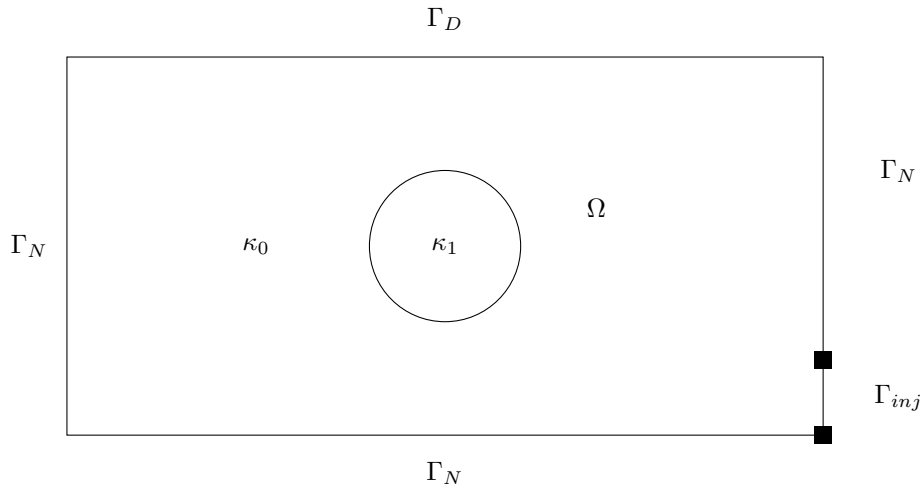
radioactive decay coefficient is chosen to be $\lambda = 1.0$. For the porosity coefficient, the functionnal is define by $\mu(\boldsymbol{x}) = 2.x^2 + 3.y^2$.

Figure 4.4.2: Reconstruction on two parameters κ and $\mu(x)$ using ipopt for one source placed on the bottom right in 2D. The two first columns shows respectively the state and adjoint solutions for the first and last optimization iterations (by row). The two last colums shows repectively, on the top, the coefficients for the diffusion and absorption desired (inverse problem exact solutions). At the bottom, the paramaters obtained after 84 iterations. The current optimization process did not converge since the optimization process is stuck in a local minimum. We remark that the diffuse inclusion can be captured from the right front (where the light source is located). But the absorption is not captured due to the chosen functionnal and the fact that the source is completly diffused before catching the whole domain.
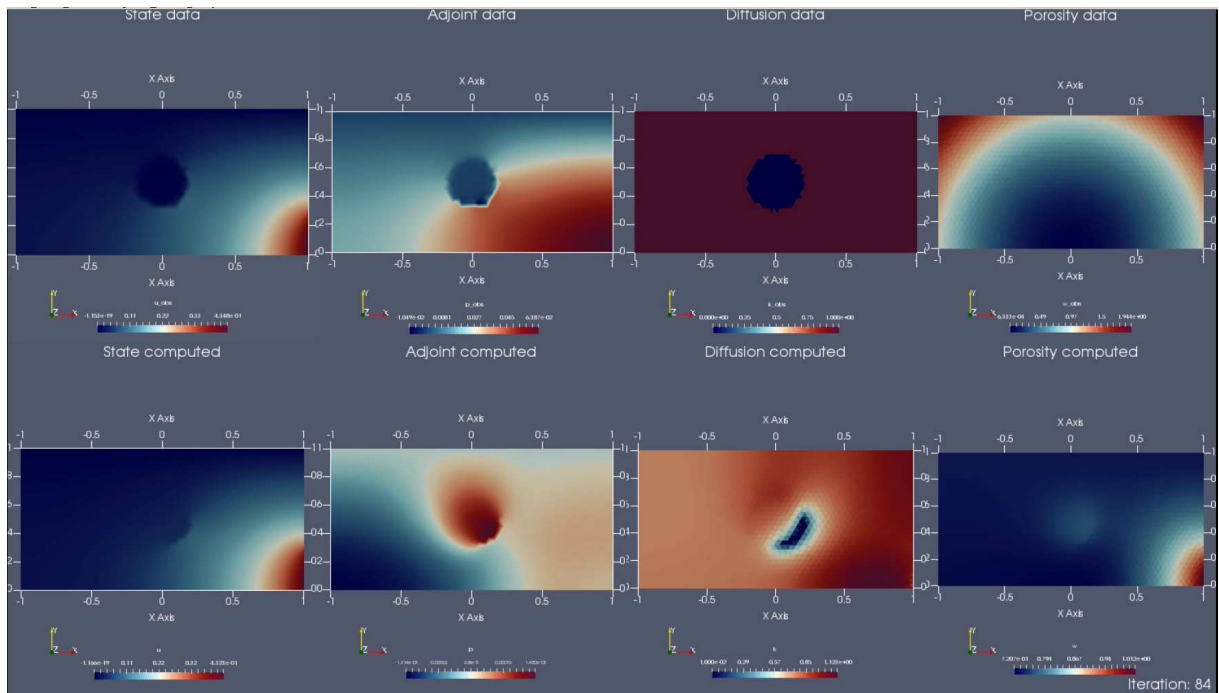
4.5 Conclusion

In the chapter 4, the inverse problem has been detailed for the coupled system of equations presented in (2.1.1). An argument is given to justify that we can only reconstruct up to two parameters. In order to handle the inverse problem, we proposed in section 4.2 to present the different cost functions to use depending on the type of data sampling. For the inverse problem, we based our solving strategy on an adjoint method. We proposed two strategies to compute the adjoint. One method consists in computing the adjoint based on the system of PDE presented in (2.1.1). Therefore, the memory source term for the fluorescence problem has to be calculated explicitly. A second method proposed consists in computing the adjoint based on the ODE introduced in (2.3.24). These two methods let us have two ways to obtain the gradients used in the optimization process. In this last case, the fluorescence source term can be deduced from the solution of the ODE. Therefore, we have a method to convert a storage cost to a computing cost. Finally, we proposed preliminary results for the inverse problem on a stationnary testcase in 2D. The reconstuction presented does not provide good results. This can be explained by different reasons. A first hypothesis is that there might be problem within the code implementation. We can also assume that the optimization algorithm used in this specific case is stuck in a local minima and can't reach the global minimum. One of the future perspective concerning the inverse problem is to be able to obtain better reconstructions, then consider the unsteady case on one source, then on multisource. All numerical ingredients are ready to be used to handle the reconstruction for the unsteady case, and an early implementation is almost ready. However, the code is still in an early state and results won't be presented in this document. However, chapter 5 will introduce the numerical ingredient in order to achieve this goal.

References

[2] S.R Arridge. "Optical tomography in medical imaging". In: *IOPScience Inverse problem* 15.2 (1999).

[3] Y. Yamada and S. Okawa. "Diffuse Optical Tomography: Present Status and Its Future". In: *Optical Review* 21.3 (2014), pp. 185–205.

[9] Farouk Nouizi. "Tomographie optique diffuse et de fluorescence préclinique : instrumentation sans contact, modélisation et reconstruction 3D résolue en temps". PhD thesis. Université de Strasbourg, 2011.

[18] Murielle Torregrossa. "Reconstruction d'images obtenues par tomographie optique dans le proche infrarouge". PhD thesis. Université de Strasbourg, 2003.

[20] B Canuto and O Kavian. "Determining coefficients in a class of heat equations via boundary measurements". In: *SIAM Journal on Mathematical Analysis* 32.5 (2001), pp. 963–986.

[21] Grégoire Allaire, Diogo Silva, and Olivier Pantz. "Sur un probleme inverse de détermination de coefficients de diffusion". In: (Nov. 2004).

III Computational framework

Chapter 5 - Numerical ingredients

In this chapter, different generic tools used to solve numerically the system of PDEs are detailed. In the first section 5.1 the FEEL++ library is presented. This library introduces a finite element programming language embedded in the C++ language. Several mathematical tools used in the previous chapters are detailed for a better understanding. The second section 5.2 focus on the BDF method. FEEL++ introduces a generic time scheme framework which relies on BDF formula. This framework has been slightly modified to be adapted to the inverse problem. In particular, we are interested in this part to the approach used to handle the memory term of the fluorescence equation in (2.1.1). The strategy relies on the BDF framework. For the adjoint equation, the problem is solved backward in time. Thus, to compute the source ter, we have to retrieve the solution of the diffusion at each iterations. Therefore the existing BDF framework has been adapted to be more versatile and add the possibility switch from forward to backward iteration.

5.1 Feel++ framework

The FEEL++ framework is a generic library to solve PDE though generalized Galerkin methods for any topology 1D, 2D, 3D [22] and arbitrary order methods. This open source framework is part of big family of free Finite Element Methods (FEM) software with the same goal of a generic tool for PDE. For example, Free Finite Element Method in C++ (Freefem++), FEniCS (FEniCS) can be mentioned as famous software in the scientific community. All the library code sources are available on the A web-based hosting service for Version control software (Git) *GitHub, Inc.* (GitHub) platform. FEEL++ introduces a Domain Specific Embedded Language (DSEL) in C++. This language is very close to the mathematical one and is based on the variationnal formulation of the problem. The FEEL++ framework is based on generalized Galerkin methods.

At the current time, different methods are available to get started with FEEL++ that are more or less convenient depending on the user programming experience. To facilitate the installation process and easier the access to the framework, container technologies are used. Two solutions among container software leaders are provided (i) Docker containerization platform (Docker) and (ii) Singularity containerization platform (Singularity). (i) is more adapted for cloud environment where (ii) focus more on HPC architectures. We provide with these containers a full FEEL++feel programming environment. One introduced the FEEL++ toolboxes that are based on the core language of the library to provide generic simple but powerful tools to solve classical monophysic problem such as Computational Fluid Dynamics (CFD), Computational Solid Mechanics (CSM), etc. or multiphysic problem such as Fluid Structure Interaction (FSI), Thermo-Electric (TE), etc. New toolboxes are added on research project based. The targeted audience with these toolboxes are typically research physicists or engineers that are more interested in using customizable models instead of creating new ones. Nevertheless, reusing the existing toolboxes to build new model in order to solve new innovative problems is still possible.

Remark 25. *One of the perspectives for this project is to add a DOT toolbox to provide a fast access to DOT reconstruction for external end-users (hospital doctors), improve the reproducibility, or adapt to new DOT modalities.*
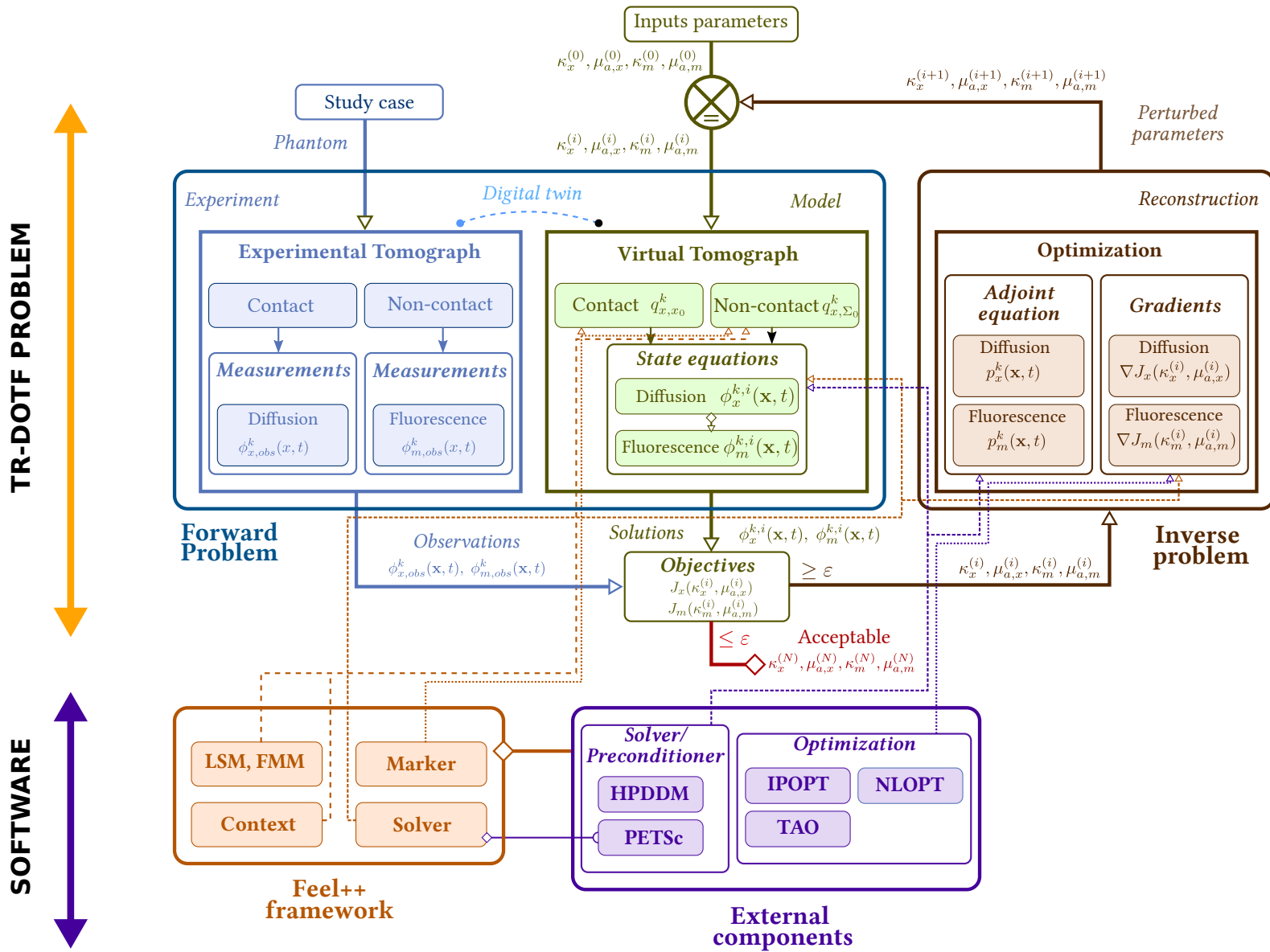
Figure 5.0.1: General scheme for the TR-DOT problem and implementation. $k \in 1, N_s$ and $i \in [1, N]$ denote respectively the sources and the optimization iteration number. Each software component contribution is presented in chapter 5.

For the initial problem (2.1.1) we will use exclusively Lagrange finite Elements for any dimension $d = 1, 2, 3$ and arbitrary polynomial and geometric order. For an overview of different elements supported by the library and an idea of their implementation, we recommend the reader to consult the former thesis [23]. The language defines necessary structures to easier manipulation of the mathematical functional tools such as functions spaces, bilinear forms, linear forms but also integration, projection, interpolation. We highlight hereafter the key ingredients of FEEL++ that are also useful for our project purpose.

First, let us introduce the notations. Following the standard definition of finite elements, we consider $(K, \mathbb{P}, \Sigma)$ a triplet with K is a convex, $\mathbb{P}$ a polynomial space and Σ the dual space. We define $\hat{K} \subset \mathbb{R}^d$ ($d = 1, 2, 3$) a convex as reference element (*e.g.* simplex or hypercube). We consider a domain Ω and $\mathcal{T}_\delta$ a partition of Ω as a finite collection of nonempty, disjoint open simplices or hypercubes $\mathcal{T}_\delta$ with δ a discretization parameter. We denote $h = \max_{K \in \mathcal{T}_\delta} h_K$ with h_K the characteristic length of an element $K \in \mathcal{T}_\delta$. We consider the mapping $\phi_{K,k}^{\text{geo}}$, a polynomial of degree k, for the geometric transformation. $\phi_{K,k}^{\text{geo}}$ maps the reference element $\hat{K}$ to the real one K (fig. 5.1.1). The partition $\mathcal{T}_\delta$ induces a discretization of Ω, denoted Ω_δ, defined as the union of the closure of
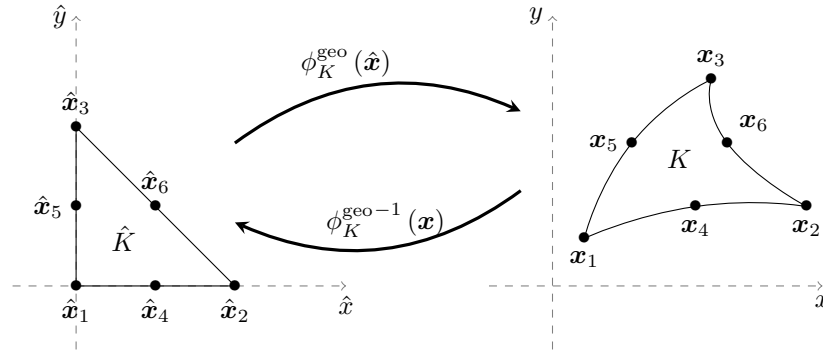
Figure 5.1.1: Geometrical transformation from reference to real domain on a 2D simplex

all elements in this partition. With these notations, a *mesh face* represents an hyperplanar closed subset F of $\overline{\Omega_\delta}$ with a positive $(d-1)$-dimensional measure.

- F is an *internal face* if there exist two elements K_i, $K_j \in \mathcal{T}_\delta$ for $i \neq j$ such that the intersection $F = \partial K_1 \cap \partial K_2$.

- F is a *boundary face* if there exists $K \in \mathcal{T}_\delta$ such that $F = \partial K \cap \partial \Omega_h$.

Internal faces are collected in the set $\mathcal{F}_\delta^i$, boundary faces in $\mathcal{F}_\delta^b$ and we let $\mathcal{F}_\delta := \mathcal{F}_\delta^i \cup \mathcal{F}_\delta^b$. For all $F \in \mathcal{F}_\delta$, we define $\mathcal{T}_F := \{K \in \mathcal{T}_\delta \mid F \subset \partial K\}$. For every interface $F \in \mathcal{F}_\delta^i$ we introduce two associated normals to the elements in $\mathcal{T}_F$ and we have $\mathbf{n}_{K_1,F} = -\mathbf{n}_{K_2,F}$, where $\mathbf{n}_{K_i,F}, i \in \{1, 2\}$, denotes the unit normal to F pointing out of $K_i \in \mathcal{T}_F$. On a boundary face $F \in \mathcal{F}_\delta^b$, $\mathbf{n}_F = \mathbf{n}_{K,F}$ denotes the unit normal pointing out of Ω_δ.

Interpolation   Without loss of generality we suppose from now on that we work with simplicial elements. Given a positive integer N, we denote by $\mathbb{P}^N(\hat{K})$ and $\mathbb{P}^N(K)$ the spaces of polynomials of total degree less or equal than N defined in $\hat{K}$ and K respectively. We define $P_c^N(\Omega_\delta \equiv \Omega_{(h,k)})$ and $[P_c^N(\Omega_\delta \equiv \Omega_{(h,k)})]^d$ with $k \geqslant 1$:

FEEL++ allows to define interpolation operators based on De Rham Diagram (5.1.1)

$$
\begin{array}{ccccccccccc}
\mathbb{R} & \xrightarrow{id} & H_1(\Omega) & \xrightarrow{grad} & H_{\text{curl}}(\Omega) & \xrightarrow{curl} & H_{\text{div}}(\Omega) & \xrightarrow{div} & L_2(\Omega) & \xrightarrow{0} & \{0\} \\
& & \downarrow \pi_{\mathcal{N}}^U & & \downarrow \pi_{\mathcal{N}}^V & & \downarrow \pi_{\mathcal{N}}^W & & \downarrow \pi_{\mathcal{N}}^Z & & \\
\mathbb{R} & \xrightarrow{id} & U_{\mathcal{N}} & \xrightarrow{grad} & V_{\mathcal{N}} & \xrightarrow{curl} & W_{\mathcal{N}} & \xrightarrow{div} & Z_{\mathcal{N}} & \xrightarrow{0} & \{0\}
\end{array} \tag{5.1.1}
$$

The listing 5.1 gives an example how to create an interpolation operator. First we create two meshes of simplices of dimension 2 for a custom representative geometries of a domain Ω. Then we define two $\mathbb{P}1$ and $\mathbb{P}2$ functional spaces living on this two meshes with different polynomial orders. We create the interpolation operators between the origin and the image domain. Finally we can construct a function and its interpolated image.

Listing 5.1: Example of interpolator usage

```
1 using MeshType = Mesh<Simplex<2>>;
2 // Create two mesh
3 auto mesh1 loadMesh( _mesh=new MeshType ); // default mesh size h1
4 auto mesh2 loadMesh( _mesh=new MeshType ); // default mesh size h2
5 auto P1h1 = Pch<1>( mesh1 );
6 auto P2h2 = Pch<2>( mesh2 );
7 auto Ih = I( _domain=P1h1, _image=P2h2 );
8 auto u = P1h1->element();
9 auto v = Ih(u); // P2h2;
```

This feature is used to handle the non contact mode (remark 26).

Remark 26. *An interpolation operator use case is for the non contact mode case, when we have to determine the location of sources. Basically, the idea consists in creating a $d-1$ mesh from a functional for the sources located inside the domain based on a distance function from the boundary using a levelset method section 5.4.*

Algebraic representation   FEEL++ interfaces PETSc thanks to a wrapper for the algebraic layer. Different backend can be created to customize linear/non-linear system depending on the problem type. Trilinos was previously supported, but is unmaintainted. Concerning optimization part, FEEL++ has been interfaced with different optimization libraries such as NLopt, IPopt "as is" remark 27. In particular, this last library has been used within this project for the inverse problem chapter 4. In section 5.5 we will present some ingredients used to solve the inverse problem using these libraries. Remark that with the Portable, Extensible Toolkit for Scientific Computation (PETSc) interface, we have also access to the Toolkit for Advanced Optimization (TAO) library that has the same purpose than IPopt, but based on PETSc algebraic parallel data structures which enable a wide range of parallel linear and non linear solvers inherent to PETSc.

Remark 27. *The optimization libraries interfaced are not yet fully integrated with the FEEL++ language. One of the future perspective is to create a new wrapper for general optimization problems in the FEEL++ library usable via the backend mechanism.*

Backend   The underlying algebraic representation hidden under the FEEL++ keywords is always accessible for custom manipulation thanks to a backend mechanism. The listing 5.2 gives a short example about how to create a new backend to have a specific custom preconditionner for the diffusion problem. We use also a second backend for the fluorescence for treating each problem separately.

Listing 5.2: Example of backend usage. The prefix precised in the backend is used for the command line options. This allow us to configure the type of preconditioner, solver, etc. per backend

```
1 auto mesh = loadMesh(_mesh=new Mesh<Simplex<2>>);
2 auto Xh = Pch<1>( mesh );
3 auto phi_x = Vh->element();
4
5 // We create the bilinear form for the diffusion equation.
6 auto a_x = form2( _trial=Vh, _test=Vh); // Underlying matrix A
7 auto l_x = form1( _trial=Vh, _test=Vh); // Underlying vector B
8
9 // Problem AX = B assembling...
10
11 // We create a new backend with a prefix.
12 auto backend_diffusion = backend(_prefix="diffusion");
13
14 // We create a specific preconditionner used for the diffusion problem.
15 auto prec_diffusion = preconditioner(
16             _prefix="diffusion",
17             _matrix=a_x.matrixPtr(), /* Matrix A */
18             _pc=backend_diffusion->pcEnumType() /*LU_PRECOND*/,
19             _pcfactormatsolverpackage=backend_diffusion->
                  ↪ matSolverPackageEnumType(),
```

```
20              _backend=backend_diffusion
21              );
22
23 // We solve the system AX = B
24 at_x.solveb( _rhs=lt_x,
25              _solution=phi_x,
26              _backend=backend_diffusion,
27              _prec=prec_diffusion
28            );
```

This gives the possibility to customize the solver used in section 5.3 and available via PETSc based on the problem type.

Context The context has been introduced in FEEL++ to handle Certified Reduced Basis (CRB) issues in particular for an efficient evaluation of Finite Element (FE) or Reduced Basis (RB) [24]. The idea behind this feature is to create a context to evaluate a FEEL++ expression on a certain number of nodes and performing only point to point MPI communication to share the information on all processes. The context system is advantageous when the number of nodes to evaluate is small since it reduces the cost of MPI communications. The listing 5.3 details how to create a context for a 2D problem.

Listing 5.3: Example of FEEL++ context used to evaluate an expression in parallel on specific nodes

```
1 int dim=2;
2 auto Xh = Pch<1>( mesh );
3 auto u = Xh->element("solution");
4 auto ctx = Xh->context();
5 node_type n1(dim);
6 node_type n2(dim);
7 auto u_n12 = evaluateFromContext( _context=ctx , _expr=idv( u ) );
```

This functionality is used in the contact case in order to retrieve the forward solution of our problem (2.1.1) in parallel, but only the degree of freedom values that corresponds to N_s fibers. This feature is required to compute the errors for the minimisation problem et retrieve all contributions efficiently. In practice, this can be also used to save each TPSFs without performing any parallel writing.

Geometries and mesh FEEL++ relies mainly on a three-dimensional finite element mesh generator with built-in pre- and post-processing facilities (GMSH) to manage CAD geometries and mesh generation. Different mesh generators are supported. We handle our own Hierarchical Data Format 5 (HDF5) mesh format which is used for efficient computation. In particular, MPI standard for parallel input/output operations (MPIIO) is used to write in parallel the mesh file on hard disk drives.

Remark 28. *For specific testcase, we desire to avoid interpolating the sources since it introduces an error that can be repercuted on the inverse problem solution. Therefore, we desire to build a mesh which takes into account the source areas as exact nodes for the contact measurement mode, or edges (respectively surfaces) for the non contact mode in 2d (respectively 3d). The distance from the boundary correspond to $\frac{1}{\mu'_s}$, thus it depends on the initialization of the diffusion parameter in the computing code. A feature has been added the have the possibility to parametrize the GMSH geometry by parsing the GMSH file directly via FEEL++.*

Markers and mesh element range FEEL++ defines markers that can be used to select a range of elements on the mesh. The marker is represented by a $\mathbb{P}_0$ function where the element constant value corresponds to the index of the marker. A nice feature with this tool is the possibility to calculate new marker from function expression based on $\mathbb{P}_0$ functionals. The default FEEL++ marker is generated from GMSH physical entities. The listing 5.4 shows how to retrieve a range of mesh elements as a C++ iterator that can be used in a wide range of FEEL++ math operator such as for integration, projection, etc.

Listing 5.4: Example which demonstrate how to create range on mesh elements and perform a nodal projection from a FEEL++ an expression

```
1 auto mesh = loadMesh(_mesh=new Mesh<Simplex<2>>);
```

```cpp
2  auto Xh = Pch<0>( mesh );
3  auto f = Xh->element();
4  auto g = Xh->element();
5
6  // We create several range of mesh elements.
7  auto omega = elements( mesh );
8  auto bound = boundaryfaces( mesh );
9  auto r1 = markedelements( mesh, "range1name" );
10 auto r2 = marked2elements( mesh, "range2name" );
11
12 // Nodal projection.
13 f.on( _range=s1, _expr=cst(1.0) );
14 g.on( _range=s2, _expr=cst(2.0) );
```

ODE   With the Eye2Brain [**Eye2Brain**] project, an interface to OpenModelica (OpenModelica) has been added to the FEEL++ library. OpenModelica is an open-source modeling and simulation software used within the project to create and solve ODEs based on electrical scheme. The key idea is to be able to perform 0D-3D coupling by replacing some model components using model exchange and co-simulation capabilities via the respectively Functional Mock-up Interface (FMI) and the Functional Mock-up Unit (FMU). An advange of this software is to avail fast modeling and give a quick access to a wide range of ODE solvers. This software could be used as a perspective to test a wide range of numerical scheme for the ODE-PDE coupling problem introduced in eq. (2.3.24).

5.2   BDF methods

The backward differentiation formulas (BDF)   BDF is the implicit method used to develop the time-dependent term of the equation. The general formula is given by

$$\sum_{k=0}^{p} \alpha_k \mathbf{r}_{n+k} = h\beta\phi(\mathbf{r}, t) \tag{5.2.1}$$

where α_k and β are coefficients chosen for the order p. For a given time grid such that $t_n = n\Delta t$ for $n \in \mathbb{N}$ and Δt the chosen time step, the solution ϕ for $t = t_n$ is denoted $\phi^{(n)}(\boldsymbol{x}) = \{\phi(\boldsymbol{x}, t) \mid t = t_n, \ n \in \mathbb{N}\}$ or $\phi^{(n)}$ for convenience. The time derivative can be expressed as follows

$$\frac{\partial \phi^{(n)}}{\partial t} = \frac{\alpha_0}{\Delta t}\phi^{(n+1)} - \sum_{j=1}^{p} \frac{\alpha_j}{\Delta t}\phi^{(n+1-j)} + \mathcal{O}(\Delta t) \tag{5.2.2}$$

BDF coefficients are detailed in table 5.2.1.

Table 5.2.1: **BDF** α_i coefficient for order $p = \{1, 2, 3\}$ and β_i for time extrapolation [25]

p	α_0	α_1	α_2	α_3	β_0	β_1	β_2
1	1	1	-	-	1	-	-
2	3/2	2	-1/2	-	2	-1	-
3	11/6	3	-3/2	1/3	3	-3	1

For order $p = 1$ we have the well known Backward Euler scheme.

Table 5.2.2: $\phi^{(n)}$ time derivative expressed for **BDF**$_1$ and **BDF**$_2$

BDF$_n$	Expression
BDF$_1$	$\frac{\partial \phi^{(n)}}{\partial t} = \frac{\phi^{(n+1)} - \phi^{(n)}}{\Delta t}$

$$\boxed{\textbf{BDF}_2 \quad \frac{\partial \phi^{(n)}}{\partial t} = \frac{3}{2\Delta t}\phi^{(n+1)} - \frac{2}{\Delta t}\phi^{(n)} + \frac{1}{2\Delta t}\phi^{(n-1)}}$$

If we consider the weak form of the diffusion equation with $\textbf{BDF}_1$, we obtain a backward Euler formula. The diffusion equation written such that

$$\int_\Omega (\kappa\nabla\phi^{(n+1)}\nabla v + c_e\mu_a\phi^{(n+1)}v) + \int_\Omega \frac{\phi^{(n+1)} - \phi^{(n)}}{\Delta t}v + \int_{\partial\Omega} \frac{1}{2\text{A}}\phi^{(n+1)}v = \int_\Omega fv \, , \qquad (5.2.3)$$

or after rearranging terms,

$$\int_\Omega (\kappa\nabla\phi^{n+1}\nabla v + c_e\mu_a\phi^{(n+1)}v) + \int_\Omega \frac{\phi^{(n+1)}}{\Delta t}v + \int_{\partial\Omega} \frac{1}{2\text{A}}\phi^{(n+1)}v = \int_\Omega fv \, + \int_\Omega \frac{\phi^{(n)}}{\Delta t}v \, . \qquad (5.2.4)$$

The library Feel++ framework can manage this kind of methods. The listing 5.5 shows a sample of code demonstrating how to create a BDF object using the framework for the forward problem.

Listing 5.5: Example of code sample which shows how to create a BDF object and handle the time loop.

```
1  auto mesh = loadMesh( _mesh=new Mesh<Simplex<2>>);
2  auto Vh = Pch<1>( mesh );
3  auto u = Vh->element("u");
4
5  // We construct the bdf object (From 0 to T).
6  auto ts_fwd = bdf( _space=Vh, _name="ts_forward");
7  ts_fwd->start( u ); // init
8
9  // Assemble the bilinear form, we can construct the left hand side of the time
10 // dependent term. Here's an example of feel expression.
11 auto lhs_dt_expr = c1*idt( u )*id( v )*ts_fwd->polyDerivCoefficient( 0 )
12
13 // ...
14
15 for( ; not ts_fwd->isFinished(); )
16 {
17   // Update the linear form for the time dependent part in the
18   // right hand side.
19   auto rhs_dt_expr = ts_fwd->polyDeriv();
20
21   // ...
22
23
24   // next time step and shift u
25   ts_fwd->next( u ); // t(n) -> t(n+1), u(n) = u(n+1)
26
27   // The solution u(n+1) is saved on disk here!
28 }
```

Remark 29. *With the FEEL++ BDF framework, the solution is saved on the disk at each iteration. The I/O operation are performed in parallel thanks to MPIIO. This strategy is less memory consuming but has an impact on performance since we have to read from the file (in particular for restarting purpose, and especially in high order). Note also this strategy is useful to handle the source term of the fluorescence forward problem by avoiding to store all previous solution ϕ_x in order to compute the integral q_m (see (2.1.3).)*

For the inverse problem, it becomes more complex. We have to compute the adjoint of the diffusion detailed in (4.3.28). First, we have to solve the problem backward in time. Moreover, the source term of the equation depends on the solution of the forward problem. If we expand the time dependent term for $\textbf{BDF}_1$, the weak form reads

$$\int_\Omega (\kappa\nabla p^{n+1}\nabla v + c_e\mu_a p^{(n+1)}v) - \int_\Omega \frac{p^{(n+1)}}{\Delta t}v + \int_{\partial\Omega} \frac{1}{2\text{A}}p^{(n+1)}v = \int_\Omega (\phi^{(n+1)} - \phi_{obs}^{(n+1)})v - \int_\Omega \frac{p^{(n)}}{\Delta t}v \, . \quad (5.2.5)$$

The FEEL++ BDF framework is designed to save solution on disk remark 29 by forward iteration. We added the possibility to switch the direction of the BDF to iterate in reverse mode. In terms of development, we added the

possibility to retrieve the solution from BDF instance that have already saved the solution on the disk. We had to adapt the framework to avoid overwriting the saved solution and update the indexes to guarantee the read from the last time iteration t_N to the first t_0. Since we have to work with a different time stepping strategy for the adjoint equation, we have to introduce a new BDF object which is dedicated to the adjoint.

Remark 30. *The forward and adjoint equation have different backend, thus we can use different time stepping problem. In particular, it gives us the possibility to work with two different time grids for the forward problem and the adjoint problem. Since the adjoint is used mainly to compute the gradient, a smart strategy can be used to improve performances by using a coarse grid for the adjoint. It would impact only the quality of the descent direction $< \frac{\partial J(\kappa,\mu)}{\partial \kappa}, \delta \kappa >$ and $< \frac{\partial J(\kappa,\mu)}{\mu}, \delta \mu >$ (4.3.31) for the diffusion problem (see section 4.3) In that case, we still have to be careful since we have to guarantee that the times match for both time grids. Moreover, to compute the gradient, the time step chosen for the coarse grid has to be used for the finest one.*

The code sample listing 5.6 demonstrates how to reverse a BDF method to deal with the adjoint problem.

Listing 5.6: Example for the adjoint BDF time loop. In this example, we construct an observation from a forward solution

```
1  auto mesh = loadMesh( _mesh=new Mesh<Simplex<2>>);
2  auto Vh = Pch<1>( mesh );
3  auto u = Vh->element("u");
4  auto obs = Vh->element("obs");
5
6  // BDF iterations from 0 to T.
7  auto ts_fwd = bdf( _space=Vh, _name="ts_forward");
8  auto ts_obs = bdf( _space=Vh, _name="ts_observation");
9
10  // obs is constructed from one run of the forward solution for (k_d, mu_d).
11  // u is solved forward for (k, mu).
12
13  auto p = Vh->element("p");
14
15  // We construct the adjoint bdf object backward (From T to 0).
16  auto ts_inv = bdf( _space=Vh, _name="ts_inverse");
17  ts_inv->start( p ); // init
18
19  // Assemble the bilinear form, we can construct the left hand side of the time
20  // dependent term. Here is an example of expression for this term to be used in
21  // the expression of the integral.
22  auto lhs_dt_expr = c1*idt( p )*id( v )*ts_inv->polyDerivCoefficient( 0 )
23
24  // ...
25
26  // change BDF iteration from (0 to T) -> (T to 0).
27  ts_fwd->setReverse(true);
28  ts_fwd->start()
29
30  for( ; not ts_fwd->isFinished(),
31          not ts_inv->isFinished(); )
32  {
33    // We load the forward solution from the last saved file.
34    ts_fwd->loadCurrent(); // read and store.
35    ts_obs->loadCurrent(); // read and store.
36    auto u = ts_fwd->unknown(0); // access the element u.
37    auto obs = ts_obs->unknown(0); // access the element obs.
38
39    // Update the linear form for the time dependent part in the
40    // right hand side.
41    auto rhs_dt_expr = ts_inv->polyDeriv();
42
43    // The source term independent in time.
```

```
44   auto rhs_expr = ( idv(u) - idv(obs) ) * id(v);
45
46   // Solve the system here...
47
48   // next time step and shift u
49   ts_inv->next( p ); // t(n) -> t(n-1), p(n) = p(n+1).
50   // The solution p is saved for time t(n+1) on the disk here!
51
52   // Next time step. No shift!
53   ts_fwd->next(); // t(n) -> t(n-1)
54   ts_obs->next(); // t(n) -> t(n-1)
55 }
```

5.2.1 Disk I/O strategy

Currently, the framework use by default a disk Input/Output (I/O) approach in the sense that each function space element are saved into the hard drive disk. This method gives a solution for the fluorescence memory term. The memory cost is tranformed into a storage cost. Moreover, performances depend on read and write access capabilities of the available hardware, but also the installed file system. For example, we can expect faster simulation using Solid-State Drive (SSD) disk instead of classical Hard Disk Drive (HDD). Also file system impacts I/O performances (parallel file system General Parallel File System (GPFS), Lustre file system (LUSTRE), etc.). Solutions are save into a HDF5 format that allows easier parallel writing thanks to MPIIO operations.

As the BDF framework is used within FEEL++to solve the forward problem in time, it seemed natural for us to reuse this framework to solve the adjoint problem which is solved backward in time. In particular, we wished to keep the possibility to reuse the high order capability for the adjoint. Thus, the BDF framework has been adapted according to this requirement. Note that we have to be careful with file indexing, since we have to read the forward solution from a file (for the adjoint source term (4.3.28)), in parallel, but backward from the last save.

5.3 Efficient solvers

This section describes the different solvers used to solve the linear problem. We are interested more specifically to the multi-source case for eq. (2.1.1), since specific solvers can be used for problem with multiple RHS. The linear problem we desire to solve in parallel can be formulated such that

$$AX = B \tag{5.3.1}$$

with A the matrix associated to the bilinear form and B the right hand side is a matrix with N_s columns. The TR-DOT problem can be treated in different manners. Since the problem is weakly coupled, the forward linear system associated to the model (2.1.1) can be seen as two linear systems, one for the diffusion and one for the fluorescence, solved independently (and eventually in parallel using different Message Passing Interface standard (MPI) communicators). Since the fluorescence source term depends on the diffusion solution, we have either to store the memory term or to compute the RHS using the ODE introduced in chapter 2 be solved as a global system. A second possibility is to consider the global system, however this method introduces a memory cost while assembling the matrices which can be huge depending on the size of the problem.

5.3.1 Direct and iterative solvers

To solve the system (5.3.1) for the DOT problem case, iterative methods are considered. The advantage of these methods is to have a lower complexity per iteration compared to direct methods (Gauss elimination, LU Factorization (LU), Cholesky factorization, etc.) [25]. This method becomes competitive depending on the number of iteration required to to converge to the solution. Among the existing iterative methods, the conjugate gradient CG can be cited as an example. The CG method consists in minimizing the energy of the system (5.3.1). The generalization of this method so-called the Krylov methods, involves projections on specific Krylov subspaces which allows to construct approximation of the solution using simple operations Vector Matrix, scalar products, linear combination.

The PETSc library [26], on which the FEEL++ library relies on, provides a suite of sequential and parallel data structures and routines to be used within computation software for scalable solution (parallel). A wide range of efficient iterative solvers (CG, generalized minimum residual (GMRES), biconjugate gradient stabilized (BICGSTAB), etc.) [27] are available though PETSc [28]. The efficiency of these iterative solvers, in terms of convergence speed, depends on the condition of the matrix A. PETSc provides also a wide range of preconditionners, such as direct solver (LU, etc.), algebraic multigrid (gamg) , domain decomposition (Schwarz additif family), block preconditioning (Gauss-Seidle, Schur, etc.) to enhance the condition number of A. For the TR-DOT problem, algebraic multigrid preconditionner were used for the particular the 3D cases and which is well suited for parabolic problems. GMRES was used more specifically for 2D cases. These solvers can be tuned per problem (diffusion or fluorescence) thanks to the backend system mentioned in section 5.1

5.3.2 Multiple RHS solvers

We consider the multi-source problem (2.3.6) with $k \in [1, N_s]$ sources $N_s > 1$, explicited in the section 2.3. For simplicity, we drop the fluorescence part in the following section. To solve the multi-sources problem, we distinguish two methods. The naive way is to compute the forward solution iteratively for each source. The linear system to solve is $AX = B$ with A a diagonal matrix. Since A is the same for all sources, the matrix is assembled only once.

HPDDM   For solving this large scale problem with multiple right hight sides, an efficient method consists in solving each individual problem simultaneously. A framework for high-performance domain decomposition methods (HPDDM) was used [29, 30]. This library that provide several domain decomposition methods (RAS, ORAS, FETI, etc.) and obtained good performance results for microwave tomographic imaging problems [31]. In particular, this library recently proposed domain decomposition with memory recycling solver (Generalized Conjugate Residual method with inner Orthogonalization and Deflated Restarting method (GCRO-DR)) [32]. This solver is particularly interesting since in our case since only the RHS is changing for the source $k \in [1, N_s]$. FEEL++ provides an explicit interface for HPDDM, in the sense solvers are not accessible directly via the backend system. Thus an specific implementation has been made in order to use the HPDDM solvers.

PETSc   Another possibility for the multisource problem is to consider the RHS of (5.3.1) as a matrix of δ-Dirac sources. PETSc provides a solver for $AX = B$ problems with $A, X, B \in \mathcal{M}_{n,m}(\mathbb{R})$ where m the number of fibers and n the problem size (`MatMatSolve`)[26]. In particular, remark that if Krylov subspace (KSP) are used, the problem is solved iteratively column by column. A possibility is to use the parallel version of the direct solver SuperLU `SuperLU_Dist` can be used in order to handle the RHS simultenaously in parallel.

5.4   Level set method

We introduce in this section an algorithm developed to determine the location of the sources for the non contact and for arbitrary geometries. This algorithm is based on LSM, a method introduced into FEEL++ framework in a former phd thesis [33] for applications in rheology. We first gives an introduction to the LSM then explain our algorithm implementation in our framework.

5.4.1   LSM principle

The LSM is a method that has been successfully developed and used in the context of interface tracking over time. This interface is described by a levelset function equal to zero on the interface which separates two domains Ω_1 and Ω_2 and opposite sign value in each domain. Let $\Omega = \Omega_1 \cup \Omega_2$ the domain of study, we denote $\Gamma = \Omega_1 \cap \Omega_2$ the subdomain interface, and $\partial\Omega$ the boundary. To get a unit gradient value on the interface, we define the following smooth levelset function

$$\varphi(\boldsymbol{x}) = \begin{cases} \text{dist}(\boldsymbol{x}, \Gamma), & \boldsymbol{x} \in \Omega_1, \\ 0, & \boldsymbol{x} \in \Gamma, \\ -\text{dist}(\boldsymbol{x}, \Gamma), & \boldsymbol{x} \in \Omega_2, \end{cases} \tag{5.4.1}$$

which represents the distance function to the interface between the domains and such that

$$\text{dist}(\boldsymbol{x}, \Gamma) = \min_{y \in \Gamma}(|\boldsymbol{x} - \boldsymbol{y}|), \tag{5.4.2}$$

By definition, the levelset function has the gradient property

$$|\nabla \varphi| = 1. \tag{5.4.3}$$

The levelset function naturally owns the following interesting properties on the normal $\boldsymbol{n}$ to the interface and the curvature κ

$$\boldsymbol{n} = \frac{\nabla \varphi}{|\nabla \varphi|},$$

$$\kappa = \nabla \cdot \boldsymbol{n} = \nabla \cdot \left(\frac{\nabla \varphi}{|\nabla \varphi|} \right). \tag{5.4.4}$$

Remark 31. *Note that the advection equation (5.4.5) describes the evolution of the interface over time*

$$\partial_t \varphi + \boldsymbol{u} \cdot \nabla \varphi = 0, \tag{5.4.5}$$

with $\boldsymbol{u}$ is the velocity of the moving interface. We are interested in our case to the levelset function $\varphi(\boldsymbol{x})$ as a distance to the interface.

Remark 32. *A second remark regarding remark 31. For the DOT, the equation (5.4.5) might be used to follow the motion of mesh elements for sources and detectors for unsteady geometries over time. Note that since measurements are performed over time, we might have to take into account this motion for specific study case such as living beeing breath (even under anesthesia). Then the velocity field $\boldsymbol{u}$ can be determined from the boundary surface measurement over time via the conoscope for instance.*

5.4.2   LSM reinitialization and Fast marching method

The levelset function defined in (5.4.1) does not conserve the property (5.4.3) as a signed distance function after transport and depending on the velocity field (Typically, isosurfaces can accumulate). For that case, we have to be able to reinitialize the levelset function to a distance function. There exists several methods [33] such as the advection by extended velocity, the interface local projection or by solving the Hamilton Jacobi problem. Another method is the Fast Marching Method (FMM) which defines a way to iterate efficiently over the Degree of freedom (DOF) updating the visited point only once. First we have to initialize the function as explained in algorithm 1. The idea is to select points where the distance is known. We mark them as accepted. Then we find their neighbor points from which we compute their relative distance. This distance is stored in a heap.

> **Data:** $\varphi(x_i)$ known for x_i points $i > 0$
> **Result:** $\tilde{\varphi}(\boldsymbol{x})$ in ordered heap
> **1** accept ;
> **2** far ;
> **3** close ;
> **4 forall** x_i **do**
> **5** $\quad$ accept $\leftarrow x_i$;
> **6 end**
> **7** /* select *close* and *far* points */
> **8 forall** $x_j, \; j \neq i$ **do**
> **9** $\quad$ **if** $dist(x_j, x_i) < \varepsilon$ **then**
> **10** $\quad\quad$ close $\leftarrow x_j$;
> **11** $\quad$ **else**
> **12** $\quad\quad$ far $\leftarrow x_j$;
> **13** $\quad$ **end**
> **14 end**
> **15 forall** x_j *in close* **do**
> **16** $\quad$ close $\leftarrow \tilde{\varphi} = \text{dist}(x_j, x_i)$;
> **17 end**
> **18** /* lowest value is at top */

Algorithm 1: FMM init

Then we can proceed with the fast marching procedure detailed in the algorithm 2. The choice of using an ordered heap to store the computed distance impact the performance of the algorithm.

Data: initialized arrays *accept*, *far*, and heap *close* (algorithm 1)
Result: $\tilde{\varphi}(\boldsymbol{x})$

1 **while** x_j *in close* **do**
2   x = front(close) /* minimum */ ;
3   close →x ;
4   accept ←x ;
5   **forall** x_j *in far* **do**
6   **if** $dist(x_j, x) < \varepsilon$ **then**
7   close ←x_j ;
8   **end**
9   **end**
10   **forall** x_j *in close* **do**
11   close ←$\tilde{\varphi} = \text{dist}(x_j, x_i)$;
12   **end**
13 **end**

Algorithm 2: FMM procedure

The algorithm has a complexity of order $O(N)$. The current FEEL++ used $\mathbb{P}^1$ elements. For high order, the current implementation creates a $\mathbb{P}^1$ space from $\mathbb{P}^n$, proceed with the fast marching, then execute the inverse operation.

In our context and as an extension of the method, we can compute a distance function from the boundary using the FMM approach. For that purpose, we have to initialize the interface on the boundary where the points with a known distance are located on the interface (distance 0). In particular, this approach let efficiently computes this distance function for complex geometries.

The levelset FEEL++ framework can be found under the official FEEL++ repository in the *feel/feells* directory. The listing 5.7 gives an short code example of how to build a distance function from the wall.

Listing 5.7: Example of interpolator usage

```
// Construct the space from a mesh for a given dimension and a geometric order.
auto Lsh = ls_space_type<DIM,G_ORDER>::New( mesh );
// Create a function for the fast marching.
auto phio = Lsh->element();
// We initialize the interface on the boundary by setting different signs on the
// boundary
phio = vf::project( Lsh, markedelements(mesh(),"Omega"), h());
phio += vf::project( Lsh, markedfaces(mesh(),"Wall"),
        -idv(phio) - h()/100 );
// Then we call the fast marching procedure.
auto phi = thefms->march(phio);
```

In the section 5.4.3, we demonstrate how to use this distance function to create new iterators on elements and retrieve the N_f sources and detectors located in the mesh and on the boundary for the contact and non contact mode. The fig. 5.4.1 shows an example of distance function from the boundary computed on a complex geometry.

Figure 5.4.1: This figure shows the levelset reinitialized as distance function from the boundary on a complex geometry (frog).
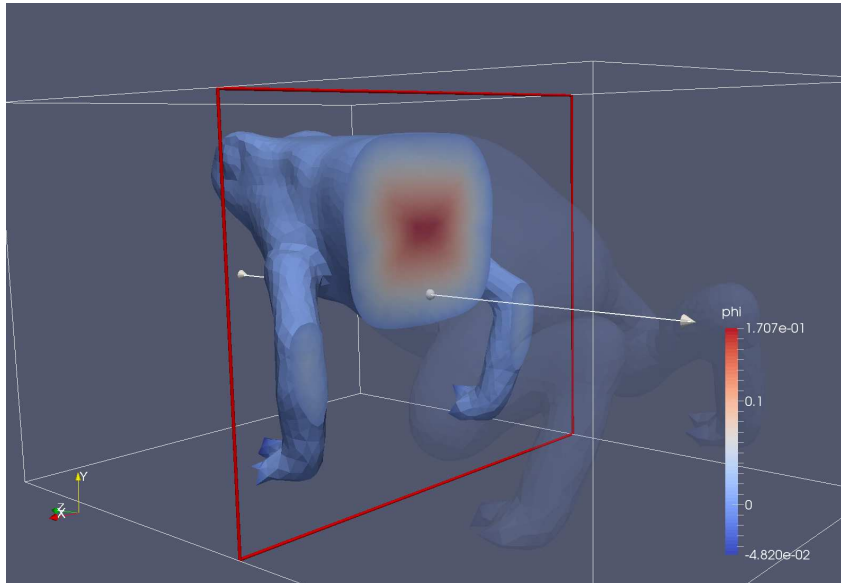
5.4.3 LSM application to non contact

In this section, the difference between the contact and non-contact mode from a numerical point of view is detailed. An algorithm is proposed to handle the non contact mode for complex geometries. The strategy consists in retrieving a family of mesh elements for the $k \in [1, N_s]$ sources and $d \in [N_d]$ detectors. Note that if N_f is the number of fibers, then the best configuration for the current setup is when $N_d = N_f - 1$ (1 fiber is a source and all other fibers area in detection mode). In practice, due to a limited number of equipments (diodes and detectors), the number of detectors was chosen $N_d = 7$ for practical reasons section 1.1.

Contact In contact mode, the fiber is set directly on the boundary of the domain (the skin), then the measurement is pointwise on the boundary. Thus, if the contact point is a mesh node, one has to determine the corresponding DOF in the DOF table. If the point is located in a mesh element, then we would have to interpolate. The source has to be defined in the geometry section 2.1, therefore we have to take into account this constraint while generating the mesh for the N_s sources. To avoid to interpolate and introduce an error on the source remark 33, we will define N_d points in the geometry (See fig. 5.4.2a) at the mean free path distance (See remark 3).

Remark 33. *An error on the source can have potentially a non neglectible impact on the inverse problem solution since the error which affects the quality of the forward solution is propagated in the adjoint equation via the source term.*

The fig. 5.4.2 gives an example of mesh generated with GMSH on a cylinder where the sources have been set as geometrical points in the 2D/3D geometry. These points are taken into account as mesh nodes in the mesh generation process. Note that for more complex geometries, determining this points location is more difficult. For that purpose, we will then use the non contact algorithm detailed hereafter.

Non-contact For the non contact, the measurement is not anymore pointwise and we have to take into account all the areas located in the cone of vision of the N_f fibers. The sources are located inside the domain Ω, like for contact measurement, at a distance corresponding to the mean free path. The viewed elements are located in the fiber cone of vision. For the detectors, as explained in section 2.1, the photon counting is made from an estimation of the number of photons that are seen by the fiber in detection mode. Thus, we consider only the area on the boundary domain $\partial\Omega$, but restricted to the fiber cone of vision. From a numerical view point, we retrieve $F \in \mathcal{F}_\delta^b$, the elements at a distance $\frac{1}{\mu_s'}$. The scheme fig. 5.4.3a represents the non-contact problem. Then the RHS source term can be assembled either by setting exactly the δ-Dirac value in the RHS vector or by projecting

Figure 5.4.2: This figure shows different type of cylinder meshes realised for contact measurements in 2D and 3D. The red points on the mesh boundary denotes the differents detecting areas for the N_s fibers. The red points inside the geometry denotes the N_s source where the δ-Dirac is set. The distance from the boundary is parametrized, thus can be evaluated during the program initialization.
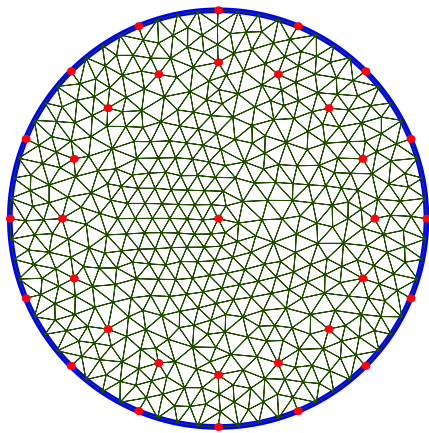
(a): Mesh $\mathcal{T}_h$ in contact mode.
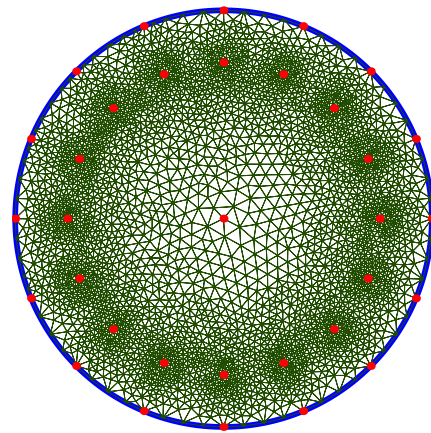
(b): Refine mesh $\mathcal{T}_h$ around sources in contact mode.
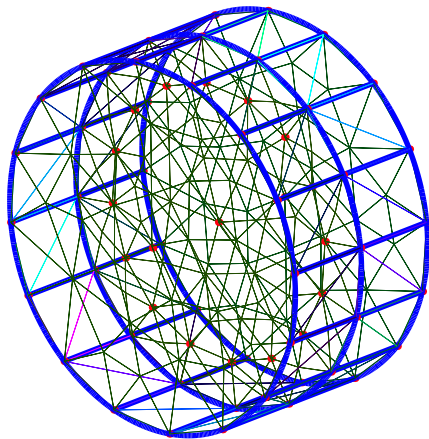
(c): Mesh $\mathcal{T}_h$ in contact mode.
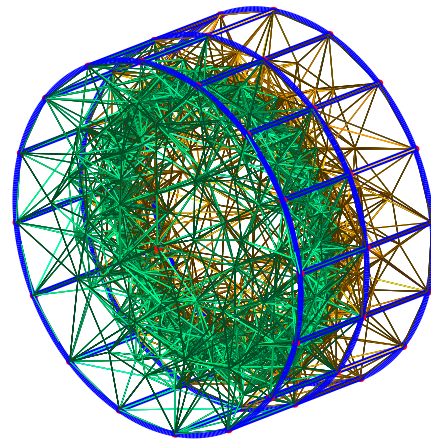
(d): Refine mesh $\mathcal{T}_h$ around sources in contact mode.

a regularized δ-Dirac version on the corresponding source elements instead of performing a projection on the whole space which is less efficient.

From a theoretical view point, we should consider the $d-1$ dimension surfaces F_s, F_d for the source and the detectors. If these surfaces are part of the mesh $F_s \in \mathcal{F}_\delta^i$, $F_d \in \mathcal{F}_\delta^b$ then, as for the contact mode, we can assemble the RHS by setting the value exactly (fig. 5.4.3b). Else if $F_s \notin \mathcal{F}_\delta^i$ and $F_d \notin \mathcal{F}_\delta^b$ then we have to interpolate the $d-1$ source mesh entities to assemble the RHS. In practice, it is difficult to generate numerically a mesh with these inner lines or surfaces. It introduces a strong constraint on the mesh since they are located very close to the domain boundary. Moreover, it becomes even more complex for non simple geometries. The fig. 5.4.3 gives

Figure 5.4.3: This figure shows a scheme which represent non contact measurements with the cone of vision for the kth fiber denoted F_k and an example of mesh generated in 2D containing the 1D lines for the N_s sources.

(a): Scheme for the non contact measurements. The red areas Σ_0^k denotes the source when the kth fiber is a source in non contact. The green area Σ_d^k denotes the fiber view on the boundary where the measure is taken (see table 4.2.1)

(b): This figure shows a 2D mesh $\mathcal{T}_h$ with submeshes $\mathcal{T}_h^s$, $\mathcal{T}_h^d$ for the sources and the detectors. The red points delimits these submeshes. The inner blue lines represents the sources whereas the detectors are the delimited lines on the boundary.

an example of meshing for a 2d disk where the blue thick lines represents geometry curves and red points, also inside the geometry, delimitate the N_f detectors on the boundary and the N_s sources in the domain.

Instead of adding a geometrical constraint on the mesh, we propose hereafter a method to handle the non contact measurement based on the levelset methods and the marker feature detailed in the section 5.1. Let us introduce some notations. We denote $\mathcal{C}^k$ the cone of vision for the kth fiber. We denote $T_s^i := \{K \in \mathcal{T}_\delta \mid K \subset \Omega_\delta \cap \mathcal{C}^i\}$ and $T_d^j := \{K \in \mathcal{T}_\delta \mid \partial K \subset \partial \Omega_\delta \cap \mathcal{C}^i\}$ two sets of N_f mesh partitions depicting respectively the $i \in [1, N_f]$ source areas and the $j \in [1, N_f]$ detectors areas. The key idea of the proposed method is to be able to construct numerically these sets. Then build iterators on elements of the mesh to perform different mathematical operations, but only on these elements of interest.

From a numerical view point, for simple geometries, the sources and detectors elements can be constructed directly as geometrical element entities (fig. 5.4.4a). In that case, we can set the δ-dirac function exactly on the DOF corresponding to the physical lines for the RHS of our problem (2.1.1). The fig. 5.4.3b gives an example of construction using GMSH and the associated Delaunay mesh for an arbitrary mesh size. For more complex geometries this type of construction becomes more difficult. Moreover, in practice, the real tomograph acquires a cloud point of the surface of the object. Then we proceed first to a surface reconstruction before extending meshing to the 3D volume. In that case, the mesh is used directly and the different source can not be determined in a parametric manner.

The algorithm 3 describes the method to retrieve the mesh elements for the sources. Therefore we wish to be able to retrieve a positive function only if $||\phi - \frac{1}{\mu_s'}||^2 \le h^2/4$ The algorithm 5 describes the methods for the boundary.

Figure 5.4.4: This figures represents 2D meshes and the different ways to handle the non contact sources, when the source are submeshes, are interpolated meshes or elements crossed by the source areas.
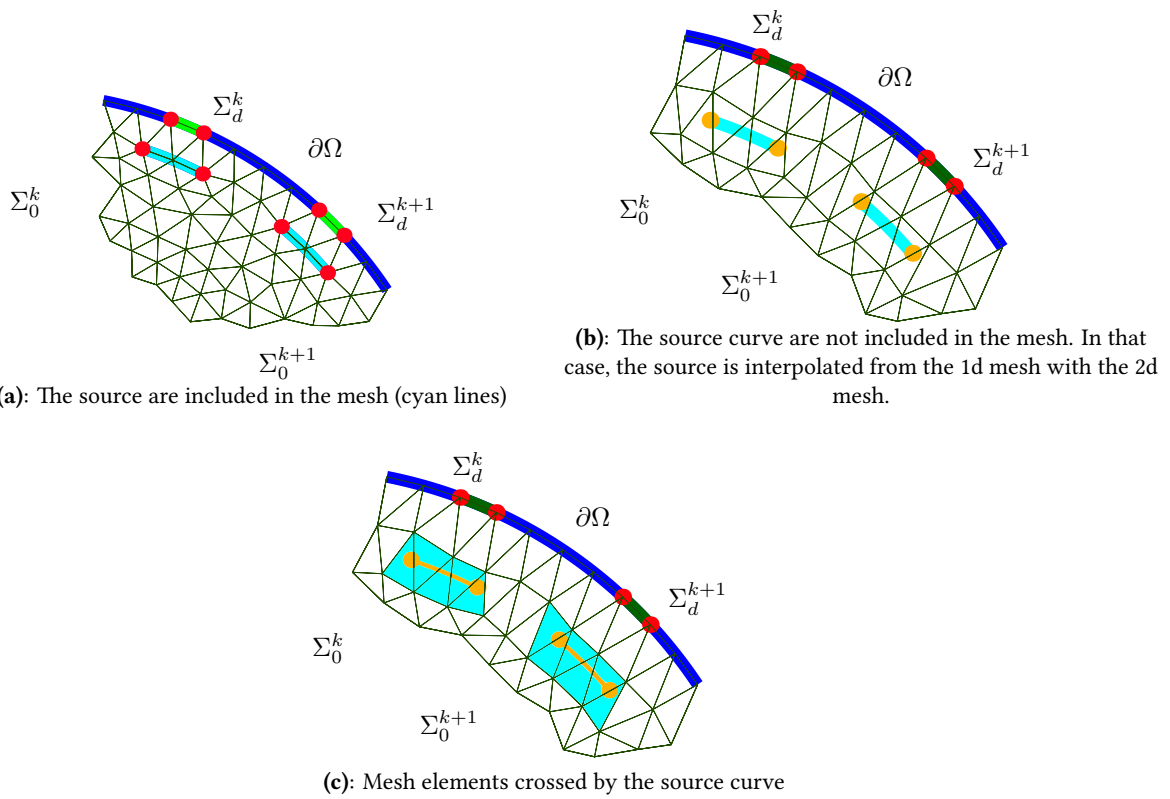
(a): The source are included in the mesh (cyan lines)

(b): The source curve are not included in the mesh. In that case, the source is interpolated from the 1d mesh with the 2d mesh.

(c): Mesh elements crossed by the source curve

Data: Mesh $\mathcal{T}_h$
Result: FEEL++ marker for the N_s sources
1 create φ_0 $\mathbb{P}_1$ function positive if $x \in \Omega$, negative if $x \in \partial\Omega$;
2 initialize the levelset φ, $\mathbb{P}_1$ with φ_0 ;
3 FMM to reinitialize to a distance function φ ;
4 project *ring* $\in \mathbb{P}_0 \rightarrow$ mesh elements ;
5 create a FEEL++ *marker2* $\leftarrow$ inner *ring*;
6 project levelset normals (5.4.4) $\rightarrow$ inner *ring* (*marker2*) ;
7 **forall** *k source* **do**
8   project k^{th} *cone* $\in \mathbb{P}_0 \rightarrow$ inner *ring* (*marker2*);
9   project *near* $\in \mathbb{P}_0 \rightarrow$ inner *ring* (*marker2*) ;
10   project *indexes* = k*cone*near $\rightarrow$ inner *ring (marker2)* ;
11 **end**
12 update the FEEL++ *marker2* $\leftarrow$ *indexes* ;
13 **forall** *k source* **do**
14   update *marker2* names $\rightarrow$ "source-k" ;
15 **end**

Algorithm 3: Mesh element marker construction for sources in non contact

Data: Mesh $\mathcal{T}_h$
Result: FEEL++ marker for the N_s sources
1 create φ_0 $\mathbb{P}_1$ function positive if $x \in \Omega$, negative if $x \in \partial\Omega$;
2 initialize the levelset φ, $\mathbb{P}_1$ with φ_0 ;
3 FMM to reinitialize to a distance function φ ;
4 create a FEEL++ *marker2* $\leftarrow$ *ring*;
5 project levelset normals (5.4.4) on the *ring* (*marker* boundary elements) ;
6 **forall** *k source* **do**
7   project k^{th} *cone* $\in \mathbb{P}_0 \rightarrow$ *ring* (*marker* boundary elements);
8   project *near* $\in \mathbb{P}_0 \rightarrow$ *ring* (*marker* boundary elements) ;
9   project *indexes* = k * *cone* * *near* $\rightarrow$ *ring* (*marker* boundary elements) ;
10 **end**
11 update a FEEL++ *marker2* $\leftarrow$ *indexes* ;
12 **forall** *k source* **do**
13   update *marker3* names $\rightarrow$ "detector-k" ;
14 **end**

Algorithm 5: Mesh element marker construction for sources in non contact

Figure 5.4.5: This figure shows a clip representation of mesh and volume representation of the elements for $N_s = 16$ sources on a sphere when the simulation has to be performed in non contact mode. The colors define the fiber identifier. The fig. 5.4.4c shows a scheme representing in 2D and the process to select these elements.
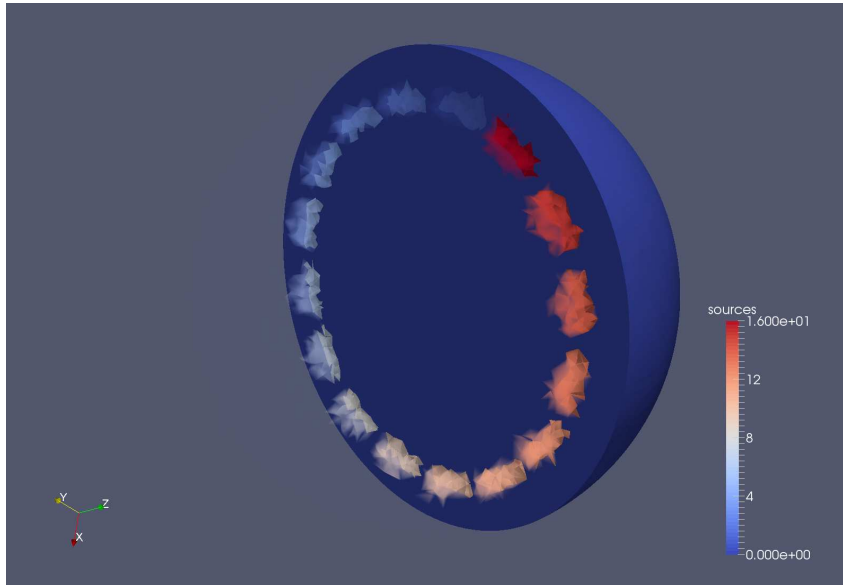
Figure 5.4.6: This figure shows the 3d volume representation of elements selected to be the N_s sources seen in fig. 5.4.5 the diffusion problem
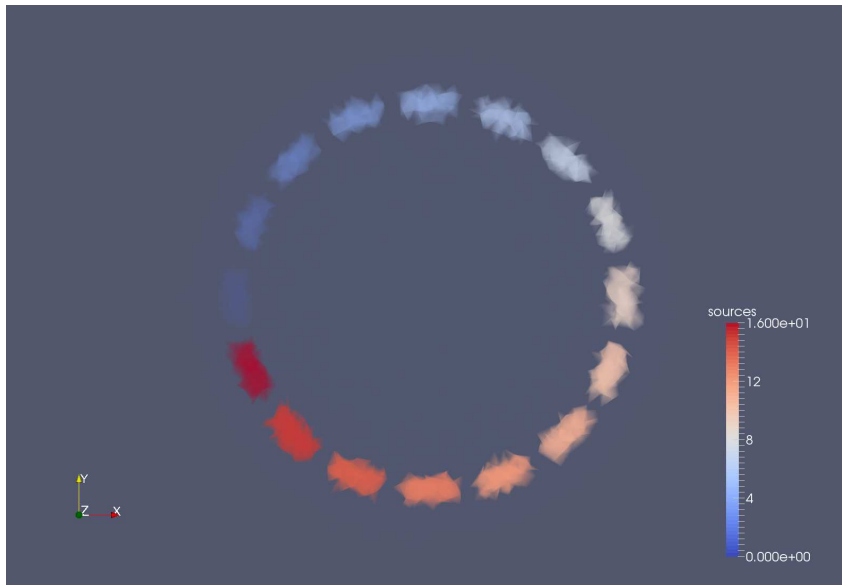
Figure 5.4.7: This figure shows the 3d volume isometric representation of elements selected to be the N_s sources seen in fig. 5.4.5 the diffusion problem.
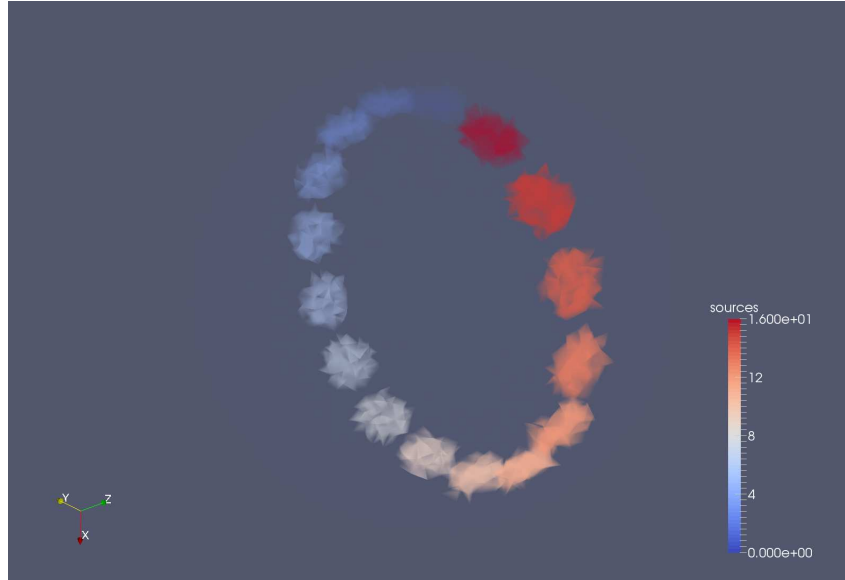
Figure 5.4.8: Similar to the sources, this figure shows a mesh with boundary elements used for the detectors to perform the measurement. The color define the index of the fiber. The algorithm is described in algorithm 5. Remark that the solution of the diffusion and fluorescence problem is evaluated at these areas as a weight function.
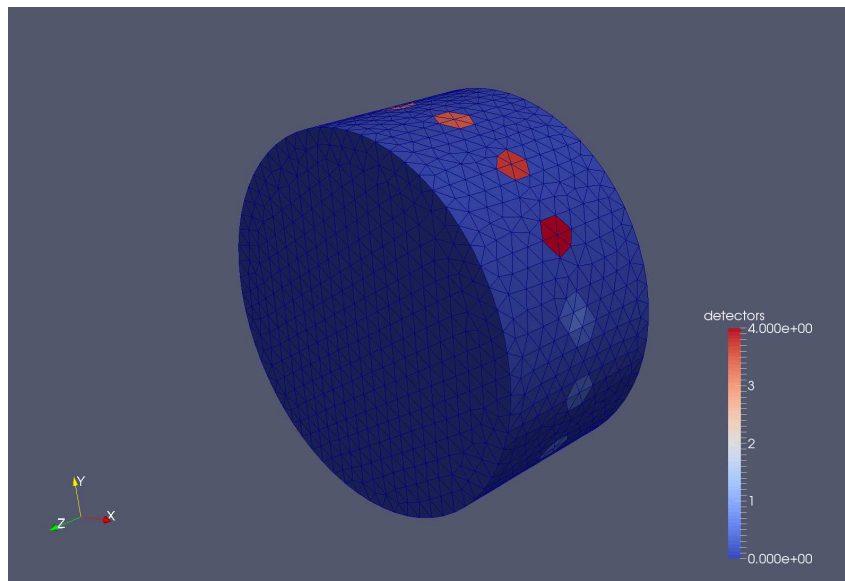
Figure 5.4.9: Similar to figure fig. 5.4.1, this figure represents both the levelset (in a clip view) and the different sources determined from the levelset function and the fiber cone of vision. The different volume areas displayed represent the sources. The color associated to these volume areas represent the index of the fiber in the measuring section. The algorithm used is detailed in algorithm 3.
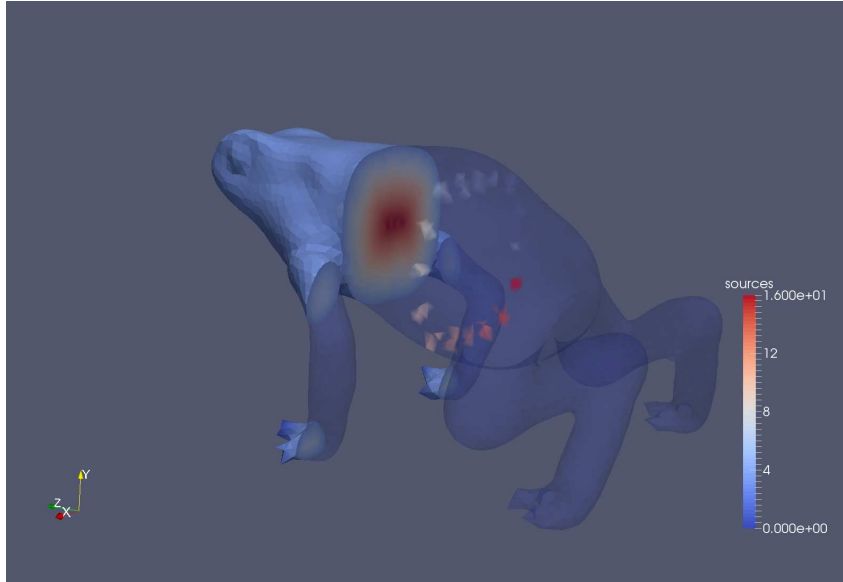
5.5 Optimization tools

The FEEL++ library interfaces several libraries specialized in opmitization. We can cite for example IPopt [34], NLopt. There exists also a library the TAO library provided with PETSc which implements different parallel solvers for optimization problems. The TAO library is built upon PETSc data structures. These libraries provide several methods to solve optimization problems. There are derivative-free methods, gradient based methods, local and global optimizers. In order to use these libraries, we have to provide via our code different implementation. Currently, FEEL++ does not provide a generic interface for optimization libraries such as the one presented at the beginning of this section. This is one of the expected developments to be realized in the future remark 34.

We focus in this section mainly on IPopt which is based on interior point optimization. One of the main advantage of relying on such library is to have access to a wide range of solvers. Therefore, having an Ipopt implementation for the reconstruction enables the access to these solvers. Furthermore, we have the possibility to tune these solvers depending on the FEEL++ testcases we are studying.

Remark 34. *Note that using an existing optimization library greatly improves the robustness of our codes. Indeed, since these libraries are widely used by the scientific community, they are less prone to bugs than a custom implementation. We mention also that one of the possible future feature for FEEL++ would be to provide a generic interface for optimization tools and rely on the backend system to select the prefered tool. This perspective would also enable the possibility to cross-validate optimization methods, either provided by different library, or our custom implementation for a specific method.*

We provide an implementation of the inverse problem based on IPopt. IPopt provides several type of linear solver. Most of the parallel solvers available are multithread based. IPopt provides a sequential version using Multifrontal Massively Parallel sparse direct Solver (MUMPS). There exists some developments using a parallel version of MUMPS, which can be seen on the "parallel" branch of the official GitHub repository (coin-or/Ipopt), but the development seems to be currently frozen. Since the core of the FEEL++ library parallelism is based on MPI, it seemed natural to reuse the mumps version of the library within IPopt. IPopt is currently provided within FEEL++ as a forked submodule of the official repository which has been patched to handle the MUMPS parallel MPI communicator. Since FEEL++ application is written in the C++ language, then the IPopt API written in C is used directly within our application. In order to use a NLP solver of the IPopt library we have to provide several information to the library such as the objective function, the gradient of the objective and eventually a second order derivative. Depending on the data sample and as described in the chapter 4, we choose a well adapted cost

function to solve the inverse problem based on an adjoint method. With regards to the section 4.2, computing the solution of the state equation and the adjoint equation let us determine the gradient of the objective function.

To work with IPopt, our current strategy consists in solving in parallel the linear systems for the forward problem described in chapter 2, the adjoint described in chapter 4 and to compute the gradient thanks to PETSc solvers (gamg) and interfaced in FEEL++ or using a memory recycling Krylov solver such as GCRO-DR provided by HPDDM. Then the optimization problem in sequential on every MPI process. Eventually, we could use an

Figure 5.5.1: This figure gives an example of partitioned domain Ω and the parallel operations realized.

(a): All scatter/gather operations for the diffusion finite element field into a sequential vector. The colors represents the 2 partitions.

(b): Example of a domain Ω partitioned in two parts 1 and 2 with local and global indices. The colors represents the 2 partitions.
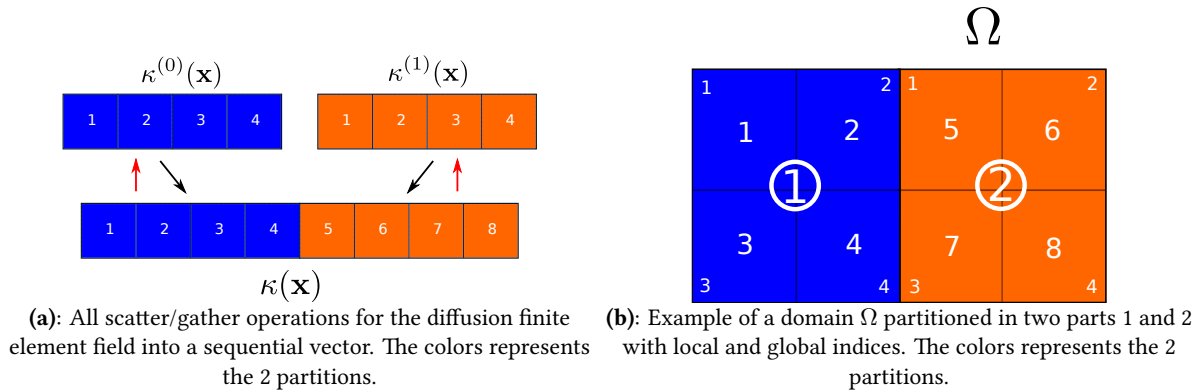
hybrid method and solve the minimization problem using a multithreads solver such as PARDISO Project for example. Since we solve the minimization problem in sequential, we have to deal with the parallel information on the state and adjoint solution and update the finite element fields regarding the parameters κ, μ. In practice, we have an all-gather operation to retrieve local dofs into a sequential petsc vector. Then IPopt operates on the underlying C array of this petsc vector. Then a "all-scatter" operation is performed to push back the new computed parameter into the local arrays. The fig. 5.5.2 and fig. 5.5.1 schematizes these operation and listing 5.8 This choice is questionable since we introduce new communications performed each time we have to update the

Figure 5.5.2: This figure schematize the process for a IPopt usage for parallel FEEL++ applications. The underlying container of the finite element fields κ, μ are gathered in sequential Petsc vector. Ipopt optimize the parameters using this vector underlying array then push back the updated value to the local petsc MPI vector.
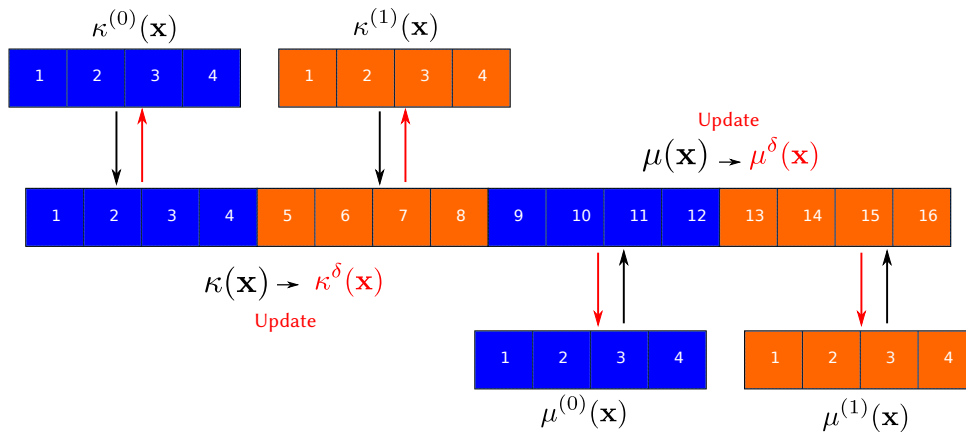
coefficients κ and μ and the gradient of the objective function over these two parameters. Moreover the whole sequential vector has a memory cost since we duplicate it for every process. Note that since the global vector is present on every process, the scatter operation used in our code perform a local copy only.

Remark 35. *Remark we could have created the sequential on the master process only, but we would have to deal with different communicators for the state/adjoint problems and the optimization problem. This mean we should have a better interface in order to tune the Ipopt MPI communicator.*

Using this strategy suggests that we have to adapt the size of the problem to have enough gain more performance with the FEEL++ linear solvers compared to the cost of the communication and the memory.

Listing 5.8: Example showing how to retrieve a petsc vector from the FEEL++ finite element field

```
1  auto mesh = loadMesh(_mesh=new Mesh<Simplex<2>>);
2  auto Xh = Pch<0>( mesh );
3  auto Xh = Pch<0>( mesh );
4  auto k = Xh->element();
5  auto mu = Xh->element();
6
7  // Transform k underlying container to a petsc MPI vector.
8  auto k_local = toPETScPtr( k.container() )->vec();
9  auto mu_local = toPETScPtr( mu.container() )->vec();
10
11 // Petsc sequential vector
12 Vec k_global;
13 // We create a petsc context for allgather/allscatter operation.
14 VecScatter ctx;
15 VecScatterCreateToAll( k_local, &ctx, &k_global )
16
17 double* k_array;
18
19 // Gather all the global vector to all process.
20 VecPlaceArray( k_global, k_array );
21 VecScatterBegin( ctx, k_local, k_global, INSERT_VALUES, SCATTER_FORWARD );
22 VecScatterEnd( ctx, k_local, k_global,  INSERT_VALUES, SCATTER_FORWARD );
23 VecResetArray( kPetscGlobalVecSeq );
24
25 // NLP Ipopt work on the k_array directly. The petsc vector is updated by Ipopt,
26 // the parallel operation are handled by petsc.
27
28 // Copy back to the local vector (no gather, no comm).
29 VecPlaceArray( k_global, k_array );
30 VecScatterBegin( ctx, k_global, k_local, INSERT_VALUES, SCATTER_REVERSE_LOCAL );
31 VecScatterEnd( ctx, k_global, k_local,  INSERT_VALUES, SCATTER_REVERSE_LOCAL );
32 VecResetArray( kPetscGlobalVecSeq );
33 // Update ghosts
34 k_local->localize();
```

This implementation is clearly for prospective purpose for FEEL++ application performing this type of reconstruction with ipopt in parallel. We should certainly favorized in the future parallel optimization libraries such as TAO for production codes, or implement a selected algorithm using the FEEL++ language directly.

Still, we have a nice framework to test our code within FEEL++. Ipopt options can be passed though the FEEL++ option system as shown in listing 5.9 to test our problem in 2D/3D for different functions spaces in parallel and tuning the Ipopt solvers.

Listing 5.9: Example showing how to use ipopt option via the FEEL++ option system

```
1  ./reconstruct --ipopt.barrier.mu_strategy=adaptative \
2               --ipopt.termination.tol=1e-8 \
3               --ipopt.solver.linear_solver=mumps #ma27 (ipopt default)
4
5  # Display all ipopt options:
6  # ./reconstruct --help-lib | grep "ipopt."
```

The fig. 5.5.3 shows an example of resolution for the parameters precised in table 5.5.1 for the testcase presented in section 4.4.

In terms of perspectives, an interesting feature would be to add the automatic differentiation to compute directly the adjoint in a generic manner.

Table 5.5.1: Model parameters for the simulation with one inclusions presented in fig. 5.5.3. The diffusion κ is deduced from the absorption μ_a and reduced scattering μ'_s. Also the fluorochrome coefficient Γ is computed from the model (See chapter 1)

parameter	description	background	inclusion 1
κ_d	observation	0.5	0.2
μ_d	observation	0.1	0.05
κ_0	init	0.5	0.5
μ_0	init	0.1	0.1
μ_{min}	min bound	0.001	0.1
μ_{max}	max bound	2.0	0.1
κ_{min}	min bound	0.01	0.1
κ_{max}	max bound	2.0	0.1

Figure 5.5.3: Diffusion problem 2D reconstruction on the testcase described in section 4.4 and using Ipopt. This time only one inclusion is added with different optical properties from the background for both diffusion and absorption parameters. We use an adaptative strategy for the line search μ barrier. Parameters are detailed in table 5.5.1. This figure shows at the bottom and on the left the observed diffusion parameters κ_d and the right one the absorption μ_d. The top row shows the computed parameters for the diffusion κ and the absorption μ after 22 optimization steps. As we can see, the solution obtained for the diffusion parameter κ seems to provide better results. However this is still not the case for the absorption μ compared to the testcase in fig. 4.4.2.
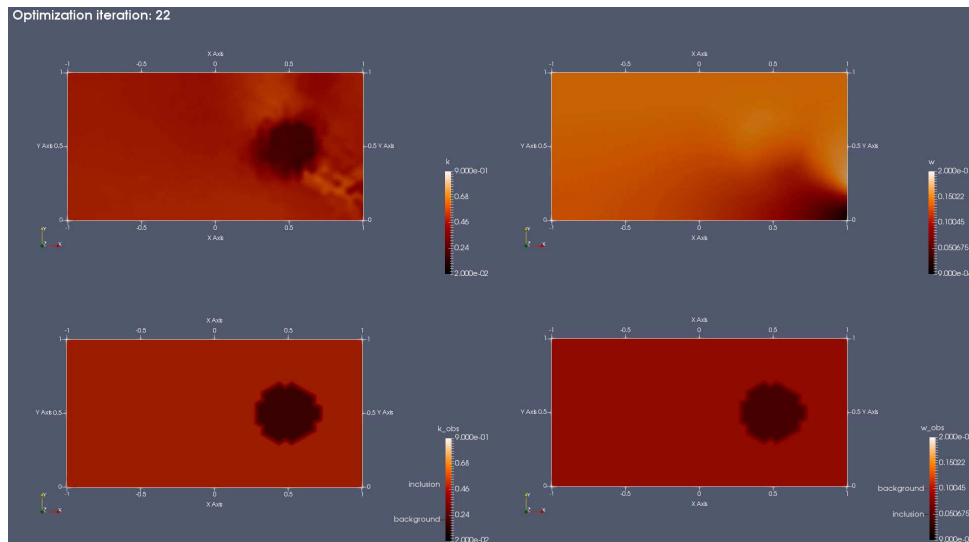
5.6 Conclusion

In the section 5.1, several components of the FEEL++ library used to solve the TR-DOT problem have been presented. The state and adjoint equations are solved in time using a BDF method. In the section 5.2, the adaptation made to the FEEL++ BDF framework has been detailed. These adaptations prepare the framework to handle the adjoint problem which is solved backward in time. The strategy used to handle the memory term of the fluorescence equation is based on I/O operations on hard drive disk. A perspective is to consider the ODE introduced in section 2.1 instead of relying on the BDF framework directly. Thus, we would transform the storage cost (on disk) into a computing cost. The section 5.3 introduces different solvers used within our testcase and adapted for the 2d and 3d cases. In particular, some specific solvers for multiple RHS problems have been presented and tested via the HPDDM library. In the future, we would like to adapt the FEEL++ interface for HPDDM in order to provide a more integrated solution.

To handle non contact measurements numerically, an algorithm has been suggested in section 5.4. This algorithm is based on the LSM and a FMM algorithm. It allows us to retrieve the mesh elements located close to the boundary of the domain $\Omega \in \mathbb{R}^d$ and used to set the δ-Dirac sources element-wise. A possible improvement would be to extract from the levelset, reinitialized as a distance function, a mesh of dimension $\mathbb{R}^{d-1}$ for the sources. Then verify the convergence results for the non-contact case presented in section 2.3.4, therefore working with different mesh (An interpolation error on the source would be introduced for the worst scenario). The section 5.5 finally details the different optimization tools used within the FEEL++ implementation. In particular, the IPopt library adaptation is presented to be used with the FEEL++ MPI parallel environment. As a perspective, we would like to provide a more generic interface for optimization problem in the future. This interface would wrap existing library such as IPopt, NLopt or TAO.

References

[22] Christophe Prud'Homme, Vincent Chabannes, Vincent Doyeux, Mourad Ismail, Abdoulaye Samake, and Gonçalo Pena. "Feel++: A computational framework for galerkin methods and advanced numerical methods". In: *ESAIM: Proceedings*. Vol. 38. EDP Sciences. 2012, pp. 429–455.

[23] Cecile Daversin - Catty. "Reduced basis method applied to large non-linear multi-physics problems : application to high field magnets design". Theses. Université de Strasbourg, Sept. 2016. URL: https://tel.archives-ouvertes.fr/tel-01361722.

[24] Stephane Veys. "A computational reduced basis framework : applications to nonlinears multiphysics problems". Theses. Université de Grenoble, Nov. 2014. URL: https://tel.archives-ouvertes.fr/tel-01525889.

[25] Alfio Quarteroni and Silvia Quarteroni. *Numerical models for differential problems*. Vol. 2. Springer, 2009.

[26] Satish Balay, Shrirang Abhyankar, Mark F. Adams, Jed Brown, Peter Brune, Kris Buschelman, et al. *PETSc Users Manual*. Tech. rep. ANL-95/11 - Revision 3.9. Argonne National Laboratory, 2018. URL: http://www.mcs.anl.gov/petsc.

[27] Yousef Saad. *Iterative methods for sparse linear systems*. Vol. 82. siam, 2003.

[28] Satish Balay, William D. Gropp, Lois Curfman McInnes, and Barry F. Smith. "Efficient Management of Parallelism in Object Oriented Numerical Software Libraries". In: *Modern Software Tools in Scientific Computing*. Ed. by E. Arge, A. M. Bruaset, and H. P. Langtangen. Birkhäuser Press, 1997, pp. 163–202.

[29] Victorita Dolean, Pierre Jolivet, and Frâdâric Nataf. *An introduction to domain decomposition methods: algorithms, theory, and parallel implementation*. Vol. 144. SIAM, 2015.

[30] Pierre Jolivet, Frédéric Hecht, Frédéric Nataf, and Christophe Prud'homme. "Scalable Domain Decomposition Preconditioners for Heterogeneous Elliptic Problems". In: *Proceedings of the International Conference on High Performance Computing, Networking, Storage and Analysis*. SC '13. Denver, Colorado: ACM, 2013, 80:1–80:11. ISBN: 978-1-4503-2378-9. DOI: 10.1145/2503210.2503212. URL: http://doi.acm.org/10.1145/2503210.2503212.

[31] Pierre-Henri Tournier, Ioannis Aliferis, Marcella Bonazzoli, Maya de Buhan, Marion Darbas, Victorita Dolean, et al. "Microwave Tomographic Imaging of Cerebrovascular Accidents by Using High-Performance Computing". working paper or preprint. July 2016. URL: https://hal.archives-ouvertes.fr/hal-01343687.

[32] Pierre Jolivet and Pierre-Henri Tournier. "Block Iterative Methods and Recycling for Improved Scalability of Linear Solvers". In: *SC16 - International Conference for High Performance Computing, Networking, Storage and Analysis*. Proceedings of SC16: International Conference for High Performance Computing, Networking, Storage and Analysis. Salt Lake City, Utah, United States, Nov. 2016. URL: https://hal.archives-ouvertes.fr/hal-01357998.

[33] Vincent Doyeux. "Modeling and simulation of multi-fluid systems. Application to blood flows." Theses. Université de Grenoble, Jan. 2014. URL: https://tel.archives-ouvertes.fr/tel-00939930.

[34] Andreas Wächter and Lorenz T Biegler. "On the implementation of an interior-point filter line-search algorithm for large-scale nonlinear programming". In: *Mathematical programming* 106.1 (2006), pp. 25–57.

Conclusion

Thoughout this thesis, we have studied from a mathematical point of view the TR-DOT problem. The physical phenomena and the associated model are presented in chapter 1. The model is based on the diffusion approximation of the RTE. We consider the coupled problem with the fluorescence. One of the primary goal for the ICube/IMIS team when they suggested this project was to be able to propose solutions to solve the fluorescence problem with four parameters and perform reconstruction which was one of their blocking issue.

To tackle this problem, we have proposed an analysis of the forward problem chapter 2 first with a new implementation of the forward code based on the FEEL++, a generic framework for PDEs developed by our research team at the Institut de Recherche Mathmatique Avancée (IRMA) laboratory (University of Strasbourg (UDS)) and written in C++. This implementation adds new features unavailable in the existing Matlab code such as parallelism, high order methods in space and time, and the possibility to describe the reconstruction problem in 2D/3D in an almost seemless way. An other improvement is the code readability which has been greatly improved since the proposed programming language (DSEL) is close to the mathematical variational formulation. Thus, adding new regularization, modifying equations, or modifying the existing code should be simpler in the future. The forward problem correctness has been checked in section 3.1 thanks to cross-verification with the existing code first, then the diffusion problem has been validated with measurements taken from an homogeneous object. This essential step allowed us to find several bugs which are solved in both codes. Different solvers have been tested thoughout FEEL++ to solve the multi-RHS forward problem. One of the more or less long term perspective would be to update FEEL++ to wrap these solvers directly whithin the existing interface.

Then the inverse problem has been tackled in chapter 4. The reconstruction is based on an adjoint method. An argument from [20] has been higlighted in section 4.1 to show we have only the possibility to reconstruct up to two parameters at a time. Two methods have been proposed to handle theoretically the fluorescence problem adjoint. Preliminary numerical results have been showed for the inverse problem and should be improved in the future. From the FEEL++ perspective, different optimization libraries have been checked and tested to prepare a future generic interface for optimization problems. The BDF framework has been adapted to handle the time dependent problem backward in time within the existing on disk I/O strategy.

Appendices

Appendix A - Forward model notes

The goal in this section is to prove the theorem 3 (chapter 2 section 2.2.2) with the Faedo-Galerkin method. Let $(w_k)_{1 \le k \le \infty} \subset V$ be a sequence of smooth functions which form an orthogonal basis in $H^1(\Omega)$ and an orthonormal basis in $L^2(\Omega)$ ([35]). We may choose the eigenfunctions of the Robin-Laplacian

$$\begin{cases} -\Delta u + \lambda u = 0, & \text{in } \Omega, \\ \dfrac{\partial u}{\partial n} + \beta u = 0, & \text{on } \partial\Omega. \end{cases} \tag{A.0.1}$$

We set $V_m = \text{span}[w_1, \ldots, w_m]$ and we denote $v' = \frac{\partial v}{\partial t}$ for brevity. We seek for a function $u_m : C([0, T]) \longrightarrow V_m$,

$$u_m(t, x) = \sum_{k=1}^{m} d_k^m(t) w_k(x), \tag{A.0.2}$$

such that

$$\begin{cases} u_m' - \text{div}\,(\kappa\,\nabla u_m) = f, \\ \dfrac{\partial u_m}{\partial n} + A\,u_m = 0, \\ \qquad u_m(0, .) = u_{0,m}. \end{cases} \tag{A.0.3}$$

Note that since $V_m \subset V \subset H \subset V' \subset V_m'$, we may set for $1 \le k \le m$,

$$d_k^m(0) = <u_0, w_k>_{V',V}, \tag{A.0.4}$$

where u_0 appears as the restriction to V' of $u_{m,0} \in V_m'$. For $1 \le k \le m$,

$$\begin{cases} (u_m', w_k) + (\kappa\,\nabla u_m, \nabla w_k) + A(u_m, w_k)_{L^2(\partial\Omega)} = <f, w_k>_{V',V}, \\ \qquad \dfrac{\partial u_m}{\partial n} + A\,u_m = 0, \\ \qquad u_m(0, .) = \sum_{k=1}^{m} d_k^m(0) w_k. \end{cases} \tag{A.0.5}$$

Noting that

$$\begin{cases} (\kappa\,\nabla w_\ell, \nabla w_k) + A(w_\ell, w_k)_{L^2(\partial\Omega)} = a_{\ell,k}, \\ \qquad (u_m'(t), w_k) = d_k^{m\,'}(t), \end{cases} \tag{A.0.6}$$

the system (A.0.5) becomes an ordinary differential system of equations: $f^k(t) = <f(t), w_k>_{V',V}$

$$\begin{cases} d_k^{m\,'}(t) + \sum_{\ell=1}^{m} a_{\ell,k} d_\ell^m(t) = f^k(t), \\ \qquad d_k^m(0) = <u_0, w_k>_{V',V} \ . \end{cases} \tag{A.0.7}$$

The existence and uniqueness of the solution of this ordinary differential system is standard and as a consequence we have the existence and uniqueness of $u_m \in C([0, T], V_m)$ solution of (A.0.5). Notice that

$$\begin{cases} \|u_m(0)\|_{L^2(\Omega)}^2 = \sum_{k=1}^{m} d_k^m(0)^2, \\ \qquad \le \sum_{k=1}^{m} \left(<u_0, w_k>_{V',V}\right)^2, \\ \qquad \le C \, \|u_0\|_{V'}^2. \end{cases} \tag{A.0.8}$$

Lemma 3. *(A priori estimates) We have*

$$\max_{0 \le t \le T} \|u_m(t)\|_{L^2(\Omega)} + \|u_m\|_{L^2(0,T;V)} + \|u_m'\|_{L^2(0,T;V')} \le C \, \left(\|u_0\|_{V'} + \|f\|_{L^2(0,T;V')} \right). \tag{A.0.9}$$

Proof. Multiplying (A.0.3) by $u_m(t)$ and integrating over Ω, we obtain

$$< u_m'(t), u_m(t) >_{V',V} + (\kappa \, \nabla u_m, \nabla u_m)_{V'}) + A(u_m, u_m)_{L^2(\partial\Omega)} = < f, u_m(t) >_{V',V} \quad \text{a.e. } t. \tag{A.0.10}$$

From the ellipticity assumption, we get for $\gamma \ge 0$,

$$\kappa_0 \|u_m\|_V^2 \le (\kappa \, \nabla u_m, \nabla u_m)_{L^2(\Omega)} + A(u_m, u_m)_{L^2(\partial\Omega)} + \gamma \, \|u_m\|_{L^2(\Omega)}^2. \tag{A.0.11}$$

It follows that

$$\frac{\partial}{\partial t} \left((u_m(t), u_m(t))_{L^2(\Omega)} \right) + 2 \kappa_0 \|u_m\|^2 \le C \left(\|u_m(t)\|_{L^2(\Omega)}^2 + \|f\|_{V'}^2 \right). \tag{A.0.12}$$

Setting $\eta(t) = \|u_m(t)\|_{L^2(\Omega)}^2$ and using the Gronwall inequality (since $\eta(t)' \le C \, (\eta(t) + \|f\|_{V'}^2)$), we obtain

$$\eta(t) \le C \, \exp C \, (\eta(0) + \int_0^t \|f(s)\|_{V'}^2 \, ds). \tag{A.0.13}$$

Since $\eta(0) = \|u_m(0)\|_{L^2(\Omega)} \le C \, \|u_0\|_{V'}$, we have

$$\max_{0 \le t \le T} \|u_m(t)\|_{L^2(\Omega)} \le C \, (\|u_0\|_{V'}^2 + \|f\|_{L^2(0,T;V')}^2). \tag{A.0.14}$$

Now, integrating over $[0,T]$ (A.0.10), we get,

$$\|u_m\|_{L^2(0,T;V)} \le C \, (\|u_0\|_{V'}^2 + \|f\|_{L^2(0,T;V')}^2). \tag{A.0.15}$$

Let $v \in V$, $\|v\|_V \le 1$, we write $v = v^1 + v^2$, $v^2 \in (V_m)^\perp$ and

$$< u_m'(t), v^1 >_{V',V} + (\kappa \, \nabla u_m, \nabla v^1)_{L^2(\Omega)} + A(u_m, v^1)_{L^2(\partial\Omega)} = < f, v^1 >_{V',V}, \tag{A.0.16}$$

$$< u_m'(t), v >_{V',V} = (u_m'(t), v^1) = -(\kappa \, \nabla u_m, \nabla v^1)_{L^2(\Omega)} - A(u_m, v^1)_{L^2(\partial\Omega)} - < f, v^1 >_{V',V}, \tag{A.0.17}$$

thus with Cauchy-Schwarz,

$$| < u_m'(t), v >_{V',V} | \le C \, (\|u_m\|_V^2 + \|f\|_{V'}^2), \quad \text{a.e. } t. \tag{A.0.18}$$

which yields

$$\|u_m'\|_{L^2(0,T;V')} \le C \, (\|u_0\|_{V'}^2 + \|f\|_{L^2(0,T;V')}^2). \tag{A.0.19}$$

$$\square$$

From the lemma 3, we deduce that

$$\begin{cases} \{u_m\} \text{ is bounded in } L^2(0,T;V), \\ \{u_m'\} \text{ is bounded in } L^2(0,T;V'), \end{cases} \tag{A.0.20}$$

so, we can extract a subsequence, still denoted (u_m), such that

$$\begin{cases} u_m \rightharpoonup u \text{ in } L^2(0,T;V), \\ u_m' \rightharpoonup u' \text{ in } L^2(0,T;V'). \end{cases} \tag{A.0.21}$$

Given a fixed integer N, we set $v = \sum_{k=1}^N d^k(t) w_k$, with $(d^k)_k$, smooth functions such that $v \in C^1([0,T];V)$. Taking v as a test function, we have

$$\int_0^T \left(< u_m', v > + (\kappa \, \nabla u_m, \nabla v)_{L^2(\Omega)} + A(u_m, v)_{L^2(\partial\Omega)} \right) \, dt = \int_0^T < f, v >_{V',V} \, dt. \tag{A.0.22}$$

Passing to the limit on the subsequence (u_m), we deduce by density

$$\begin{cases} \int_0^T \left(<u',v> + (\kappa\,\nabla u, \nabla v)_{L^2(\Omega)} + A(u,v)_{L^2(\partial\Omega)} \right) dt = \int_0^T <f,v>_{V',V}\ dt, \\ \qquad\qquad\qquad\qquad\qquad\qquad\qquad\qquad\qquad \forall v \in L^2(0,T;V). \end{cases} \tag{A.0.23}$$

and

$$<u',v> + (\kappa\,\nabla u, \nabla v)_{L^2(\Omega)} + A(u,v)_{L^2(\partial\Omega)}) = <f,v>_{V',V}, \quad v \in V, \quad \text{a.e. } t. \tag{A.0.24}$$

Next, we have

$$\begin{cases} \int_0^T \left(- <u,v'>_{V',V} + (\kappa\,\nabla u, \nabla v)_{L^2(\Omega)} + A(u,v)_{L^2(\partial\Omega)} \right) dt \\ \qquad\qquad\qquad\qquad = (u(0),v(0)) + \int_0^T <f,v>_{V',V}\ dt, \\ v \in C^1([0,T];V), v(T) = 0, \end{cases} \tag{A.0.25}$$

and similarly

$$\int_0^T \left(- <v',u_m>_{V',V} + (\kappa\,\nabla v, \nabla u_m)_{L^2(\Omega)} + A(v,u_m)_{L^2(\partial\Omega)} \right) dt$$
$$= <u_m(0),v(0)> + \int_0^T <f,v>_{V',V}\ dt. \tag{A.0.26}$$

Passing to the limit in this last equation, on the subsequence (u_m), we have

$$\int_0^T \left(- <v',u>_{V',V} + (k\,\nabla v, \nabla u)_{L^2(\Omega)} + A(v,u)_{L^2(\partial\Omega)} \right) dt$$
$$= <u_0,v(0)> + \int_0^T <f,v>_{V',V}\ dt. \tag{A.0.27}$$

This gives the initial condition in the problem (2.2.2). Note that $u \in C([0,T];H)$, so that $u(0) \in H$, and the condition $u(0) = u_0$ is to be understood in the sense of the Riesz-Fréchet theorem, i.e., $u(0)$ is the unique representative in $H = L^2(\Omega)$ (identified to its dual) of u_0.

References

[35]   Haim Brezis. *Functional analysis, Sobolev spaces and partial differential equations.* Springer Science & Business Media, 2010.

Appendix B - SiViBir++

This part details a side project realised during a CEMRACS (2015). This event consist in a 6 modeling weeks where Phd students from several horizons gather to work on one project. We are interested in the modelization of a bioreactor. During this session, we develop preliminary computational framework based on FEEL++, used also in the DOT project, as a bioreactor digital twin.

The proceeding presented hereafter details the complete model that describe the physical phenomena and that encompasses different interactions fluid, gas and heat.

MATHEMATICAL MODELING AND NUMERICAL SIMULATION OF A BIOREACTOR LANDFILL USING FEEL++ [*]

Guillaume Dollé[1], Omar Duran[2], Nelson Feyeux[3], Emmanuel Frénod[4], Matteo Giacomini[5, 6] and Christophe Prud'homme[1]

Abstract. In this paper, we propose a mathematical model to describe the functioning of a bioreactor landfill, that is a waste management facility in which biodegradable waste is used to generate methane. The simulation of a bioreactor landfill is a very complex multiphysics problem in which bacteria catalyze a chemical reaction that starting from organic carbon leads to the production of methane, carbon dioxide and water. The resulting model features a heat equation coupled with a nonlinear reaction equation describing the chemical phenomena under analysis and several advection and advection-diffusion equations modeling multiphase flows inside a porous environment representing the biodegradable waste. A framework for the approximation of the model is implemented using Feel++, a C++ open-source library to solve Partial Differential Equations. Some heuristic considerations on the quantitative values of the parameters in the model are discussed and preliminary numerical simulations are presented.

1. Introduction

Waste management and energy generation are two key issues in nowadays societies. A major research field arising in recent years focuses on combining the two aforementioned topics by developing new techniques to handle waste and to use it to produce energy. A very active field of investigation focuses on bioreactor landfills which are facilities for the treatment of biodegradable waste. The waste is accumulated in a humid environment and its degradation is catalyzed by bacteria. The main process taking place in a bioreactor landfill is the methane generation starting from the consumption of organic carbon due to waste decomposition. Several by-products appear during this reaction, including carbon dioxide and leachate, that is a liquid suspension containing particles of the waste material through which water flows.

---

[1] Université de Strasbourg, IRMA UMR 7501, 7 rue René Descartes, 67084 Strasbourg, France. e-mail: `dolle@math.unistra.fr`; `prudhomme@unistra.fr`

[2] State University of Campinas, SP, Brazil. e-mail: `omar@dep.fem.unicamp.br`

[3] MOISE team, INRIA Grenoble Rhône-Alpes. Université de Grenoble, Laboratoire Jean Kuntzmann, UMR 5224, Grenoble, France. e-mail: `nelson.feyeux@imag.fr`

[4] Université de Bretagne-Sud, UMR 6205, LMBA, F-56000 Vannes, France. e-mail: `emmanuel.frenod@univ-ubs.fr`

[5] CMAP Ecole Polytechnique, Route de Saclay, 91128 Palaiseau, France. e-mail: `matteo.giacomini@polytechnique.edu`

[6] DRI Institut Polytechnique des Sciences Avancées, 15-21 rue M. Grandcoing, 94200 Ivry-sur-Seine, France.

Several works in the literature have focused on the study of bioreactor landfills but to the best of our knowledge none of them tackles the global multiphysics problem. On the one hand, [20, 21, 25] present mathematical approaches to the problem but the authors deal with a single aspect of the phenomenon under analysis focusing either on microbiota activity and leachates recirculation or on gas dynamic. On the other hand, this topic has been of great interest in the engineering community [3, 16, 17] and several studies using both numerical and experimental approaches are available in the literature. We refer the interested reader to the review paper [1] on this subject.

In this work, we tackle the problem of providing a mathematical model for the full multiphysics problem of methane generation inside a bioreactor landfill. Main goal is the development of a reliable model to simulate the long-time behavior of these facilities in order to be able to perform forecasts and process optimization [19]. This paper represents a preliminary study of the problem starting from the physics of the phenomena under analysis and provides a first set of equations to describe the methane generation inside a bioreactor landfill. In a more general framework, we aim to develop a model sufficiently accurate to be applied to an industrial context limiting at the same time the required computational cost. Thus, a key aspect of this work focused on the identification of the most important features of the functioning of a bioreactor landfill in order to derive the simplest model possible to provide an accurate description of the aforementioned methanogenic phenomenon. The proposed model has been implemented using FEEL++ and the resulting tool to numerically simulate the dynamic of a bioreactor landfill has been named SiViBiR++ which stands for *Simulation of a Virtual BioReactor using* FEEL++.

The rest of the paper is organized as follows. After a brief description of the physical and chemical phenomena taking place inside these waste management facilities (Section 2), in section 3 we present the fully coupled mathematical model of a bioreactor landfill. Section 4 provides details on the numerical strategy used to discretize the discussed model. Eventually, in section 5 preliminary numerical tests are presented and section 6 summarizes the results and highlights some future perspectives. In appendix A, we provide a table with the known and unknown parameters featuring our model.

2. What is a bioreactor landfill?

As previously stated, a bioreactor landfill is a facility for the treatment of biodegradable waste which is used to generate methane, electricity and hot water. Immediately after being deposed inside a bioreactor, organic waste begins to experience degradation through chemical reactions. During the first phase, degradation takes place via aerobic metabolic pathways, that is a series of concatenated biochemical reactions which occur within a cell in presence of oxygen and may be accelerated by the action of some enzymes. Thus bacteria begin to grow and metabolize the biodegradable material and complex organic structures are converted to simpler soluble molecules by hydrolysis.

The aerobic degradation is usually short because of the high demand of oxygen which may not be fulfilled in bioreactor landfills. Moreover, as more material is added to the landfill, the layers of waste tend to be compacted and the upper strata begin to block the flow of oxygen towards the lower parts of the bioreactor. Within this context, the dominant reactions inside the facility become anaerobic. Once the oxygen is exhausted, the bacteria begin to break the previously generated molecules down to organic acids which are readily soluble in water and the chemical reactions involved in the metabolism provide energy for the growth of population of microbiota.

After the first year of life of the facility, the anaerobic conditions and the soluble organic acids create an environment where the methanogenic bacteria can proliferate [28]. These bacteria become the major actors inside the landfill by using the end products from the first stage of degradation to drive the methane fermentation and convert them into methane and carbon dioxide. Eventually, the chemical reactions responsible for the generation of these gases gradually decrease until the material inside the landfill is inert (approximately after 40 years).

In this work, we consider the second phase of the degradation process, that is the methane fermentation during the anaerobic stage starting after the first year of life of the bioreactor.

(A) 3D render of a bioreactor landfill. (B) Scheme of the structure of an alveolus.
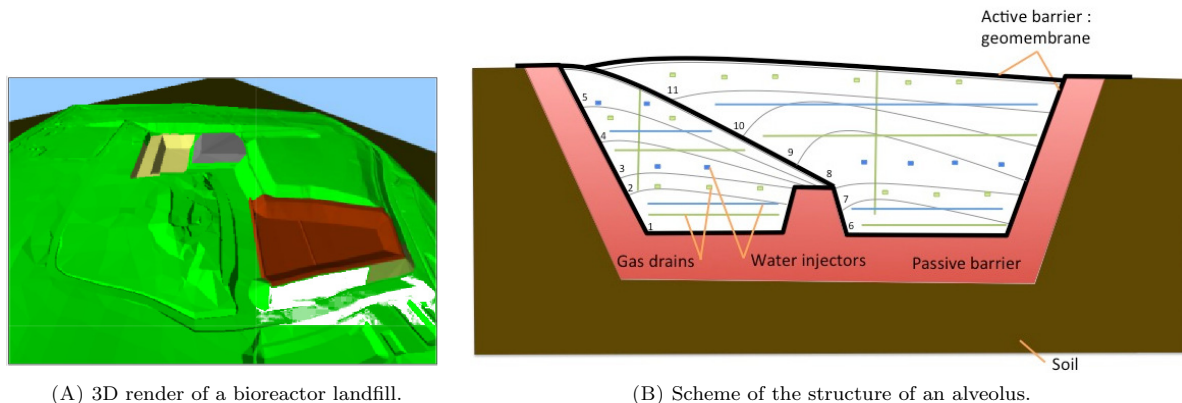
FIGURE 1. Structure of a bioreactor landfill and its composing alveoli. Image courtesy of Entreprise Charier http://www.charier.fr.

2.1. Structure of a bioreactor landfill

A bioreactor landfill counts several unit structures - named alveoli - as shown in the 3D rendering of a facility in Drouès, France (Fig. 1A). We focus on a single alveolus and we model it as a homogeneous porous medium in which the bulk material represents the solid waste whereas the void parts among the organic material are filled by a mixture of gases - mainly methane, carbon dioxide, oxygen, nitrogen and water vapor - and leachates, that is a liquid suspension based on water. For the rest of this paper, we will refer to our domain of interest by using indifferently the term alveolus and bioreactor, though the latter one is not rigorous from a modeling point of view.

Each alveolus is filled with several layers of biodegradable waste and the structure is equipped with a network of horizontal water injectors and production pipes respectively to allow the recirculation of leachates and to extract the gases generated by the chemical reactions. Moreover, each alveolus is isolated from the surrounding ground in order to prevent pollutant leaks and is covered by means of an active geomembrane. Figure 1B provides a schematic of an alveolus in which the horizontal pipes are organized in order to subdivide the structure in a cartesian-like way. Technical details on the construction and management of a bioreactor landfill are available in [8,14].

2.2. Physical and chemical phenomena

Let us define the porosity ϕ as the fraction of void space inside the bulk material:

$$\phi = \frac{\text{Pore Volume}}{\text{Total Volume}}. \tag{2.1}$$

For biodegradable waste, we consider $\phi = 0.3$ as by experimental measurements in [26], whereas it is known in the literature that for generic waste the value drops to 0.1. Within this porous environment, the following phenomena take place:

- chemical reaction for the methane fermentation;
- heat transfer driven by the chemical reaction;
- transport phenomena of the gases;
- transport and diffusion phenomena of the leachates;

Here, we briefly provide some details about the chemical reaction for the methane generation, whereas we refer to section 3 for the description of the remaining phenomena and the derivation of the full mathematical model for the coupled system. As previously mentioned, at the beginning of the anaerobic stage the bacteria break the previously generated molecules down to organic acids, like the propionic acid CH_3CH_2COOH. This acid acts as a reacting term in the following reaction:

$$CH_3CH_2COOH + H_2O \longrightarrow 3\,H_2O + CO_2 + 2CH_4. \tag{2.2}$$

The microbiota activity drives the generation of methane (CH_4) and is responsible for the production of other by-products, mainly water (H_2O) and carbon dioxide (CO_2). As per equation (2.2), for each consumed mole of propionic acid - equivalently referred to as organic carbon with an abuse of notation -, two moles of methane are generated and three moles of water and one of carbon dioxide are produced as well.

Remark 2.1. We remark that in order for reaction (2.2) to take place, water has to be added to the propionic acid. This means that the bacteria can properly catalyze the reaction only if certain conditions on the temperature and the humidity of the waste are fulfilled. This paper presents a first attempt to provide a mathematical model of a bioreactor landfill, thus both the temperature and the quantity of water inside the facility will act as unknowns in the model (cf. section 3). In a more general framework, the proposed model will be used to perform long-time forecasts of the methane generation process and the temperature and water quantity will have the key role of control variables of the system.

3. Mathematical model of a bioreactor landfill

In this section, we describe the equations modeling the phenomena taking place inside an alveolus. As stated in the introduction, the final goal of the SiViBiR++ project is to control and optimize the functioning of a real bioreactor landfill, hence a simple model to account for the phenomena under analysis is sought. Within this framework, in this article we propose a first mathematical model to describe the coupled physical and chemical phenomena involved in the methanogenic fermentation. In the following sections, we will provide a detailed description of the chemical reaction catalyzed by the methanogenic bacteria, the evolution of the temperature inside the alveolus and the transport phenomena driven by the dynamic of a mixture of gases and by the liquid water. An extremely important aspect of the proposed model is the interaction among the variables at play and consequently the coupling among the corresponding equations. In order to reduce the complexity of the model and to keep the corresponding implementation in FEEL++ as simple as possible, some physical phenomena have been neglected. In the following subsections, we will detail the simplifying assumptions that allow to neglect some specific phenomena without degrading the reliability of the resulting model, by highlighting their limited impact on the global behavior of the overall system.

Let $\Omega \subset \mathbb{R}^3$ be an alveolus inside the landfill under analysis. We split the boundary $\partial\Omega$ of the computational domain into three non-void and non-overlapping regions Γ_t, Γ_b and Γ_l, representing respectively the membrane covering the top surface of the bioreactor, the base of the alveolus and the ground surrounding the lateral surface of the structure.

3.1. Consumption of the organic carbon

As previously stated, the functioning of a bioreactor landfill relies on the consumption of biodegradable waste by means of bacteria. From the chemical reaction in (2.2), we may derive a relationship between the concentration of bacteria b and the concentration of the consumable organic material which we denote by C^{org}. The activity of the bacteria takes place if some environmental conditions are fulfilled, namely the waste humidity and the bioreactor temperature. Let $w_{\max}$ and T_{opt} be respectively the maximal quantity of water and the optimal temperature that allow the microbiota to catalyze the chemical reaction (2.2). We introduce the

following functions to model the metabolism of the microbiota:

$$\Psi_1(w) = w \, \max\left(0, 1 - \frac{w}{w_{\max}}\right), \qquad \Psi_2(T) = \max\left(0, 1 - \frac{|T - T_{\text{opt}}|}{A_T}\right) \tag{3.1}$$

where A_T is the amplitude of the variation of the temperature tolerated by the bacteria. On the one hand, Ψ_1 models the fact that the bacterial activity is proportional to the quantity of liquid water - namely leachates - inside the bioreactor and it is prevented when the alveolus is flooded. On the other hand, according to Ψ_2 the microbiota metabolism is maximum when the current temperature equals T_{opt} and it stops when it exceeds the interval of admissible temperatures $[T_{\text{opt}} - A_T; T_{\text{opt}} + A_T]$.

Since the activity of the bacteria mainly consists in consuming the organic waste to perform reaction (2.2), it is straightforward to deduce a proportionality relationship between b and C^{org}. By combining the information in (3.1) with this relationship, we may derive the following law to describe the evolution of the concentration of bacteria inside the bioreactor:

$$\partial_t b \propto b \; C^{\text{org}} \; \Psi_1(w) \; \Psi_2(T) \tag{3.2}$$

and consequently, we get a proportionality relationship for the consumption of the biodegradable material C^{org}:

$$\partial_t C^{\text{org}} \propto -\partial_t b. \tag{3.3}$$

Let a_b and c_b be two proportionality constants associated respectively with (3.2) and (3.3). By integrating (3.3) in time and introducing the proportionality constant c_b, we get that the concentration of bacteria reads as

$$b(x,t) = b_0 + c_b(C_0^{\text{org}} - C^{\text{org}}(x,t)) \tag{3.4}$$

where $b_0 := b(\cdot, 0)$ and $C_0^{\text{org}} := C^{\text{org}}(\cdot, 0)$ are the initial concentrations respectively of bacteria and organic material inside the alveolus. Thus, by plugging (3.4) into (3.2) we get the following equation for the consumption of organic carbon between the instant $t = 0$ and the final time S^{fin}:

$$\begin{cases} (1 - \phi)\partial_t C^{\text{org}}(x,t) = -a_b \; b(x,t) \; C^{\text{org}}(x,t) \; \Psi_1(w(x,t)) \; \Psi_2(T(x,t)) \, , & \text{in } \Omega \times (0, S^{\text{fin}}] \\ C^{\text{org}}(\cdot, 0) = C_0^{\text{org}} \, , & \text{in } \overline{\Omega} \end{cases} \tag{3.5}$$

We remark that the organic material filling the bioreactor is only present in the bulk part of the porous medium and this is modeled by the factor $1 - \phi$ which features the information about the porosity of the environment. Moreover, we highlight that in equation (3.5) a non-linear reaction term appears and in section 4 we will discuss a strategy to deal with this non-linearity when moving to the Finite Element discretization.

For the sake of readability, from now on we will omit the dependency on the space and time variables in the notation for both the organic carbon and the concentration of bacteria.

3.2. Evolution of the temperature

The equation describing the evolution of the temperature T inside the bioreactor is the classical heat equation with a source term proportional to the consumption of bacteria. We consider the external temperature to be fixed by imposing Dirichlet boundary conditions on $\partial\Omega$.

Remark 3.1. Since we are interested in the long-time evolution of the system ($S^{\text{fin}} = 40$ years), the unit time interval is sufficiently large to allow daily variations of the temperature to be neglected. Moreover, we assume that the external temperature remains constant during the whole life of the bioreactor. From a physical point of view, this assumption is not realistic but we conjecture that only small fluctuations would arise by the relaxation of this hypothesis. A future improvement of the model may focus on the integration of dynamic boundary conditions in order to model seasonal changes of the external temperature.

The resulting equation for the temperature reads as follows:

$$\begin{cases} \partial_t T(x,t) - k_T \Delta T(x,t) = -c_T \partial_t C^{\text{org}}(x,t) \ , & \text{in } \Omega \times (0, S^{\text{fin}}] \\ T(x,\cdot) = T_{\text{m}} \ , & \text{on } \Gamma_{\text{t}} \times (0, S^{\text{fin}}] \\ T(x,\cdot) = T_{\text{g}} \ , & \text{on } \Gamma_{\text{b}} \cup \Gamma_{\text{l}} \times (0, S^{\text{fin}}] \\ T(\cdot, 0) = T_0 \ , & \text{in } \overline{\Omega} \end{cases} \tag{3.6}$$

where k_T is the thermal conductivity of the biodegradable waste and c_T is a scaling factor that accounts for the heat transfer due to the chemical reaction catalyzed by the bacteria. The values T_{m}, T_{g} and T_0 respectively represent the external temperature on the membrane Γ_{t}, the external temperature of the ground $\Gamma_{\text{b}} \cup \Gamma_{\text{l}}$ and the initial temperature inside the bioreactor.
For the sake of readability, from now on we will omit the dependency on the space and time variables in the notation of the temperature.

3.3. Velocity field of the gas

In order to model the velocity field of the gas inside the bioreactor, we have to introduce some assumptions on the physics of the problem. First of all, we assume the gas to be incompressible. This hypothesis stands if a very slow evolution of the mixture of gases takes place and this is the case for a bioreactor landfill in which the methane fermentation gradually decreases along the 40 years lifetime of the facility. Additionally, the decompression generated by the extraction of the gases through the pipes is negligible due to the weak gradient of pressure applied to the production system. Furthermore, we assume low Reynolds and low Mach numbers for the problem under analysis: this reduces to having a laminar slow flow which, as previously stated, is indeed the dynamic taking place inside an alveolus. Eventually, we neglect the effect due to the gravity on the dynamic of the mixture of gases: owing to the small height of the alveolus (approximately 90 m), the variation of the pressure in the vertical direction due to the gravity is limited and in our model we simplify the evolution of the gas by neglecting the hydrostatic component of the pressure.

Under the previous assumptions, the behavior of the gas mixture inside a bioreactor landfill may be described by a mass balance equation coupled with a Darcy's law

$$\begin{cases} \nabla \cdot u = 0 \ , & \text{in } \Omega \\ u = -\nabla p \ , & \text{in } \Omega \end{cases} \tag{3.7}$$

where $p := \frac{D}{\phi \mu_{\text{gas}}} P$, D is the permeability of the porous medium, ϕ its porosity and μ_{gas} the gas viscosity whereas P is the pressure inside the bioreactor. In (3.7), the incompressibility assumption has been expressed by stating that the gas flow is isochoric, that is the velocity is divergence-free. This equation is widely used in the literature to model porous media (cf. e.g. [10, 18]) and provides a coherent description of the phenomenon under analysis in the bioreactor landfill. As a matter of fact, it is reasonable to assume that the density of the gas mixture is nearly constant inside the domain, owing to the weak gradient of pressure applied to extract the gas via the production system and to the slow rate of methane generation via the fermentation process, that lasts approximately 40 years.

To fully describe the velocity field, the effect of the production system that extracts the gases from the bioreactor has to be accounted for. We model the production system as a set of N_g cylinders Θ_g^i's thus the effect of the gas extraction on each pipe results in a condition on the outgoing flow. Let $J_{\text{out}} > 0$ be the mass flow rate exiting from the alveolus through each production pipe. The system of equations (3.7) is coupled with the following conditions on the outgoing normal flow on each drain used to extract the gas:

$$\int_{(\partial \Theta_g^i)^{\text{n}}} (C^{\text{dx}} + M + O + N + h) \, u \cdot n \, d\sigma = J_{\text{out}} \qquad \forall i = 1, \ldots, N_g. \tag{3.8}$$

In (3.8), n is the outward normal vector to the surface, $(\partial\Theta_g^i)^{\mathrm{n}}$ is the part of the boundary of the cylinder Θ_g^i which belongs to the lateral surface of the alveolus itself and the term $(C^{\mathrm{dx}} + M + O + N + h)$ represents the total concentration of the gas mixture starring carbon dioxide, methane, oxygen, nitrogen and water vapor.

Since the cross sectional area of the pipes belonging to the production system is negligible with respect to the size of the overall alveolus, we model these drains as 1D lines embedded in the 3D domain. Owing to this, in the following subsection we present a procedure to integrate the information (3.8) into a source term named F^{out} in order to simplify the problem that describes the dynamic of the velocity field inside a bioreactor landfill.

Remark 3.2. According to conditions (3.8), the velocity u depends on the concentrations of the gases inside the bioreactor, thus is a function of both space and time. Nevertheless, the velocity field at each time step is independent from the previous ones and is only influenced by the distribution of gases inside the alveolus. For this reason, we neglect the dependency on the time variable and we consider u being only a function of space.

3.3.1. *The source term F^{out}*

As previously stated, each pipe Θ_g^i is modeled as a cylinder of radius R and length L. Hence, the cross sectional area $(\partial\Theta_g^i)^{\mathrm{n}}$ and the lateral surface $(\partial\Theta_g^i)^{\mathrm{l}}$ respectively measure πR^2 and $2\pi RL$.

We assume the gas inside the cylinder to instantaneously exit the alveolus through its boundary $(\partial\Theta_g^i)^{\mathrm{n}}$, that is the outgoing flow (3.8) is equal to the flow entering the drain through its lateral surface. Thus we may neglect the gas dynamic inside the pipe and (3.8) may be rewritten as

$$\int_{(\partial\Theta_g^i)^{\mathrm{n}}} (C^{\mathrm{dx}} + M + O + N + h)\, u\cdot n\, d\sigma = \int_{(\partial\Theta_g^i)^{\mathrm{l}}} (C^{\mathrm{dx}} + M + O + N + h)\, u\cdot n\, d\sigma = J_{\mathrm{out}} \qquad \forall i = 1,\ldots,N_g. \quad (3.9)$$

Moreover, under the hypothesis that the quantity of gas flowing from the bioreactor to the inside of the cylinder Θ_g^i is uniform over its lateral surface, that is the same gas mixture surrounds the drain in all the points along its dominant size, we get

$$\left(\int_{(\partial\Theta_g^i)^{\mathrm{l}}} (C^{\mathrm{dx}} + M + O + N + h)\, d\sigma\right) u\cdot n = J_{\mathrm{out}} \ \text{ on } (\partial\Theta_g^i)^{\mathrm{l}} \qquad \forall i = 1,\ldots,N_g. \quad (3.10)$$

We remark that gas densities may be considered uniform along the perimeter of the cylinder only if the latter is small enough, that is the aforementioned assumption is likely to be true if the radius of the pipe is small in comparison with the size of the alveolus. Within this framework, (3.10) reduces to

$$u\cdot n = \frac{J_{\mathrm{out}}}{2\pi R \displaystyle\int_{\mathfrak{L}^i} (C^{\mathrm{dx}} + M + O + N + h)\, dl} \ \text{ on } (\partial\Theta_g^i)^{\mathrm{l}} \qquad \forall i = 1,\ldots,N_g \quad (3.11)$$

where $\mathfrak{L}^i$ is the centerline associated with the cylinder Θ_g^i. By coupling (3.7) with (3.11), we get the following PDE to model the velocity field:

$$\begin{cases} -\Delta p = 0\,, & \text{in } \Omega \\ \nabla p \cdot n = -\dfrac{J_{\mathrm{out}}}{2\pi R \displaystyle\int_{\mathfrak{L}^i} (C^{\mathrm{dx}} + M + O + N + h)\, dl}\,, & \text{on } (\partial\Theta_g^i)^{\mathrm{l}} \qquad \forall i = 1,\ldots,N_g \end{cases} \quad (3.12)$$

Let us consider the variational formulation of problem (3.12): we seek $p \in H^1(\Omega)$ such that

$$\int_\Omega \nabla p \cdot \nabla \delta p\, dx = \sum_{i=1}^{N_g} -\frac{J_{\mathrm{out}}}{2\pi R \displaystyle\int_{\mathfrak{L}^i} (C^{\mathrm{dx}} + M + O + N + h)\, dl} \int_{(\partial\Theta_g^i)^{\mathrm{l}}} \delta p\, d\sigma \qquad \forall \delta p \in \mathcal{C}_0^1(\Omega). \quad (3.13)$$

We may introduce the term F^{out} as the limit when R tends to zero of the right-hand side of (3.13):

$$F^{\text{out}} := \sum_{i=1}^{N_g} -\frac{J_{\text{out}}}{\displaystyle\int_{\mathfrak{L}^i} \left(C^{\text{dx}} + M + O + N + h\right) dl} \delta_{\mathfrak{L}^i} \tag{3.14}$$

where $\delta_{\mathfrak{L}^i}$ is a Dirac mass concentrated along the centerline $\mathfrak{L}^i$ of the pipe Θ_g^i.
Hence, the system of equations describing the evolution of the velocity inside the alveolus may be written as

$$\begin{cases} \nabla \cdot u = F^{\text{out}} \, , & \text{in } \Omega \\ u = -\nabla p \, , & \text{in } \Omega \\ u \cdot n = 0 \, , & \text{on } \partial\Omega \end{cases} \tag{3.15}$$

where the right-hand side of the mass balance equation may be either (3.14) or a mollification of it.

3.4. Transport phenomena for the gas components

Inside a bioreactor landfill the pressure field is comparable to the external atmospheric pressure. This low-pressure does not provide the physical conditions for gases to liquefy. Hence, the gases are not present in liquid phase and solely the dynamic of the gas phases has to be accounted for. Within this framework, in section 3.5 we consider the case of water for which phase transitions driven by heat transfer phenomena are possible, whereas in the current section we focus on the remaining gases (i.e. oxygen, nitrogen, methane and carbon dioxide) which solely exist in gas phase.

Let u be the velocity of the gas mixture inside the alveolus. We consider a generic gas whose concentration inside the bioreactor is named G. The evolution of G fulfills the classical pure advection equation:

$$\begin{cases} \phi \partial_t G(x,t) + u \cdot \nabla G(x,t) = F^G(x,t) \, , & \text{in } \Omega \times (0, S^{\text{fin}}] \\ G(\cdot, 0) = G_0 \, , & \text{in } \overline{\Omega} \end{cases} \tag{3.16}$$

where ϕ is again the porosity of the waste. The source term $F^G(x,t)$ depends on the gas and will be detailed in the following subsections.

3.4.1. *The case of oxygen and nitrogen*

We recall that the oxygen concentration is named O, whereas the nitrogen one is N. Neither of these components appears in reaction (2.2) thus the associated source terms are $F^O(x,t) = F^N(x,t) = 0$. The resulting equations (3.17) are closed by the initial conditions $O(\cdot,0) = O_0$ and $N(\cdot,0) = N_0$.

$$\begin{aligned} \phi \partial_t O + u \cdot \nabla O = 0 \\ \phi \partial_t N + u \cdot \nabla N = 0 \end{aligned} \tag{3.17}$$

Both the oxygen and the nitrogen are extracted by the production system thus their overall concentration may be negligible with respect to the quantity of carbon dioxide and methane inside the alveolus. Hence, for the rest of this paper we will neglect equations (3.17) by considering $O(x,t) \simeq O_0 \simeq 0$ and $N(x,t) \simeq N_0 \simeq 0$.

3.4.2. *The case of methane and carbon dioxide*

As previously stated, (2.2) describes the methanogenic fermentation that starting from the propionic acid drives the production of methane, having carbon dioxide as by-product. Equation (3.16) stands for both the methane M and the carbon dioxide C^{dx}. For these components, the source terms have to account for the production of gas starting from the transformation of biodegradable waste. Thus, the source terms are

proportional to the consumption of the quantity C^{org} through some constants c_M and c_C specific to the chemical reaction and the component:

$$F^j(x,t) = -c_j \partial_t C^{\mathrm{org}} \quad , \quad j = M, C$$

In a similar fashion as before, the resulting equations read as

$$\phi \partial_t M + u \cdot \nabla M = -c_M \partial_t C^{\mathrm{org}}$$
$$\phi \partial_t C^{\mathrm{dx}} + u \cdot \nabla C^{\mathrm{dx}} = -c_C \partial_t C^{\mathrm{org}}$$

$$(3.18)$$

and they are coupled with appropriate initial conditions $M(\cdot,0) = M_0$ and $C^{\mathrm{dx}}(\cdot,0) = C_0^{\mathrm{dx}}$.

3.5. Dynamic of water vapor and liquid water

Inside a bioreactor landfill, water exists both in vapor and liquid phase. Let h be the concentration of water vapor and w the one of liquid water. The variation of temperature responsible for phase transitions inside the alveolus is limited, whence we do not consider a two-phase flow for the water but we describe separately the dynamics of the gas and liquid phases of the fluid. On the one hand, the water vapor inside the bioreactor landfill evolves as the gases presented in section 3.4: it is produced by the chemical reaction (2.2), it is transported by the velocity field u and is extracted via the pipes of the production system; as previously stated, no effect of the gravity is accounted for. This results in a pure advection equation for h. On the other hand, the dynamic of the liquid water may be schematized as follows: it flows in through the injector system at different levels of the alveolus, is transported by a vertical field u_w due to the effect of gravity and is spread within the porous medium. The resulting governing equation for w is an advection-diffusion equation. Eventually, the phases h and w are coupled by a source term that accounts for phase transitions.

Owing to the different nature of the phenomena under analysis and to the limited rate of heat transfer inside a bioreactor landfill, in the rest of this section we will describe separately the equations associated with the dynamics of the water vapor and the liquid water, highlighting their coupling due to the phase transition phenomena.

3.5.1. *Phase transitions*

Two main phenomena are responsible for the production of water vapor inside a bioreactor landfill. On the one hand, vapor is a product of the chemical reaction (2.2) catalyzed by the microbiota during the methanogenic fermentation process. On the other hand, heat transfer causes part of the water vapor to condensate and part of the liquid water to evaporate.

Let us define the vapor pressure of water P^{vp} inside the alveolus as the pressure at which water vapor is in thermodynamic equilibrium with its condensed state. Above this critical pressure, water vapor condenses, that is it turns to the liquid phase. This pressure is proportional to the temperature T and may be approximated by the following Rankine law:

$$P^{\mathrm{vp}}(T) = P_0 \exp\left(s_0 - \frac{s_1}{T}\right)$$

$$(3.19)$$

where P_0 is a reference pressure, s_0 and s_1 are two constants known by experimental results and T is the temperature measured in Kelvin. If we restrict to a range of moderate temperatures, we can approximate the exponential in (3.19) by means of a linear law. Let H_0 and H_1 be two known constants, we get

$$P^{\mathrm{vp}}(T) \simeq H_0 + H_1 T.$$

$$(3.20)$$

Let P^h be the partial pressure of the water vapor inside the gas mixture. We can compute P^h multiplying the total pressure p by a scaling factor representing the ratio of water vapor inside the gas mixture:

$$P^h = \frac{h}{C^{\mathrm{dx}} + M + O + N + h} p.$$

$$(3.21)$$

The phase transition process features two different phenomena. On the one hand, when the pressure P^h is higher than the vapor pressure of water P^{vp} the vapor condensates. By exploiting (3.21) and (3.20), the condition $P^h > P^{\mathrm{vp}}(T)$ may be rewritten as

$$h - H(T) > 0 \qquad , \qquad H(T) := (C^{\mathrm{dx}} + M + O + N + h)\frac{H_0 + H_1 T}{p}.$$

We assume the phase transition to be instantaneous, thus the condensation of water vapor may be expressed through the following function

$$F^{\mathrm{cond}} := c_{h \to w} \max(h - H(T), 0) \tag{3.22}$$

where $c_{h \to w}$ is a scaling factor. As per (3.22), the production of vapor from liquid water is 0 as soon as the concentration of vapor is larger than the threshold $H(T)$, that is the air is saturated.

In a similar fashion, we may model the evaporation of liquid water. When P^h is below the vapor pressure of water P^{vp} - that is $h - H(T) < 0$ - part of the liquid water generates vapor. The evaporation rate is proportional to the difference $P^{\mathrm{vp}}(T) - P^h$ and to the quantity of liquid water w available inside the alveolus. Hence, the evaporation of liquid water is modeled by the following expression

$$F^{\mathrm{evap}} := c_{w \to h} \max(H(T) - h, 0) w. \tag{3.23}$$

Remark 3.3. Since the quantity of water vapor inside a bioreactor landfill is negligible, we assume that the evaporation process does not significantly affect the dynamic of the overall system. Hence, in the rest of this paper, we will neglect this phenomenon by modeling only the condensation (3.22).

3.5.2. *The case of water vapor*

The dynamic of the water vapor may be modeled using (3.16) as for the other gases. In this case, the source term has to account for both the production of water vapor due to the chemical reaction (2.2) and its decrease as a consequence of the condensation phenomenon:

$$F^h(x, t) := -c_h \partial_t C^{\mathrm{org}} - F^{\mathrm{cond}}$$

where c_h is a scaling factor describing the relationship between the consumption of organic carbon and the generation of water vapor. The resulting advection equation reads as

$$\phi \partial_t h + u \cdot \nabla h = -c_h \partial_t C^{\mathrm{org}} - F^{\mathrm{cond}} \tag{3.24}$$

and it is coupled with the initial condition $h(\cdot, 0) = h_0$.

3.5.3. *The case of liquid water*

The liquid water inside the bioreactor is modeled by an advection-diffusion equation in which the drift term is due to the gravity, that is the transport phenomenon is mainly directed in the vertical direction and is associated with the liquid flowing downward inside the alveolus.

$$\begin{cases} \phi \partial_t w(x, t) + u_w \cdot \nabla w(x, t) - k_w \Delta w(x, t) = F^{\mathrm{cond}}(x, t) \, , & \text{in } \Omega \times (0, S^{\mathrm{fin}}] \\ k_w \nabla w(x, t) \cdot n = 0 \text{ and } u_w \cdot n = 0 \, , & \text{on } \Gamma_{\mathrm{t}} \cup \Gamma_{\mathrm{l}} \times (0, S^{\mathrm{fin}}] \\ k_w \nabla w(x, t) \cdot n = 0 \, , & \text{on } \Gamma_{\mathrm{b}} \times (0, S^{\mathrm{fin}}] \\ w(\cdot, 0) = w_0 \, , & \text{in } \overline{\Omega} \end{cases} \tag{3.25}$$

where $u_w := (0, 0, -\|u_w\|)^T$ is the vertical velocity of the water and k_w is its diffusion coefficient. The right-hand side of the first equation accounts for the water production by condensation as described in section 3.5.1. On the one hand, the free-slip boundary conditions on the lateral and top surfaces allow water to slide but

prevent its exit, that is the top and lateral membranes are waterproof. On the other hand, the homogeneous Neumann boundary condition on the bottom of the domain describes the ability of the water to flow through this membrane. These conditions are consistent with the impermeability of the geomembranes and with the recirculation of leachates which are extracted when they accumulate in the bottom part of the alveolus and are reinjected in the upper layers of the waste management facility.

Remark 3.4. It is well-known in the literature that the evolution of an incompressible fluid inside a given domain is described by the Navier-Stokes equation. In (3.25), we consider a simplified version of the afore-mentioned equation by linearizing the inertial term. As previously stated, the dynamic of the fluids inside the bioreactor landfill is extremely slow and we may assume a low Reynolds number regime for the water as well. Under this assumption, the transfer of kinetic energy in the turbulent cascade due to the non-linear term may be neglected. Moreover, by means of a linearization of the inertial term, the transport effect is preserved and the resulting parabolic advection-diffusion problem (3.25) may be interpreted as an unsteady version of the classical Oseen equation [9].

Remark 3.5. Equation (3.25) may be furtherly interpreted as a special advection equation modeling the transport phenomenon within a porous medium. As a matter of fact, the diffusion term $-k_w \Delta w$ accounts for the inhomogeneity of the environment in which the water flows and describes the fact that the liquid spreads in different directions while flowing downwards due to the encounter of blocking solid material along its path. The distribution of the liquid into different directions is random and is mainly related to the nature of the surrounding environment thus we consider an isotropic diffusion tensor k_w. The aforementioned equation is widely used (cf. e.g. [27]) to model flows in porous media and is strongly connected with the description of the porous environment via the Darcy's law introduced in section 3.3.
Within the framework of our problem, the diffusion term is extremely important since it models the spread of water and leachates inside the bioreactor landfill and the consequent humidification of the whole alveolus and not solely of the areas neighboring the injection pipes.

Eventually, problem (3.25) is closed by a set of conditions that describe the injection of liquid water and leachates through N_w pipes Θ_w^i's. As previously done for the production system, we model each injector as a cylinder of radius R and length L and we denote by $(\partial\Theta_w^i)^{\mathrm{n}}$ and $(\partial\Theta_w^i)^{\mathrm{l}}$ respectively the part of the boundary of the cylinder which belongs to the boundary of the bioreactor and its lateral surface. The aforementioned inlet condition reads as

$$\int_{(\partial\Theta_w^i)^{\mathrm{n}}} k_w \nabla w \cdot n \, d\sigma = -J_{\mathrm{in}} \qquad \forall i = 1, \ldots, N_w$$

where $J_{\mathrm{in}} > 0$ is the mass flow rate entering the alveolus through each injector. As for the production system in section 3.3.1, we may now integrate this condition into a source term for equation (3.25). Under the assumption that the flow is instantaneously distributed along the whole cylinder in a uniform way, we get

$$\int_{(\partial\Theta_w^i)^{\mathrm{n}}} k_w \nabla w \cdot n \, d\sigma = -\int_{(\partial\Theta_w^i)^{\mathrm{l}}} k_w \nabla w \cdot n \, d\sigma = -J_{\mathrm{in}} \qquad \forall i = 1, \ldots, N_w.$$

Consequently the condition on each injector reads as

$$k_w \nabla w \cdot n = \frac{J_{\mathrm{in}}}{2\pi RL} \ \text{ on } (\partial\Theta_w^i)^{\mathrm{l}} \qquad \forall i = 1, \ldots, N_w$$

and we obtain the following source term F^{in}

$$F^{\mathrm{in}} := \sum_{i=1}^{N_w} \frac{J_{\mathrm{in}}}{L} \delta_{\mathfrak{L}^i} \tag{3.26}$$

where $\delta_{\mathfrak{L}^i}$ is a Dirac mass concentrated along the centerline $\mathfrak{L}^i$ of the pipe Θ_w^i. Hence, the resulting dynamic of the liquid water inside an alveolus is modeled by the following PDE:

$$\begin{cases} \phi\partial_t w + u_w \cdot \nabla w - k_w \Delta w = F^w \ , & \text{in } \Omega \times (0, S^{\text{fin}}] \\ k_w \nabla w \cdot n = 0 \text{ and } u_w \cdot n = 0 \ , & \text{on } \Gamma_t \cup \Gamma_l \times (0, S^{\text{fin}}] \\ k_w \nabla w \cdot n = 0 \ , & \text{on } \Gamma_b \times (0, S^{\text{fin}}] \end{cases} \quad (3.27)$$

with $F^w \coloneqq F^{\text{cond}} + F^{\text{in}}$ and the initial condition $w(\cdot, 0) = w_0$. By analyzing the right-hand side of equation (3.27), we remark that neglecting the effect of evaporation in the phase transition allows to decouple the dynamics of liquid water and water vapor. Moreover, as previously stated for equation (3.15), F^{in} may be chosen either according to definition (3.26) or by means of an appropriate mollification.

4. Numerical approximation of the coupled system

This section is devoted to the description of the numerical strategies used to discretize the fully coupled model of the bioreactor landfill introduced in section 3. We highlight that one of the main difficulties of the presented model is the coupling of all the equations and the multiphysics nature of the problem under analysis. Here we propose a first attempt to discretize the full model by introducing an explicit coupling of the equations, that is by considering the source term in each equation as function of the variables at the previous iteration.

4.1. Geometrical model of an alveolus

As previously stated, a bioreactor landfill is composed by several alveoli. Each alveolus may be modeled as an independent structure obtained starting from a cubic reference domain (Fig. 2A) to which pure shear transformations are applied (Fig. 2B-2C). For example, the pure lateral shear in figure 2B allows to model

(A) Cubic reference domain.   (B) Lateral shear on a face.   (C) Pyramidal domain.
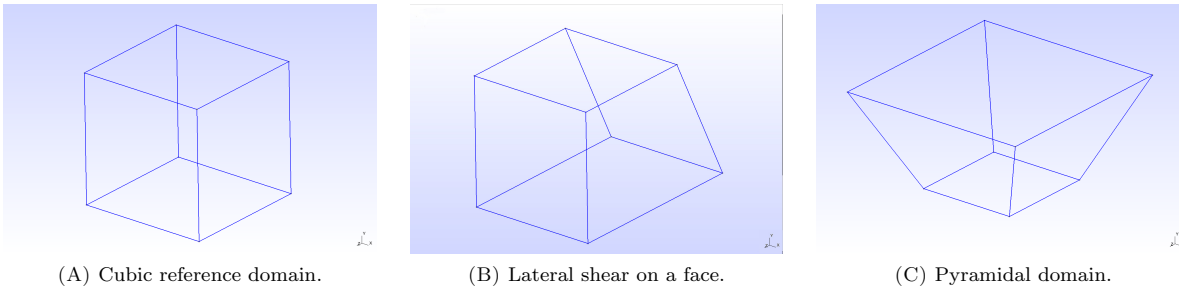
Figure 2. Reference domain for an alveolus and admissible transformations.

the left-hand side alveolus in figure 1B whereas the right-hand side one may be geometrically approximated by means of the pyramid in figure 2C.

In order to model the network of the water injectors and the one of the drains extracting the gas, the geometrical domains in figure 2 are equipped with a cartesian distribution of horizontal lines, the 1D model being justified by the assumption in section 3.

4.2. Finite Element approximations of the organic carbon and heat equations

Both equations (3.5) and (3.6) are discretized using Lagrangian Finite Element functions. In particular, the time derivative is approximated by means of an implicit Euler scheme, whereas the basis functions for the spatial discretization are the classical $\mathbb{P}_k$ Finite Element functions of degree k.

Let $t = t_n$. We consider the following quantities at time t_n as known variables: $C_n^{\text{org}} \coloneqq C^{\text{org}}(x, t_n)$, $T_n \coloneqq$

$T(x, t_n)$ and $w_n := w(x, t_n)$. The consumption of organic carbon is described by equation (3.5) coupled with equation (3.4) for the dynamic of the bacteria. At each time step, we seek $C_{n+1}^{\text{org}} \in H^1(\Omega)$ such that

$$\int_\Omega (1 - \phi) \frac{C_{n+1}^{\text{org}} - C_n^{\text{org}}}{\Delta t} \delta C \, dx = - \int_\Omega a_b \, C_{n+1}^{\text{org}} \, [b_0 + c_b(C_0^{\text{org}} - C_n^{\text{org}})] \, \Psi_1(w_n) \, \Psi_2(T_n) \, \delta C \, dx \qquad \forall \delta C \in H^1(\Omega)$$

We remark that in the previous equation the non-linear reaction term has been handled in a semi-implicit way by substituting $(C_{n+1}^{\text{org}})^2$ by $C_{n+1}^{\text{org}} C_n^{\text{org}}$ in the right-hand side. Hence, the bilinear and linear forms associated with the variational formulation at $t = t_n$ respectively read as

$$a_{C^{\text{org}}}(C_{n+1}^{\text{org}}, \delta C) = \int_\Omega A_C \, C_{n+1}^{\text{org}} \, \delta C \, dx \qquad , \qquad l_{C^{\text{org}}}(\delta C) = \int_\Omega (1 - \phi) \, C_n^{\text{org}} \, \delta C \, dx \qquad (4.1)$$

where $A_C = (1 - \phi) + \Delta t \, a_b \, [b_0 + c_b(C_0^{\text{org}} - C_n^{\text{org}})] \, \Psi_1(w_n) \, \Psi_2(T_n)$ and $a_{C^{\text{org}}}(C_{n+1}^{\text{org}}, \delta C) = l_{C^{\text{org}}}(\delta C) \, \forall \delta C \in H^1(\Omega)$.

In a similar fashion, we derive the variational formulation of the heat equation and at $t = t_n$ we seek $T_{n+1} \in H^1(\Omega)$ such that $T_{n+1}|_{\Gamma_t} = T_m$, $T_{n+1}|_{\Gamma_b \cup \Gamma_l} = T_g$ and $a_T(T_{n+1}, \delta T) = l_T(\delta T) \, \forall \delta T \in H_0^1(\Omega)$, where

$$a_T(T_{n+1}, \delta T) = \int_\Omega T_{n+1} \, \delta T \, dx + \Delta t \int_\Omega k_T \nabla T_{n+1} \cdot \nabla \delta T \, dx, \qquad (4.2)$$

$$l_T(\delta T) = \int_\Omega T_n \, \delta T \, dx - \int_\Omega c_T(C_{n+1}^{\text{org}} - C_n^{\text{org}}) \, \delta T \, dx. \qquad (4.3)$$

Remark 4.1. In (4.2) and (4.3), we evaluate the time derivative $\partial_t C^{\text{org}}$ at $t = t_n$, that is we consider the current value and not the previous one as stated at the beginning of this section. This is feasible because the solution of problem (4.1) precedes the one of the heat equation thus the value C_{n+1}^{org} is known when solving (4.2)-(4.3).

Remark 4.2. In (4.3) we assume that the same time discretization is used for both the organic carbon and the temperature. If this is not the case, the second term in the linear form $l_T(\cdot)$ would feature a scaling factor $\frac{\Delta t_T}{\Delta t_C}$, the numerator being the time scale associated with the temperature and the denominator the one for the organic carbon. For the rest of this paper, we will assume that all the unknowns are approximated using the same time discretization.

By substituting C_n^{org} and T_n with their Finite Element counterparts $C_{h,n}^{\text{org}}$ and $T_{h,n}$ in (4.1), (4.2) and (4.3) we obtain the corresponding discretized equations for the organic carbon and the temperature.

4.3. Stabilized dual-mixed formulation of the velocity field

A good approximation of the velocity field is a key point for a satisfactory simulation of all the transport phenomena. In order for problem (3.15) to be well-posed, the following compatibility condition has to be fulfilled

$$\int_\Omega F^{\text{out}} = 0. \qquad (4.4)$$

Nevertheless, (4.4) does not stand for the problem under analysis thus we consider a slightly modified version of problem (3.15) by introducing a small perturbation parameter $\lambda = \mathcal{O}(\ell_K)$, ℓ_K being the diameter of the element K of the triangulation $\mathcal{T}_h$:

$$\begin{cases} \nabla \cdot u + \lambda p = F^{\text{out}}, & \text{in } \Omega \\ u = -\nabla p, & \text{in } \Omega \\ u \cdot n = 0, & \text{on } \partial\Omega \end{cases} \qquad (4.5)$$

Hence the resulting problem (4.5) is well-posed even if (4.4) does not stand.

It is well-known in the literature [12] that classical discretizations of problem (4.5) by means of Lagrangian Finite Element functions lead to poor approximations of the velocity field. A widely accepted workaround relies on the derivation of mixed formulations in which a simultaneous approximation of pressure and velocity fields is performed by using different Finite Element spaces [24].

4.3.1. *Dual-mixed formulation*

Let $H(\mathrm{div}) = \{v \in [L^2(\Omega)]^3 \text{ s.t. } \nabla \cdot v \in L^2(\Omega)\}$ and $H_0(\mathrm{div}) = \{v \in H(\mathrm{div}) \text{ s.t. } v \cdot n = 0 \text{ on } \partial\Omega\}$. The dual-mixed formulation of problem (4.5) is obtained by seeking $(u, p) \in H_0(\mathrm{div}) \times L^2(\Omega)$ such that

$$\begin{cases} \displaystyle\int_\Omega \nabla \cdot u \delta p \ dx + \int_\Omega \lambda p \delta p \ dx = \int_\Omega F^{\mathrm{out}} \delta p \ dx \\ \displaystyle\int_\Omega u \cdot \delta u \ dx - \int_\Omega p \nabla \cdot \delta u \ dx = 0 \end{cases} , \quad \forall (\delta u, \delta p) \in H_0(\mathrm{div}) \times L^2(\Omega).$$

Hence, the bilinear and linear forms associated with the variational formulation of the problem respectively read as

$$a_{\mathrm{vel}}(\{u, p\}, \{\delta u, \delta p\}) = \int_\Omega u \cdot \delta u \ dx - \int_\Omega p \nabla \cdot \delta u \ dx - \int_\Omega \nabla \cdot u \delta p \ dx - \int_\Omega \lambda p \delta p \ dx \qquad (4.6)$$

$$l_{\mathrm{vel}}(\{\delta u, \delta p\}) = -\int_\Omega F^{\mathrm{out}} \delta p \ dx \qquad (4.7)$$

To overcome the constraint due to the LBB compatibility condition that the Finite Element spaces have to fulfill [5], several stabilization approaches have been proposed in the literature over the years and in this work we consider a strategy inspired by the Galerkin Least-Squares method and known as CGLS [11].

4.3.2. *Galerkin Least-Squares stabilization*

The GLS formulation relies on adding one or more quantities to the bilinear form of the problem under analysis in order for the resulting bilinear form to be strongly consistent and stable. Let L be the abstract operator for the Boundary Value Problem $L\varphi = g$. We introduce the solution φ_h of the corresponding problem discretized via the Finite Element Method. The GLS stabilization term reads as

$$\mathcal{L}^{\mathrm{GLS}}(\varphi_h, g; \psi_h) = d \int_\Omega (L\varphi_h - g) L\psi_h \ dx.$$

GLS formulation of Darcy's law

Following the aforementioned framework, we have

$$L_1(\{u, p\}) = g_1 \qquad \text{with} \qquad L_1(\{u, p\}) := u + \nabla p, \qquad g_1 := 0.$$

Thus the GLS term associated with Darcy's law reads as

$$\mathcal{L}_1^{\mathrm{GLS}}(\{u_h, p_h\}, g_1; \{\delta u_h, \delta p_h\}) = d_1 \int_\Omega (u_h + \nabla p_h) \cdot (\delta u_h + \nabla \delta p_h) \ dx. \qquad (4.8)$$

GLS formulation of the mass balance equation

The equation describing the mass equilibrium may be rewritten as

$$L_2(\{u, p\}) = g_2 \qquad \text{with} \qquad L_2(\{u, p\}) := \nabla \cdot u + \lambda p, \qquad g_2 := F^{\mathrm{out}}.$$

Consequently, the Least-Squares stabilization term has the following form

$$\mathcal{L}_2^{\text{GLS}}(\{u_h, p_h\}, g_2; \{\delta u_h, \delta p_h\}) = \underbrace{d_2 \int_\Omega (\nabla \cdot u_h + \lambda p_h)(\nabla \cdot \delta u_h + \lambda \delta p_h) \, dx}_{\mathcal{L}_{2a}^{\text{GLS}}(\{u_h, p_h\}, g_2; \{\delta u_h, \delta p_h\})} - \underbrace{d_2 \int_\Omega F^{\text{out}}(\nabla \cdot \delta u_h + \lambda \delta p_h) \, dx}_{\mathcal{L}_{2l}^{\text{GLS}}(\{u_h, p_h\}, g_2; \{\delta u_h, \delta p_h\})}. \quad (4.9)$$

GLS formulation of the curl of Darcy's law

Let us consider the rotational component of Darcy's law. Since p is a scalar field, $\nabla \times (\nabla p) = 0$ and we get

$$L_3(\{u, p\}) = g_3 \qquad \text{with} \qquad L_3(\{u, p\}) := \nabla \times u, \qquad g_3 := 0.$$

Thus, the GLS term associated with the curl of Darcy's law reads as

$$\mathcal{L}_3^{\text{GLS}}(\{u_h, p_h\}, g_3; \{\delta u_h, \delta p_h\}) = d_3 \int_\Omega (\nabla \times u_h)(\nabla \times \delta u_h) \, dx. \quad (4.10)$$

The stabilized CGLS dual-mixed formulation

The stabilized CGLS formulation arises by combining the previous terms. In particular, we consider the bilinear form (4.6), we subtract the Least-Squares stabilization (4.8) for Darcy's law and we add the corresponding GLS terms (4.9) and (4.10) for the mass balance equation and the curl of Darcy's law itself. In a similar fashion, we assemble the linear form for the stabilized problem, starting from (4.7). The resulting CGLS formulation of problem (4.5) has the following form:

$$\begin{aligned}
a_{\text{CGLS}}(\{u_h, p_h\}, \{\delta u_h, \delta p_h\}) =& a_{\text{vel}}(\{u_h, p_h\}, \{\delta u_h, \delta p_h\}) - \mathcal{L}_1^{\text{GLS}}(\{u_h, p_h\}, g_1; \{\delta u_h, \delta p_h\}) \\
& + \mathcal{L}_{2a}^{\text{GLS}}(\{u_h, p_h\}, g_2; \{\delta u_h, \delta p_h\}) + \mathcal{L}_3^{\text{GLS}}(\{u_h, p_h\}, g_3; \{\delta u_h, \delta p_h\})
\end{aligned} \quad (4.11)$$

$$l_{\text{CGLS}}(\{\delta u_h, \delta p_h\}) = l_{\text{vel}}(\{\delta u_h, \delta p_h\}) + \mathcal{L}_{2l}^{\text{GLS}}(\{u_h, p_h\}, g_2; \{\delta u_h, \delta p_h\}) \quad (4.12)$$

To accurately approximate problem (4.11)-(4.12), we consider the product space $RT_0 \times \mathbb{P}_0$, that is we use lowest-order Raviart-Thomas Finite Element for the velocity and piecewise constant functions for the pressure.

4.4. Streamline Upwind Petrov Galerkin for the dynamics of gases and liquid water

The numerical approximation of pure advection and advection-diffusion transient problems has to be carefully handled in order to retrieve accurate solutions. It is well-known in the literature [4] that classical Finite Element Method suffers from poor accuracy when dealing with steady-state advection and advection-diffusion problems and requires the introduction of numerical stabilization to construct a strongly consistent scheme. When moving to transient advection and advection-diffusion problems, time-space elements are the most natural setting to develop stabilized methods [15].

Let L_{ad} be the abstract operator to model an advection - respectively advection-diffusion - phenomenon. The resulting transient Boundary Value Problem may be written as

$$\phi \partial_t \varphi + L_{\text{ad}} \varphi = g_{\text{ad}}. \quad (4.13)$$

We consider the variational formulation of (4.13) by introducing the corresponding abstract bilinear form $B_{\text{ad}}(\varphi, \psi)$ which will be detailed in next subsections. Let φ_h be the solution of the discretized PDE via the Finite Element Method. The SUPG stabilization term for the transient problem reads as

$$\mathcal{L}^{\text{SUPG}}(\varphi_h, g_{\text{ad}}; \psi_h) = d \int_\Omega (\phi \partial_t \varphi_h + L_{\text{ad}} \varphi_h - g_{\text{ad}}) L_{\text{ad}}^{\text{SS}} \psi_h \, dx$$

where $L_{\mathrm{ad}}^{\mathrm{SS}}$ is the skew-symmetric part of the advection - respectively advection-diffusion - operator and d is a stabilization parameter constant in space and time. Let $\mathcal{T}_h$ be the computational mesh that approximates the domain Ω and ℓ_K the diameter of each element $K \in \mathcal{T}_h$. We choose:

$$d \coloneqq \frac{1}{2\|u\|_2} \max_{K \in \mathcal{T}_h} \ell_K. \tag{4.14}$$

Let $V_h \coloneqq \{\psi_h \in \mathcal{C}(\overline{\Omega}) \text{ s.t. } \psi_h|_K \in \mathbb{P}_k(K) \ \forall K \in \mathcal{T}_h\}$ be the space of Lagrangian Finite Element of degree k, that is the piecewise polynomial functions of degree k on each element K of the mesh $\mathcal{T}_h$. The stabilized SUPG formulation of the advection - respectively advection-diffusion - problem (4.13) reads as follows: for all $t \in (0, S^{\mathrm{fin}}]$ we seek $\varphi_h(t) \in V_h$ such that

$$\int_\Omega \phi \partial_t \varphi_h \psi_h \, dx + B_{\mathrm{ad}}(\varphi_h, \psi_h) + \mathcal{L}^{\mathrm{SUPG}}(\varphi_h, g_{\mathrm{ad}}; \psi_h) = \int_\Omega g_{\mathrm{ad}} \psi_h \, dx \qquad \forall \psi_h \in V_h. \tag{4.15}$$

Concerning time discretization, it is well-known in the literature that implicit schemes tend to increase the overall computational cost associated with the solution of a PDE. Nevertheless, precise approximations of advection and advection-diffusion equations via explicit schemes usually require high-order methods and are subject to stability conditions that may be responsible of making computation unfeasible. On the contrary, good stability and convergence properties of implicit strategies make them an extremely viable option when dealing with complex - possibly coupled - phenomena and with equations featuring noisy parameters. In particular, owing to the coupling of several PDE's, the solution of the advection and advection-diffusion equations presented in our model turned out to be extremely sensitive to the choice of the involved parameters. Being the tuning of the unknown coefficients of the equations one of the main goal of the SiViBiR++ project, a numerical scheme unconditionally stable and robust to the choice of the discretization parameters is sought. Within this framework, we consider an implicit Euler scheme for the time discretization and we stick to low-order Lagrangian Finite Element functions for the space discretization. The numerical scheme arising from the solution of equation (4.15) by means of the aforementioned approximation is known to be stable and to converge quasi-optimally [6].

In the following subsections, we provide some details on the bilinear and linear forms involved in the discretization of the advection and advection-diffusion equations as well as on the formulation of the associated stabilization terms.

4.4.1. *The case of gases*

Let us consider a generic gas G whose Finite Element counterpart is named G_h. Within the previously introduced framework, we get

$$L_G G \coloneqq u \cdot \nabla G, \qquad g_G \coloneqq F^G, \qquad B_G(G, \delta G) = \int_\Omega (u \cdot \nabla G) \delta G \, dx.$$

Hence, the SUPG stabilization term reads as

$$\mathcal{L}_G^{\mathrm{SUPG}}(G_h, g_G; \delta G_h) = d \int_\Omega (\phi \partial_t G_h + u \cdot \nabla G_h - F^G)(u \cdot \nabla \delta G_h) \, dx.$$

By introducing an implicit Euler scheme to approximate the time derivative in (4.15), we obtain the fully discretized advection problem for the gas G: at $t = t_n$ we seek $G_{h,n+1} \in V_h$ such that $a_G(G_{h,n+1}, \delta G_h) = l_G(\delta G_h) \ \forall \delta G_h \in V_h$, where

$$a_G(G_{h,n+1}, \delta G_h) = \int_\Omega \phi G_{h,n+1}(\delta G_h + d \, u \cdot \nabla \delta G_h) \, dx + \Delta t \int_\Omega u \cdot \nabla G_{h,n+1}(\delta G_h + d \, u \cdot \nabla \delta G_h) \, dx, \tag{4.16}$$

$$l_G(\delta G_h) = \int_\Omega \phi G_{h,n}(\delta G_h + d \, u \cdot \nabla \delta G_h) \, dx + \Delta t \int_\Omega F^G(\delta G_h + d \, u \cdot \nabla \delta G_h) \, dx. \tag{4.17}$$

Remark 4.3. As the authors highlight in [4], from a practical point of view the implementation of (4.16)-(4.17) may not be straightforward due to the non-symmetric mass matrix resulting from the discretization of the first term in (4.16).

By considering $F^O = F^N = 0$, we get the linear forms associated with the dynamic of oxygen and nitrogen:

$$l_O(\delta O_h) = \int_\Omega \phi O_{h,n}(\delta O_h + d\ u \cdot \nabla \delta O_h)\, dx\,,$$
$$l_N(\delta N_h) = \int_\Omega \phi N_{h,n}(\delta N_h + d\ u \cdot \nabla \delta N_h)\, dx. \tag{4.18}$$

In a similar way, when $F^j = -c_j \partial_t C^{\mathrm{org}}\ \ j = M, C$, we obtain the linear forms for methane and carbon dioxide:

$$l_M(\delta M_h) = \int_\Omega \phi M_{h,n}(\delta M_h + d\ u \cdot \nabla \delta M_h)\, dx - \int_\Omega c_M(C^{\mathrm{org}}_{h,n+1} - C^{\mathrm{org}}_{h,n})(\delta M_h + d\ u \cdot \nabla \delta M_h)\, dx\,,$$
$$l_{C^{\mathrm{dx}}}(\delta C_h) = \int_\Omega \phi C^{\mathrm{dx}}_{h,n}(\delta C_h + d\ u \cdot \nabla \delta C_h)\, dx - \int_\Omega c_C(C^{\mathrm{org}}_{h,n+1} - C^{\mathrm{org}}_{h,n})(\delta C_h + d\ u \cdot \nabla \delta C_h)\, dx. \tag{4.19}$$

Eventually, the dynamic of the water vapor is obtained when considering $F^h = -c_h \partial_t C^{\mathrm{org}} - F^{\mathrm{cond}}$:

$$l_h(\delta h_h) = \int_\Omega \phi h_{h,n}(\delta h_h + d\ u \cdot \nabla \delta h_h)\, dx - \int_\Omega c_h(C^{\mathrm{org}}_{h,n+1} - C^{\mathrm{org}}_{h,n})(\delta h_h + d\ u \cdot \nabla \delta h_h)\, dx - \Delta t \int_\Omega F^{\mathrm{cond}}(\delta h_h + d\ u \cdot \nabla \delta h_h)\, dx. \tag{4.20}$$

4.4.2. The case of liquid water

The dynamic of the liquid water being described by an advection-diffusion equation, the SUPG framework may be written in the following form:

$$L_w w := u_w \cdot \nabla w - k_w \Delta w, \qquad g_w := F^{\mathrm{cond}} + F^{\mathrm{in}}, \qquad B_w(w, \delta w) = \int_\Omega \left((u_w \cdot \nabla w)\delta w + k_w \nabla w \cdot \nabla \delta w \right) dx.$$

Hence the stabilization term reads as

$$\mathcal{L}^{\mathrm{SUPG}}_w(w_h, g_w; \delta w_h) = d_w \int_\Omega (\phi \partial_t w_h + u_w \cdot \nabla w_h - k_w \Delta w_h - F^{\mathrm{cond}} - F^{\mathrm{in}})(u_w \cdot \nabla \delta w_h)\, dx$$

where d_w is obtained by substituting u_w in (4.14). We obtain the fully discretized problem in which at each $t = t_n$ we seek $w_{h,n+1} \in V_h$ such that

$$a_w(w_{h,n+1}, \delta w_h) = l_w(\delta w_h) \qquad \forall \delta w_h \in V_h$$
$$a_w(w_{h,n+1}, \delta w_h) = \int_\Omega \phi w_{h,n+1}(\delta w_h + d_w\ u_w \cdot \nabla \delta w_h)\, dx + \Delta t \int_\Omega u_w \cdot \nabla w_{h,n+1}(\delta w_h + d_w\ u_w \cdot \nabla \delta w_h)\, dx$$
$$+ \Delta t \int_\Omega k_w \nabla w_{h,n+1} \cdot \nabla \delta w_h\, dx - \Delta t \int_\Omega k_w \Delta w_{h,n+1}(d_w\ u_w \cdot \nabla \delta w_h)\, dx\,, \tag{4.21}$$

$$l_w(\delta w_h) = \int_\Omega \phi w_{h,n}(\delta w_h + d_w\ u_w \cdot \nabla \delta w_h)\, dx + \Delta t \int_\Omega (F^{\mathrm{cond}} + F^{\mathrm{in}})(\delta w_h + d_w\ u_w \cdot \nabla \delta w_h)\, dx. \tag{4.22}$$

5. Numerical results

In this section we present some preliminary numerical simulations to test the proposed model. The SiViBiR++ project implements the discussed numerical methods for the approximation of the phenomena inside a bioreactor landfill. It is based on a C++ library named Feel++ which provides a framework to solve PDE's using the Finite Element Method [23].

5.1. **Feel++**

Feel++ stands for *Finite Element Embedded Language in C++* and is a C++ library for the solution of Partial Differential Equations using generalized Galerkin methods. It provides a framework for the implementation of advanced numerical methods to solve complex systems of PDE's. The main advantage of Feel++ for the applied mathematicians and engineers community relies on its design based on the Domain Specific Embedded Language (DSEL) approach [22]. This strategy allows to decouple the difficulties encountered by the scientific community when dealing with libraries for scientific computing. As a matter of fact, DSEL provides a high-level language to handle mathematical methods without loosing abstraction. At the same time, due to the continuing evolution of the state-of-the-art techniques in computer science (e.g. new standards in programming languages, parallel architectures, etc.) the choice of the proper tools in scientific computing may prove very difficult. This is even more critical for scientists who are not specialists in computer science and have to reach a compromise between user-friendly interfaces and high performances.

Feel++ proposes a solution to hide these difficulties behind a user-friendly language featuring a syntax that mimics the mathematical formulation by using a a much more common low-level language, namely C++.
Moreover, Feel++ integrates the latest C++ standard - currently C++14 - and provides seamless parallel tools to handle mathematical operations such as projection, integration or interpolation through C++ keywords. Feel++ is regularly tested on High Performance Computing facilities such as the PRACE research infrastructures (e.g. Tier-0 supercomputer CURIE, Supermuc, etc.) via multidisciplinary projects mainly gathered in the Feel++ consortium.

The embedded language provided by the Feel++ framework represents a powerful engineering tool to rapidly develop and deploy production of ready-to-use softwares as well as prototypes. This results in the possibility to treat physical and engineering applications featuring complex coupled systems from early-stage exploratory analysis till the most advanced investigations on cutting-edge optimization topics. Within this framework, the use of Feel++ for the simulation of the dynamic inside a bioreactor landfill seemed promising considering the complexity of the problem under analysis featuring multiphysics phenomena at different space and time scales.

A key aspect in the use of Feel++ for industrial applications like the one presented in this paper is the possibility to operate on parallel infrastructures without directly managing the MPI communications. Here, we briefly recall the main steps for the parallel simulation of the dynamic inside a bioreactor landfill highlighting the tools involved in Feel++ and in the external libraries linked to it:

- we start by constructing a computational mesh using Gmsh [13];
- a mesh partition is generated using Chaco or Metis and additional information about ghost cells with communication between neighbors is provided [13];
- Feel++ generates the required parallel data structures and create a table with global and local views for the Degrees of Freedom;
- Feel++ assembles the system of PDE's starting from the variational formulations and the chosen Finite Element spaces;
- the algebraic problem is solved using the efficient solvers and preconditioners provided by PETSc [2].

A detailed description of the high performance framework within Feel++ is available in [7].

5.2. **Geometric data**

We consider a reverse truncated pyramid domain as in figure 2C. The base of the domain measures $90\,\mathrm{m}\times 90\,\mathrm{m}$ and its height is $90\,\mathrm{m}$. All the lateral walls feature a slope of $\pi/6$. The alveolus counts 20 extraction drains

(A) Geometry of the alveolus.   (B) Surface mesh.   (C) Volume mesh.
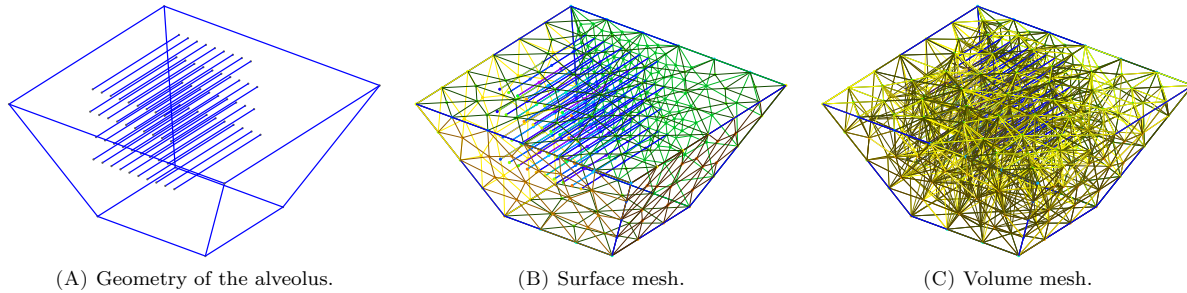
FIGURE 3. Geometry of the alveolus and computational mesh generated using GMSH. Each layer of 1D lines alternatively represents a set of water injectors or a group of extraction drains for the gas.

organized on 2 levels and 20 injection pipes, distributed on 2 levels as well. All the pipes are $25\,\mathrm{m}$ long and are modeled as 1D lines since their diameters are of order $10^{-1}\,\mathrm{m}$. A simplified scheme of the alveolus under analysis is provided in figure 3A and the corresponding computational domain is obtained by constructing a triangulation of mesh size $5\,\mathrm{m}$ (Fig. 3C).

5.3. Heuristic evaluation of the unknown constants in the model

The model presented in this paper features a large set of unknown variables (i.e. diffusion coefficients, scaling factors, ...) whose role is crucial to obtain realistic simulations. In this section, we propose a first set of values for these parameters that have been heuristically deduced by means of some qualitative and numerical considerations. A major improvement of the model is expected by a more rigorous tuning of these parameters which will be investigated in future works.

Porous medium

The physical and chemical properties of the bioreactor considered as a porous environment have been derived by experimental results in the literature. In particular, we consider a porosity $\Phi = 0.3$ and a permeability $D = 10^{-11}\,\mathrm{m}^2$.

Bacteria and organic carbon

We consider both the concentration of bacteria b and of organic carbon C^{org} as non-dimensional quantities in order to estimate their evolution. Thus we set $b_0 = 1$ and $C_0^{\mathrm{org}} = 1$ and we derive the values $a_b = 10^{-5}\,\mathrm{m}^6\mathrm{kg}^{-2}\mathrm{d}^{-1}$ and $c_b = 1$ respectively for the rate of consumption of the organic carbon and for the rate of reproduction of bacteria. Within this framework and under the optimal conditions of reaction prescribed by (3.1), C^{org} decreases to $2‰$ of its initial value during the lifetime of the bioreactor whereas bacteria concentration b remains bounded ($b < 2b_0$).

Temperature

As per experimental data, the optimal temperature for the methanogenic fermentation to take place is $T_{opt} = 35\,°\mathrm{C} = 308\,\mathrm{K}$ with an admissible variation of temperature of $\pm A_T = 20\,°\mathrm{C} = 20\,\mathrm{K}$ to guarantee the survival of bacteria. The factor c_T represents the heat produced per unit of consumed organic carbon and per unit of time and is estimated to $c_T = 10^2\,\mathrm{K}\,\mathrm{m}^2\mathrm{d}^{-1}$. The thermal conductivity of the waste inside the alveolus is fixed at $k_T = 9 \times 10^{-2}\,\mathrm{m}^2\mathrm{d}^{-1}$. In order to impose realistic boundary conditions for the heat equation, we consider different values for the temperature of the lateral surface of the alveolus $T_g = 5\,°\mathrm{C} = 278\,\mathrm{K}$ and the one of the top geomembrane $T_m = 20\,°\mathrm{C} = 293\,\mathrm{K}$.

Water

The production of methane takes place only when less than 10% of water is present inside the bioreactor. Since the alveolus is completely flooded when $w = 1000 \, \mathrm{kg \, m^{-3}}$, we get that $w_{\max} = 100 \, \mathrm{kg \, m^{-3}}$. The vertical velocity drift due to gravity is estimated from Darcy's law to the value $\|u_w\| = 2.1 \, \mathrm{m \, d^{-1}}$ and the diffusion coefficient is set to $k_w = 8.6 \times 10^{-2} \, \mathrm{m^2 d^{-1}}$.

Phase transition

In order to model the phase transitions, we have to consider the critical values of the pressure associated with evaporation and condensation. The Rankine law for the vapor pressure of water is approximated using the following values: $P_0 = 133.322 \, \mathrm{Pa}$, $s_0 = 20.386$ and $s_1 = 5132K$ and its linearization arises when considering $H_0 = -9.56 \times 10^4 \, \mathrm{Pa}$ and $H_1 = 337.89 \, \mathrm{Pa \, K^{-1}}$ for the range of temperatures $[288 \, \mathrm{K}; 328 \, \mathrm{K}]$. Moreover, we set the value $c_{h \to w}$ that represents the speed for the condensation of vapor to liquid water: $c_{h \to w} = 10^{-1} \, \mathrm{d^{-1}}$.

Gases

We consider a gas mixture made of methane, carbon dioxide and water vapor. Its dynamical viscosity is set to $\mu_{\mathrm{gas}} = 1.3 \, \mathrm{Pa \, d^{-1}}$. Other parameters involved represent the rate of production of a specific gas (methane, carbon dioxide and water vapor) per unit of consumed organic carbon and per unit of time: $c_M = 1.8 \times 10^7 \, \mathrm{kg \, m^{-3}}$; $c_C = 2.6 \times 10^7 \, \mathrm{kg \, m^{-3}}$; $c_h = 2.5 \times 10^6 \, \mathrm{kg \, m^{-3}}$.

Remark 5.1. A key aspect in the modeling of a bioreactor landfill is the possibility to adapt the incoming flow of water and leachates J_{in} and the outgoing flow of biogas J_{out}. These values are user-defined parameters which are kept constant to $258 \, \mathrm{m^3 \, d^{-1}}$ for the simulations in this paper but should act as control variables in the framework of the forecast and optimization procedures described in the introduction.

5.4. **A preliminary test case**

In this section we present some preliminary numerical results obtained by using the SiViBiR++ module developed in FEEL++ to solve the equations presented in section 3 using the numerical schemes discussed in section 4. In particular, we remark that in all the following simulations we neglect the effects due to the gas and fluid dynamics inside the bioreactor landfill. Though this choice limits the ability of the discussed results to correctly describe the complete physical behavior of the system, this simplification is a necessary starting point for the validation of the mathematical model in section 3. As a matter of fact, the equations describing the gas and fluid dynamics feature several unknown parameters whose tuning - independent and coupled with one another - has to be accurately performed before linking them to the problems modeling the consumption of organic carbon and the evolution of the temperature.
Thus, here we restrict our numerical simulations to two main phenomena occurring inside the bioreactor landfill: first, we describe the consumption of organic carbon under some fixed optimal conditions of humidity and temperature; then we introduce the evolution in time of the temperature and we discuss the behavior of the coupled system given by equations (3.5)-(3.6).

The test cases are studied in the computational domain introduced in section 5.2: in particular, we consider the triangulation of mesh size $5 \, \mathrm{m}$ in figure 3C and we set the unit measure for the time evolution to $\Delta t = 365 \, \mathrm{d}$. The final time for the simulation is $S^{\mathrm{fin}} = 40$ years. The parameters inside the equations are set according to the values in section 5.3 but a thorough investigation of these quantities has to be performed to verify their accuracy. The computations have been executed using up to 32 processors and below we present some simulations for the aforementioned preliminary test cases.

Evolution of the organic carbon under optimal hydration and temperature conditions

First of all, we consider the case of a single uncoupled equation, that is the evolution of the organic carbon in a scenario in which the concentration of water and the temperature are fixed. Starting from equation (3.5), we assume fixed optimal conditions for the humidity and the temperature inside the bioreactor landfill. We set

a fixed amount of water $w = \frac{w_{\max}}{2}$ inside the alveolus and a constant temperature $T = T_{\mathrm{opt}}$. Thus, from (3.1) we get

$$\Psi_1(w) \equiv \frac{w_{\max}}{4}, \qquad \Psi_2(T) \equiv 1$$

and equation (3.5) reduces to

$$\begin{cases} (1-\phi)\partial_t C^{\mathrm{org}}(x,t) = -a_b \dfrac{w_{\max}}{4}\left[b_0 + c_b(C_0^{\mathrm{org}} - C^{\mathrm{org}}(x,t))\right] C^{\mathrm{org}}(x,t) , & \text{in } \Omega \times (0, S^{\mathrm{fin}}] \\ C^{\mathrm{org}}(\cdot,0) = C_0^{\mathrm{org}} , & \text{in } \overline{\Omega} , \end{cases} \tag{5.1}$$

It is straightforward to observe that equation (5.1) only features one unknown variable - namely the organic carbon - since the concentration of bacteria $b(x,t)$ is an affine function of the concentration of organic carbon itself (cf. equation (3.4)).

As stated in section 4.2, the key aspect in the solution of equation (5.1) is the handling of the non-linear reaction term. In order to numerically treat this term as described, at each time step we need the value C_n^{org} at the previous iteration to compute the semi-implicit quantity $C_{n+1}^{\mathrm{org}} C_n^{\mathrm{org}}$. To provide a suitable value of C_n^{org} during the first iteration, we solve a linearization of equation (5.1) and we use the corresponding solution to evaluate $C_{n+1}^{\mathrm{org}} C_n^{\mathrm{org}}$.

The initial concentration of organic carbon inside the bioreactor is set to 1 and in figure 4 we observe several snapshots of the quantity of organic carbon inside the alveolus at time $t = 1$ year, $t = 10$ years, $t = 20$ years and $t = 40$ years. At the end of the life of the facility, the amount of organic carbon inside the alveolus is $C^{\mathrm{org}} = 2.0 \times 10^{-3}$. In figure 5, we plot the evolution of the overall quantity of organic carbon with respect to

(A) Lifetime: 1 year.

(B) Lifetime: 10 years.

(C) Lifetime: 20 years.

(D) Lifetime: 40 years.
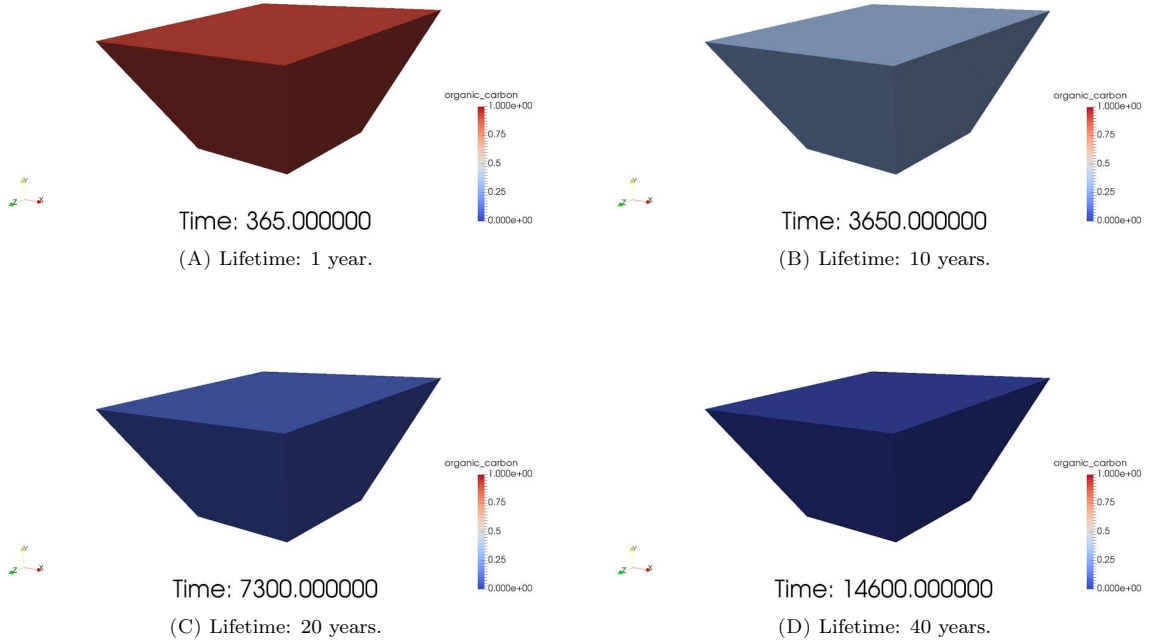
FIGURE 4. Evolution of the organic carbon inside the alveolus at $t = 1$ year, $t = 10$ years, $t = 20$ years and $t = 40$ years.

time. In particular, as expected we observe that C^{org} decreases in time as the methanogenic fermentation takes place.
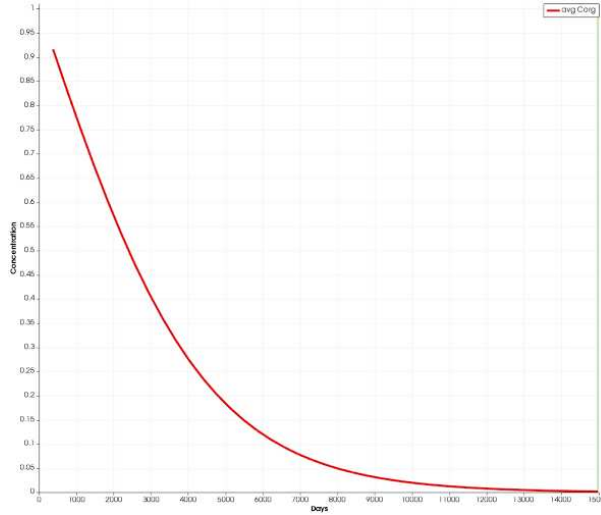
FIGURE 5. Evolution of the organic carbon between $t = 0$ and $t = 40$ years under optimal hydration and temperature conditions.

Evolution of the temperature as a function of organic carbon

We introduce a novel variable depending both on space and time to model the temperature inside the bioreactor. Figure 6 presents the snapshots of the value of the temperature in a section of the alveolus under analysis at time $t = 1$ year, $t = 10$ years, $t = 20$ years and $t = 40$ years. These result from the solution of equation (3.6) for a given trend of the organic carbon. Let us consider the evolution of the organic carbon obtained from the previous test case. The corresponding profile is given by

$$C^{\mathrm{org}}(x,t) = e^{-\alpha t} \qquad , \qquad \alpha = 10^{-3}.$$

We observe that the consumption of organic carbon by means of the chemical reaction (2.2) is responsible for the generation of heat in the middle of the domain. As expected by the physics of the problem, the heat tends to diffuse towards the external boundaries where the temperature is lower. After a first phase which lasts approximately 10 years in which the methanogenic process produces heat and the temperature rises, the consumption of organic carbon slows down and the temperature as well starts to decrease until the end-of-life of the facility (Fig. 7A-7B).

Evolution of the coupled system of organic carbon and temperature under optimal hydration condition

Starting from the previously discussed cases, we now proceed to the coupling of the organic carbon with the temperature. We keep the optimal hydration condition as in the previous simulations - that is $w = \frac{w_{\max}}{2}$ - and we consider the solution of the coupled equations (3.5)-(3.6).

From the numerical point of view, this scenario introduces several difficulties, mainly due to the fact that the two equations are now dependent on one another. As mentioned in section 4, the coupling is handled explicitly, that is, first we solve the problem featuring the organic carbon with fixed temperature then we approximate the heat equation using the information arising from the previously computed C^{org}.

(A) Lifetime: 1 year.

(B) Lifetime: 10 years.

(C) Lifetime: 20 years.

(D) Lifetime: 40 years.
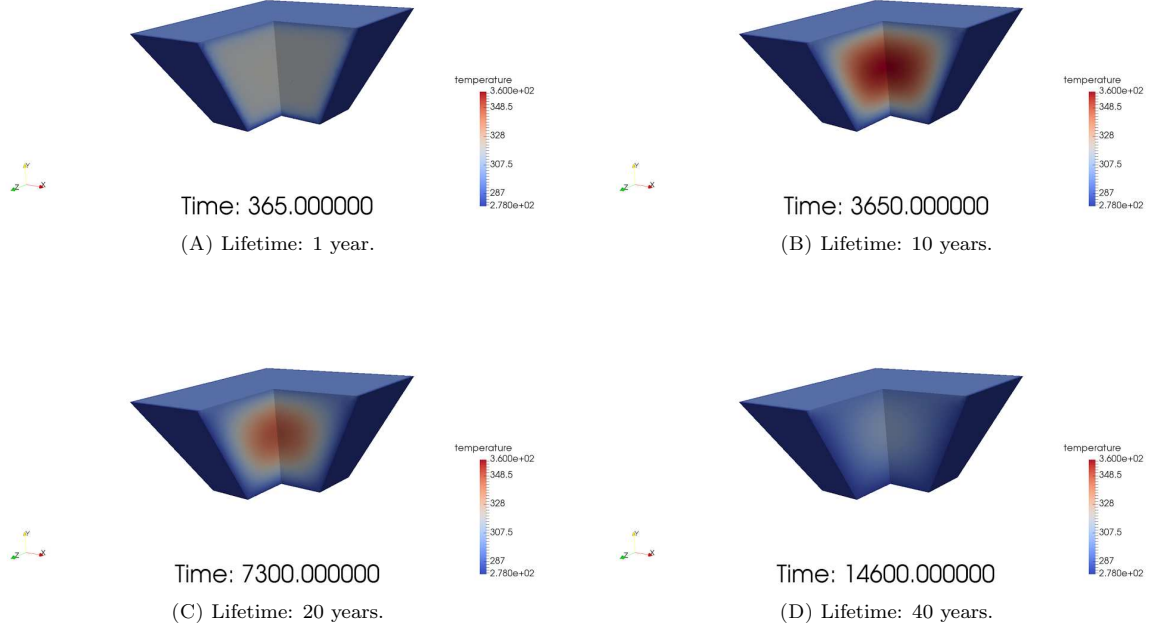
FIGURE 6. Evolution of the temperature inside the alveolus at $t = 1$ year, $t = 10$ years, $t = 20$ years and $t = 40$ years.

Within this framework, at time $t = t_n$ the conditions of humidity and temperature for the organic carbon equation read as

$$\Psi_1(w) \equiv \frac{w_{\max}}{4}, \qquad \Psi_2(T) = \max\left(0, 1 - \frac{|T_n - T_{\mathrm{opt}}|}{A_T}\right)$$

where T_n is the temperature at the previous iteration.

As in the previous case, we consider an initial concentration of organic carbon equal to 1 and we observe it decreasing in figure 8A due to the bacterial activity. We verify that the quantity of organic carbon inside the bioreactor landfill decays towards zero during the lifetime of the facility. At the same time, the temperature increases as a result of the methanogenic process catalyzed by the microbiota (Fig. 8B). Nevertheless, when the temperature goes beyond the tolerated variation A_T, the second condition in (3.1) is no more fulfilled and the chemical reaction is prevented. We may observe this behavior in figures 8A-8B between $t = 3$ years and $t = 20$ years. Once the temperature is inside the admissible range $[T_{\mathrm{opt}} - A_T; T_{\mathrm{opt}} + A_T]$ again (starting approximately from $t = 20$ years), the reaction (2.2) is allowed, the organic carbon is consumed and influences the temperature which slightly increases again before eventually decreasing towards the end-of-life of the bioreactor. Eventually, in figure 9 we report some snapshots of the solutions of the coupled system (3.5)-(3.6).

6. CONCLUSION

In this work, we proposed a first attempt to mathematically model the physical and chemical phenomena taking place inside a bioreactor landfill. A set of 7 coupled equations has been derived and a Finite Element discretization has been introduced using FEEL++. A key aspect of the discussed model is the tuning of the

(A) Evolution of the organic carbon.

(B) Evolution of the temperature.
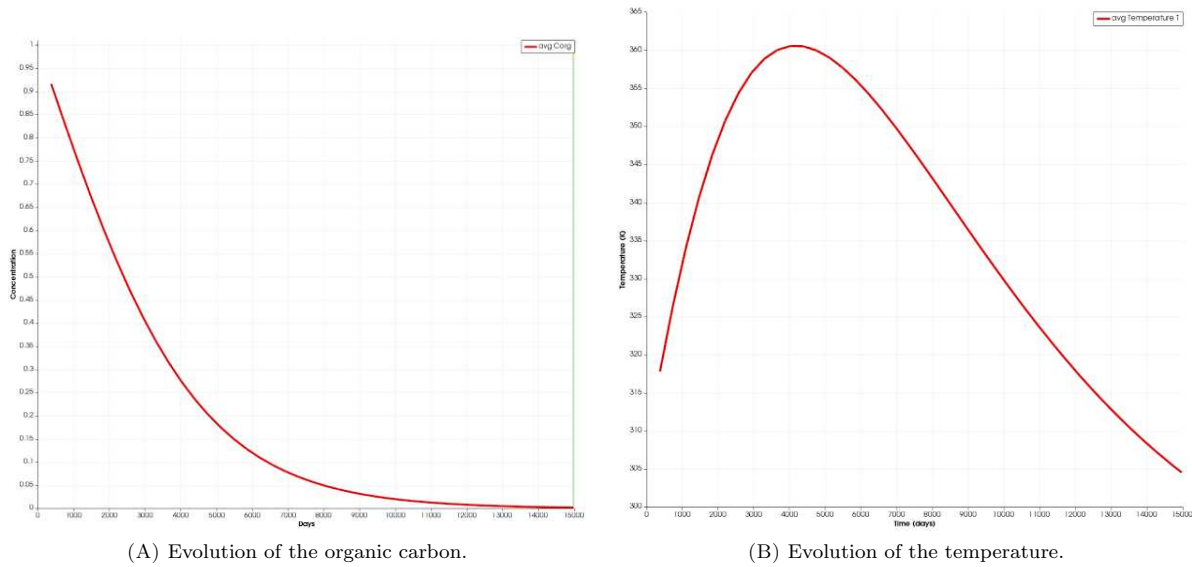
FIGURE 7. Evolution of the quantity of organic carbon and temperature inside the alveolus between $t = 0$ and $t = 40$ years.

(A) Evolution of the organic carbon.

(B) Evolution of the temperature.
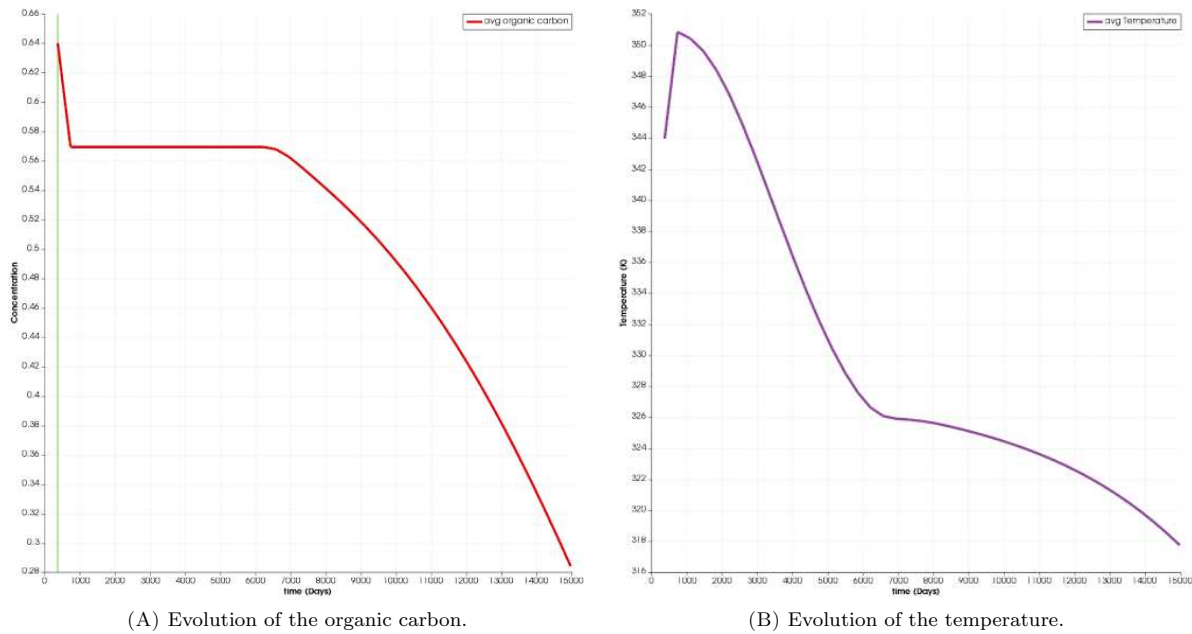
FIGURE 8. Evolution of the quantity of organic carbon and the temperature inside the alveolus between $t = 0$ and $t = 40$ years.
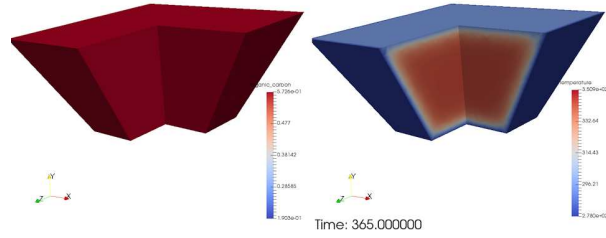
(A) Lifetime: 1 year.
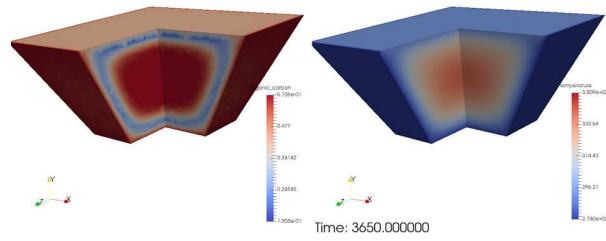
(B) Lifetime: 10 years.
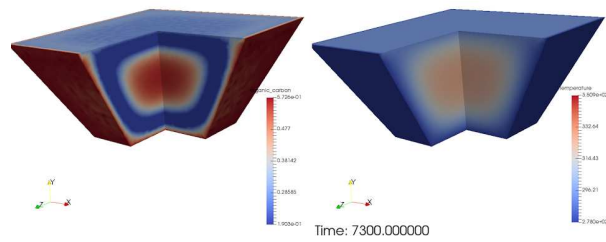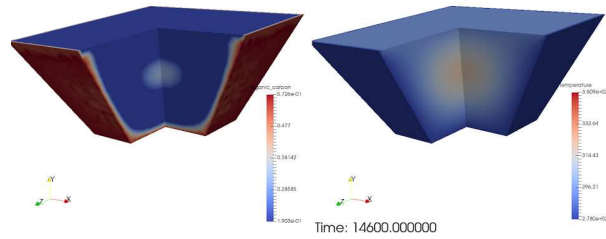
(C) Lifetime: 20 years.

(D) Lifetime: 40 years.

FIGURE 9. Coupled evolution of the organic carbon (left) and the temperature (right) inside the alveolus at $t = 1$ year, $t = 10$ years, $t = 20$ years and $t = 40$ years.

coefficients appearing in the equations. On the one hand, part of these unknowns represents physical quantities whose values may be derived from experimental studies. On the other hand, some parameters are scalar factors that have to be estimated by means of heuristic approaches. A rigorous tuning of these quantities represents a major line of investigation to finalize the implementation of the model in the SiViBiR++ module and its validation with real data.

The present work represents a starting point for the development of mathematically-sound investigations on bioreactor landfills. From a modeling point of view, some assumptions may be relaxed, for example by adding a term to account for the death rate of bacteria or the cooling effect due to water injection inside the bioreactor. The final goal of SiViBiR++ project is the simulation of long-time behavior of the bioreactor in order to perform forecasts on the methane production and optimize the control strategy. The associated inverse problems and PDE-constrained optimization problems are likely to be numerically intractable due to their complexity and their dimension thus the study of reduced order models may be necessary to decrease the overall computational cost.

A. Summary of the unknown parameters

In the following table, we summarize the values of some unknown parameters which were deduced during the present work. We highlight that all these quantities have been estimated via heuristic approaches and a rigorous verification/validation procedure remains necessary before their application to real-world problems.

Parameter	Description	Value	Unit
Φ	Porosity of the medium	0.3	
D	Permeability	10^{-11}	m^2
b_0	Initial concentration of bacteria	1.0	
C_0^{org}	Initial concentration of organic carbon	1.0	
a_b	Rate of consumption of organic carbon	10^{-5}	$m^6 kg^{-2} d^{-1}$
c_b	Rate of creation of bacteria	1.0	
T_{opt}	Optimal temperature for the reaction	308	K
A_T	Tolerated variation of temperature	20	K
c_T	Rate of production of heat by the chemical reaction	10^2	K
k_T	Thermal conductivity	9×10^{-2}	$m^2 d^{-1}$
T_g	Temperature of the soil	278	K
T_m	Temperature of the geomembrane	293	K
T_0	Initial temperature	293	K
$w_{\max}$	Maximal admissible quantity of water	100	$kg\,m^{-3}$
$\|u_w\|$	Velocity of the water	2.1	$m\,d^{-1}$
k_w	Diffusion coefficient of the water	8.6×10^{-2}	$m^2 d^{-1}$
w_0	Initial quantity of water	50	$kg\,m^{-3}$
H_0	Constant for the vapor pressure	-9.56×10^4	Pa
H_1	Constant for the vapor pressure	337.89	$Pa\,K^{-1}$
$c_{h \to w}$	Condensation rate	10^{-1}	d^{-1}
μ_{gas}	Dynamical viscosity of the gas	1.3	$Pa\,d^{-1}$
c_M	Rate of production of methane	1.8×10^7	$kg\,m^{-3}$

Parameter	Description	Value	Unit
c_C	Rate of production of carbon dioxide	2.6×10^7	$\mathrm{kg\,m^{-3}}$
c_h	Rate of production of water vapor	2.5×10^6	$\mathrm{kg\,m^{-3}}$
M_0	Initial concentration of methane	1.0	
C_0^{dx}	Initial concentration of carbon dioxide	1.0	
h_0	Initial concentration of water vapor	1.0	
J_{out}	Outgoing flow of biogas	258	$\mathrm{m^3 d^{-1}}$
J_{in}	Incoming flow of water and leachates	258	$\mathrm{m^3 d^{-1}}$

TABLE 1. Summary of the parameters involved in the 7-equations model.

Acknowledgments

References

[1] F. Agostini, C. Sundberg, and R. Navia. Is biodegradable waste a porous environment? A review. *Waste Manage. Res.*, 30(10):1001–1015, 2012.

[2] S. Balay, S. Abhyankar, M. Adams, J. Brown, P. Brune, K. Buschelman, L. Dalcin, V. Eijkhout, W. Gropp, D. Karpeyev, D. Kaushik, M. Knepley, L. Curfman McInnes, K. Rupp, B. Smith, S. Zampini, and H. Zhang. PETSc Users Manual. Technical report, Argonne National Laboratory, 2015.

[3] F. Bezzo, S. Macchietto, and C. C. Pantelides. General hybrid multizonal/CFD approach for bioreactor modeling. *AIChE Journal*, 49(8):2133–2148, 2003.

[4] P. B. Bochev, M. D. Gunzburger, and J. N. Shadid. Stability of the SUPG finite element method for transient advection-diffusion problems. *Comput. Method. Appl. M.*, 193(23-26):2301–2323, 2004.

[5] F. Brezzi and M. Fortin. *Mixed and hybrid finite elements methods*. Springer series in computational mathematics. Springer-Verlag, 1991.

[6] E. Burman. Consistent SUPG-method for transient transport problems: Stability and convergence. *Comput. Method. Appl. M.*, 199(17-20):1114–1123, 2010.

[7] V. Chabanne. *Vers la simulation des écoulements sanguins*. Ph.D. thesis, Université Joseph Fourier, Grenoble, 2013.

[8] T. Chassagnac. Etat des connaissances techniques et recommandantions de mise en oeuvre pour une gestion des installations de stockage de déchets non dangereux en mode bioréacteur. Technical report, ADEME - Agence Nationale de l'Environnement et de la Maîtrise de l'Energie. FNADE - Fédération Nationale des Activités de la Dépollution et de l'Environnement, 2007.

[9] A. J. Chorin and J. E. Marsden. *A mathematical introduction to fluid mechanics*, volume 4 of *Texts in Applied Mathematics*. Springer-Verlag, New York, third edition, 1993.

[10] D. Córdoba, F. Gancedo, and R. Orive. Analytical behavior of two-dimensional incompressible flow in porous media. *J. Math. Phys.*, 48(6):065206, 2007.

[11] M. R. Correa and A. F. D. Loula. Unconditionally stable mixed finite element methods for Darcy flow. *Comput. Method. Appl. M.*, 197(17-18):1525–1540, 2008.

[12] L. J. Durlofsky. Accuracy of mixed and control volume finite element approximations to Darcy velocity and related quantities. *Water Resour. Res.*, 30(4):965–973, 1994.

[13] C. Geuzaine and J.-F. Remacle. Gmsh: a three-dimensional finite element mesh generator with built-in pre- and postprocessing facilities, 2009.

[14] C. Johnson et al. Characterization, Design, Construction and Monitoring of Bioreactor Landfills. Technical report, ITRC - Interstate Technology & Regulatory Council, 2006.

[15] C. Johnson, U. Nävert, and J. Pitkäranta. Finite element methods for linear hyperbolic problems. *Comput. Method. Appl. M.*, 45(1):285–312, 1984.

[16] J. Kindlein, D. Dinkler, and H. Ahrens. Numerical modelling of multiphase flow and transport processes in landfills. *Waste Manage. Res.*, 24(4):376–387, 2006.

[17] T. Kling and J. Korkealaakso. Multiphase modeling and inversion methods for controlling landfill bioreactor. In *Proceedings of TOUGH Symposium*. Lawrence Berkeley National Laboratory, Berkeley, CA, USA, 2006.

[18] M. Lebeau and J.-M. Konrad. Natural convection of compressible and incompressible gases in undeformable porous media under cold climate conditions. *Comput. Geotech.*, 36(3):435–445, 2009.

[19] C. N. Liu, R. H. Chen, and K. S. Chen. Unsaturated consolidation theory for the prediction of long-term municipal solid waste landfill settlement. *Waste Manage. Res.*, 24(1):80–91, 2006.

[20] S. Martín, E. Marañón, and H. Sastre. Mathematical modelling of landfill gas migration in MSW sanitary landfills. *Waste Manage. Res.*, 19(5):425–435, 2001.

[21] P. McCreanor. *Landfill leachate recirculation systems: Mathematical modelling and validation*. PhD thesis, University of Central Florida, USA, 1998.

[22] C. Prud'homme. A Domain Specific Embedded Language in C++ for automatic differentiation, projection, integration and variational formulations. *Sci. Program.*, 14(2):81–110, 2006.

[23] C. Prud'homme, V. Chabannes, V. Doyeux, M. Ismail, A. Samake, and G. Pena. Feel++: A computational framework for Galerkin methods and advanced numerical methods. *ESAIM: ProcS*, 38:429–455, 2012.

[24] P. A. Raviart and J. M. Thomas. A mixed finite element method for second order elliptic problems. In I. Galligani and E. Magenes, editors, *Mathematical Aspects of Finite Element Methods*, volume 606 of *Lect. Notes Math*, pages 292–315. Springer-Verlag, 1977.

[25] D. R. Reinhart and B. A. Al-Yousfi. The impact of leachate recirculation on municipal solid waste landfill operating characteristics. *Waste Manage. Res.*, 14(4):337–346, 1996.

[26] H. S. Sidhu, M. I. Nelson, and X. D. Chen. A simple spatial model for self-heating compost piles. In W. Read and A. J. Roberts, editors, *Proceedings of the 13th Biennial Computational Techniques and Applications Conference, CTAC-2006*, volume 48 of *ANZIAM J.*, pages C135–C150, 2007.

[27] K. Vafai. *Handbook of porous media*. Crc Press, 2015.

[28] J. J. Walsh and R. N. Kinman. Leachate and gas production under controlled moisture conditions. In *Municipal Solid Waste: Land Disposal, Proceedings of the 5th Annual Research Symposium*, pages 41–57. EPA-600/9-79-023a, 1979.

Bibliography

[1]   Egan W.G. and T.W. Hilgeman. *Optical Properties of Inhomogeneous Materials*. Academic Press, 1979.

[10]   Ridgway Scott. "Finite element convergence for singular data". In: *Numerische Mathematik* 21.4 (1973), pp. 317–327.

[11]   Benoit Fabrèges and Bertrand Maury. "Approximation of single layer distributions by Dirac masses in Finite Element computations". In: *Journal of Scientific Computing* 58.1 (2014), pp. 25–40.

[2]   S.R Arridge. "Optical tomography in medical imaging". In: *IOPScience Inverse problem* 15.2 (1999).

[3]   Y. Yamada and S. Okawa. "Diffuse Optical Tomography: Present Status and Its Future". In: *Optical Review* 21.3 (2014), pp. 185–205.

[4]   Feng Gao, Huijuan Zhao, and Yukio Yamada. "Improvement of image quality in diffuse optical tomography by use of full time-resolved data". In: *Applied Optics* 41 (2012).

[5]   Elizabeth MC Hillman. "Experimental and theoretical investigations of near infrared tomographic imaging methods and clinical applications." PhD thesis. 2002.

[6]   Liu Kai, Tian Jie, Lu Yujie, Qin Chenghu, Yang Xin, Zhu Shouping, et al. "A fast bioluminescent source localization method based on generalized graph cuts with mouse model validations". In: *Optics Express* 18.4 (2010).

[7]   Jun Xia, Junjie Yao, and Lihong V Wang. "Photoacoustic tomography: principles and advances". In: *Electromagnetic waves (Cambridge, Mass.)* 147 (2014), p. 1.

[8]   Bruno Montcel and Patrick Poulet. "An instrument for small-animal imaging using time-resolved diffuse and fluorescence optical methods". In: *Nuclear Instruments and Methods in Physics Research* A 569 (2006).

[9]   Farouk Nouizi. "Tomographie optique diffuse et de fluorescence préclinique : instrumentation sans contact, modélisation et reconstruction 3D résolue en temps". PhD thesis. Université de Strasbourg, 2011.

[12]   Jacques Louis Lions and Enrico Magenes. *Non-homogeneous boundary value problems and applications*. Vol. 1. Springer Science & Business Media, 2012.

[13]   Lucio Boccardo and Thierry Gallouët. "Non-linear elliptic and parabolic equations involving measure data". In: *Journal of Functional Analysis* 87.1 (1989), pp. 149–169.

[14]   Thierry Gallouët. "Measure data and numerical schemes for elliptic problems". In: *Elliptic and parabolic problems* (2005), pp. 279–290.

[15]   Alain Prignet. "Conditions aux limites non homogenes pour des problemes elliptiques avec second membre mesure". In: *annales-faculte des sciences toulouse mathematiques*. Vol. 6. Citeseer. 1997.

[16]   Avner Friedman. *Partial differential equations of parabolic type*. Courier Dover Publications, 2008.

[17]   Olga Aleksandrovna Ladyzhenskaia, Vsevolod Alekseevich Solonnikov, and Nina N Ural'ceva. *Linear and quasi-linear equations of parabolic type*. Vol. 23. American Mathematical Soc., 1968.

[18]   Murielle Torregrossa. "Reconstruction d'images obtenues par tomographie optique dans le proche infrarouge". PhD thesis. Université de Strasbourg, 2003.

[19]   Guillaume Dollé, Zakaria Belhachmi, Christophe Prud'homme, and Murielle Torregrossa. *Diffuse Optical Tomography and Fluorescence Simulation*. See also on youtube. June 2014. DOI: 10.5281/zenodo.11830. URL: https://doi.org/10.5281/zenodo.11830.

[20]   B Canuto and O Kavian. "Determining coefficients in a class of heat equations via boundary measurements". In: *SIAM Journal on Mathematical Analysis* 32.5 (2001), pp. 963–986.

[21]   Grégoire Allaire, Diogo Silva, and Olivier Pantz. "Sur un probleme inverse de détermination de coefficients de diffusion". In: (Nov. 2004).

[22]   Christophe Prud'Homme, Vincent Chabannes, Vincent Doyeux, Mourad Ismail, Abdoulaye Samake, and Gonçalo Pena. "Feel++: A computational framework for galerkin methods and advanced numerical methods". In: *ESAIM: Proceedings*. Vol. 38. EDP Sciences. 2012, pp. 429–455.

[23]   Cecile Daversin - Catty. "Reduced basis method applied to large non-linear multi-physics problems : application to high field magnets design". Theses. Université de Strasbourg, Sept. 2016. URL: https://tel.archives-ouvertes.fr/tel-01361722.

[24]   Stephane Veys. "A computational reduced basis framework : applications to nonlinears multiphysics problems". Theses. Université de Grenoble, Nov. 2014. URL: https://tel.archives-ouvertes.fr/tel-01525889.

[25]   Alfio Quarteroni and Silvia Quarteroni. *Numerical models for differential problems*. Vol. 2. Springer, 2009.

[26]   Satish Balay, Shrirang Abhyankar, Mark F. Adams, Jed Brown, Peter Brune, Kris Buschelman, et al. *PETSc Users Manual*. Tech. rep. ANL-95/11 - Revision 3.9. Argonne National Laboratory, 2018. URL: http://www.mcs.anl.gov/petsc.

[27]   Yousef Saad. *Iterative methods for sparse linear systems*. Vol. 82. siam, 2003.

[28]   Satish Balay, William D. Gropp, Lois Curfman McInnes, and Barry F. Smith. "Efficient Management of Parallelism in Object Oriented Numerical Software Libraries". In: *Modern Software Tools in Scientific Computing*. Ed. by E. Arge, A. M. Bruaset, and H. P. Langtangen. Birkhäuser Press, 1997, pp. 163–202.

[29]   Victorita Dolean, Pierre Jolivet, and Frâdâric Nataf. *An introduction to domain decomposition methods: algorithms, theory, and parallel implementation*. Vol. 144. SIAM, 2015.

[30]   Pierre Jolivet, Frédéric Hecht, Frédéric Nataf, and Christophe Prud'homme. "Scalable Domain Decomposition Preconditioners for Heterogeneous Elliptic Problems". In: *Proceedings of the International Conference on High Performance Computing, Networking, Storage and Analysis*. SC '13. Denver, Colorado: ACM, 2013, 80:1–80:11. ISBN: 978-1-4503-2378-9. DOI: 10.1145/2503210.2503212. URL: http://doi.acm.org/10.1145/2503210.2503212.

[31]   Pierre-Henri Tournier, Ioannis Aliferis, Marcella Bonazzoli, Maya de Buhan, Marion Darbas, Victorita Dolean, et al. "Microwave Tomographic Imaging of Cerebrovascular Accidents by Using High-Performance Computing". working paper or preprint. July 2016. URL: https://hal.archives-ouvertes.fr/hal-01343687.

[32]   Pierre Jolivet and Pierre-Henri Tournier. "Block Iterative Methods and Recycling for Improved Scalability of Linear Solvers". In: *SC16 - International Conference for High Performance Computing, Networking, Storage and Analysis*. Proceedings of SC16: International Conference for High Performance Computing, Networking, Storage and Analysis. Salt Lake City, Utah, United States, Nov. 2016. URL: https://hal.archives-ouvertes.fr/hal-01357998.

[33]   Vincent Doyeux. "Modeling and simulation of multi-fluid systems. Application to blood flows." Theses. Université de Grenoble, Jan. 2014. URL: https://tel.archives-ouvertes.fr/tel-00939930.

[34]   Andreas Wächter and Lorenz T Biegler. "On the implementation of an interior-point filter line-search algorithm for large-scale nonlinear programming". In: *Mathematical programming* 106.1 (2006), pp. 25–57.

[35]   Haim Brezis. *Functional analysis, Sobolev spaces and partial differential equations*. Springer Science & Business Media, 2010.

List of figures

List of tables

Listings

Acronym

Index

Résumé   La tomographie optique diffuse et de fluorescence résolue en temps (TR-TODF) est une méthode qui permet de fournir une information sur les propriétés optiques de diffusion et d'absorption des tissus biologiques. Ce manuscrit de thèse fait l'état de l'art de la méthode et propose des pistes pour reconstruire des images multidimensionnelles 2D/3D des cartes optiques du milieu. L'objectif ultime du projet présenté dans ce document est de concevoir un appareil de mesure (tomographe), éventuellement portatif, pour détecter la présence de tumeurs. Le défi est de pouvoir obtenir des images avec une résolution suffisante pour être utilisée en milieu hospitalier à des fins de diagnostic préclinique. Hors le caractère naturellement mal posé du problème inverse rend la tâche complexe.
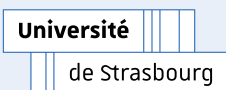
La première partie du document est consacrée à la modélisation du problème physique. En particulier nous nous intéressons à l'approximation de diffusion de l'équation du transfert radiatif dans un milieu quelconque. Dans une deuxième partie, nous traitons le problème du point de vue mathématiques en considérant le problème direct de diffusion couplé avec de la fluorescence pour deux type de mesures: en mode contact et non-contact. Puis nous nous intéressons au problème inverse comme un problème de minimisation d'une fonctionnelle que nous traitons par une méthode de l'adjoint. Enfin et pour finir, la troisième partie du document détaille les différents aspects numérique pour parvenir à un code de reconstruction efficace à l'aide de techniques issues du calcul haute performance.

Mots-clés : *tomographie, diffusion, fluorescence, reconstruction, feel++*

Summary   The Time-Resolved Diffuse Optical Tomography and Fluorescence (TR-DOTF) is a method to obtain optical properties information on diffusion and asbsorption of biological tissues. This Phd manuscript details this method state of the art and highlight the different possible path to reconstruct multidimensionnal 2D/3D images for the optical maps of the turbid medium. The project ultimate goal is to build a measurement instrument (tomograph), eventually portative, in order to detect tumours presence. The challenge is to obtain images with sufficient resolution to be used in medical environment for preclinical diagnosis. However the inverse problem ill-posedness makes the situation more difficult.

The first part of this document is devoted to the problem modelization. In particular, we are interested to the diffusion approximation for the radiative transfer equation in a turbid medium. In a second part, we treat this problem from a mathematical point of view considering the diffusion problem coupled with fluorescence for two measurement types: contact and non-contact. Then we focus on the inverse problem as a minimization problem for cost objective function solved by an adjoint method. Last, but not least, the third part of this document details the different numerical aspects involved to achieve an efficient reconstruction code using advanced technics from the high performance computing world.

keywords: *tomography, diffusion, fluorescence, reconstruction, feel++*